UNIVERSITY OF LEICESTER

Assessment of a novel small field of view medical hybrid gamma camera

---

A thesis submitted for the degree of Doctoral of Philosophy

By

MOHAMMED SAEED M ALQAHTANI

Space Research Centre

Department of Physics and Astronomy

DECEMBER 2017

Assessment of a novel small field of view medical hybrid gamma camera

Mohammed Saeed M Alqahtani

Abstract

Small field of view (SFOV) gamma detection and imaging technologies for monitoring in vivo tracer uptake are rapidly expanding and being introduced for bed-side imaging and image guided surgical procedures. The Hybrid Gamma Camera (HGC) has been developed, at the University of Leicester, to enhance the localisation of targeted radiopharmaceuticals during surgical procedures, for example in sentinel lymph node (SLN) biopsies, and for bed-side imaging in small organ gamma imaging procedures such as lacrimal scintigraphy and thyroid scintigraphy.

In this thesis, prototype medical phantoms including anthropomorphic three-dimensional printed phantoms have been designed, constructed, and evaluated using representative modelled medical scenarios to study the capability of the HGC to detect SLNs and image small organs. Furthermore, the results of the first clinical feasibility study of the HGC has been discussed. The HGC was used to perform non-invasive hybrid gamma-optical imaging procedures on patients attending their routine scint32igraphic imaging appointments in a nuclear medicine clinic.

Various quantitative and qualitative assessments have been conducted on different phantom configurations including simulating targeted tissues at several depths and using different radioactivity concentrations. Two generations of the HGC have been utilised, having two different thicknesses of columnar CsI(Tl) scintillator, and two pinhole collimator diameters (0.5 mm and 1.0 mm). Additionally, the behaviour of the HGC at a range of imaging distances and acquisition times has been examined. All of these factors were considered to judge the detection limitations of the HGC.

The results demonstrate that the HGC was ideally suited for small organ imaging. The HGC capability to detect low activity uptake in small SLNs indicates its usefulness as an intraoperative imaging system during surgical SLN procedures. The ability of the HGC to utilise both pinhole collimators enhances its practicality and improves its ability to meet the needs of SFOV gamma imaging.

Acknowledgment

List of publications and conferences

Publications

1. **Mohammed S Alqahtani**, John E Lees, Sarah L Bugby, Piyal Samara-Ratna, Aik H Ng, Alan C. Perkins. *Design and implementation of a prototype head and neck phantom for the performance evaluation of gamma imaging systems*. EJNMMI Physics, 2017. **4**(1): p. 19.

2. Aik H. Ng, Patricia E. Blackshaw, **Mohammed S. Alqahtani**, Layal K. Jambi, Sarah L. Bugby, John E. Lees and Alan C. Perkins. *A novel compact small field of view hybrid gamma camera: first clinical results*. Nuclear Medicine Communications, 2017. **38**(9).

3. Lees, J.E., S.L. Bugby, **M.S. Alqahtani**, L.K. Jambi, N.S. Dawood, W.R. McKnight, A.H. Ng, and A.C. Perkins, *A Multimodality Hybrid Gamma-Optical Camera for Intraoperative Imaging.* Sensors (Basel), 2017. 17(3).

4. **MS Alqahtani**, JE Lees, SL Bugby, LK Jambi, BS Bhatia, WR McKnight, NS Dawood, AH Ng and AC Perkins. *Capability of a novel small field of view hybrid gamma camera (HGC) for sentinel lymph node and small organ imaging*. Soc. Nuclear Med. 58(Supplement 1): 157, 2017.

5. LK Jambi, JE Lees, SL Bugby, **MS Alqahtani**, BS Bhatia, WR McKnight, NS Dawood, AH Ng and AC Perkins. *A hand-held hybrid gamma-near-infrared fluorescence imaging camera*. Soc. Nuclear Med. 58(Supplement 1): 220, 2017.

6. Layal K. Jambi, John E. Lees, Sarah L. Bugby, Bahadar S. Bhatia, **Mohammed S. Alqahtani**, Numan S. Dawood, Aik H. Ng, Alan C. Perkins. Comparison of columnar and pixelated scintillators for small field of view hybrid gamma camera imaging. IEEE Xplore. 2016 IEEE Nuclear Science Symposium, Medical Imaging Conference and Room-Temperature Semiconductor Detector Workshop (NSS/MIC/RTSD), Strasbourg, France, 2017, p.1-4.

7. **M.S. Alqahtani**, J.E. Lees, S.L. Bugby, L.K. Jambi, A.C. Perkins. Quantitative investigation of a novel small field of view hybrid gamma camera (HGC) capability for sentinel lymph node detection. The British Journal of Radiology, 2016(89): p. 20160435.

8. **MS Alqahtani**, JE Lees, SL Bugby, LK Jambi, BS Bhatia, WR McKnight, NS Dawood, AH Ng, AC Perkins. *Quantitative analysis of sentinel node detection using a novel small field of view hybrid gamma camera (HGC)*. Soc. Physica Medica. 32(Supplement 3): 256-257, 2016

9. Bugby, S.L., J.E. Lees, A.H. Ng, **M.S. Alqahtani**, and A.C. Perkins, *Investigation of an SFOV hybrid gamma camera for thyroid imaging.* Phys Med, 2016. **32**(1): p. 290-6

10. AC Perkins, AH Ng, SL Bugby, PE Blackshaw, **MS Alqahtani**, LK Jambi, JE Lees. *A novel compact hybrid optical gamma camera: First clinical results*. Soc. Nuclear Med. 57(Supplement 2):531, 2016.

11. **MS Alqahtani**, JE Lees, SL Bugby, LK Jambi, BS Bhatia, WR McKnight, NS Dawood, AH Ng, AC Perkins. *Investigation of a novel small field of view hybrid compact gamma camera (HCGC) for scintigraphic imaging*. Insights Imaging 7(Supplement 1):162, 2016.

12. **M.S. Alqahtani**, J.E. Lees, S.L. Bugby, L.K. Jambi, A.C. Perkins. Lymphoscintigraphic imaging study for quantitative evaluation of a small field of view (SFOV) gamma camera. J. Inst. 10(7):P07011, 2015.

13. L.K. Jambi, J.E. Lees, S.L. Bugby, S. Tipper, **M.S. Alqahtani**, A.C. Perkins. Evaluation of XRI-UNO detector for nuclear medical imaging. J. Inst. 10(6):P06012, 2015.

14. J.E. Lees, S.L. Bugby, B.S. Bhatia, L.K. Jambi, **M.S. Alqahtani**, W.R. McKnight, A.H.Ng, A.C. Perkins. A small field of view camera for hybrid gamma and optical imaging. J. Inst. 9(12):C12020, 2014.

Conferences

1. JE Lees, SL Bugby, **MS Alqahtani**, LK Jambi, NS Dawood, WR McKnight, BS Bhatia, AH Ng and AC Perkins. Hybrid gamma camera for medical applications. PSD11: 11th International Conference on Position Sensitive Detectors, Milton Keynes, UK, 2017.

2. JE Lees, SL Bugby, **MS Alqahtani**, LK Jambi, NS Dawood, WR McKnight, BS Bhatia, AH Ng and AC Perkins. A multimodality camera for intraoperative imaging. Cancer Imaging Conference. London, UK, 2017.

3. NS Dawood, JE Lees, SL Bugby, **MS Alqahtani**, LK Jambi, WR McKnight, AH Ng and AC Perkins. Radionuclide depth estimation using a novel SFOV hybrid gamma-optical camera with an anthropomorphic breast phantom. The 45th Annual Spring BNMS Meeting. Birmingham, UK, 2017.

4. AH Ng, **MS Alqahtani**, LK Jambi, SL Bugby, JE Lees and AC Perkins. Use of a novel small field of view hybrid gamma camera (HGC) for Iodine-125 seed localisation. The 45th Annual Spring BNMS Meeting. Birmingham, UK, 2017.

5. SL Bugby, JE Lees, AH Ng, **MS Alqahtani**, LK Jambi, MA Stammes, HJM Handgraaf, AC Perkins. Portable hybrid gamma-near-infrared fluorescence imaging. European Association of Nuclear Medicine (EANM) Annual Congress. Barcelona, Spain, 2016. DOI: 10.1007/s00259-016-3484-4

6. JE Lees, SL Bugby, **MS Alqahtani**, LK Jambi, AH Ng, NS Dawood, AC Perkins. A high-resolution hybrid gamma-optical camera for intraoperative imaging. European Association of Nuclear Medicine (EANM) Annual Congress. Barcelona, Spain, 2016. DOI: 10.1007/s00259-016-3484-4

7. **MS Alqahtani**, JE Lees, SL Bugby, LK Jambi, BS Bhatia, WR McKnight, NS Dawood, AH Ng, AC Perkins. Investigation of a novel small field of view hybrid compact gamma camera (HCGC) for scintigraphic imaging. European Congress of Radiology (ECR), Vienna, Austria, 2016. Abstract available in: http://dx.doi.org/10.1594/ecr2016/B-0033

8. LK Jambi, JE Lees, SL Bugby, **MS Alqahtani**, BS Bhatia, WR McKnight, NS Dawood, AH Ng, AC Perkins. Development of a small field of view gamma camera for medical imaging. European Congress of Radiology (ECR), Vienna, Austria, 2016. Abstract available in: http://dx.doi.org/10.1594/ecr2016/C-2206

9. AH Ng, SL Bugby, LK Jambi, **MS Alqahtani**, PE Blackshaw, PS Morgan, JE Lees, AC Perkins. Development of a hybrid optical-gamma camera: A new innovation in bedside molecular imaging. World Congress on Medical Physics and Biomedical Engineering, Toronto, Canada, 2015.

10. NS Dawood, JE Lees, SL Bugby, LK Jambi, **MS Alqahtani**, WR McKnight, AC Perkins. A method of source-depth estimation using a Hybrid Gamma Camera. British Institute of Radiology (BIR) Annual Congress, London, UK, 2015. Abstract available in: http://www.eposters.net/poster/a-method-for-source-depth-estimation-using-a-hybrid-gamma-camera-

11. **MS Alqahtani**, JE Lees, SL Bugby, LK Jambi, AC Perkins. Assessment of a novel hybrid optical-gamma camera for nuclear scintigraphic imaging, UK Radiological Congress (UKRC), Liverpool, UK, 2015.

12. JE Lees, AC Perkins, SL Bugby, BS Bhatia, LK Jambi, **MS Alqahtani**, WR McKnight, NS Dawood, AH Ng. A high-resolution handheld hybrid camera for gamma and optical imaging. British Nuclear Medicine Society (BNMS) Autumn Meeting, London, UK, 2015.

13. **MS Alqahtani**, JE Lees, SL Bugby, LK Jambi, AC Perkins. Assessment of a novel hybrid optical-gamma camera for nuclear scintigraphic imaging, KFMC Conference on Medical Physics and Engineering in Medicine, Riyadh, Kingdom of Saudi Arabia, 2015.

14. LK Jambi, JE Lees, SL Bugby, **MS Alqahtani**, BS Bhatia, WR McKnight, AH Ng, AC Perkins. A high-resolution gamma-optical hybrid camera for medical imaging, KFMC Conference on Medical Physics and Engineering in Medicine, Riyadh, Kingdom of Saudi Arabia, 2015.

15. AH Ng, SL Bugby, LK Jambi, **MS Alqahtani**, D Clay, PE Blackshaw, PS Morgan, JE Lees, AC Perkins. Hybrid optical-gamma camera for intraoperative imaging: A flexible phantom to assess system performances for sentinel node detection. International Conference on Clinical PET-CT and Molecular Imaging (IPET), Vienna, Austria, 2015.

16. **MS Alqahtani**, JE Lees, SL Bugby, BS Bhatia, LK Jambi, AH Ng, AC Perkins. A lymphoscintigraphic phantom study using a novel hybrid optical-gamma camera. British Institute of Radiology (BIR) Annual Congress, London, UK, 2014. Abstract available in: http://www.eposters.net/poster/a-lymphoscintigraphic-phantom-study-using-a-novel-hybrid-optical-gamma-camera

17. LK Jambi, JE Lees, SL Bugby, BS Bhatia, **MS Alqahtani**, WR McKnight, AH Ng, AC Perkins. Performance of a hybrid gamma-optical camera for improved utility in diagnostic imaging. British Institute of Radiology (BIR) Annual Congress, London, UK, 2014. Abstract available in: http://www.eposters.net/poster/performance-of-a-hybrid-gamma-optical-camera-for-improved-utility-in-diagnostic-imaging

18. JE Lees, SL Bugby, BS Bhatia, LK Jambi, **MS Alqahtani**, AH Ng, AC Perkins. A small field of view camera for hybrid gamma and optical imaging. PSD10: 10th International Conference on Position Sensitive Detectors, Guildford, UK, 2014.

Contents

Chapter 1. Introduction

1.1. General role of nuclear medicine in healthcare services

Over the past decade, significant technological developments have led to a remarkable shift in diagnosing disease and delivering treatment. As a result, the majority of advanced diagnostic and therapeutic decisions are based on imaging technologies and analysis of biological probes (1). Advanced computer calculations and radiation detector technology support the growth of available medical imaging technologies, such as magnetic resonance imaging (MRI), ultrasound (US) and X-ray imaging. Such technologies are able to generate morphological images of targeted human tissues and trace gas and fluid distributions inside the human body (1). Despite the success of these technologies, they are limited as most are unable to evaluate the precise functionality of a targeted tissue (2).

To visually investigate the physiological processes in biological tissues, a sensitive, functional imaging tool that is able to measure and quantify physiological changes is required. Nuclear medicine technology uses radiopharmaceutical agents (i.e. radioactive atoms attached to a carrier molecule) to provide functional imaging, and is the only medical imaging technology able to depict and investigate real-time physiological, cellular processes. Currently, this technology is utilised to provide clinical information about the functionality of a targeted tissue; furthermore, this technology can be supplemented by morphological imaging technologies that are effective in displaying structural changes in the tissue (1).

Diagnostic radiopharmaceuticals and nuclear medicine technology are important in oncology to indicate the grading and aggressiveness of potential tumours and metastases in the whole human body. Moreover, in a new era of precision medicine, nuclear medicine technology is used to tailor therapeutic procedures to the specific needs of each patient; diverse new molecules can predict the likely efficacy or

inefficiency of a treatment. These principles underpin diagnostic radiopharmaceuticals and are expanding the scope of nuclear medicine services to include personalised medicine. For example, for cardiac patients, nuclear medicine technologies are facilitating the identification of ischemic or necrotic cardiac tissue, and for neurological patients, these technologies enable degenerative diseases to be diagnosed long before clinical manifestations, such as in Alzheimer disease (3, 4).

Furthermore, using alpha or beta-emitting isotopes, in place of the gamma-emitting isotopes typically used, diagnostic radiopharmaceuticals can become highly efficient selective therapeutic tools. Additionally, using dual-purpose radionuclides that can be utilised for both diagnostic and therapeutic purposes extends the scope of nuclear medicine considerably (5).

In surgical settings, nuclear medicine technologies and techniques play an integral role in localising potential affected, cancerous tissues, such as sentinel lymph nodes (SLNs). During cancer surgeries, SLNs are localised utilising a non-imaging gamma probe, after the administration of radiopharmaceutical agents (such as ^{99m}Tc-nanocolloids) tracing affected tissues (6). Non-imaging intraoperative probes are still routinely-used as tools for tracing radioactivity accumulation sites during surgical procedures; however, they are unable to provide precise information about radioactivity distribution (more explanation is provided in the following chapter).

In this regard, intraoperative real-time gamma imaging with a compact, small field of view (SFOV) imaging system could offer a suitable solution; as it can provide two-dimensional (2D) images of the radioactivity accumulation within its field of view (FOV) (6, 7). Such a camera could facilitate the surgical oncology procedure and provide valuable information through localisation of affected tissues in critical situations, such as a targeted SLN residing close to the radioactivity injection site, which could be flooded when using the gamma probe.

Currently, there are several SFOV compact gamma imaging systems available, some of these are commercial, and some of them still in the research and testing stage (8). The Hybrid Gamma Camera (HGC) has been designed and manufactured at the Space Research Centre (SRC) - University of Leicester in collaboration with the University of

Nottingham (UK). The BioImaging Unit researchers at the SRC have been able to employ their experience in radiation detection instrumentation development to facilitate the construction process of a novel high-resolution SFOV compact hybrid gamma camera (HGC) with the capability of providing hybrid optical-gamma imaging simultaneously. The research work presented in this thesis focusses on assessing the hybrid optical-gamma imaging capabilities of the HGC in various experimental, real and simulated clinical settings.

1.2. Research motivation and aims

Through employing existing approaches, for instance, non-imaging gamma probes, preoperative gamma camera imaging, and the "blue dye" technique, there is a relatively high confidence of finding sentinel lymph nodes (SLNs) during sentinel lymph node biopsy (SLNB) procedures. A meta-analysis of almost 70 published breast cancer studies was carried out by Newman (9) and a general sensitivity (i.e. the ability to detect an established abnormality) of above 90 % and a false negative rate (i.e. the incidence rate of negative test results in patients known to have the abnormality) of only 8.4 % were reported.

Additionally, it has been observed that 72-85 % detection rates for SLNs using preoperative gamma camera imaging can be achieved (10). With the use of intraoperative gamma probes, sentinel lymph nodes were successfully detected in 98 % of patients, with a 7 % false-negative rate. Furthermore, for intraoperative procedures, there was a 90 % detection rate for sentinel lymph nodes that were not detected by preoperative lymphoscintigraphy.

For sentinel node detection in breast cancer, the sensitivity of 85 % and a false-negative rate of 5 % have been recommended by the American Society of Breast Surgeons as tolerable (11). However, the need for further improvement exists, hence, optimum methods need to be developed to improve the sensitivity and reduce the false-negative rates of sentinel lymph node detection. The requisite improvement in SLN detection might be delivered by intraoperative gamma camera imaging. For instance, it was discussed by Mathelin et al. (12-14) that it was a useful approach to operate an intraoperative small field of view gamma camera (5 × 5 cm) for finding the SLNs in

breast cancer. In a case report, (13) the existence of an additional metastatic sentinel lymph node (with low radiotracer uptake), that was not detected by a gamma probe or with preoperative imaging, was actually observed by intraoperative gamma camera imaging, and it has been suggested that the false-negative detection rate can be reduced by using an intraoperative gamma camera.

Regardless of this promising initial data, within gamma probe-based detection of sentinel lymph nodes, the variable level of proficiency among surgeons is one of the considerations (11), and a detection rate of 90 % or better is not accomplished by all surgeons even with substantial exposure and training.

Furthermore, there may be structural or visibility issues linked with sentinel lymph nodes; i.e. nodes may be located within the high-activity normal tissues, which could be unusually deep (~ 30 mm), close to the injection site or have a low (below 1 %) radiotracer uptake (10, 13, 15, 16). These problematic nodes would be most likely visualised by intraoperative gamma cameras. Compared to gamma probes, additional practical benefits are to be delivered by SFOV imaging systems. For example, small gamma cameras produce a larger field of view (several centimetres) than probes (less than 1 cm), providing faster interrogation of large areas, with a reduction in statistical ambiguity (i.e. noise); in contrast to a variable-frequency tone or a numerical display, the signal is displayed as a scintigraphic image.

This work describes various assessment protocols in experimental settings (i.e. through using different bespoke phantoms simulating clinical scenarios) and during routine gamma imaging procedures in nuclear medicine clinics. The prime goal of this thesis is to evaluate the suitability of the HGC for clinical imaging during routine (such as thyroid scintigraphy, lacrimal scintigraphy, or lymphoscintigraphy) and surgical gamma imaging procedures (such as SLNs biopsy procedures). To achieve this, quantitative and qualitative evaluation of the HGC imaging system was performed; such evaluation explored potential uses to aid technical and practical improvement for the systems, which leads to an improvement in patient management during surgical or routine nuclear medicine procedures.

1.3. Overview of the thesis

The research work presented in this thesis is described over 9 chapters. Figure 1.1 gives an overview schematic (i.e. mind map) of the conducted research work. Chapter 1 gives the reader a general introduction to the work, describing the motivation and aims underlying this research with an overview of the thesis components. Chapter 2 aims to delineate recent improvements and related anatomical and physiological concepts relating to lymphatic visualisation, focusing on available intraoperative gamma detecting technologies used for the visualisation of lymph nodes and the functionality testing. Chapter 3 will provide the reader with a review of the SFOF gamma imaging systems and a background to the HGC's development. Furthermore, the similarities and differences between a SFOV gamma imaging system (i.e. HGC) and conventional gamma cameras will be illustrated.

Chapter 4 discusses the initial investigation of the hybrid gamma camera (HGC) in terms of its suitability for lymphoscintigraphic imaging, while Chapter 5 describes the lymph-node contrast (LNC) phantom construction, and evaluation of the HGC's capability to detect different sizes of simulated SLNs having various radioactivity concentrations placed at different depths. Chapter 6 introduces the development and the standardisation of a test object (i.e. an anthropomorphic head and neck phantom) and protocols particularly suited for SFOV compact gamma imaging systems, but which can be equally useful for large field of view (LFOV) systems.

Chapter 7 initiates a qualitative evaluation of the HGC to detect simulated SLNs distributed in the head and neck region through utilising an anthropomorphic head and neck phantom. In Chapter 8, the results of clinical evaluation, conducted at nuclear medicine clinics at Queen's Medical Centre and Nottingham City hospital (Nottingham Universities NHS trust), are discussed. Chapter 9 presents the overall conclusions, and draws a map of possible future work that can be conducted utilising the HGC.
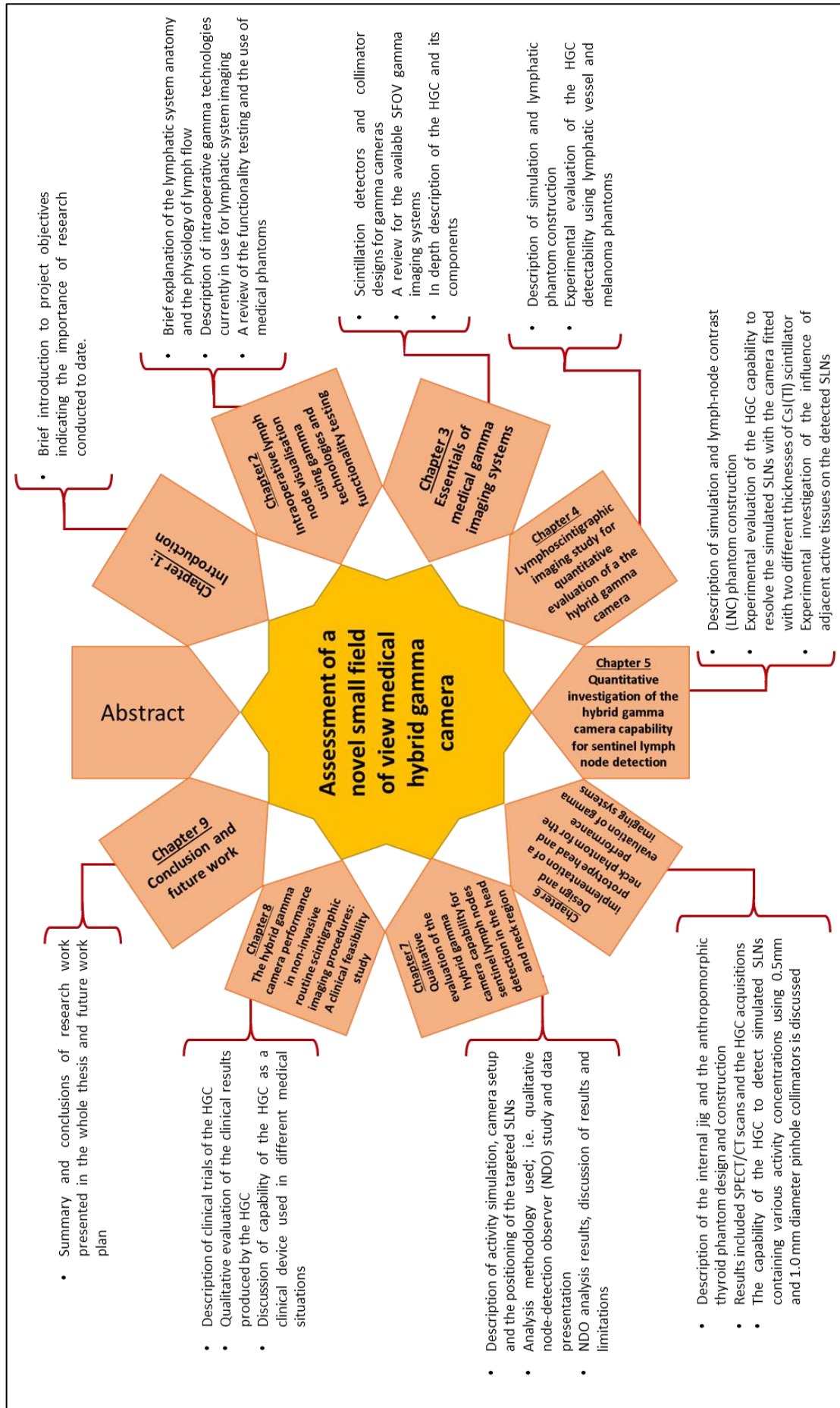
Figure1.1. Mind map showing the research aspects evaluated and discussed in this thesis

1.4. Personal contribution to this research work

The HGC imaging system evaluated in this research work was developed by the BioImaging unit research group prior to the start of my PhD course. The imaging software was developed by software developers at the Space Research Centre (SRC): Mr Oliver E. Blake and Mr Adam P. Bark. I designed and guided the construction of all prototype medical phantoms described in the research chapters. All of these medical phantoms were manufactured in the physics workshop, University of Leicester. The 3D thyroid phantom (discussed in Chapter 6) was designed by a mechanical engineer at the SRC: Mr Piyal Samara-Ratna. All computer-aided designs included in this work were produced using Siemens NX 8.05 software. The radioactive materials (i.e. Technetium-99m [^{99m}Tc]) used to conduct the presented experiments in this thesis have been provided by the nuclear medicine team at the Leicester Royal Infirmary (LRI).

I fully planned and conducted the experiments, and analysed the produced data of all research chapters in this thesis. I also developed the bespoke Java-script code used for the qualitative study in Chapter 7; this code has been criticised and improved by Mrs Malak Alqahtani, Software Engineering student at De Montfort University, Leicester. In addition, I was heavily involved in performing and analysing the data of the gamma imaging procedures for all clinical cases presented in Chapter 8. This feasibility study was carried out in collaboration with the nuclear medicine clinic at Queen's Medical Centre, University of Nottingham. Professor Alan C. Perkins and Professor John E. Lees were responsible for obtaining ethical approval for this clinical study; Ms Elaine Blackshaw and Professor Alan Perkins recruited patients for this study.

Chapter 2: Intraoperative lymph node visualisation using gamma technologies and functionality testing

2.1 Introduction

The lymphatic system is a multifaceted network of nodes and ducts that extends throughout the human body. It is through the lymphatic system that surplus interstitial fluid is taken back to the cardiovascular system. Unlike the circulation of blood, lymph flow is unidirectional, to clear fluids from various human tissues (17). Lymph is comparable to blood plasma and contains immune cells to protect against microorganisms. Additionally, lymphatic capillaries within the intestinal villi absorb the vitamins and fats that give the lymph its milky appearance throughout the lymphatic system (17). The lymphatic system shows substantial variation, between individuals, similar to other anatomical organs such as the arterial or venous plexus.

The lymphatic system has become a significant area of interest in oncology over the past few decades. It can protect against circulating tumour cells, but can also, conversely, be a course for metastatic spread and a location of cancer growth if its protection system fails. The important influence of the lymphatic system on the treatment, staging and outcomes of cancer has encouraged exploration targeted at providing additional insight into the numerous roles of the lymphatic system (18).

This chapter aims, not to offer a comprehensive anatomical and physiological overview of the lymphatic system, but to delineate recent improvements and related anatomical and physiological concepts to lymphatic visualisation, focusing on available intraoperative gamma detecting technologies used for the visualisation of lymph nodes.

2.2   Anatomy of the Lymphatic System

Although some unique aspects exist, the lymphatic ducts of the various organs and tissues within the body are broadly comparable. Lymphatic capillaries are heavily distributed within the skin, but also in other covering structures such as the periosteum of joints and bones. Moreover, rich lymphatic plexuses are located beneath the mucosa of the digestive, respiratory, and genitourinary tracts. In addition, they can be found underneath the mesothelium of the pleural, peritoneal, and pericardial cavities. Superficial or subserous lymphatic capillary plexuses are connected to the majority of solid organs in the human body, such as the spleen, liver, adrenal gland, prostate, kidney, uterus, testes, and ovaries (19). In addition, recent evidence has proven the existence of deep lymphatic plexuses inside the parenchyma within the adrenal gland, ovary, and kidney. Lymphatic capillaries are most likely absent from the central nervous system, eyeball, striated muscles, and inner ear. Collective lymphatic vessels are present in vascularised tissues and are frequently positioned close to the blood vessels. Researchers seeking more details may consult one of many textbooks for a wide-ranging explanation of the lymphatic systems within the human body   (19, 20).

2.3   The Physiology of Lymph Flow

Lymph flow begins with interstitial fluid absorption via the inter-endothelial intersections of the lymphatic capillaries which work like valves (17). Particles equal to 25 nm in diameter or smaller might penetrate the openings at this point, while bigger particles are transferred via the lymphatic endothelium by pinocytosis. Collagen filaments, appended to neighbouring connective tissues, keep the lymphatic capillaries open. Osmotic pressure plays a significant role in the filling of lymphatic capillaries. Given that the capillaries contain no valves, the lymph liquid may flow in any direction (21).

Several bicuspid semilunar valves, situated every 2–3 mm, stop the backflow of lymph within lymphatic vessels (21), as seen in Figure 2.1. There is dynamic, continuous lymph propulsion by circular and longitudinal layers of smooth muscles that have an active contraction process (10–15 times each minute).

Lymphatic peristalsis is controlled through various delicate processes (21, 22). As a result of the existence of valves, external pressure, applied by surrounding tissues, is an additional mechanism supporting unidirectional flow.
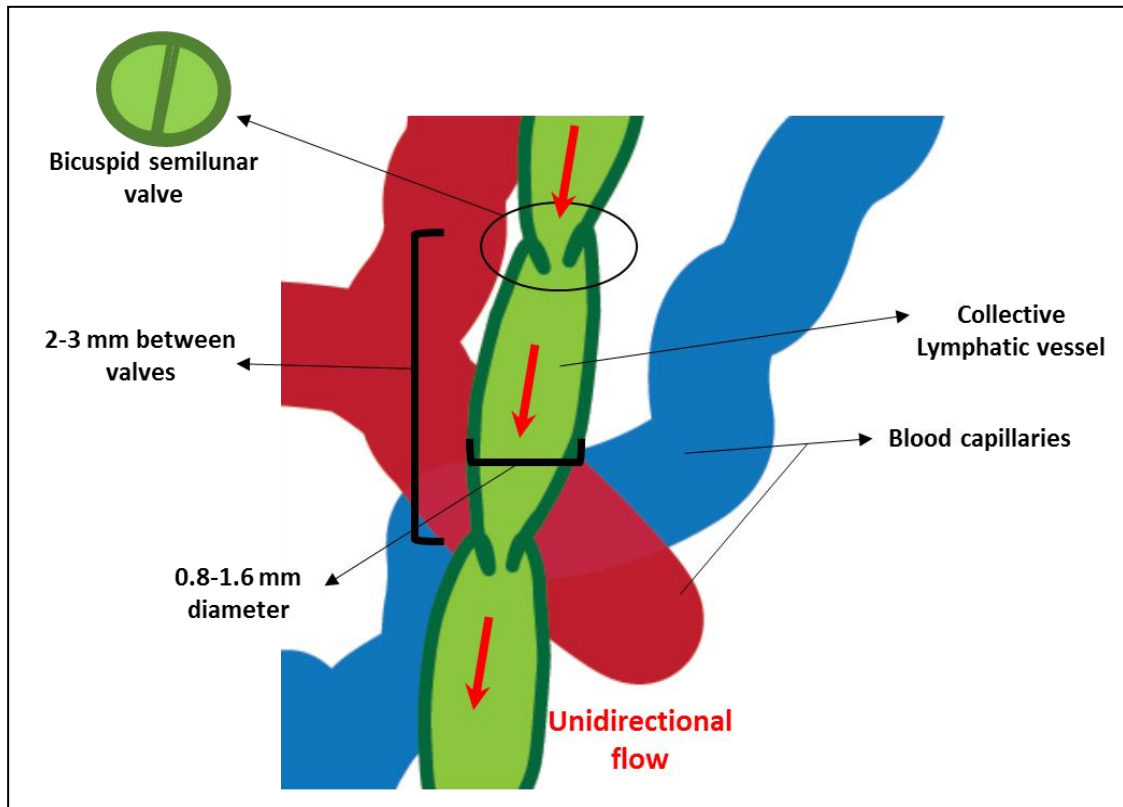
Figure 2.1. A schematic showing the anatomical shape of the collecting lymphatic vessels.

The filtered lymph is gathered at the lymph node hilum into the efferent lymphatic vessel (Figure 2.1). Various relationships exist between lymph nodes and lymph vessels, which are outside the scope of this chapter. Ultimately, a few large lymphatic trunks transfer 2–4 L of lymph daily from the entire body into the venous distribution at the intersection of the inner subclavian and jugular veins (19).

The anatomical and functional evaluation of the lymphatic systems may be undertaken using various medical imaging techniques including the use of radiopaque agents (i.e. contrast media), radiopharmaceuticals such as ^{99m}Tc-nanocolloids, coloured dyes, and fluorescent contrast agents. Some of these techniques will be briefly discussed in the following sections, with more focus on radioactive agents and intraoperative gamma detection technologies.

2.4 The concept of the sentinel lymph node (SLN)

The idea of lymphatic mapping in cancer is dependent on the concept that lymph fluid from a primary tumour site drains to a specific regional lymph node (Figure 2.2) (23). The sentinel lymph node (SLN) is the first node in the lymphatic network. Lymph fluid drains from the SLN through efferent lymph vessels to other nodes. When cancerous cells disseminate, they will initially be embedded within the SLN. This is the node that would receive any spread of the primary tumour site. Consequently, other lymph nodes might become involved via a stepwise approach. The afferent lymphatic vessel is the main component of the SLN concept, gathering lymph fluid from the cancerous tissues and supplying it to the lymph node that serves as the primary filter.
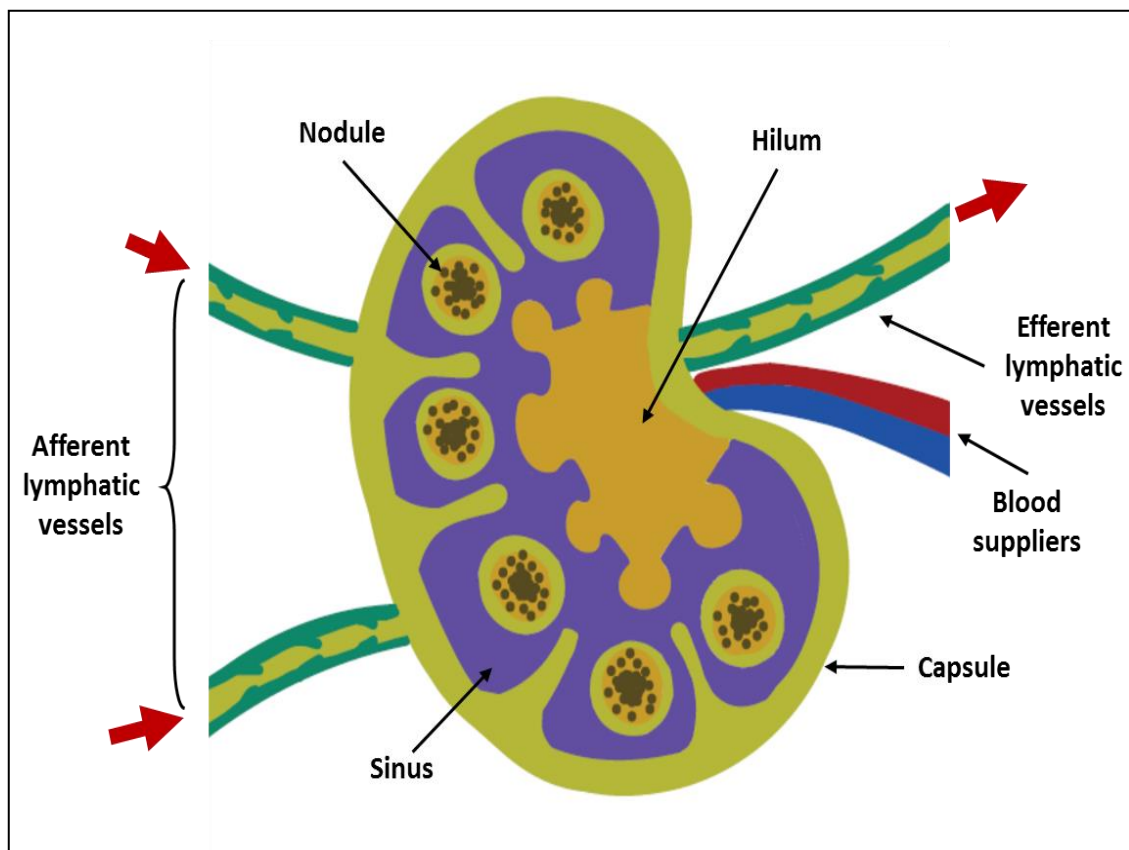
Figure 2.2. Schematic representation of the structure of the lymph node. Red arrows indicate lymph flow.

According to Morton et al., 'a sentinel lymph node is the initial lymph node at which point the primary cancer drains' (24) (see Figure 2.3). The term 'initial' is responsible for the potential misunderstanding of this definition. For example, many lymph vessels might connect the cancerous tissues to numerous lymph nodes, but these might not emerge concurrently in the medical images. To prevent confusion, the description has been customised slightly to read, 'a sentinel lymph node is any lymph node on the direct drainage route from the primary site of a tumour'.

This description mirrors the functioning of lymph drainage and the stepwise propagation of tumour growth through the lymphatic system. This is the description that most professionals and cancer surgeons follow (24, 25). However, it has been criticised (26-28), and a range of alternative descriptions have been developed based on the use of radiopharmaceuticals and blue dye (Table 2.1) (29-31).

Table 2.1. Summary of alternative scientific definitions describing the sentinel lymph node

Proposed definitions for the Sentinel lymph node
A lymph node containing radioactive material following intradermal administration of radioactivity.
The closest lymph node to the main site of the lesion
A lymph node that has a count rate value beyond a specific threshold based on the hottest lymph node detected
A lymph node that has a count rate value beyond a specific threshold higher than the background or nonsentinel lymph nodes
A lymph node containing the highest activity
A lymph node containing blue dye
The first lymph node detected during the lymphoscintigraphic imaging procedure

Several researchers describe the SLN as the lymph node bordering the main site of a tumour (32). Often, it is true that the lymph node next to the primary site of tumour is indeed the one into which the lymph vessel from the cancerous tissues flows, but this

is not always the case. As a result, this description based on the anatomical localisation of the lymph node does not consider the function of lymphatic drainage.

Some researchers introduced the concept that the SLN can be characterised based on the amount of accumulated radiocolloid within it. However, the amount of radiocolloids collected by a lymph node relies not only on its place within the drainage order, but also on the number of lymphatic channels that go into the node, and on other parameters such as the lymph speed, size of colloids and the anatomical location of the targeted site (27).
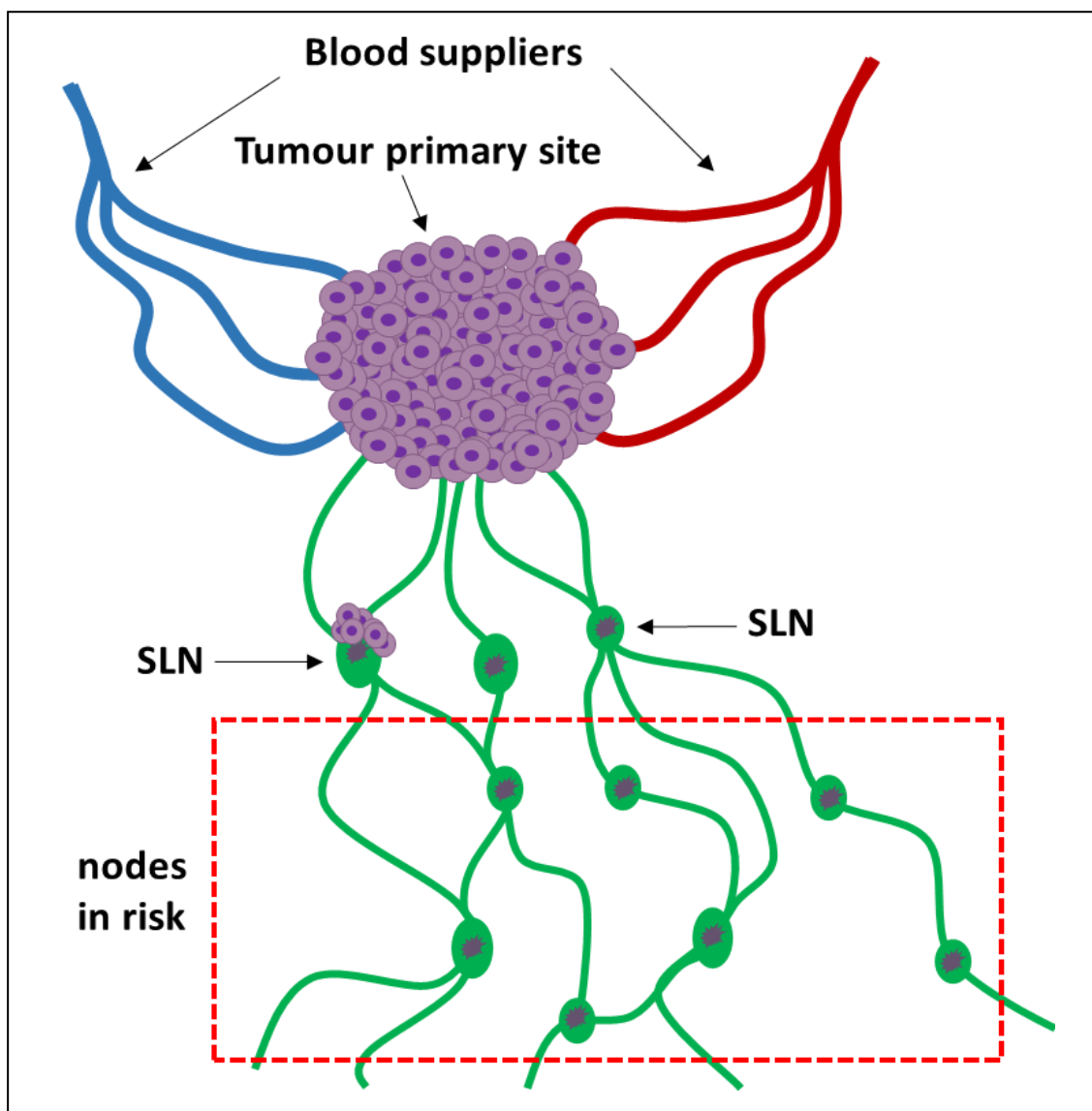
Figure 2.3. A schematic showing the spread of cancerous cells from the tumour primary site to sentinel lymph nodes (SLNs) through lymphatic vessels.

2.5   Intraoperative lymphatic visualisation using gamma technologies

2.5.1 Radiopharmaceuticals

The choice of particle sizes to perform a sentinel lymph node biopsy (SLNB) may be a source of confusion for surgeons, as they attempt to locate the true SLN(s) from other radioactive accumulations in human tissues. Medical studies have revealed that an average of 1.3 lymph nodes can be detected using colloids whose sizes ranged from 20 nm to 1000 nm, compared to 1.7 lymph nodes detected using particles smaller than 80 nm (33-35). The larger molecules appear to be retained within the area of the injection site, thereby failing to penetrate the lymphatic ducts. This results in delayed, and even absent, visualisation of the lymph nodes (36). This observation supports the proposed use of colloids particle size of at least 80 nm and ideally less than 200 nm for an optimal lymphoscintigraphic outcome (37).

The use of filtered ^{99m}Tc nanocolloids (mainly sulphur colloid) in SLN detection procedures has proved beneficial in most clinical scenarios. Potential advantages stem from the low production costs, good safety profile and proven medical value. On the other hand, using this agent brings with it several limitations such as minimal absorption rate at the site of administration (below 5 %), particularly during subcutaneous injections. This limits the entire process, unlike intradermal administration where faster absorption and visualisation is accomplished in cutaneous lymphatics within 60 s of injecting the radiocolloids (37). Table 2.2 summaries the available ^{99m}Tc based radiopharmaceuticals used for radioguided SLNs detection procedures.

Table 2.2. Particle sizes of ^{99m}Tc based radiopharmaceuticals used for radioguided SLNs detection procedures (23, 34, 38, 39).

Agent	Mean particle size (nm)
Antimony trisulphide	3–30
Calcium phytate	150–200
Hydroxyethyl starch	100–1,000
Labelled dextran	10–400
Nanocolloidal albumin	5–80
Rhenium sulphide nanocolloid	50–200
Stannous/stannic hydroxide	30–200
Stannous phytate	200–400
Sulphide nanocolloid	10–50
Sulphur colloid (filtered)	100–220
Tin colloid	30–250

2.5.2 Volume and activity of the administered radioactive material

The consequences of changing the concentrations of molecules, the amount of activity, and the impact of the injected quantity on the results of various lymphoscintigraphic procedures are as yet uncertain. The consequences of utilising variable quantities of radioactive material (^{99m}Tc-human serum albumin (HSA) nanocolloids, 0.02 mg and 0.2 mg in a varied volume of 0.2 ml and 1.0 ml) have been explored (40). In each case, the ^{99m}Tc HSA nanocolloids were administered subcutaneously in the first interdigital space in the foot, and the lymph nodes' uptake examined after 60 minutes during a peripheral lymphoscintigraphic procedure. It has been noted that there was a high accumulation of radioactivity in the inguinal region when the highest quantity and lowest volume were used (40). Furthermore, an improvement in the SLN detection rate, from 83 % to 94 %, was recorded with a 50 % rise in the quantity of the injected activity (41). Injecting a large volume of radioactive solution could, however, result in drainage occurring towards both regional non-metastasised lymph nodes and other untargeted neighbouring regions, due to the abnormal increase in interstitial pressure (42).

2.5.3 Factors affecting radioactivity uptake

Massaging the radioactivity administration site mechanically, and physical exercise, increases uptake while weakening the inverse correlation between lymphatic flow and the size of the radiocolloid particles (43, 44). The uptake of particles in the lymphatic system also varies with temperature; This implies that increased temperature is found to enhance the transportation of protein across the canine lymphatic endothelium (45). As well as temperature variation, pH levels in the interstitial fluid cause alterations in the lymphatic transport and uptake process of particles. Increasing pH levels cause the colloid osmotic pressure to rise at 2.1 mmHg per pH unit (46). However, there are no published investigations to determine the effect of varying pH levels occurring in the interstitial and lymphatic fluid on the uptake process in vivo.

Physical exercise has been evaluated as a way to stimulate the process of lymph flow in the upper and lower extremities. Performing physical exercises during the examination improves the flow of lymph fluid in lower extremities (47, 48). This shows that different types of exercise and exercise intensity influences lymphatic function and the outcomes obtained in the lymphoscintigraphic examination.

2.5.4 Instrumentation

The following sections give examples of available intraoperative gamma probes and portable gamma imaging devices summarising their functionality and ability to perform clinical procedures. To date, most medical nuclear methods for SLNs detection have employed non-imaging gamma probes. The recent development of intraoperative portable gamma cameras has proven advantageous in obtaining intraoperative imaging, thereby offering the potential to enhance the ability to monitor targeted lymph nodes during surgical procedures, unlike the traditional gamma imaging method utilising large field of view (LFOV) gamma cameras.

2.5.4.1 Intraoperative gamma probes

Intraoperative gamma probes can be defined as non-imaging handheld highly collimated gamma detectors used to identify a specific region of radioactivity accumulation. This equipment has been successfully employed for various purposes including identifying the extent to which targeted tissues, such as the sentinel lymph nodes (SLN), uptake radiopharmaceuticals during surgical procedures. Through the injection of a radiopharmaceutical agent that can selectively concentrate in the tissues of the SLNs, specialists can use probe systems to identify sites in which radioactivity uptake is intensified. This subsequently facilitates the identification of the focal uptake of the tracer in lesions, thereby allowing the surgeon to identify which tissues should be surgically removed.

These probes deploy a working principle that involves converting gamma photons emitted by a tracer, usually ^{99m}Tc, into electrons along with producing signals processed using conventional readout electronics or audible outputs.

The intraoperative gamma probes utilised in SLNB procedures may be classified into two groups. The first group uses scintillation detectors, while the second group uses semiconductor-based detectors (49-53). Figure 2.4 displays a classic configuration of a scintillator-based non-imaging intraoperative gamma probe.
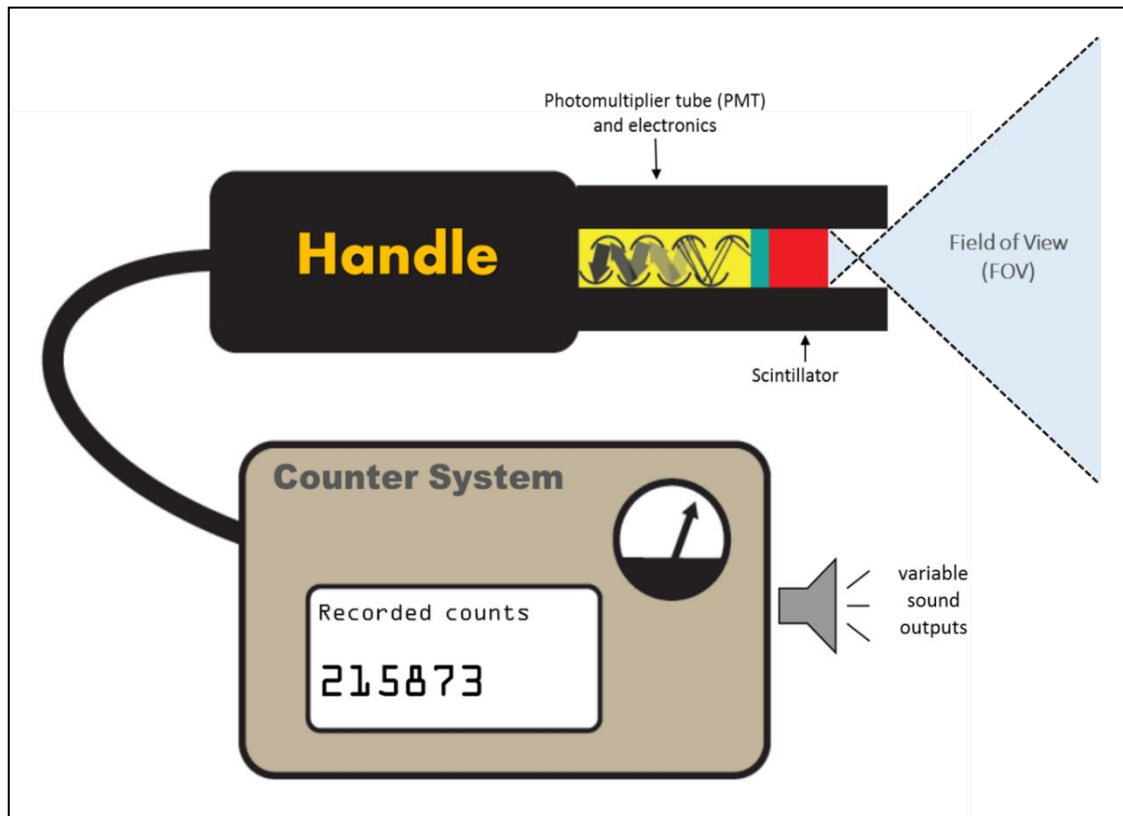
Figure 2.4. Common configuration of intraoperative gamma probes, these probes give numerical and audible outputs during the process of targeting radioactivity accumulation.

The performance of intraoperative gamma probes is defined by a number of parameters including spatial resolution, sensitivity, energy resolution, and signal to noise ratio. Radial resolution is the measurement of the field of view (FOV) width (cone shape) in which the targeted tissue is recognised at a certain distance. When using an intraoperative gamma probe with a broader FOV (i.e. wider cone), the background signal might overlap the signal from the targeted, potentially cancerous, tissues. With a narrower cone, the background signal will be minimised and the ability to detect the primary accumulation in the targeted tissues will be more effective. Lateral spatial resolution is the probe's capability to precisely localise the location of a target tissue and its ability to distinguish two adjacent active features. Sensitivity is defined as the count rate detected for each decay event at the probe tip (54).

Energy resolution is the capability of the gamma probe to differentiate between the energies of photons emitted from various gamma-emitting radioisotopes. This property is necessary to distinguish primary from scattered photons and to differentiate between two concurrently administered radionuclides that produce different energies. The final property is the capability of the probe to distinguish the signal from the targeted tissues from the noise (i.e. scattered radiation) emitted from the adjacent tissues.

Scintillators absorb gamma photons and release a number of photons of lower energy - typically optical photons - relative to the energy absorbed. These optical photons are measured by an optical photon detector, normally a photomultiplier tube (PMT). The scintillation crystals employed within intraoperative gamma probes include cerium-doped lutetium orthosilicate (LSO[Ce]), thallium-doped caesium iodide (CsI[Tl]), thallium-doped sodium iodide (NaI[Tl]) and gadolinium orthosilicate doped with cerium (GSO[Ce]) (54).

Semiconductors are an alternative option to scintillators as a detector mechanism for intraoperative gamma probes. When gamma photons are absorbed within a solid-state detector, ionisation happens by exciting electrons out of the valence band into the conduction band, producing a detectable signal.

When the electron shifts to the conduction band from the valence band, a positive charge (hole) is created. Under the influence of an electric field excess charge is gathered by electrodes, producing a signal that is relative to the energy deposited within the detector (Figure 2.5). Crystalline substances employed within gamma probes include cadmium zinc telluride (CdZnTe), cadmium telluride (CdTe).
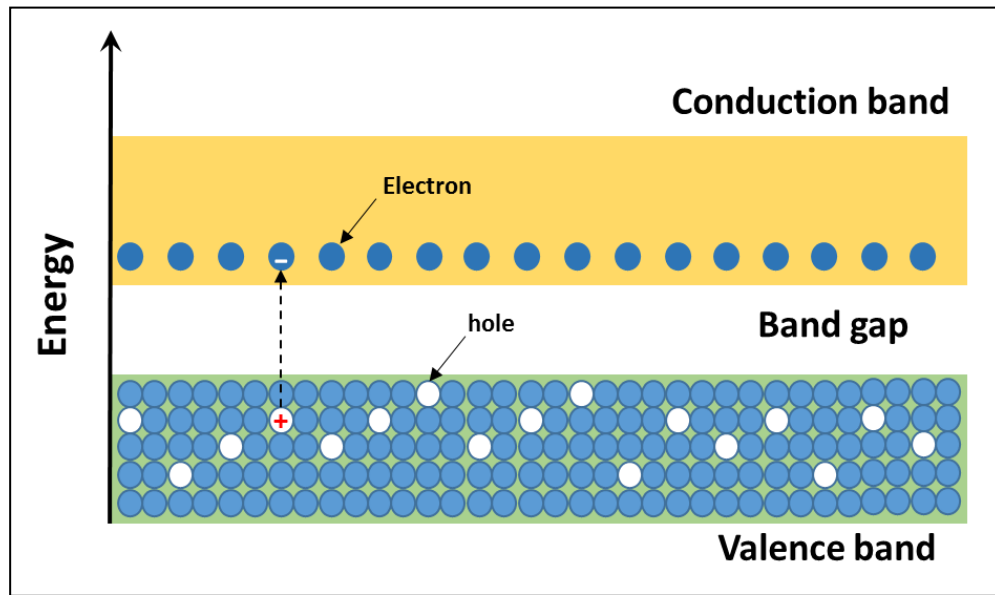
Figure 2.5. A schematic diagram showing the semiconductor band structure.

Scintillation-based gamma probes offer both pros and cons compared to semiconductor-based mechanisms. Scintillators have superior sensitivity due to their natural structure (higher atomic number and density), and they are appropriate for detection systems of high and medium gamma energies. Nevertheless, they have poor energy resolution, owing to indirect detection: the primary gamma photons are converted within the scintillator to optical photons, then the light must be transferred to the PMT and the signal converted from optical to electrical (using the photocathode). Moreover, scintillation-based gamma probes have a bulkier probe head outline and greater weight (54).

Conversely, semiconductor-based probes are direct detectors (the charge created within the material through radiation interaction is directly changed into an electrical signal) and, therefore, they have a superior energy resolution. Similarly, semiconductor-based detection systems have a far more compact probe head design; they can be produced in smaller sizes and may have an extremely thin entry window that allows gamma rays and low-energy particles to be counted. Several commercial intraoperative gamma probes are available (54).

The penetration capability of high energy gamma photons means that background gamma photons can originate from untargeted regions in the patient outside of the

gamma probe's field of view. Some of these gamma photons are attenuated naturally by human tissues located between the probe and the source of gamma photons; however, to eliminate the effect of the background photons, the intraoperative gamma probes are fitted with a shielding cover (such as tungsten, lead, or platinum) and collimators, constructed with various lengths and aperture diameters for different detecting purposes, that attenuate scattered radiation from active tissues located outside the field of view.

The shielding for both lateral and back directions can be significant when there is a regional active source (e.g. the heart) or adjacent injected radioactive source (e.g. the remaining activity in the injection site of the ^{99m}Tc during intraoperative SLN detection procedures) in close proximity with the targeted tissues (the SLN). Collimation of the detector's head leads to enhanced spatial resolution and signal-to-noise ratio. Nevertheless, when the collimation is increased, this decreases the overall system sensitivity of the intraoperative gamma probe by reducing the sensitive aperture and increasing the distance to the targeted source site. Moreover, a thicker shielding wall or a longer collimator is required when identifying a high energy gamma source, but this raises the general gamma probe weight and size (49-53).

The last components of the system are the readout and the electronics. The probe count rate is fed to a rate meter that also drives an acoustic output. An increase in volume (incident events) shows the surgeon the proximity of the probe to the targeted tissues.

Numerous aspects determine the selection of a specific intraoperative probe. From a surgeon's viewpoint, many additional ergonomic design factors of probe systems are relevant (55). Gamma probes for radioguided biopsy need good spatial resolution to enhance the ability to localise potential lymph nodes. Other aspects such as the weight, shape and ergonomics of an intraoperative probe are important. The audible signal and digital output of the detector control unit are also important for offering clear output information to the surgeon, facilitating speedy and precise localisation of the radionuclide with no distraction from the accumulated radioactivity in the neighbouring tissues within the probe's field of view. Adaptability and flexibility of the system are also

pertinent to diverse medical issues; significant properties include detachable side shielding, interchangeable collimators, and user-adjustable energy windows for different isotopes. Lastly, more recent improvements include hand-held self-contained gamma-detection probes using wireless technology (55).

2.5.4.2 SFOV gamma cameras for intraoperative gamma imaging

Non-imaging intraoperative probes are still the most widely-used tools for identification of radio-labelled tissue within the operating room; however, they cannot provide reliable information on the distribution of radiolabelled areas. The precise localisation of a source can only be determined if the tip is in direct contact with the tissue following dissection.

In this respect, intraoperative real-time imaging with a compact gamma camera offers an outline of all radioactive hotspots within the surgical area (6, 7, 56, 57). For example, the camera position may be changed to also image sentinel nodes close to the injection area that could be overlooked when employing the non-imaging gamma probe (58). Discrimination between a SLN and a normal lymph node may be determined based on the number of counts concurrently recorded by the cameras, and linked to the preoperative scintigraphic imaging procedures.

Gamma imaging systems should meet various needs if they are to be used during intraoperative procedures. These include a moveable and fixed design, no delay between image accumulation and display (real-time imaging) and the potential for spatial localisation on the display screen. These systems need to be capable of detecting gamma photon energies that span the entire spectrum of useful diagnostic radionuclides such as ^{99m}Tc, ^{201}Tl, ^{123}I, ^{125}I and ^{111}In (within the photon range 50-300 keV). Lastly, they must also have adequate sensitivity, spatial resolution, and field of view. Two examples of such cameras are shown in Figure 2.6. Whereas the first cameras were relatively heavy and bulky systems, new-generation compact gamma cameras are lighter and/or fitted with steady support mechanisms. In-depth discussion of the principles, components and characteristics of such intraoperative gamma imaging systems will be provided in the following chapter.
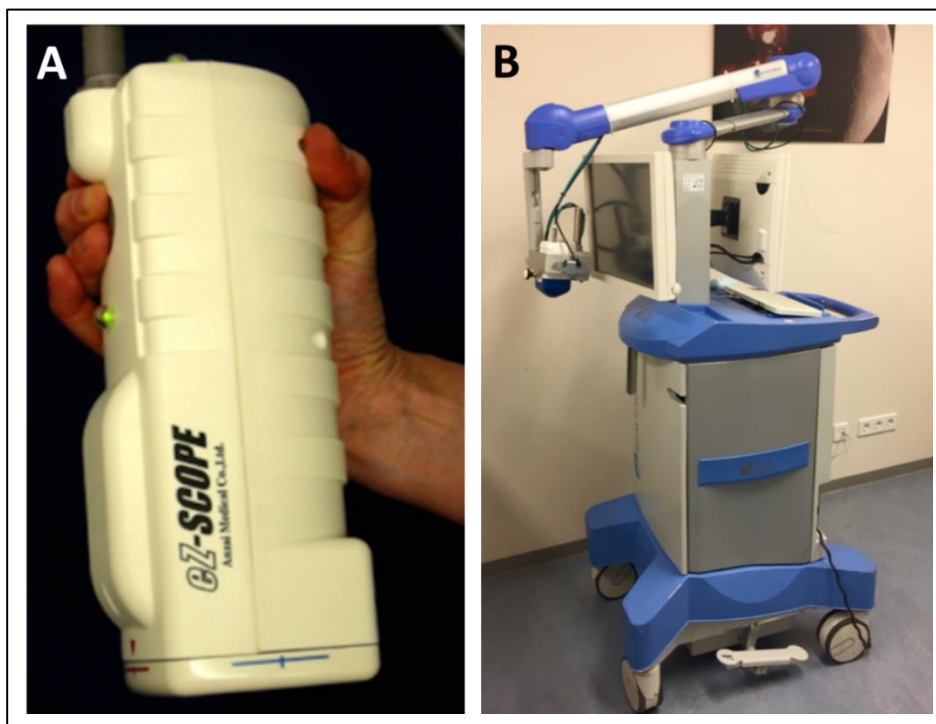
Figure 2.6. Photographs of portable gamma imaging systems; (A) the eZSCOPE SFOV gamma camera, (B) the Sentinella 102 SFOV gamma imaging system (59).

2.6 Functionality testing and the use of medical phantoms

Generally, manufacturers of medical gamma technologies routinely utilise well-established testing protocols to evaluate the performance and perform regular quality assurance checking of a gamma imaging system. These testing protocols have been accepted and published by various regulatory and accreditation bodies such as the European Association of Nuclear Medicine (NEMA) Standard NU1-2007 (60). Nevertheless, these testing protocols for various gamma imaging modalities are outside the scope of this research work, and an extensive explanation of these tests has been provided elsewhere (61-64).

Testing protocols for gamma imaging modalities have been designed to assess the overall performance; however, these protocols do not aim to provide specific methods of evaluating a gamma imaging system's capabilities and limitations for a specific clinical scanning procedure. This is the area where medical phantoms are used to assess the performance of such systems. Medical phantoms, i.e. entities that offer representations of the human body, have been employed for medical/health physics reasons since the

inception of medical imaging. Shortly after X-ray imaging was discovered, the beneficial effects of radiation became widely known. Professor Wilhelm Roentgen took the first human X-ray in 1896, using his wife's hand (65). Unfortunately, the adverse effects of radiation in high doses quickly became obvious, with cell squamation and erythema becoming prevalent among those exposed to early experiments with radiation. Consequently, the number of subjects on whom radioactive imaging could be practised was limited. In response, physicists created phantoms that were able to take the place of human subjects, thereby allowing for the assessment of system limitations and for the taking of dosimetric measurements.

The ultimate rationale for phantoms is the simulation of human tissue for particular procedures and experiments. The physical designs of these phantoms (composition, shape, size, etc.) are dictated by their purpose. Phantoms come in many shapes and compositions; however, broadly speaking, they can be categorised into two types: imaging phantoms and dosimetry phantoms. Imaging phantoms are employed for testing and imaging a system's limitations and for assessing imaging quality. Dosimetry phantoms are used for quantifying how much radiation is being applied to a particular point, whether during therapy or imaging. The materials employed to construct phantoms frequently attempt to offer simulated human tissue. Unfortunately, the employed materials will change their properties depending on their level of radiation exposure. Therefore, while at certain levels of exposure a material may simulate human tissue, it will not necessarily react in the same manner as human tissue at all levels of radiation.

2.6.1 Medical phantom materials

Selecting the right material is crucial when designing and operating effective phantoms. Generally, phantoms are intended to offer a simulation of a certain type of tissue, e.g., lung, bone, or muscle. Water is another material that is frequently simulated, since employing real water in some scenarios can be problematic and awkward. Various tissues have varied properties, radiologically and physically, and phantom materials aim to provide as accurate a representation of radiological and physical properties as can be achieved.

Several elements may be measured to test how closely a phantom replicates tissue. For a basic comparison, effective atomic number and physical density can be employed. These measurements will provide an idea of how closely the material's physical attributes match tissue; however, they will not show how it will react with radiation. The parameter that is most frequently employed and generally accepted is the mass attenuation coefficient, which offers evidence of the quantity of energy the material absorbs locally (66, 67). Ideally, the phantom material will match the tissue in question according to all aspects mentioned in this paragraph. This, however, is seldom possible, and therefore, the prime objective should be to find a material that accurately simulates the chosen tissue's radiological properties.

In the majority of instances, materials can be found that offer extremely accurate simulations of tissue. However, when employing phantoms, practitioners need to be aware of several issues. Frequently, a material's radiological properties vary significantly depending on the level of radiation to which they are exposed. While a material can offer accurate tissue simulations at certain levels, when these levels change, the accuracy may decline. Phantom materials are frequently divided into different classes depending on the appropriate level of energy to which they can be exposed while still accurately simulating tissue. Some materials will fall into kilovoltage classes, which are good for diagnostic simulation, or megavoltage classes, which are good for treatment simulation. Certain materials have been created that are capable of tissue simulation in both of these classes; however, even when the energy range remains within material-appropriate parameters, the beam spectrum can be extremely broad, and as a result, there will always be a certain degree of error. The preceding paragraphs refer to phantoms employed with ionising radiation fields. When requiring phantom materials for experimentation with MRI or US practices, the mass attenuation coefficient for the material will not always be accurate, as these types of imaging function according to different physical laws.

2.6.2 Gamma imaging phantoms

In nuclear medicine, radioactive materials are injected into a patient either as a form of therapy or for an imaging procedure. Procedures in which this practice is commonly employed include thyroid cancer treatment, functional brain imaging, bone density scanning, and heart perfusion scanning. Imaging systems employing nuclear medicine are tested in much the same way as other scanning systems. Phantoms are employed to test the limits of what a system can detect, the imaging quality it offers, and how uniform it may be (68). Nuclear medicine phantoms are in a class of their own, as they have to be capable of accepting an injection of radioactive material. This means that these phantoms are frequently constructed in such a way that they contain inserts or cavities, which retain injected materials while imaging takes place.

Physical phantoms employed for nuclear medicine are generally hollow chambers, of greater or lesser intricacy, and have entry points that permit the introduction of water (or sometimes a different liquid based on the radiation properties that are being examined) and radioactive material, allowing for uniform mixing. These phantoms are generally employed for quality control, to calibrate, and to undertake acceptance testing for clinical devices; to develop new types of imaging machinery; and to provide simulation benchmark levels. There are various examples of these phantoms, including the thyroid uptake neck phantom that is used to assess the sensitivity of the thyroid uptake system during in-vivo assessments (69). Another example is the Jaszczak SPECT Phantom, which is utilised to provide performance information for different SPECT and positron emission tomography (PET) systems (70, 71).

2.6.2.1 Anthropomorphic gamma imaging phantoms

In the selection or design of a phantom, researchers must take into account both the shape to be employed and the construction materials, and how these factors will influence accurate measurement. Over time, various nuclear medicine phantoms have been created that offer a more realistic simulation of geometry and predicted clinical distribution for radiopharmaceuticals. These phantoms have proved effective for offering qualitative measurements regarding the ways in which gamma imaging instruments perform. An anthropomorphic thyroid phantom was the first nuclear

medicine organ phantom that was obtainable commercially (Picker Nuclear, Part no. 3602, volume: 35 cc, Cleveland, OH) (72). As there are different volumes for the chambers in the thyroid lobes, the left lobe will have double the apparent radioactivity concentration of the right. There are two circular nodules in each lobe; three of them are solid, preventing radioactivity from being distributed around them. The right lobe contains another nodule with a comparable water depth to the left lobe, which appears as a 'hot' (enhanced radioactivity accumulation) nodule. A number of thyroid phantoms have been prototyped to evaluate the capabilities of planar scintigraphic procedures in evaluating thyroid abnormalities, such as hypo- or hyperthyroidism, or to use for imaging quality control purposes (73, 74).

Initial PET studies focused on metabolic imaging of the brain. Researchers at the University of California, Los Angeles (UCLA) created a number of phantoms capable of simulating the brain's white matter and cortical structure, as well as the ventricles of the brain (75). The initial phantom created mimicked a single brain slice. The construction was similar to that employed for the thyroid phantom, with different chamber depths producing a grey/white matter concentration ratio of 4:1. The areas representing the ventricles were solid and therefore did not permit the accumulation of radioactivity. This phantom was later refined by creating 19 inserts that built up into a 3D representation of an entire brain (76). Each of these inserts includes five narrower slices, allowing for correct apparent radioactivity tissue concentrations to be maintained. This phantom (known as the Hoffman 3D Brain Phantom) is currently commercially available. A number of fillable brain phantoms have been developed; these phantoms provide more realistic brain structures within the head contour (77).

Recently, the rapid improvement in 3D printing technology has facilitated the development of more detailed structures with highly accurate constructions. In a study conducted by Iida et al. (78), a physical anthropomorphic head phantom, containing grey matter and bone structures including the skull and the trachea space, was developed to mimic the distribution of the cerebral blood flow in a realistic head phantom. The design of this head phantom was generated from a set of MRI images acquired for a healthy adult male, and it was constructed using a 3D printer with a laser modelling technique. This research suggested that the phantom can be used for multi-

centre assessments of SPECT/CT and PET/CT scanners, as it provides high consistency with real medical data and simplicity of reproduction.

In another phantom study, Jonasson et al. (79) described a brain phantom that was designed and 3D printed to study the effects of brain atrophy in longitudinal PET scanning. The phantom consists of the right and left striatal structures, which can be fitted in their exact anatomical locations inside the brain surface phantom that serves as a container to simulate the background uptake. Three different sizes of the striatal inserts were perfectly constructed and interchangeably fitted inside the phantom (see Figure 2.7).
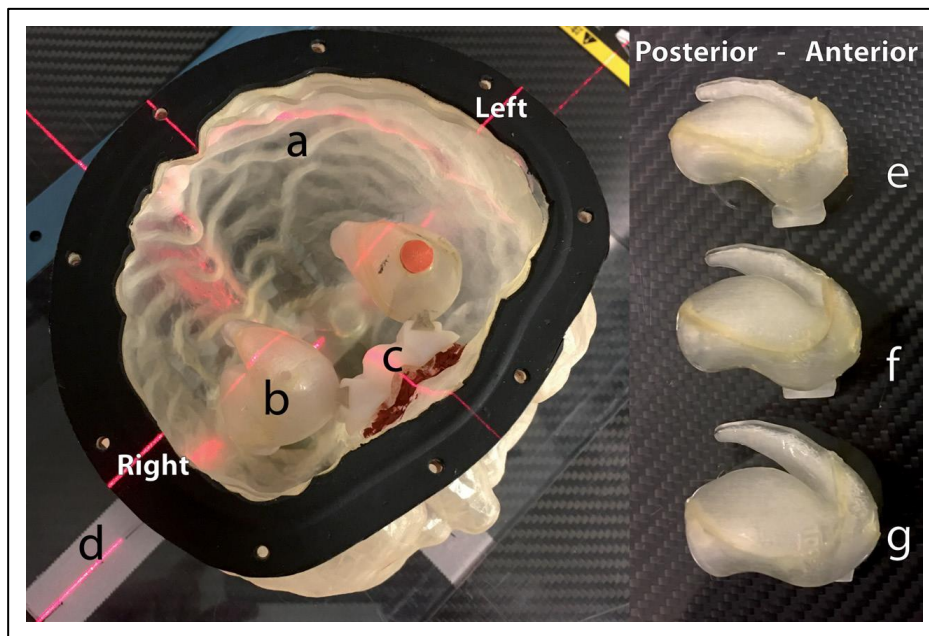
Figure 2.7. 3D printed anthropomorphic brain phantom; (a) simulated brain surface, (b) attachable simulated striatum, (c) striatum holder, (d) plastic base for the brain phantom, (e, f and g) small, medium and large simulated striata (79).

Furthermore, 3D printing technologies have been employed in constructing phantoms of other human body organs, such as the kidney. In a radiation dosimetric study, Tran-Gia et al. (80) designed and 3D printed four refillable kidney phantoms of different sizes. These kidney phantoms were utilised to evaluate the accuracy of internal renal dosimetry in a realistic kidney shape. The researchers found that using this prototyping dosimetric technique is promising for geometry-specific dose calibration of nuclear medicine scanners.

In a recent dose optimisation study (81), researchers assessed the differences when using two image reconstruction settings on the pancreas uptake quantification. To conduct this study, they designed and 3D printed anthropomorphic kidneys and pancreas compartments. These simulated organs were fitted inside the NEMA NU2 phantom casing, as shown in Figure 2.8. The results obtained suggested that the imaging outcome of this 3D printed phantom strongly aids the quantification of ^{111}In source uptake in the pancreas. These research outcomes indicate that 3D printing technologies have the potential for prototyping individualised anthropomorphic medical phantoms, which can serve in developing, improving and evaluating many clinical applications and simulating various critical scenarios in the nuclear medicine field.
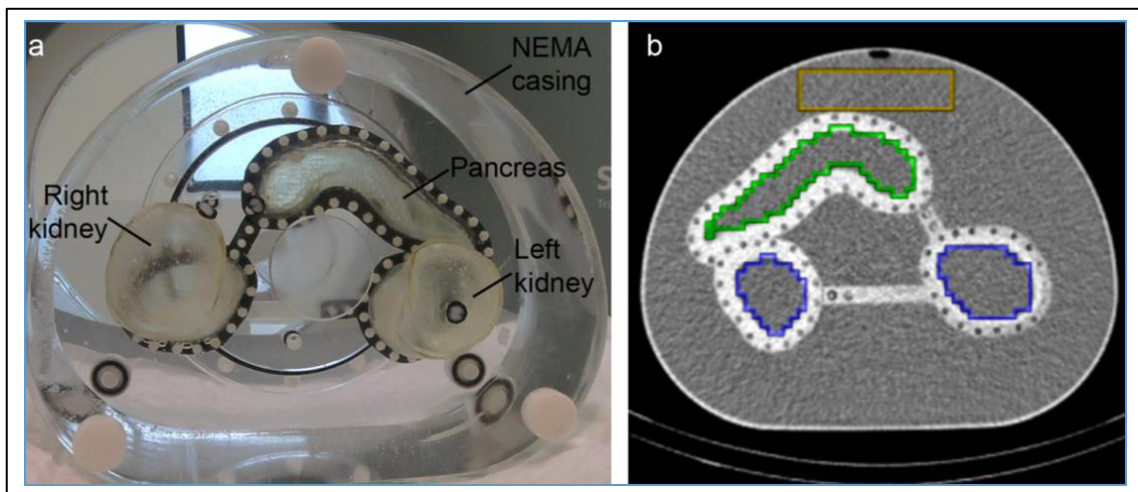
Figure 2.8. (a) A photograph of the 3D printed simulated right and left kidneys and pancreas fitted inside in the NEMA NU2 image quality phantom's outer shell, (b) a CT image of the phantom showing the simulated organs (81).

Robinson et al. (82) designed and 3D printed anthropomorphic phantoms for organ-specific activity quantification including pancreas, liver, spleen and kidneys (age 5, 10 and adult). Researchers have proved that through using these realistic 3D printed phantom inserts, the accuracy of a specific organ's radioactivity quantification has significantly improved in compared to spherical calibration tools. Such findings would pave the way towards patient-specific activity quantification and dosimetry for diagnostic and therapeutic procedures (see Figure 2.9).
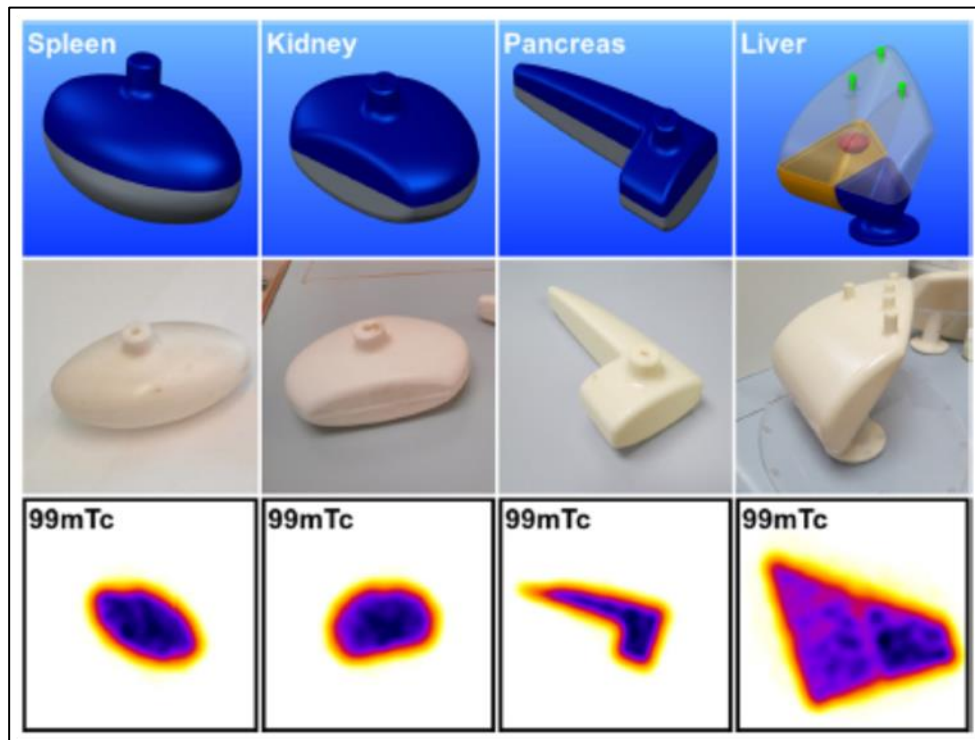
Figure 2.9. Upper row: shows the CAD designs for the simulated spleen, kidney, pancreas and liver. Middle row: represents photographs of the fillable 3D printed phantoms. Lower row: displays the gamma images acquired for the simulated organs (82).

2.6.2.2 SFOV gamma imaging phantoms

Many different phantoms are on offer for a wide range of possible medical applications, and choosing the correct one is entirely situation-dependent. However, the recent interest in developing SFOV gamma imaging systems has encouraged researchers to develop their phantoms to test the new imaging systems, as the majority of the available gamma imaging phantoms are designed for LFOV gamma imaging usage. In this subsection, the design and use of these phantoms will be discussed.

In 2005, Kopelman et al. (83) published one of the early research articles in the SFOV gamma imaging field. The researchers described a prototype intraoperative gamma imaging system (discussed in more detail in Chapter 3, page 50) and illustrated a testing method to show the capabilities of the system and its limitations for intraoperative gamma imaging procedures. The research involved developing a prototype phantom to assess their system in simulated medical scenarios. The bespoke phantom consists of a water tank (100 × 100 × 500 mm in size) and fillable hollow spheres with two different

diameters (i.e. 10 mm and 20 mm internal diameter). Theses spheres can be filled with the desired radioactivity concentrations, and they can easily be placed at any selected depth inside the water tank (see Figure 2.10). Using this phantom, several tests were conducted, including assessing the ability of the SFOV gamma camera to distinguish the margins of adjacent simulated nodes and the system's limit in detecting low uptake nodes at different depths and different acquisition periods.
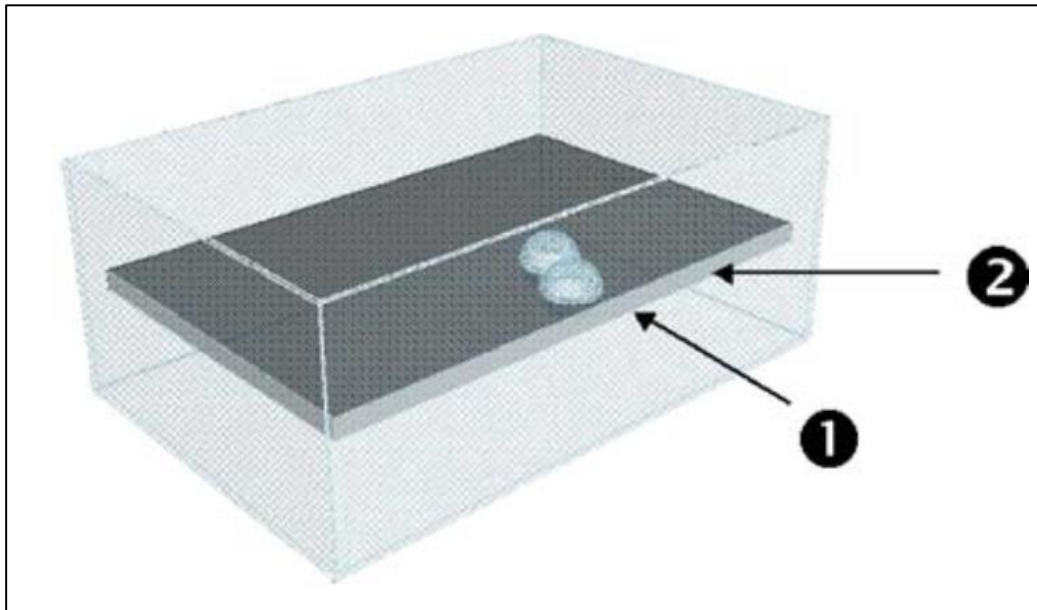
Figure 2.10. A schematic diagram illustrating the structure of the water tank and the arrangement of two fillable hollow spheres positioned inside the water tank (83).

A similar phantom design was used to evaluate optimal operating conditions during intraoperative gamma imaging procedures for melanoma SLNs (84). The phantom consists of one fillable plastic hollow sphere 8 mm in diameter and a water bath. The sphere was injected with various radioactivity concentrations (ranging between 15 kBq and 485 kBq) and positioned at different depths inside the water phantom (7 mm to 40 mm depth). The researchers examined the Sentinella 102 SFOV gamma imaging system (more details are provided in Chapter 3, page 55), and based on the data produced using this phantom, they suggested that 10 MBq of administered radioactivity prior to the surgical procedure allows the identification of an SLN up to a source to collimator distance of 100 mm in an acquisition time of 60 seconds.

In another phantom study, Lees et al. (85) developed three mini high resolution (HR) phantoms to evaluate the contrast resolution of an early version of the HGC. These phantoms were engineered from Perspex. The simplest phantom consists of three wells: one large well 3 mm in diameter and two wells 2 mm in diameter drilled in a 5 mm-thick plate of Perspex. The other two phantoms were engineered such that one phantom can provide hot spots and the other phantom provides cold spots (Figure 2.11). The wells in the hot-spot HR phantom and the pins in the cold-spot HR phantom were manufactured with same diameters (i.e. 1, 2, 3 and 4 mm in diameter). When using different radioactivity concentrations injected into these prototyped phantoms, the SFOV gamma camera showed superior spatial resolution proved by its ability to resolve the edges of closely located wells and pins. These phantoms show great potential for evaluation of SFOV gamma imaging systems.
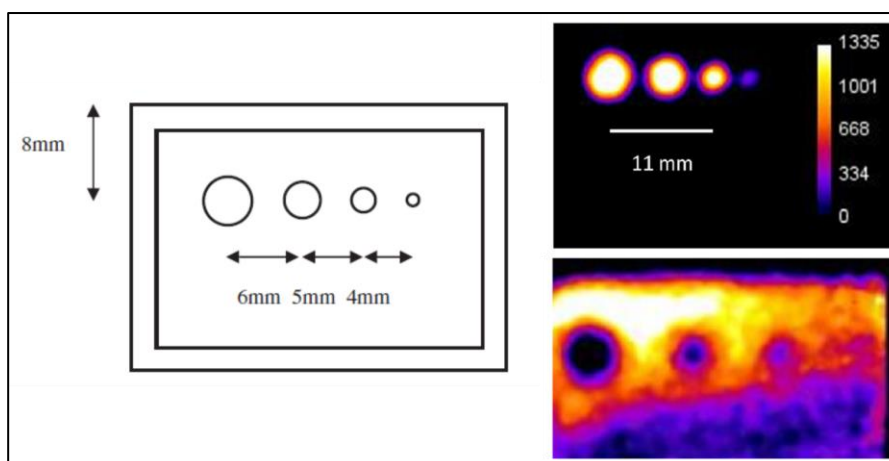
Figure 2.11. Left-hand side: a schematic diagram showing the design of the HR mini phantoms. Right-hand side: gamma images for the hot-spot HR phantom (upper) and the cold-spot HR phantom (lower) acquired using an early version of the SFOV hybrid gamma camera (85).

To conclude this section, novel technologies are continually emerging that can be used to create new phantoms, opening up many new fruitful avenues for researchers. It is worth mentioning that the characteristics of the materials used to develop the prototype medical phantoms described in this thesis and the aim of utilising them are properly explained in the material and methods subsections of the following research chapters.

2.7   Conclusion

The lymphatic system has significant involvement in the immunity and defence mechanisms of the human body. However, it is one of the prime targets for the spread and growth of cancerous cells. SLN detection plays a major role in tumour staging procedures (i.e. SLN biopsies) and other cancer surgeries. In this chapter, the basics of the anatomical structures and physiological mechanisms of the lymphatic system have been briefly described. The concept of the SLN has been illustrated, and a brief explanation of different views on the definition of the SLN was also included in this chapter. Furthermore, various aspects of the technologies and techniques used for lymphatic system imaging and SLN detection have been discussed. Medical phantoms used for functionality testing have been illustrated, and many phantom designs and purposes have been covered.

Chapter 3: Essentials of medical gamma imaging systems

3.1   Introduction

The conventional, large field of view (LFOV) gamma imaging system is the primary equipment used to perform a wide range of nuclear scanning procedures, such as thyroid and parathyroid scintigraphy, bone scintigraphy, renal scintigraphy, and myocardial perfusion scintigraphy (86, 87). The currently used conventional gamma imaging systems are still based on the principles of, and use similar components to, early Anger cameras (88).

More recently, design and technological developments have enabled gamma imaging equipment manufacturers to significantly improve the functionality and capabilities of gamma imaging systems and also provide hybrid imaging. As a result of a number of successful inventions in the area of hybrid imaging, many contemporary hybrid imaging systems, such as single photon emission computed tomography – X-ray computed tomography (SPECT-CT) and Positron Emission Tomography – magnetic resonance imaging (PET-MRI), can now offer advanced systems by which the anatomical and functional status of targeted tissues in a patient can be assessed even on a cellular level. Such technology can also be utilised for small animal scanning (88). Although many exciting developments have emerged in this area, the essential components of traditional gamma imaging systems, and also the advanced hybrid gamma imaging systems, such as lead shielding and collimators, have not essentially changed, and their bulk and weight still limit portability.

A significant focus has been directed towards producing LFOV hybrid gamma imaging systems; however, there remains a growing interest in the development of equipment that operates at the other end of the spectrum, and can provide compact, small field of

view (SFOV), highly collimated gamma imaging systems that can be employed during intraoperative gamma imaging procedures (89). The emergence of these SFOV compact gamma imaging systems in surgical and clinical applications may improve patient outcomes as they can offer gamma imaging in a critical situation due to their size and portability. A SFOV handheld compact hybrid gamma camera (HGC) has been designed and developed at the University of Leicester. This hybrid imaging system is able to provide gamma and hybrid optical-gamma imaging simultaneously.

In this chapter, the fundamental principles and concepts of conventional LFOV gamma imaging systems will be illustrated. Furthermore, SFOV gamma imaging systems will be discussed, and more focus will be directed towards the HGC design and its integral components. The aim of this chapter is to provide the reader with sufficient background on the HGC development, illustrating the similarities and differences between a SFOV gamma imaging system (i.e. HGC) and conventional gamma cameras.

3.2 Large field of view (LFOV) gamma cameras

3.2.1 Configuration of a conventional LFOV gamma imaging system

Diversified hardware and connections are assembled together to form a medical gamma ray detection instrument, also known as the gamma camera. Each component plays an integral role in the identification of gamma photons and producing proper medical gamma images. This section elaborates on the conventional gamma imaging system's chief elements only and does not provide an explanation of every single component and their detailed functions. Figure 3.1 illustrates the fundamental elements of a conventional gamma camera. Further detailed description of gamma camera technologies can be found elsewhere (90-93).
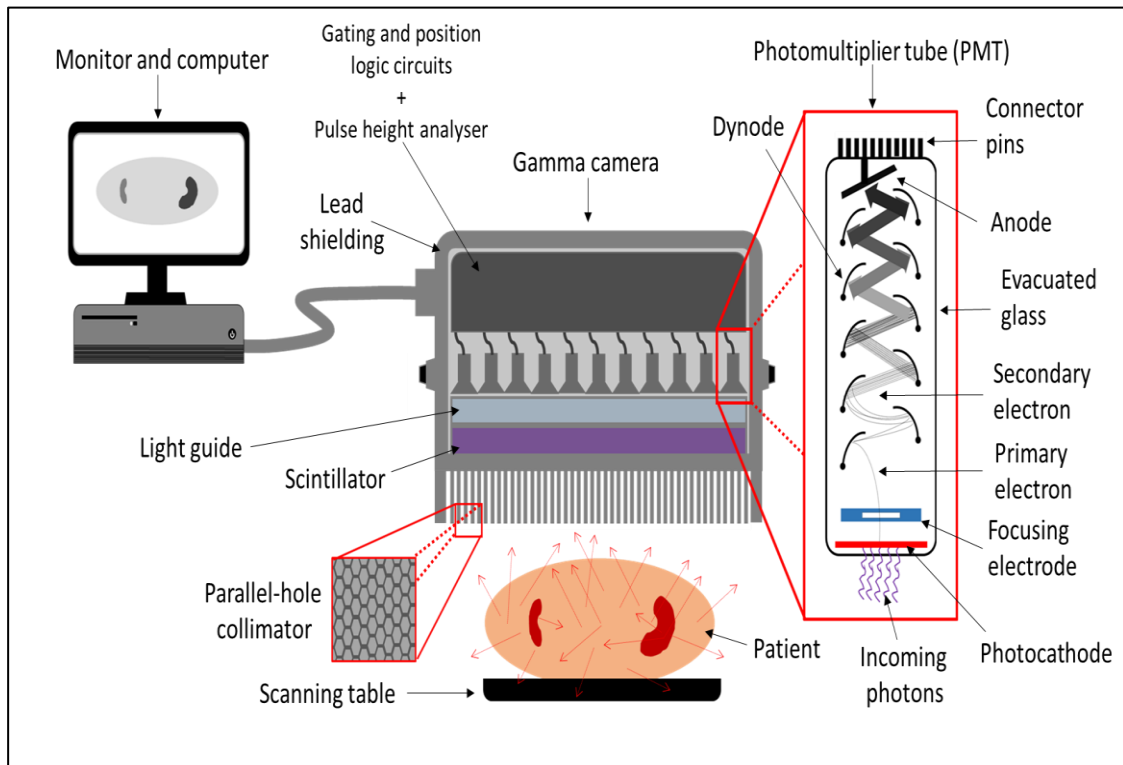
Figure 3.1. The traditionally used components of a large field of view (LFOV) gamma camera. The fundamental components of the scintillator, photomultiplier tubes (PMTs) array, a light guide, and a collimator are present in a mainstream conventional gamma camera for detecting ionising radiation.

The major components observed in each gamma camera include a light guide, photomultiplier tube array, radiation shielding, scintillation crystal, collimator, electronics for energy positioning and differentiation. Additionally, there would be a display device and a computer for processing and demonstrating images and data (94).

3.2.2 LFOV Gamma Camera Scintillators

The process of converting gamma rays into optical light is performed using a scintillation crystal. As a part of a gamma camera design, several characteristics are considered before choosing the appropriate crystal for gamma ray detection. To attain enhanced imaging performance suitable for clinical use, the scintillator chosen must be inexpensive, have short decay duration, with high atomic number, and high density and light output (95). Table 3.1 lists the common crystal materials selected for gamma camera design (95-99).

Table 3.1. Properties of common scintillators used in conventional gamma cameras

Properties	Na(Tl)	CsI(Na)	CsI(Tl)
Density (g cm^{-3})	3.67	4.51	4.51
Decay time (μs)	0.23	0.63	1
Refraction Index	1.85	1.84	1.8
Photon yield (keV)	38	39	45 − 52
Hygroscopic	Yes	Yes	Slightly
Effective atomic number (Z$_{eff}$)	50	54	54
Peak emission wavelength (nm)	415	420	540

Sodium iodide (NaI) scintillators are the most widely utilised for radiation detection in conventional gamma ray imaging systems (98). However, it has been found that NaI crystals have unwanted characteristics of moisture absorption and fragility; therefore, they are required to be sealed in airtight containers (99). To enhance the NaI crystals reaction to the incident gamma photons, they can be doped with thallium (Tl) atoms, which improves the scintillator's response to the gamma photons (100). As a result of photoelectric or Compton scattering interactions of the incident photons with the scintillator's material, an energetic electron is released and moves within the scintillator and interacts with other atoms to produce more excitations and ionisations. The resultant electrons that are in an excited state subsequently return to their stable state through realising their energy in a form of optical photons (101).

Crystal design is an integral factor influencing the scintillation process. It has been shown that consistently high sensitivity levels are recorded while utilising thick crystals, as they can absorb most incident gamma photons; however, a reduction of spatial resolution is recognised. Conversely, gamma photons can escape thinner crystals easily, which will degrade the sensitivity of the detector. For medical imaging purposes, the usual thicknesses for the manufactured scintillators of gamma cameras is in the range 6 to 12 mm, and these thicknesses match the detection of gamma photons in the 140 keV range (i.e. ^{99m}Tc isotope energy) (102).

The majority of conventional gamma camera designs utilise the standard structure of NaI crystal in the shape of a continuous slab. Nevertheless, pixelated or segmented scintillators coupled to photosensitive PMTs, where pinhole or parallel collimation geometry is used, are an effective structure, which can provide relatively better spatial resolution gamma images (103). The enhancements in the imaging system's spatial resolution are brought by the scintillation crystals' segmentation, as segmentation dimensions determine the spatial resolution improvement. However, segmentation has disadvantages such as high costs, low count rate and sensitivity (104). This scintillator structure is predominantly used in producing small animal scanners with a small field of view or for organ-specific gamma imaging systems for some specific nuclear medicine procedures such as breast-specific gamma imaging (104, 105).

Moreover, a partially slotted scintillator's structure can be preferred as an intermediate solution. Partially slotted scintillators can provide good energy resolution and enhanced detection sensitivity compared to pixelated scintillators. In addition, they preserve the spatial resolution of the gamma ray detector (106). Such a structure has several additional characteristics such as lower production costs and relative ease of manufacturing (107).

3.2.3 Photomultiplier tube (PMT)

There are two steps in the procedure of gamma detection using gamma cameras. The process commences with an interaction between the scintillation crystal and the incident gamma photons. Following this, the energy of these photons is deposited in the crystal and converted to visible optical photons. The transmitted light propagates and is guided towards an array of PMTs. The PMT is a high-voltage, sensitive, optical detector, which can detect and convert optical photons into a measurable electrical signal (90). The PMT works on the directly proportional relationship between the electric current and the number of detected optical photons (90). As shown in Figure 3.1, the PMT is a vacuum tube with an entrance window, an anode, photocathode, dynodes (electron multiplier), and focusing electrodes.

The NaI scintillator transmits optical photons at a peak wavelength of 415 nm and these optical photons are received by the photocathode, which liberates photoelectrons (i.e. low energy phenomena: photoelectric effect) (108). The photocathode consists of alkali metals coated with a photo-sensitive surface having weakly bound electrons in the valence band (108). The photoelectrons, produced by the photocathode, are directed by a focusing electrode towards the first dynode. The primary electrons are accelerated towards the first dynode by a high bias voltage. The collision between the primary electrons and the first dynode surface liberates more electrons. Consequently, the same step repeats between a series of dynodes with further stages of electron amplification. This process does not end until the electrons reach the final dynode. This cascade procedure works as all the electrons are collected at the PMT's anode (108). The procedure of transmission of the optical photon's energy into electrical signals is shown in Figure 3.1.

The gamma image produced by a conventional gamma camera is formed on a pixelated grid. The number of detected gamma photons is recorded for each pixel within the camera's field of view (109). Therefore, the formation of a gamma image is actually a true mapping for the radioactive agents in the targeted region of interest (i.e. the spatial locations of the detected gamma photons). To enhance the produced gamma image quality, scattered gamma photons should be minimised to reduce image noise. Additionally, improving the ability of the gamma camera to maximise the detection of primary gamma photons would improve the gamma imaging outcome. The appearance of the gamma image, image processing, and reconstruction algorithms have been extensively discussed elsewhere (110-113).

3.2.4 Gamma imaging collimation principles

When the process of nuclear scanning takes place, there are several elements that influence the appropriate type of collimator for gamma ray detection, such as FOV dimension, targeted areas' dimensions, and the desired level of sensitivity and spatial resolution. As shown in Figure 3.2, the gamma rays that are emitted from the examined region in the patient are mapped onto the scintillator and represent the targeted tissues' respective locations in the image. The main drawback of this approach is that only gamma photons passing through the collimator's holes can be registered and utilised to produce a gamma image; the other gamma photons will be absorbed by the collimator's material (114). Therefore, the sensitivity of the gamma camera is affected. The following section shows routinely used gamma camera collimators in nuclear medicine clinics.

3.2.4.1 Parallel hole collimator

The most common collimators for gamma image formation are the parallel hole collimators. This type of collimator consists of a high density material plate (e.g. lead is a commonly used material) with hexagonal structured holes arranged in a close-packed hexagonal array. Using this preferred hole structure and arrangement would maximise the exposed area of the gamma camera detector (90). However, these holes can be manufactured in other structures, such as triangular, square, or circular holes. Generally, the thickness of parallel hole collimators manufactured for traditional gamma cameras ranges between 25 and 80 mm, and they contain 3×10^4 - 9×10^4 holes (115). As seen in Figure 3.2 (A), the structure of the parallel bore arrays is symmetrical, with identical holes, surrounded by lead septa.
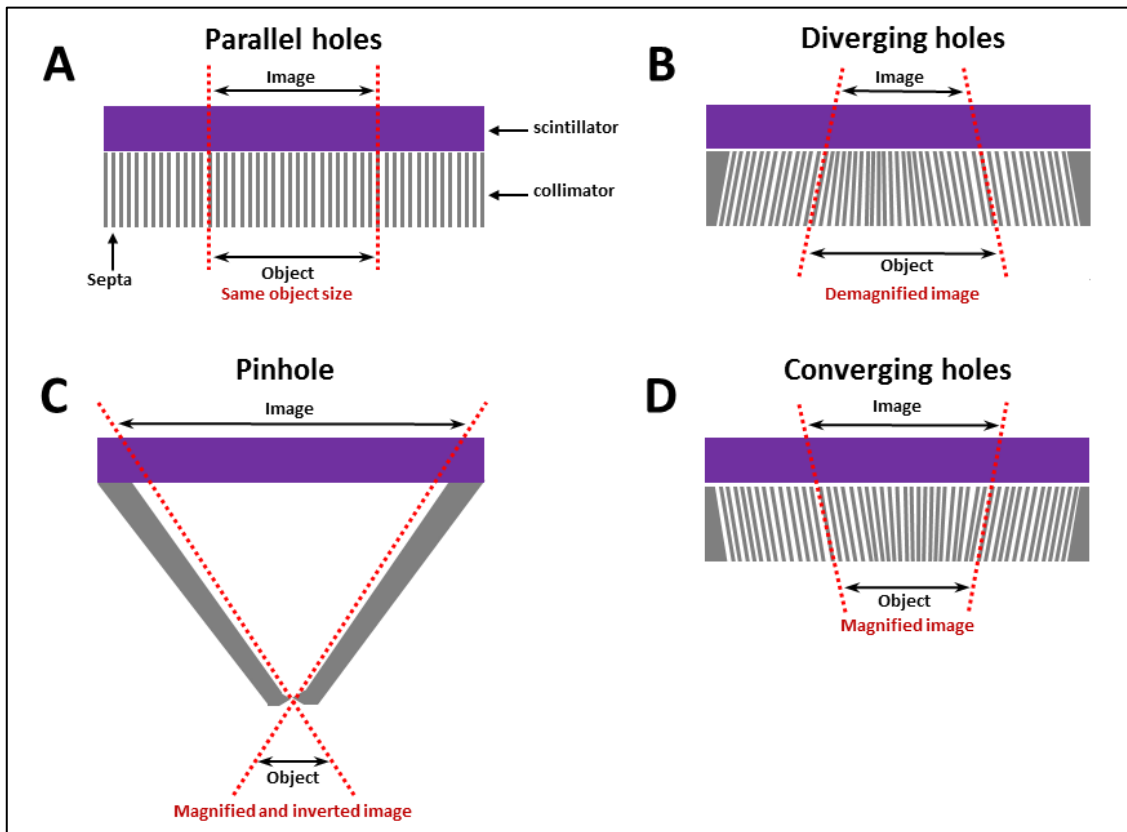
Figure 3.2. Schematics showing different shapes of commonly used collimators in medical gamma scanning procedures. (A) parallel-hole collimator; (B) diverging-hole collimator; (C) pinhole collimator; (D) converging-hole collimator. Red dashed lines illustrate the effect of different collimators on mapping the targeted object with its respective location and shape on the detector.

The parallel hole collimator allows incident gamma photons to pass through at a perpendicular angle. Parallel hole collimators provide a superior level of sensitivity compared to pinhole collimators; however, generally collimators impose considerable limitations on the FOV of the gamma imaging systems because most of the off-axis gamma photons are absorbed by the collimator body (115).

In practice, the parallel hole collimator allows several incidence angles because the hole diameter is not infinitesimally small and the spatial resolution quality of the gamma camera degrades with larger dimensions of the collimator's holes, as these will allow a wider range of acceptance angles (116).

Using different gamma emitters also plays a significant role in the selection of the appropriate parallel-hole collimator. The energy of the gamma photons is the key factor

to determine the septal thickness. This is because the scattered gamma photon penetration for the collimator body must be minimised using an appropriate septal thickness to avoid the projection of inaccurate data on the gamma image.

An exponential function represents gamma photons' attenuation process; therefore, the chosen septal thickness will not match the full absorption of all scattered gamma photons (94, 117). The accepted level of septal penetration is 5 % along the shortest septal path (116, 117). The equation below shows the geometrical relationship of the smallest path length and the septal thickness of the hexagonally arranged parallel hole collimator:

$$ t = \frac{2\,d\,p}{(l - p)} \tag{3.1} $$

Where t is the septal thickness, d corresponds to the hole diameter, and l is the length of the hole, while p is the shortest septal path length for a photon entering the collimator at the maximum acceptance angle (see Figure 3.3).
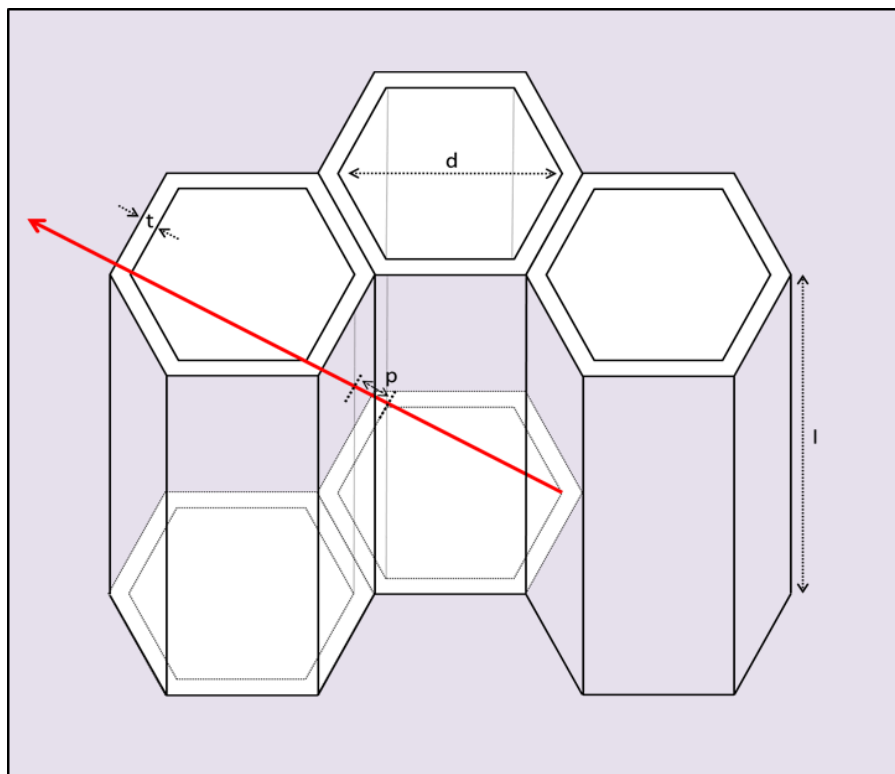
Figure 3.3. A schematic for a hexagonally arranged parallel-hole collimator showing the penetration of the collimator's septa and the relationship between the shortest septal path length (p) and the septal thickness (t).

During the design process of a parallel hole collimator, geometrical restrictions need to be considered along with the inclusion of the probable level of the wider hole dimensions for maintaining a collimator's sensitivity. Gamma photon energy determines the linear attenuation coefficient value (μ) of the absorbing material. Therefore, gamma photon energy is considered in determining the appropriate septal thickness (t) (114). This is the major reason for classifying parallel-hole collimators as Ultra-high energy (UHE), High-energy (HE), Medium Energy (ME), and Low energy (LE) collimators; i.e. the septal thickness of the LE parallel hole collimators (~0.18 mm) is in the thinner range compared to the UHE parallel hole collimators (~2 mm). Thinner septa increase the fragility of the collimator and it can lead to physical damage if not handled appropriately (115).
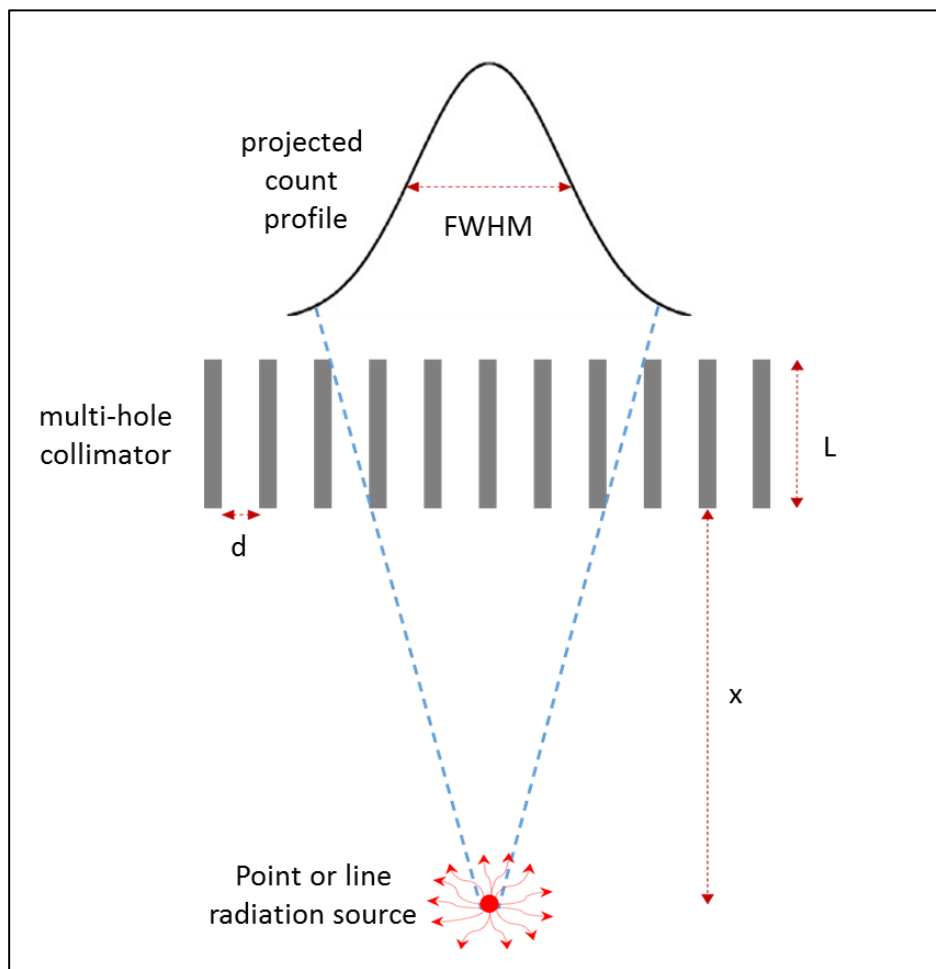
Figure 3.4. A schematic showing the count profile (point or line spread function) for a parallel hole collimator. The Full width at half maximum (FWHM) measurements are utilised to quantify the collimator resolution (R_{coll}).

The diameter and the length of the collimator holes play an integral role in determining the desired collimator resolution and efficiency. The collimator resolution (R_{coll}) is defined as the full width at half maximum (FWHM) of the count profile from a line or point radiation source placed within the field of view (FOV) of the collimator (90, 118). R_{coll} is given by the equation below:

$$R_{coll} \approx \frac{d}{L}\left(L + x\right) \tag{3.2}$$

Where d is the hole diameter, x is the distance between the collimator and the radiation source, and L is the hole length (see Figure 3.4).

3.2.4.2 Non-parallel hole collimator

Parallel hole collimators differ from diverging and converging collimators based on the field of view despite their corresponding exit plane dimensions. Figure 3.2 (B & D) demonstrates the converging collimator that gives a smaller FOV (used to scan small targeted areas such as during brain or cardiac scanning procedures); whereas, the diverging collimator provides a larger FOV in comparison to the parallel-hole collimator. Diverging-hole collimators are utilised to collect gamma photons from a large region of interest (i.e. larger than a camera's crystal) (119).

Cone and fan beam collimators are the two main types of converging collimators. The fan beam collimator consists of various parallel rows of holes and each holes' row has one single focal point. These focal points then join to formulate a focal line for the collimator (Figure 3.5 A). Therefore, the fan beam collimator provides parallel collimation in the axial direction of the ROI and converging collimation for each slice (i.e. transverse plane), which geometrically simplifies the process of producing non-overlapping profile projections (119, 120).

Additionally, during the manufacturing of cone beam collimators, holes can be tapered and organised such that all holes are focused on one specific point (i.e. a focal point). The minimal focal length is recorded at the cone beam collimator's centre and increases towards the collimator's edges (Figure 3.5 B) (120). The apertures of the cone beam collimator's holes on the front surface are identically matched across the collimator.
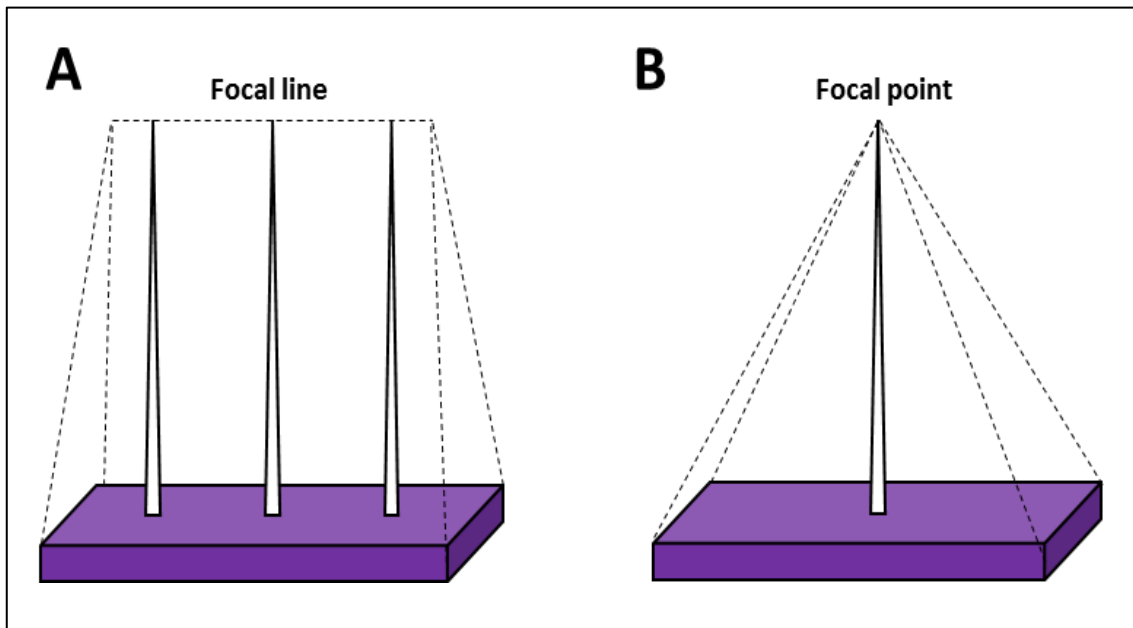
Figure 3.5. A schematic representing focal points of fan and cone beam collimators; (A) fan beam collimator with all holes in the same trans-axial slice directed to form a focal line, while in (B) all holes focus at a single point using a cone beam collimator.

In comparison to the diverging collimator, small objects are magnified using converging collimators and exhibit a relative enhancement in terms of sensitivity which peaks at the focal point. Applications, such as brain tomographic imaging, require these converging collimators, as spatial resolution is found to be optimum at the surface and declines as the source distance increases; however, the system sensitivity is enhanced while moving away from the collimator's surface, and grows until reaching the distance of the focal point (119). The major reason behind this is that the number of the holes examining the object increases with increasing distance between the object and the collimator. Therefore, enhanced sensitivity is attained when the object is observed through a larger number of holes and the object is placed at larger distances.

To satisfy the needs of nuclear medicine clinics with small organ imaging procedures, such as parathyroid and thyroid scanning, pinhole collimators are appropriate (Figure 3.2 C). The pinhole collimator has a cone-shaped structure made from metals, such as tungsten, lead or platinum, and the aperture has a diameter range of 2 to 6 mm. It further demonstrates its effectiveness in examining bone joints, paediatric scans, and skeletal extremities nuclear scanning.

The spatial resolution requirements are different (i.e. higher spatial resolution is required) for small animal gamma imaging systems as the small targeted structures require 1-2 mm pinhole diameter or even lower (121, 122).
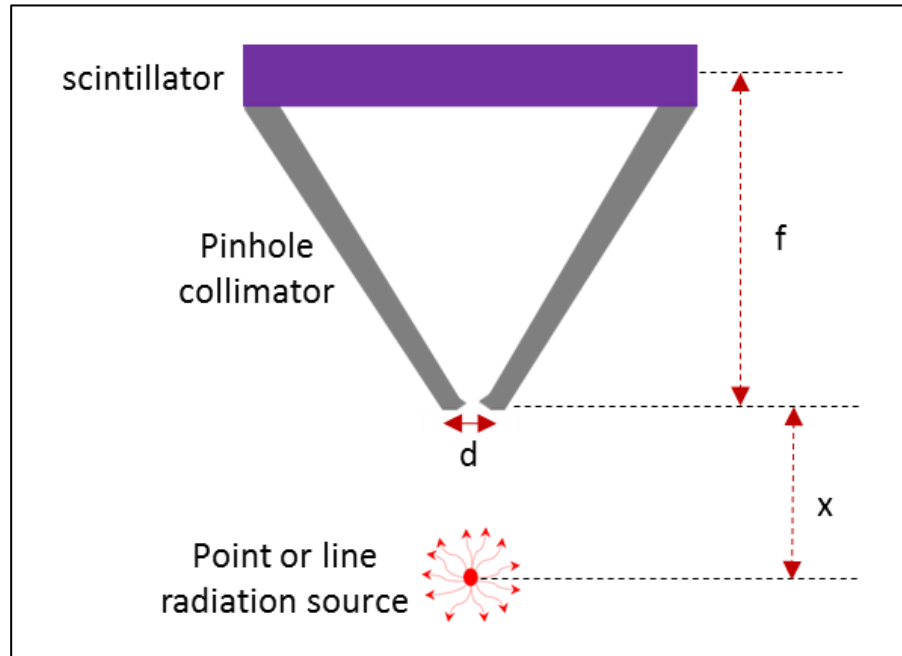
Figure 3.6. Cross- sectional illustration of a conventional pinhole collimator. The collimator's apex to radiation source distance *x*, scintillator to collimator's apex *f*, and the pinhole diameter *d*.

Moreover, the conventional pinhole collimator length range is 20-25 cm from the back surface to the aperture point (90). The following pinhole equation formula describes image formation, which gives an inverted and magnified imaging view. The computation of pinhole collimator magnification (M) is done by:

$$M = \frac{distance\ from\ scintilator\ to\ the\ collimator's\ apex\ (f)}{distance\ from\ the\ collimator's\ apex\ to\ the\ object\ (x)} \quad (3.3)$$

The collimator's physical length and object position influence the image magnification. When *f* is greater than *x*, the magnified image size is achieved and vice versa (see Figure 3.6).

The magnification effect of the pinhole collimator should be considered for R_{coll}. The geometric resolution of a pinhole collimator for a point radiation source located at the middle of the FOV is given by:

$$R_{coll} = d \left(\frac{1}{M} + 1 \right)$$

(3.4)

Where *d* is the pinhole diameter. The resolution is affected with increasing the distance between the radiation source and the pinhole collimator's apex (i.e. decreasing magnification) (118).

The spatial resolution will be enhanced using a small pinhole, while enabling the visualisation of small objects in a magnified form. With a larger pinhole aperture, the spatial resolution decreases and sensitivity level increases. Additionally, larger pinhole apertures may produce gamma image distortion (90). The final image will comprise of several undesired photons (i.e. scattered photons), giving low image quality, as some scattered photons will pass through the pinhole or collimator material and be absorbed by the scintillator.

No new improvements have been recently reported in the area of clinical gamma photon imaging. Despite their limitations, collimators are an essential element of any gamma ray imaging system.

3.3 Small field of view (SFOV) gamma cameras

LFOV conventional gamma cameras are large, bulky pieces of equipment, as they were designed primarily to produce gamma images for large targeted areas or even the whole of the patient's body; however, very little emphasis has been placed on the development of compact, highly manoeuvrable SFOV gamma imaging systems. There is a potential need for more compact nuclear imaging cameras. While some medical imaging equipment companies have invested in the development of mobile gamma cameras, the available systems were still relatively large, trolley-mounted cameras, with limited use and poor manoeuvrability (123, 124).

Recently, developments in the area of low profile position sensitive photomultiplier tubes (PSPMTs) and solid-state detecting elements have resulted in the production of more compact SFOV gamma imaging systems that are able to achieve a high quality imaging outcome. They are capable of performing imaging of small anatomical structures and organs to evaluate their function; for example, lymph nodes and thyroid glands. The emergence of SFOV gamma cameras and their utility in diagnostic applications has shown promise towards providing high quality gamma imaging with superior efficiency, uniformity, and spatial and energy resolutions (125). SFOV gamma cameras have two principal applications: involvement in routine scintigraphic procedures and in intraoperative sentinel lymph node detection procedures (126). The latter will be the focus for the remainder of this literature review.

The diagnostic performance of current modalities to identify sentinel lymph nodes, including pre-operative gamma camera probing and imaging, and the blue dye method, have high sensitivity and specificity (6). The pre-operative detection rates using these modalities have been reported to be 72-98 % with a false-negative rate of 4-7 % (10, 127). The use of radioisotopes within the blue dye is considered the gold standard for sentinel lymph node biopsy with detection rates of 96-97 %; however, its associated complications and licensing issues have meant that its utility has declined, despite its diagnostic superiority (128). Notably, the American Society of Breast Surgeons reports that the acceptable sensitivity and false-negative rate for sentinel node detection is 85% and <5 %, respectively (11). Therefore, gamma cameras with an SFOV have represented

an opportunistic means of meeting the diagnostic performance requirements and, indeed, studies have shown that a 5 x 5 cm SFOV is a pragmatic modality for identifying sentinel nodes in breast cancer patients (12, 129).

However, the utility of SFOV gamma cameras must be able to assist in addressing their potential limitations, including the reliance upon the surgeon's proficiency, whereby considerable training and experience is required to achieve detection rates >90 % (11). Moreover, in a minority of cases the SLN may not be anatomically conducive to detection, particularly those that are deep seated, close to the injection site, amongst high activity tissues, or express limited radiotracer uptake (6). The utility of SFOV gamma cameras is expected to be able to overcome these limitations, providing they have superior spatial resolution, and a number of such systems have become available in recent times (130).

The initial systems utilised conventional continuous NaI or CsI scintillator detectors, which had fields of view of 1.5-2.5 cm and could, therefore, be held by hand intraoperatively. Later, systems emerged with CdZnTe semiconductors but the very SFOV provided by these detectors rendered them difficult to operate during the period of image acquisition and thus, in more recent times, gamma cameras with slightly larger FOVs and machined onto an articulating arm for ease of operation were developed (6).

3.3.1 Handheld SFOV gamma cameras

The eZSCOPE manufactured by Anzai Medical, Tokyo, Japan is a CdZnTe-based semiconductor, which has a field of view of 3.2 x 3.2 cm with a 5 mm thickness and 16 x 16 array (256 pixels). It is light, weighing 820 grams, allowing for ease of operation and utilises exchangeable parallel hole collimators (256 holes) to match the array pattern. In an evaluation study, Abe et al. (131) found that the intrinsic energy resolution was 8.6 % full width at half maximum (FWHM) at 141 keV ^{99m}Tc emitted gamma radiation and had an efficiency of 87 %. For the low-energy high resolution collimator, the integral and differential uniformities were 1.6 % and 1.3 %, respectively, with a spatial resolution of 2.2 mm at 1 cm. For the low-energy high sensitivity collimator, the integral and differential uniformities were 1.9 % and 1.2 %, respectively, with a spatial resolution of

2.9 mm at 1 cm. The performance characteristics of this SFOV gamma camera allowed for greater lymphatic visualisation, as shown in Figure 3.7. However, the SFOV meant that searching the surgical field of interest was time-consuming, which resulted in the use of a diverging collimator to increase the effective FOV.
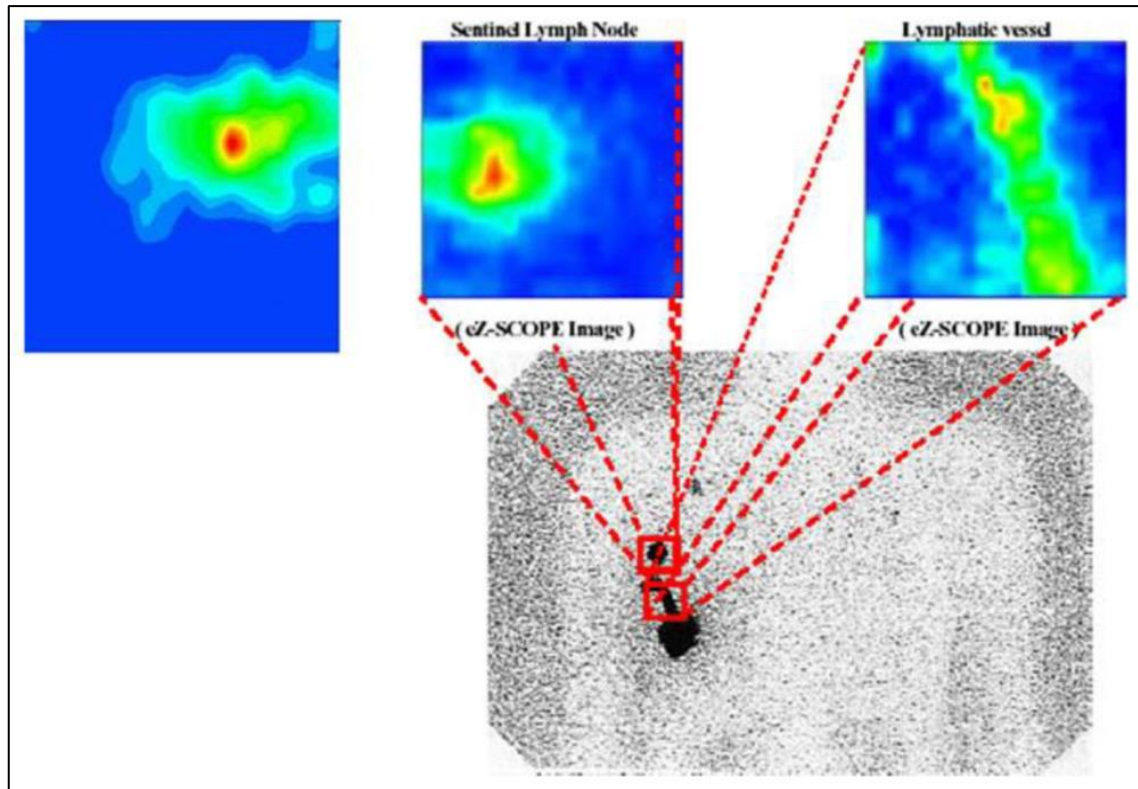

Figure 3.7. eZSCOPE acquired gamma images; lymph nodes (top left and middle), lymph vessel (top right), comparison with conventional gamma camera gamma image (bottom) (6).

Another CdZnTe-based semiconductor was developed, by General Electric, Haifa, Israel, which has a larger field of view (4 x 4 cm) but the same 16 x 16 array and pinhole collimation, when compared to the eZSCOPE (132). In phantom and animal studies, the energy resolution for ^{99m}Tc was 8.0 % and produced a spatial resolution of 5 mm at 5 cm and a sensitivity of 100 cps/MBq. This system was able to discriminate 1 cm adjacent spheres filled with ^{99m}Tc at 6 cm distances (Figure 3.8), whilst conventional gamma cameras could achieve similar images only when the spheres were 2 cm apart and at a 1 cm imaging distance (7, 83).
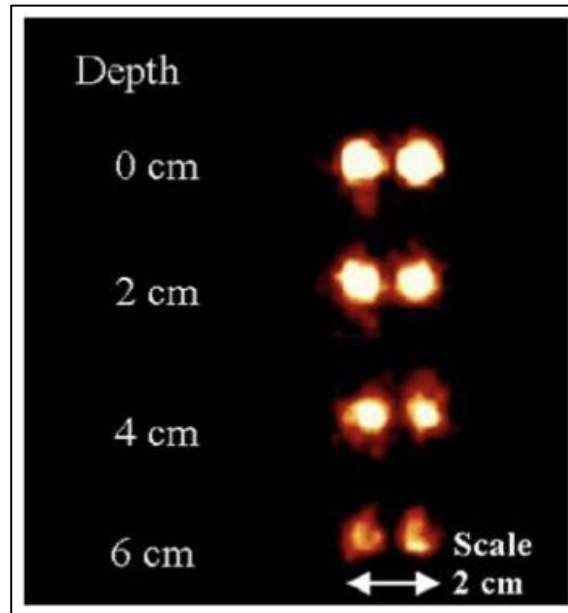
Figure 3.8. Ability of the SFOV gamma camera to discriminate ^{99m}Tc filled spheres at different depths (83).

The Per-Operative Compact Imager (POCI) was developed in France and utilises a CsI(Na) scintillator detector with an image intensifier tube, position sensitive diode and parallel hole collimator (133). The field of view is 4 x 4 cm and its performance evaluation observed a sensitivity of 250 cps/MBq at 1 cm and 125 cps/MBq at 5 cm and spatial resolution of 3.9 cm, 4.8 cm, and 7.6cm at 1 cm, 2 cm, and 5 cm, respectively. However, despite its relative ease of operation, the energy resolution was found to be 28 % and it acquired substantial amounts of scatter in the images. In preliminary human trials, the POCI correctly identified SLNs of all patients and this included recognition of two deep nodes (Figure 3.9) that were not detected by a conventional gamma probe (58). In a later prospective double-blinded trial, Kerrou et al. (134) evaluated the POCI and demonstrated its non-inferiority to conventional lymphoscintigraphy in 138 evaluable patients with breast cancer. The results showed that POCI was able to detect a greater number of SLNs in 50 subjects than conventional scintigraphy, whilst identifying the same number of nodes in 54 patients and fewer nodes in 34 patients. The noninferiority analysis was found to be statistically significant (p=0.025) and the POCI conferred faster acquisition times (<10 minutes in 84 % of patients, compared to 13 % of patients for scintigraphy, which was significant [p <0.001]).
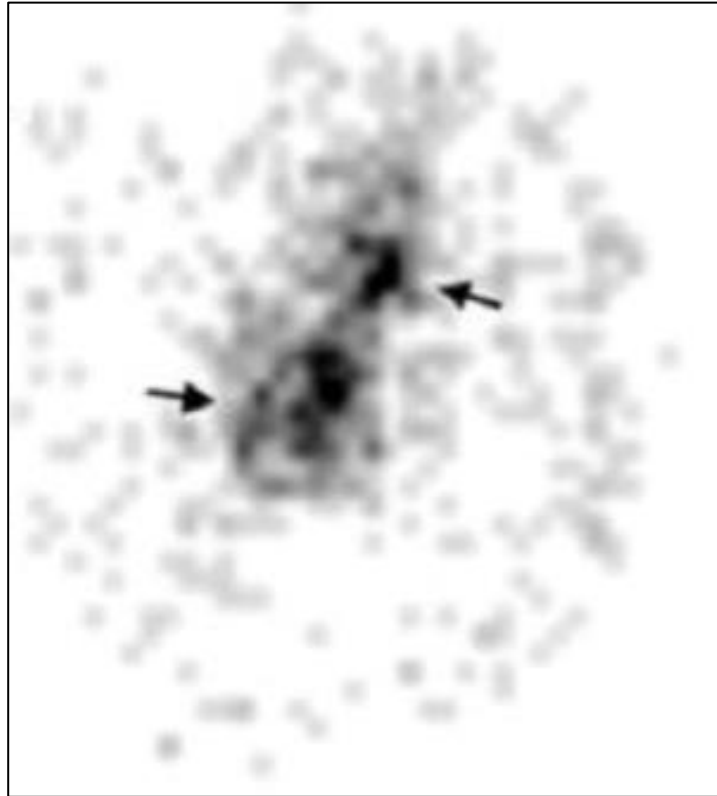
Figure 3.9. POCI acquired gamma image of two deep potential SLNs (arrows) that were not detected by a conventional gamma probe (58).

A cadmium telluride (CdTe) semiconductor was developed by Tsuchimochi et al. (57) in Japan; compared with a CdZnTe semiconductor it has superior energy resolution (7.8 %). The camera has a field of view of 4.5 x 4.5 cm with a 32 x 32 array and 1.2 x 1.2 mm pixelated matrix that is matched by a 1.2 mm square collimator aperture. The spatial resolution was found to be 3.9 mm, 6.3 mm, and 11.2 mm at distances of 2.5 cm, 5 cm, and 10 cm, respectively, whilst the sensitivity was 300 cps/MBq, which is comparable to that of the former POCI system. In a simulation based study, Oda et al. (135) found that the energy resolution was 6.9 % FWHM at 141 keV of ^{99m}Tc and the mean spatial resolution was 1.59 mm. Moreover, this gamma camera was able to better discriminate lymph nodes and identify sentinel nodes close to the injection site using high sensitivity and high resolution collimators, respectively. In a later animal and clinical study, Tsuchimochi et al. (56) found that this gamma camera was able to identify a comparable number of SLNs to the conventional gamma camera but acquired gamma images in must faster times (5-60 s), supporting its utility in lymphoscintigraphic procedures (Figure 3.10).
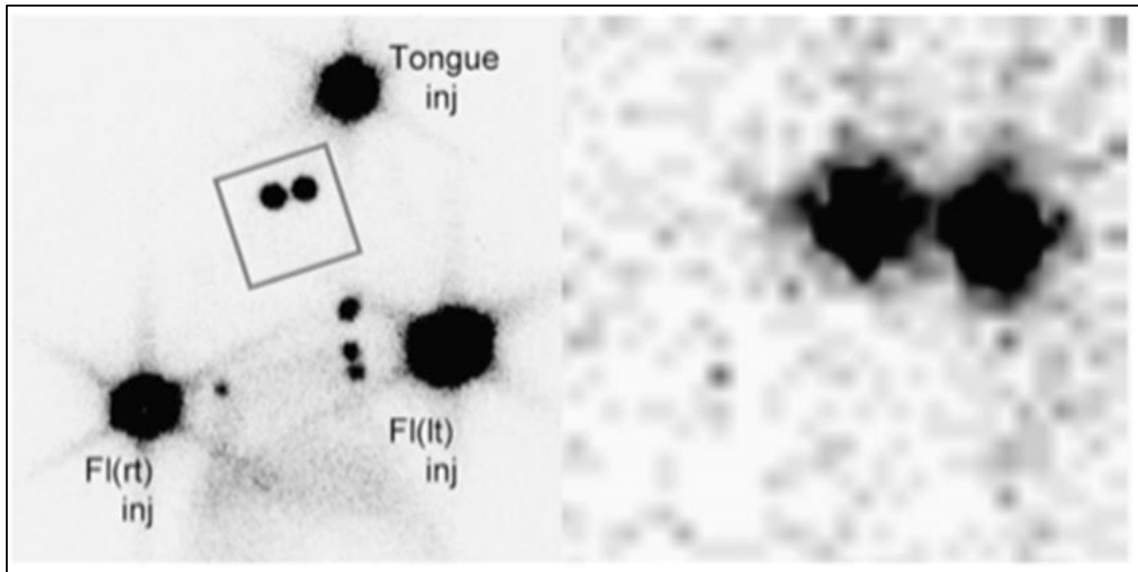
Figure 3.10. Comparison of gamma images produced by a conventional gamma camera (left) and SFOV gamma camera (right); two lymph nodes after 600 s for conventional camera and 15 s for SFOV gamma camera (56).

Several other handheld SFOV gamma cameras are reported upon in the literature but are studied to a lesser extent. Firstly, the IP-824 CsI-based detector is manufactured by Li-Tech, Montelibretti, Italy and has a 2.5 x 2.5 cm field of view. It has a sensitivity of 400 cps/MBq at 5 cm imaging distance, a spatial resolution of 3 mm at 1 cm and energy resolution of 19.1 % at 140 keV (129). In a human trial of a relatively large sample size (n=120), Scopinaro et al. (136) evaluated the use of this gamma camera in SLN detection compared to detection using conventional gamma camera lymphoscintigraphy. The authors matched subjects by age and cancer type and divided them into two groups; one receiving conventional scintigraphy and the other receiving conventional scintigraphy and the IP-824 SFOV gamma camera scanning. The results showed that the use of the SFOV gamma camera was straightforward and facilitated greater SLN detection, which allowed for a higher number of SLNs to be removed at the time of surgery. The Li-Tech manufactured gamma camera was later updated to a version known as the IP-Guardian 2, which is a CsI-based scintillator with a much larger FOV (44 x 44 cm) than its predecessor. In its phantom evaluation, the sensitivity was found to be 204 cps/MBq, the spatial resolution was 2.5 mm in-contact, and it had an integral and differential uniformity of 8.8-12 % and 4.0-5.7 %, respectively (137). During testing

in a feasibility clinical study, Chondrogiannis et al. (138) evaluated the camera's use intraoperatively for SLNs localisation in 16 patients with stage one and two breast cancer. The results showed that the gamma camera provided high spatial resolution of 2.4 mm, with a sensitivity of 180 cps/MBq, which was comparable to that in the phantom study. Moreover, although the number of detected SLNs in most patients was comparable between conventional lymphoscintigraphy and the SFOV gamma camera, the latter was able to identify an extra SLN, which contained metastatic tissue, and more easily identified difficult to detect nodes as defined by pre-operative scintigraphy.

Secondly, the Minicam II is a CdTe-based gamma camera manufactured by Euromedical in France, with a 4 x 4 cm field of view, sensitivity of 200 cps/MBq at 1 cm, spatial resolution of 2.46 mm in-contact and an energy resolution of <10 % at 140 keV. In a prospective study comparing this camera during surgery to pre-operative lymphoscintigraphy in 50 patients, the data was comparable in regard to detected numbers of SLNs, but the Minicam was better at localising SLNs in two difficult cases and was operator friendly (139).

Thirdly, Olcott et al. (140) developed a handheld, NaI-based scintillator gamma camera with a 5 x 5 cm field of view and a 29 x 29 pixelated array coupled to a parallel hole collimator and position sensitive photomultiplier tube. In its performance characterisation, the energy resolution was 12.1 % at 140 keV, the spatial resolution was 1.8 mm at 0.6 cm and its sensitivity was 5 cps/µCi at 1-5 cm. In the phantom assessment, the gamma camera was able to identify a 3 mm sphere at a depth of 3.6 cm with 5 s acquisition time. The principal author and colleagues later evaluated the camera's use in the clinical setting for SLNs identification and biopsy in melanoma and breast cancer patients and compared it to conventional pre-operative scintigraphy and intraoperative gamma probe screening (141). The results showed that the sensitivity of the gamma camera in addition to the gamma probe for sentinel node detection was 88.5 % (95 % CI 82.3, 94.6) compared to 94.2 % (95 % CI 89.7, 98.7) for conventional pre-operative scintigraphy, which was not statistically significant (p=0.24).

3.3.2 Articulated/armed SFOV gamma cameras

The Sentinella 102 system, an articulated SFOV gamma camera, is manufactured by Oncovision/GEM Imaging in Valencia, Spain. It utilises pinhole collimation and a CsI(Na) scintillator detector with exchangeable pinhole apertures with a range of 1.0-4.0 mm, which generates a 20 x 20 cm effective field of view at 18 cm imaging distance (142). The energy resolution is reported to be 13-15 % at 140 keV with absolute and differential linearities of 0.28 mm and 0.15 mm, respectively (126). The sensitivity using ^{99m}Tc ranges between 200-2000 cps/μCi and 60-160 cps/μCi at 1 cm and 10 cm imaging distances, respectively, whilst the spatial resolution readings are 5.4-8.2 mm at 3 cm, 7.3-11 mm at 5 cm and 10-18 mm at 10 cm. Notably, the larger FOV at greater distances impairs the spatial resolution but can facilitate surveillance of large anatomical areas of interest prior to more focussed assessment at smaller distances and better resolution.

In a clinical study of patients with primary hyperparathyroidism, Ortega et al. (143) found that Sentinella 102 system was able to consistently locate the parathyroid adenomas with good spatial resolution when placed at 5-10 cm distances (Figure 3.11) and conferred acceptable acquisition times of 20-60 s. In addition, the Sentinella gamma imaging system is equipped with a laser positioning system and real-time positioning using a gadolinium source (^{153}Gd), to allow precise centralisation of foci of interest for optimal gamma imaging quality (142). In a more recent study, Vidal-Sicart et al. (144) showed that the Sentinella 102 gamma camera had a 20 % higher SLNs detection rate than a conventional gamma probe, with extra SLNs identified in an additional four patients.
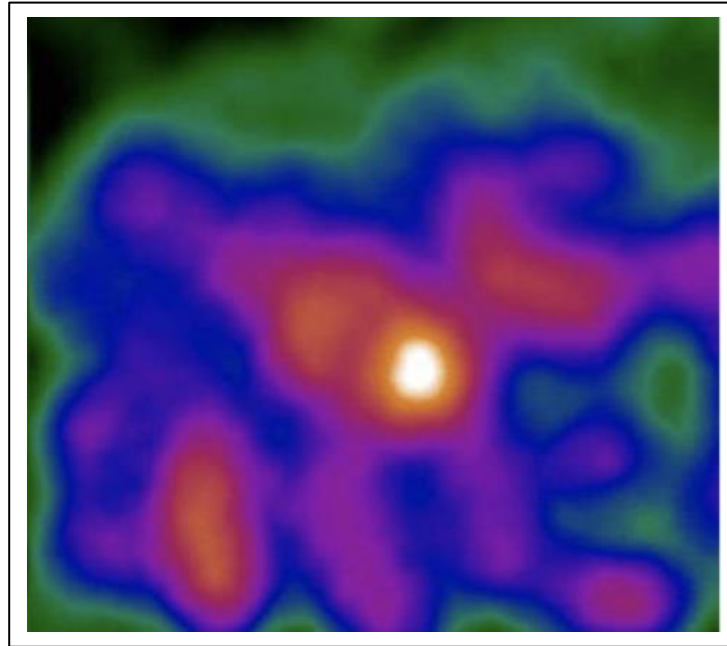
Figure 3.11. Lateral view of a parathyroid adenoma using a Sentinella 102 gamma camera showing a central area of high activity (143).

The Sentinella 102 gamma camera has also been evaluated during a radioguided occult lesion localisation (ROLL) procedure, to assess its utility in assessing the ability to resect non-palpable breast tumours. Paredes et al. (145) recruited 42 women with such cancers who had received pre-operative conventional lymphoscintigraphy and used the Sentinella gamma camera to evaluate the lumpectomy specimen and lumpectomy site to identify residual disease. The gamma camera showed that in 23 cases the lesion was centred with radioactivity in the specimens, whilst 15 were non-centred and four were in-contact, which, overall, was congruent with pathological examination of tissue by a factor of 60 %, suggesting it has some utility in predicting surgical resection margins, which has the potential to reduce the need for repeat surgery.

In a recent UK-based study of the Sentinella gamma camera, Ghosh et al. (146) evaluated its utility in SLN identification and compared it to pre-operative scintigraphy scans in 144 patients. The results showed that this SFOV gamma camera detected a significantly higher number of nodes than conventional scintigraphy (p<0.0001). Moreover, the gamma camera was able to locate nodes in five cases that were not detected by the non-imaging gamma probe and in two cases use of the gamma camera in identifying extra nodes facilitated complete axillary clearance, which would have

reduced or eliminated the occurrence of residual nodes in those subjects. In an earlier study, the Sentinella gamma camera was evaluated in a cohort of 60 patients with cutaneous malignancies for its ability to identify SLNs. It was compared to pre-operative scintigraphy and SPECT scans (147). The authors found that when used intraoperatively the gamma camera detected all lymph nodes that were visualised pre-operatively and it located an additional 23 SLNs in 15 patients, two of which contained metastatic tissue. Thus, this represents further evidence for the use of SFOV gamma cameras as an intraoperative imaging modality to reduce false-negative SLN detection results. These findings are also supported in the study by Cardona-Arbonies et al. (148) who found that use of the Sentinella gamma camera intraoperatively identified SLNs, with low radioactivity, in two cases, which were not present upon pre-operative planar and SPECT imaging.

A less well-known armed gamma camera is the 2020tc Imager, which is a multi-crystal scintillator detector that utilises a silicon photodiode, rather than a photomultiplier tube, to convert scintillation light into electrical charge. This gamma camera has a field of view of 20 x 20 cm and its performance includes a sensitivity of 54 cps/MBq at 10 cm imaging distance, a special resolution of 7 mm at 10 cm and an energy resolution of <14 % at 140 keV (129). In a study by Motomura et al. (149) this gamma camera was evaluated intraoperatively and compared to the pre-operative detection of potential SLNs using the 2020tc Imager and a conventional gamma camera. The results showed that 41 nodes among 29 patients were identified pre-operatively by both modalities, but the 2020tc Imager identified a marginally higher proportion of all nodes. Moreover, the 2020tc Imager and conventional gamma probe identified numerous additional nodes intraoperatively (n=63), whereby the 2020tc Imager helped to reduce the rates of residual nodes that would have otherwise been left in patients.

The CarollRes gamma camera was developed by the Institut Pluridisciplinaire Hubert Curien in Strasbourg, France. It utilises a 5 x 5 cm cerium-doped gadolinium orthoxysilicate scintillator detector and parallel hole collimation, conferring a ^{99m}Tc spatial resolution of 10 mm at a 5 cm imaging distance, energy resolution of 45 % and a sensitivity of 130 cpm/MBq (12). In a prototype study, Mathelin et al. (14) evaluated the CarollRes gamma camera in patients with infiltrative breast carcinoma for its ability

to identify and localise SLNs (Figure 3.12). The authors found that the depth of potential SLNs as determined by the camera correlated well with that found surgically, which was precisely correct for a total of 7 out of 11 nodes.

Moreover, in a case report of a 44-year-old female with infiltrative ductal carcinoma, the CarollRes gamma camera was able to identify a second SLN that was not detected during conventional lymphoscintigraphy scanning, suggesting that SFOV gamma detectors can reduce false-negative rates and under-staging of disease, ultimately yielding better patient outcomes (13).
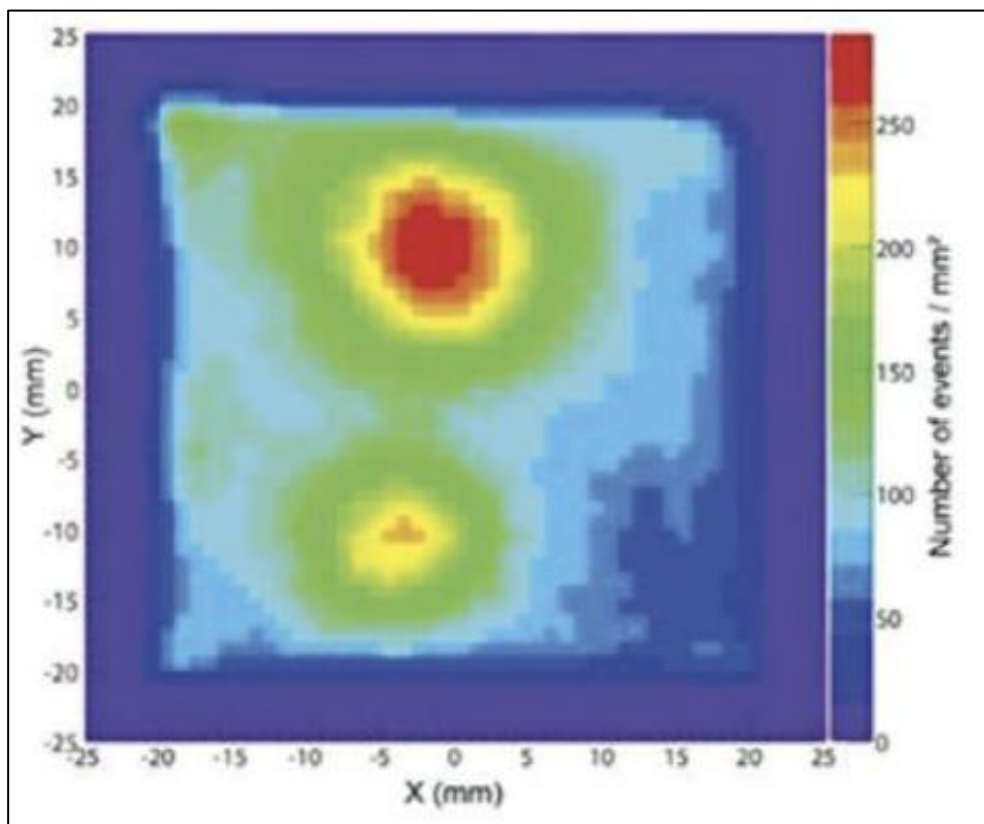
Figure 3.12. Demonstration of two sentinel lymph nodes in a right breast using the CarollRes gamma camera (12).

One of the largest SFOV gamma cameras was developed by General Electric in Haifa, Israel and Gamma Medica Ideas in Northridge, California, but this was developed for screening and pre-operative diagnostic purposes and is reviewed elsewhere (150, 151). For the reader, these gamma cameras have also been evaluated in phantom and clinical studies in more recent times (124, 152). Notably, Gamma Medica Ideas Incorporated

manufactured one of the earliest articulated arm gamma cameras that is reported in the literature, known as the GammaCAM/OR. This was evaluated in a small clinical study by Aarsvod et al. (153) for imaging SLNs in breast cancer patients intraoperatively. The authors reported that the gamma camera was able to assist in node identification, particularly in difficult cases, but no meaningful conclusions were reached, and its performance and technical characteristics were not well defined. However, Hruska et al. (152) reported that a more recent generation of the gamma camera with CdZnTe-based detection and a 20 x 16 cm FOV produced a spatial resolution of 4.8-5.6 mm at 3 cm imaging distance.

To conclude this review, when developing gamma imaging systems of this nature, it is imperative that due consideration is given to ensuring that they offer sufficient resolution and a level of sensitivity required for the appropriate clinical procedures, while administering relatively low amounts of radiation. Table 3.2 shows a summary of the available SFOV compact gamma imaging systems that have been tested in clinical settings.

Table 3.2. Available small field of view (SFOV) compact gamma imaging systems

SFOV gamma camera	Detection material	Energy Range (keV)	Collimation principle	Nuclear Medicine Procedures
Sentinella 102 (154-157)	CsI(Na) - Position-sensitive PMT	50 - 200	Pinhole	SLN detection and Intraoperative hyperthyroidism gamma imaging
Hybrid Gamma Camera (HGC) (158-160)	CsI(Tl) - EMCCD	30 - 200	Pinhole	Lacrimal scintigraphy, thyroid scintigraphy, lymphoscintigraphy, and SLN biopsy
Mediprobe (161)	CdTe:Cl	141		SLN detection
Intraoperative handheld gamma Camera (IHGC) (140, 141)	NaI(Tl) – Position-sensitive PMT	30 - 300		
GammaCAM/OR (162, 163)		141		
Preoperative Compact Imager (POCI) (58, 134)	CsI(Na) - Intensified position-sensitive diode	30 – 250		
MiniCam II (164)		30 - 200	Parallel hole	
MGC500 mini gamma camera (56, 57, 89)	CdTe	550 max.		
TreCam (165, 166)	LaBr3:Ce - Multi-Anode PMT	141		
CarollRes (12, 13)	GSO:Ce - Multi-Anode PMT	141		
CrystalCam (167, 168)		30 – 250		
eZ Scope (131, 169)	CdZnTe	71 - 364		Intraoperative hyperthyroidism gamma imaging

3.3.3 SFOV hybrid gamma camera project

This section presents an overview of a prototype high spatial resolution SFOV hybrid gamma camera that is designed and developed to facilitate intraoperative gamma imaging and small organs gamma imaging procedures. The hybrid gamma camera (HGC) is a SFOV scintillation detector based on charge coupled device (CCD) technology that was originally invented for the purposes of X-ray astronomy (160). The camera system combines optical and gamma imaging.

3.3.3.1 Developmental stages of the SFOV hybrid gamma imaging system

The BioImaging Unit at the Space Research Centre (SRC), University of Leicester, was established in 1999. Since then, the research activities of the SRC have been extended towards developing a range of prototype medical imaging instruments, such as the autoradiography camera based on microchannel plates (MCPs) and Charged Coupled Device (CCD) technology-based gamma imaging systems (170, 171). The idea of an SFOV compact gamma camera was originated by Prof John Lees (BioImaging Unit research group leader). In 2003, the BioImaging Unit research group initiated the development of SFOV medical imaging systems by developing the high-resolution gamma imager (HRGI): a CCD-based camera for medical imaging (171). A 100-μm-thick gadolinium oxysulphide (Gd_2O_2S) scintillation layer was directly attached to the CCD, and both were isolated and sealed within a plastic case. With a CCD chip sensitive area of 20 mm × 30 mm, the HRGI was developed for oral gamma imaging applications (Figure 3.13). By increasing the thickness of the scintillator, the imager was made more efficient in terms of this detection, with spatial resolution degrading to 0.60 mm from 0.44 mm (500-μm-thick Gd_2O_2S scintillator). The development of this small, un-collimated imaging system that shows potential capabilities of providing high-resolution gamma imaging encouraged the BioImaging Unit research group to develop an SFOV handheld gamma imaging system.
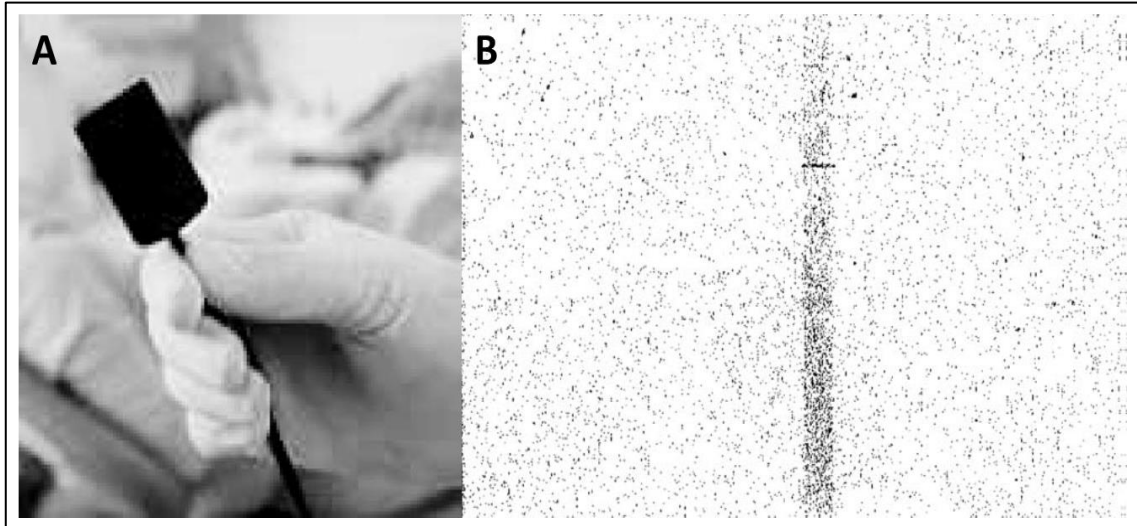
Figure 3.13. (A) charged couple device (CCD38-20) dental imaging detector produced by E2V Technologies, (B) gamma image of a 1 mm diameter tube filled with ^{99m}Tc solution (300 s acquisition time) (171).

Lees et al. (2006) described the development of a scintillator-coated CCD-based camera for the investigation of radioactivity uptakes. The HRGI was upgraded with a CCD 55-30 produced by e2v Technologies, UK, with a 500-μm-thick terbium-doped gadolinium oxysulphide (Gd$_2$O$_2$S[TB]) scintillation layer, a Peltier cooler (Melcor thermoelectric device), a parallel hole lead collimator and a finned heatsink using forced air (172). The detection head was surrounded by a plastic container for protection, which not only assisted ease of use but ensured the device was small enough to be held in the hand. The operating temperature was reduced to around -5°C with the help of the Peltier cooler, which in turn meant that the dark currents dropped to 10 electrons/ pixel/second. Within the container holding the detector a dry nitrogen atmosphere was created to stop condensation affecting the CCD (see Figure 3.14).
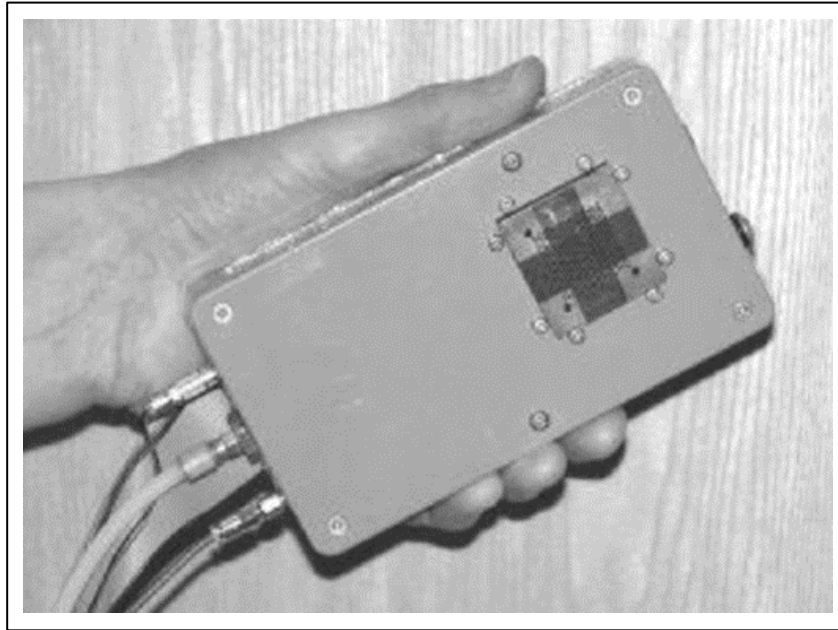
Figure 3.14. Photograph of the High-Resolution Gamma Imager fitted with high-resolution parallel hole collimator (172).

The BioImaging Unit researchers continued to work on the camera and created a novel prototype named the Mini Gamma Ray Camera (MGRC) (Figure 3.15). This camera was designed to offer improved, high-spatial-resolution images that could be employed in gamma imaging procedures. The Gd_2O_2S[TB] scintillator was switched to a thallium-doped caesium iodide (CsI[TI]) (159). A back-illuminated electron multiplier CCD (EMCCD) was employed. This was linked with a scintillation crystal employing Dow Corning optical grease. The thermoelectric technology for this handheld gamma camera was the same as that employed in the HRGI.

Apart from the front of the gamma detector, it was surrounded by a 4-mm-thick lead shield to mitigate the potential for the apparatus to detect background radiation or scattered photons. The design of the MGRC permitted the collimators to be interchanged, with a choice of parallel hole collimator or pinhole collimator. A pair of pinhole collimators, with pinhole diameters of 0.5 mm and 1.0 mm, with angular apertures of 60°, were made from tungsten discs (6 mm thick). Images were acquired utilising bespoke software written in Interactive Data Language (IDL) (more details will be provided in subsection 3.3.3.4). The MGRC design allowed photons ranging in energy between 20 and 140 keV to be detected; the MGRC was able to offer a spatial resolution of ~1 mm.

Figure 3.15. Photograph of the Mini Gamma Ray Camera (MGRC).

The camera head of the MGRC was improved with a well-engineered outer design, which makes the camera an easy-to-use device. It can also be mounted on a fabricated arm. Furthermore, this new design of the gamma camera was produced with improved cooling systems and shielding, and called the Compact Gamma Camera (CGC) (160). A new heat exchange system was introduced employing a paraffin-based phase-change material (PCM), lowering the CCD temperature to -13°C without having to employ fans powered by electricity. This reduced contamination risks, as it allowed the PCM to be held within the camera head case, so that heat exchange could occur without airflow being involved. A ridged plastic surface was added to the camera head so that it could be held steady when taking images.

Combining a number of different dual imaging modalities for medical imaging has greatly enhanced practitioners' diagnostic armoury and treatment options. Such technologies give practitioners anatomical and functional feedbacks, which is useful in managing various medically critical cases. Anatomical and functional detail related to tissue metabolism and its exact location in the anatomy can be registered using inter-modality image fusion. With that in mind, the BioImaging Unit researchers developed the currently used gamma-optical imaging system, known as the Hybrid Gamma Camera (HGC).

The available protocols for evaluating LFOV gamma imaging systems can be inappropriate, and they need to be modified to suit SFOV gamma imaging systems. Bhatia et al. (64) proposed an assessing scheme that can meet the needs of SFOV gamma camera performance evaluation. This scheme outlined the available characterisation protocols for LFOV gamma imaging systems and highlighting the required modification for evaluating SFOV gamma imaging systems. Bugby et al. (173, 174) used the above-mentioned scheme to characterise the current model of the HGC, fitting the HGC with two interchangeable thicknesses of the CsI(TI) scintillator (i.e. 600 μm and 1500 μm thick). The parameters investigated and HGC characteristics are summarised in the following subsections (Table 3.3).

Based on the previously mentioned stages in the development of the HGC, the research work conducted and presented in this thesis is designed to assess the suitability of the HGC for clinical imaging during routine and surgical gamma imaging procedures. The HGC is evaluated using various assessment protocols in experimental settings (i.e. through using different bespoke phantoms simulating clinical scenarios) and during routine gamma imaging procedures in nuclear medicine clinics (see Figure 3.16).
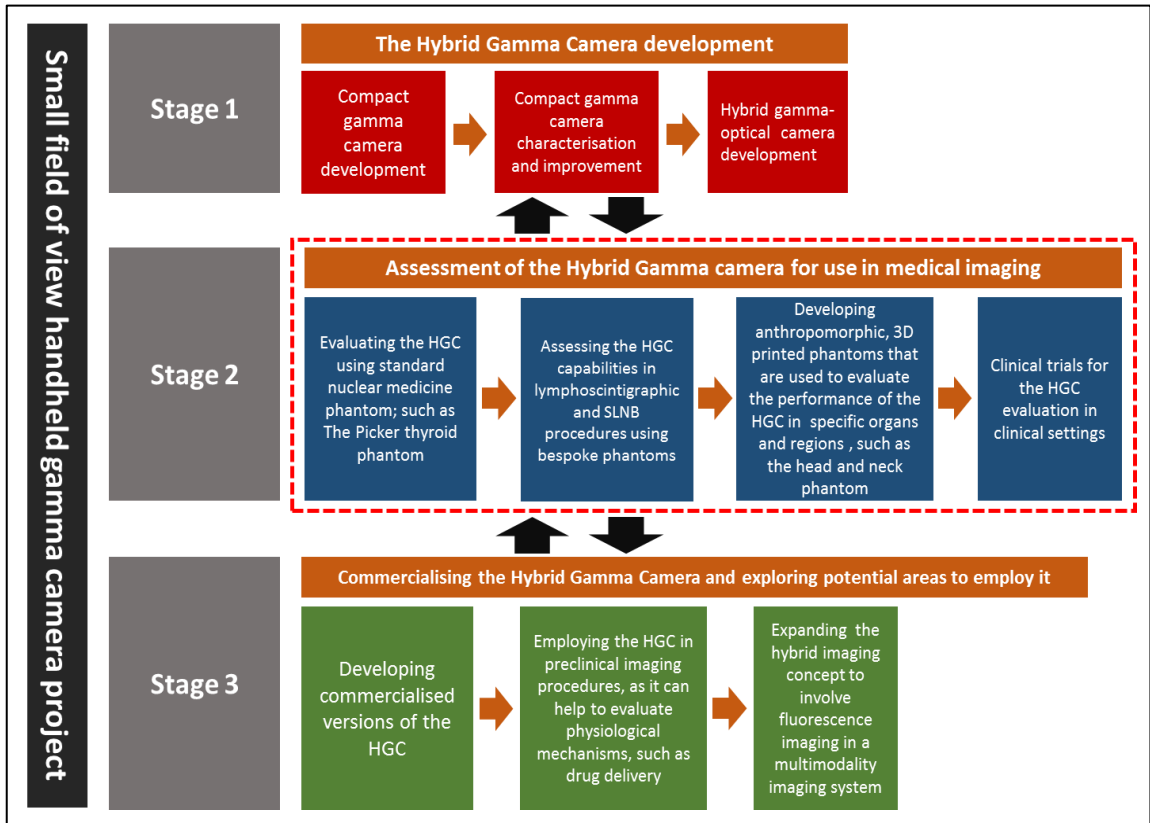
Figure 3.16. A schematic illustrating the research stages of developing and assessing the hybrid gamma camera. The red-dashed boarded box represents the scope of the conducted research presented in this thesis.

3.3.3.2 The SFOV hybrid gamma camera design and characteristics

Figure 3.17 shows an image of the hybrid gamma camera (HGC) together with a schematic of the HGC. The fundamental components of the HGC are an electron multiplication charge coupled device (EMCCD), CsI(Tl) scintillator, pinhole collimator, a miniature optical camera and a mirror (placed at 45 in front the optical camera). The distance between the EMCCD and the pinhole is fixed at 10 mm. The FOV size of the HGC is determined by the distance between the pinhole and the object that is being scanned. The detector enclosure is surrounded by tungsten shielding, which serves the purpose of minimising the level of image degradation that results from scattered photons and background radiation.

The optical module is attached to the gamma detector using an in-house fabricated aluminium mount. It is manually fitted to the HGC's head in a way that ensures an accurate positioning for the optical camera and the mirror, and ensures that the FOV of both the gamma and optical camera is identical and independent of the distance between both cameras and the targeted accumulated activity. Gamma photons, produced from radioactivity accumulated in the targeted region, pass through the mirror with minimal absorption (<1 %) and minimal scatter, whereas the optical photons are reflected by the mirror towards the optical camera. The optical camera is calibrated to provide an optical image that displays a similar ROI as the gamma camera. The HGC is capable of providing a simultaneous hybrid gamma-optical imaging facility.
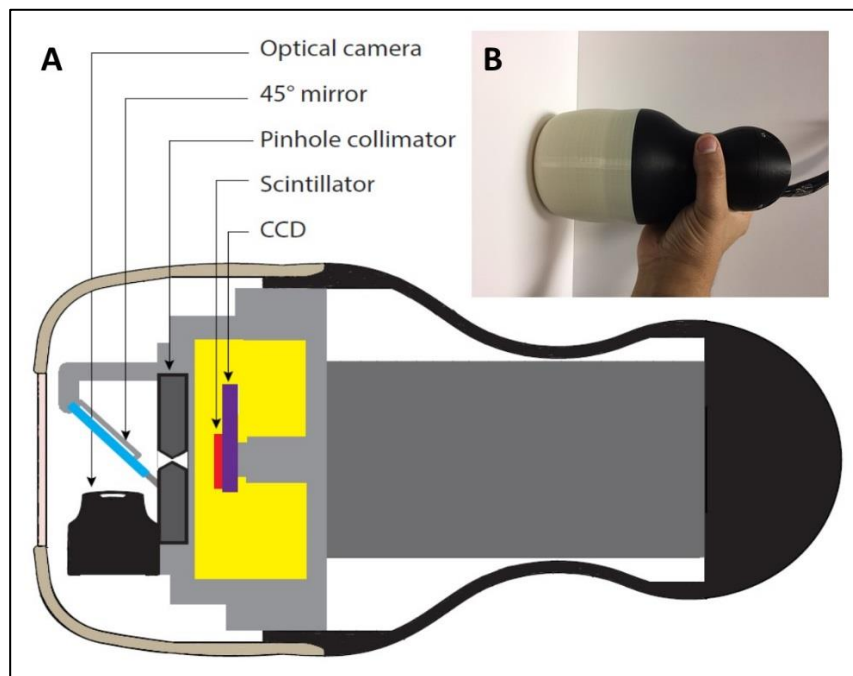
Figure 3.17. A schematic (A) and a photograph (B) of the small field of view (SFOV) compact, handheld hybrid gamma camera (HGC)

3.3.3.2.1 Columnar scintillator

Thallium-doped caesium iodide CsI(Tl) exhibits some distinct qualities that make it ideal for use with CCDs. As previously described, it incorporates high-Z components, a high density, and good scintillation light yield (54 photons/keV), which makes it suitable for use in gamma-ray detection. In addition, the scintillation photons exhibit a peak wavelength of 565 nm. This is a good match to the spectral response of the CCD, which has a quantum efficiency in excess of 90 % at this wavelength (159).

Luminescence is often activated by doping thallium (Tl) into the CsI scintillator. In choosing a scintillator there is a need to maintain a delicate balance between achieving a high spatial resolution and a high stopping efficiency. To achieve the latter, a thicker amount of material is required; however, to achieve the former, a thinner material is preferred. One approach by which to overcome this trade-off is to employ structured scintillators that have the ability to guide the scintillation light towards the CCD. It is possible to grow CsI in a micro-columnar form that is known as a columnar CsI scintillator.
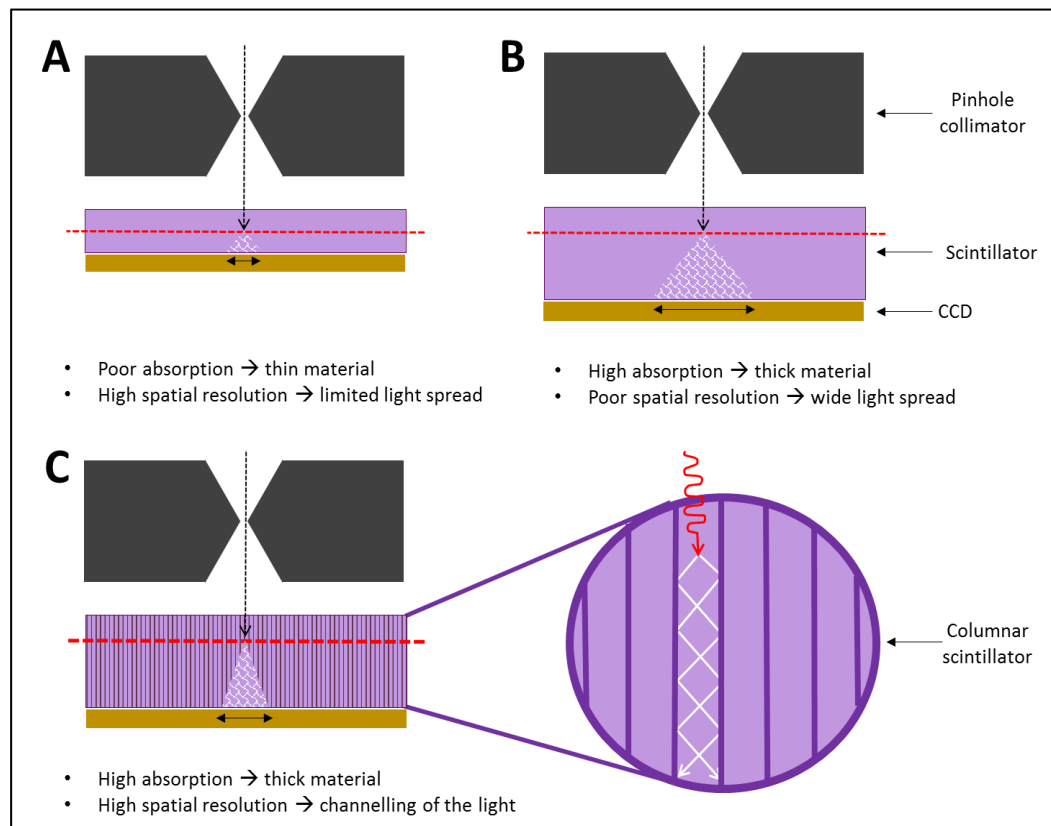
Figure 3.18. Schematics showing different behaviours of two different structures of the CsI scintillators; (A) continuous thin CsI scintillator, (B) continuous thick CsI scintillator and (C) columnar thick CsI scintillator.

This consists of needle-like columns of scintillator material that have the ability to channel scintillation light to the exit surface through total internal reflection, thereby reducing light spread and conserving spatial resolution (Figure 3.18). The HGC design generations incorporated two different thicknesses of a CsI(Tl) columnar scintillator (600 and 1500 μm thick on an amorphous carbon substrate) from Hamamatsu that were

directly coupled to the CCD (see Figure 3.19) (175). The HGC was designed to be sensitive over the 30-200 keV gamma energy range. The main characteristics of the HGC are been summarised in Table 3.3.

Table 3.3. Characteristics of the hybrid gamma camera generations (173, 174)

Scintillators			CsI:TI	
Thickness			**600 μm**	**1500 μm**
Intrinsic spatial resolution		FWHM* (μm)	170±12	230±25
		FWTM** (μm)	300±20	468±23
Extrinsic spatial resolution	No Perspex	FWHM (mm)	NA	1.8±0.03
		FWTM (mm)	NA	3.3±0.05
	Including Perspex	FWHM (mm)	1.8±0.13	2.02±0.09
		FWTM (mm)	3.25±0.26	3.6±0.12
Intrinsic uniformity		CoV*** (%)	25±9	20±15
Intrinsic sensitivity		(%)	19±1	40±3
Extrinsic sensitivity	No Perspex	(cps/MBq)	NA	6.6±0.5
	Including Perspex		0.8±0.1	3.3±0.5
Count rate capability		Maximum recorded count rate (cps)	1200±200	3537±200
Energy resolution		FWHM at 141keV (%)	58	NA

* FWHM = Full Width at Half Maximum
** FWTM = Full Width at Tenth Maximum
*** CoV = Coefficient of Variation

3.3.3.2.2. Charge coupled device (CCD) and its cooling process

The HGC incorporates an inverted mode, back-illuminated electron multiplication charge coupled device (EMCCD) that offers an extra gain register that allows internal gain through electron multiplication (avalanche multiplication) controlled by the application of a high-voltage clock pulse (40-50 V). A CCD97 EMCCD is used in the HGC (176). This offers 512×512, 16 μm×16 μm pixels in the active imaging area (see Figure 3.19). A thermoelectric cooling device that incorporates a solid-state active heat pump was used to cool the EMCCD (177). Such a cooling processes are preferable for use in clean working environment, such as operating theatres, as there is no air intake, water or oil cooling. The HGC internal housing was evacuated to prevent condensation forming on the EMCCD. The operating temperature of the device was approximately - 10° C.
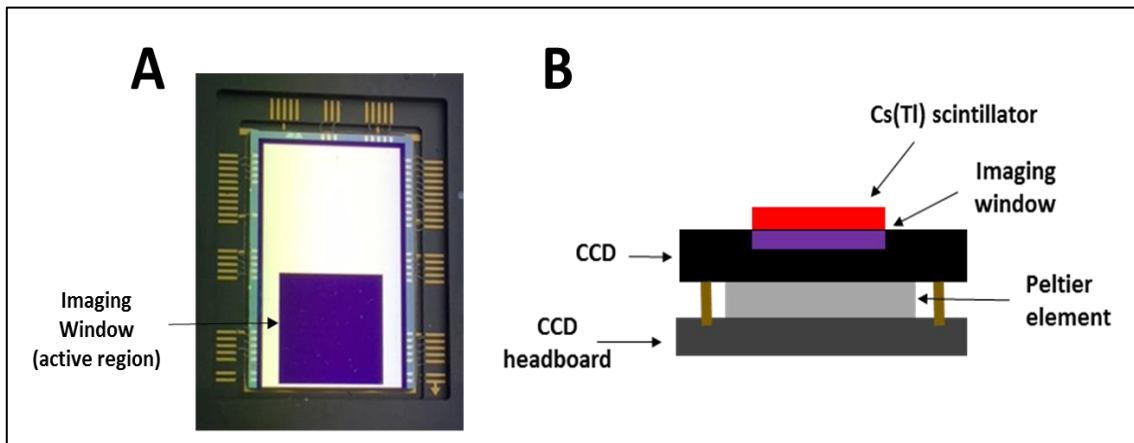
Figure 3.19. A photograph (A) and a schematic (B) of the electron multiplication charge coupled device (EMCCD)

The photons that the gamma rays generate in the scintillator are collected in the EMCCD image area during the acquisition time. The resulting charge is subsequently transferred to the storage section and then to the readout register. Once the charge has been transferred to the readout register, it is multiplied in the gain register before a charge sensitive output amplifier converts it into a voltage (159, 160).

3.3.3.2.3. The HGC gamma image acquisition

Every gamma photon that the scintillator absorbs gives rise to a large number of optical photons. The number of these that will reach the EMCCD depends on a number of factors including the depth of the interaction, the coupling efficiency of the scintillator with the EMCCD, the quality of the scintillator material, the light spread within the scintillator, and the efficiency with which the EMCCD operates at the wavelength of the optical photons. In practice, the EMCCD records a "light splash" that extends over a number of pixels. The region in which the light is absorbed in the scintillator determines the spread of the light. Gamma photons that interact far from the EMCCD generate a greater spread and, as such, a lower peak intensity is recorded. The number of optical photons that a gamma photon creates through absorption in a scintillator is correlated to its energy (for CsI(Tl) ~54 photons per keV); as such, the intensity measured by the EMCCD provides insights into the incident gamma photon energy (i.e. is proportional to the incident gamma photon's energy).

To process and measure the deposited energy in the CsI(Tl) scintillator, an automated coding algorithm has been implemented. This algorithm is able to recognise and distinguish detected light splashes, and produce information about the detected counts.

The HGC is operated using bespoke software written in IDL (Interactive Data Language) (159). This software has been programed to enable the HGC to acquire gamma and hybrid images with various acquisition times. The "blob-detection" algorithm code is integrated within this IDL software; this image processing code is used to process the raw gamma images (159). The main principle of this code is detect the gamma image's features (i.e. light splashes), then a Gaussian distribution is fitted to each light 'splash' produced by the scintillator. This allows the calculation of the deposited energy for the light splashes and their centre points. A 2D gamma image can then be reconstructed and characterised (118).
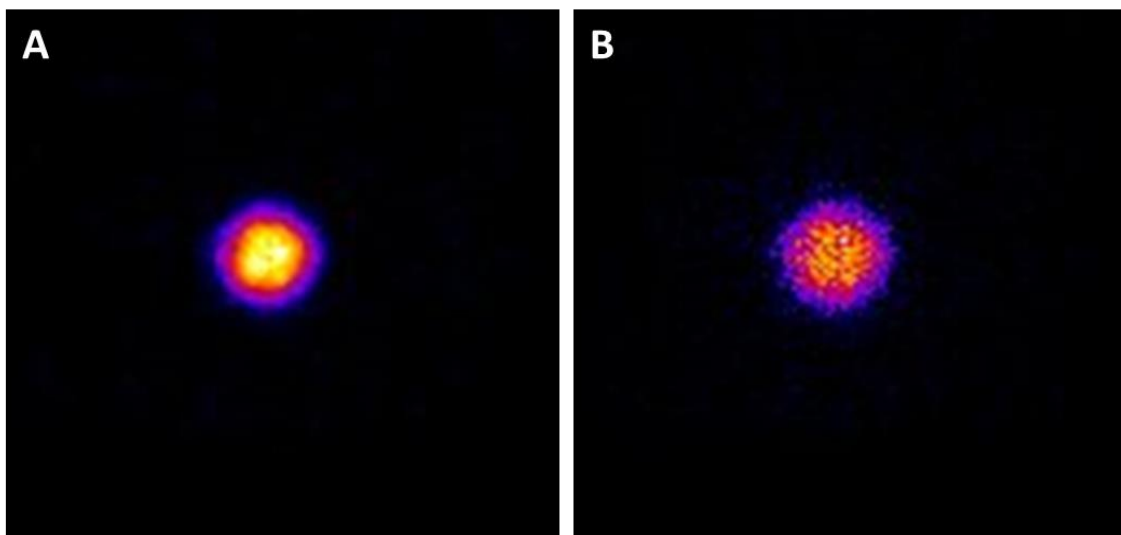
Figure 3.20. HGC gamma images of ^{57}Co source (27 MBq) placed 50 mm away from the pinhole collimator (1.0 mm in diameter). These gamma images were produced in cumulative (A) and centre-point (B) modes (60 s acquisition time).

The gamma image can be produced in two modes; cumulative and centre-point modes (Figure 3.20). Cumulative mode takes the whole Gaussian fit and plots the whole spread of each splash. In this mode, a single recorded count does not represented a single detected gamma event. Centre-Point mode plots the peak of the Gaussian fit, which represents the location of gamma events. The contrast to noise ratio (CNR) values are expected to be higher in the Cumulative mode gamma image; however, gamma images

produced using the Centre-Point mode are quantitative and comparable to those produced by a conventional LFOV gamma camera (118). It is worth mentioning that all gamma images, acquired using the HGC, analysed in this thesis are produced using the Centre-point mode of the blob-detection algorithm code.

3.3.3.2.4. HGC collimation

The camera is designed such that the type of collimator can be easily fitted. Single knife-edged pinhole collimators have been predominantly used with the HGC (Figure 3.17). In addition to simplifying the construction, this also extends the imaging field of view beyond the detector dimensions (i.e. ~ 8 mm × 8 mm). Two collimators that incorporated 1.0 mm and 0.5 mm diameter pinholes were produced from tungsten discs that had a diameter of 45 mm and a thickness of 6 mm. The pinhole collimator acceptance angle is 60°, which was selected to allow the full use of the sensitive imaging area of the detector, with the collimator placed 10 mm away from the detector. This configuration gives a nominal FOV for the HGC of ~ 40 mm × 40 mm at a 25 mm collimator-to-target distance.

The rate of transmission through 6 mm thick tungsten was determined to be $< 4 \times 10^{-9}$ at 140 keV, thus ensuring that the gamma photons were limited to those passing through the pinhole (159). Keeping in view the prerequisites of spatial resolution and sensitivity for a range of applications, both pinhole collimators can be interchangeably utilised but the essential design of the camera remains constant.

A range of different factors can directly impact the sensitivity of gamma cameras using pinhole collimators. These include acceptance angles, photon energy, pinhole diameter, and collimator material. The geometric sensitivity is also influenced by pinhole-to-object distance (178-181).

3.3.3.2.5. Shielding and casing

The back and sides of the detector enclosure are surrounded by 3 mm thick tungsten shielding that minimises any image degradation resulting from background radiation and scattered photons. Furthermore, the sensitive face of the camera is fitted with a 6 mm thick pinhole collimator and tungsten ring (surrounding the camera's head - 3 mm thick) to minimise the effect of scattered radiation.

The internal parts of the HGC are housed within an evacuated aluminium case (3 mm thick). This aluminium case has a 20 mm diameter sensitive window engraved (1 mm thickness) to minimise the attenuation of the incident gamma photon received through the collimator. The aluminium case is thermally coupled to a cooling cannister, containing phase-change material (PCM) wax, to absorb heat from the Peltier. The aluminium case and the cooling cannister are both fitted inside the outer plastic body of the HGC. The plastic body is designed to be easily handled, sterilised, and fitted to a customised supportive arm (Figure 3.16).

3.4 Conclusion

This chapter has illustrated the fundamental concepts and basic components of a routinely used LFOV gamma camera. The available intraoperative SFOV gamma imaging systems and their characteristics and imaging capabilities has been reviewed and discussed. The development of the SFOV hybrid gamma camera (HGC) has been described. The HGC characteristics and its working method have been discussed, and the similarities and differences between the HGC and standard gamma cameras described. During the research presented in this thesis, different camera configurations (scintillator thickness, pinhole diameter) have been used. The configuration used for each experiment will be specified in the following research chapters.

Chapter 4: Lymphoscintigraphic imaging study for quantitative evaluation of the hybrid gamma camera

4.1 Introduction

The lymphatic system is responsible for performing a function of crucial importance to the human body; it monitors the balance of tissue fluid by conserving a concentration of proteins and emptying interstitial pores (182). Any disturbance to the normal functioning of the lymphatic system may result in several pathological conditions. Lymphedema is the most common pathology related to the lymphatic system. In this condition, disturbance to lymphatic transport causes irreparable damage to tissues (183). Researchers are interested in studying the lymphatic system because it also contributes to dermal drug delivery and tumour metastasis (182-185). Considering the role played by the lymphatic system in the spread of disease and therapeutic processes, it has become important that substantial developments are made diagnostic tools able to measure the function of the lymphatic system.

In the field of nuclear medicine, lymphoscintigraphy refers to functional imaging of the lymphatic system (186, 187). One of the extensively used lymphoscintigraphic procedures for functional preoperative imaging is the sentinel lymph node (SLN) localisation procedure to isolate potential SLNs. This procedure is usually followed by a biopsy or surgery to determine the cancer stage, and a treatment strategy is tailored to the patient accordingly. A conventional large field of view (LFOV) gamma camera is used in lymphoscintigraphy to acquire images in routine clinical practice. These cameras are not available for imaging during surgery; therefore, non-imaging gamma probes are used to detect regions with higher accumulation of activity intraoperatively.

Intraoperative imaging is of high interest and, for that reason, researchers are working on developing innovative intraoperative gamma imaging systems (58, 89). This study aims to preliminary investigate the hybrid gamma camera (HGC) in terms of its suitability for intraoperative SLN imaging, and the ability of the HGC to distinguish the injection site from its adjacent tissues. The phantoms and methods employed in this study can be used with any SFOV gamma imaging system and for quantitative comparison of efficiency.

4.2 Materials and Methods

4.2.1 Hybrid Gamma Camera (HGC) configuration

The small field of view HGC uses a scintillator-based detector. The detector consists of an e2v CCD97 back-illuminated electron multiplying charge-coupled device (EMCCD) coupled to a 600 μm thick columnar CsI(Tl) scintillator. Imaging was carried out with a tungsten pinhole collimator of acceptance angle 60°, and the performance of the HGC was investigated with both 0.5 mm and 1.0 mm diameter pinhole collimators installed. More details about the HGC design and structure have been provided in Chapter 3.

4.2.2 Phantoms construction

Lymphatic mapping for surgical and biopsy procedures is based on the idea that the lymphatic fluid drains from a primary malignant tumour site to a specific regional lymph node. Moreover, a common definition for the SLN concept is that provided by Morton et al., which defines a sentinel lymph node as any lymph node on the afferent (i.e. towards the node) drainage pathway from the primary tumour (188); see chapter 2 for more information. This definition reflects the importance of the lymphatic vessel detection, and its integral part in detecting and determining the SLN.

To evaluate the HGC for use in sentinel node lymphoscintigraphy, two lymphoscintigraphic phantoms have been developed and fabricated in-house. These phantoms are constructed from Perspex (Poly-methyl methacrylate-PMMA) plates. Perspex has been utilised in manufacturing these medical phantoms because of its acceptable degree of similarity with human tissue [i.e. soft tissues and Perspex densities

are 1.04 g/cm^3 and 1.18 g/cm^3; the mass attenuation coefficient values for soft tissues and Perspex are 0.153 cm^2/g and 0.149 cm^2/g, respectively] (189).

4.2.2.1 Lymphatic vessel phantom design and activity simulation

The first phantom, a lymphatic vessel phantom, (Figure 4.1 A) has been constructed to assess the capability of the HGC for lymphatic vessel drainage imaging. It consists of a 10 mm diameter Eppendorf tube containing about 60 MBq of ^{99m}Tc (0.5 ml) imitating the injection site (half-life= 6 hours; Energy = 141 keV), and a lymphatic vessel simulated by an 80 mm long capillary tube (1.1 mm internal diameter) filled with approximately 16 MBq of ^{99m}Tc solution (0.1 ml). The capillary tube was placed underneath thicknesses of Perspex ranging from 5 mm to 30 mm to simulate the lymphatic vessel at different depths inside the human body with a superficial injection site. This simulated lymphatic vessel (LV) is comparable in size to natural lymphatic vessels; for instance, the diameters of lymphatic vessels in the distal parts of the lower extremities range between 0.8 mm and 1.5 mm (190). The aim behind developing this phantom is to assess the ability of the HGC to resolve the proximal part of the LV during the scanning of the drainage of the radioactive material from the injection site to the targeted tissues, i.e. SLNs.

4.2.2.2 Melanoma phantom design and activity simulation

The second phantom, a melanoma phantom, (Figure 4.1 B) is a combination phantom. It simulates the injection site, the lymphatic vessel, and a SLN of approximately average size (191). The melanoma phantom was used to evaluate the relationship between activity uptake and the HGC sensitivity at different depths. The effect of the distance from the injection site to the sentinel lymph node on the image quality was also evaluated with this phantom. The configuration of the lymphatic vessel phantom has been used as a basis for this phantom; however, two square Perspex plates (80 mm × 80 mm) with 8 mm thickness have been added. One plate contains a 7 mm diameter (6 mm depth) well to mimic a SLN, and the second plate has a 70 mm × 70 mm square well to simulate the background activity around the SLN. This phantom is constructed to evaluate the ability of the HGC to detect a simulated SLN with different radioactivity concentrations and assess the possibility of resolving lymph nodes that are anatomically localised close to the areas of high activity accumulations, such as the injection site.
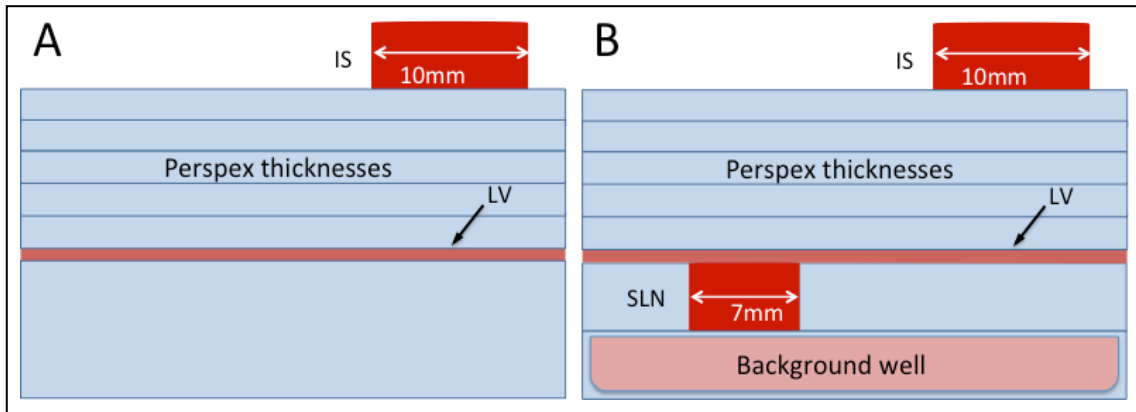
Figure 4.1. (A) A schematic of the lymphatic vessel phantom showing the simulated lymphatic vessel (LV) and the injection site (IS); (B) melanoma phantom configuration showing the simulated sentinel lymph node (SLN), IS, LV and the background well.

For the melanoma phantom, the simulated injection site (i.e. Eppendorf tube) was filled with 0.5 ml of a ^{99m}Tc solution (15 MBq total) (38). The SLN was simulated for various activities, with SLN to IS ratios ranging between 1:20 and 1:100 in 0.1 ml solutions. The simulated activity of the background was one tenth of the SLN activity (i.e. 1:10 BG to SLN ratio). The 80 mm long lymphatic vessel (capillary tube) contained the same activity as in the SLN, distributed over approximately 0.1 ml (see Table 4.1).

Table 4.1. Summary of simulated activity in the melanoma phantom

SLN to IS ratio	IS activity in 0.5 ml	SLN activity in 0.1 ml	Background activity in 4 ml
1:20		0.75 MBq	3 MBq
1:50	15 MBq	0.3 MBq	1.2 MBq
1:100		0.15 MBq	0.6 MBq

4.2.3 Injection site (IS), lymphatic vessel (LV) and sentinel lymph node (SLN) activity simulation challenge

4.2.3.1 Lymphatic vessel activity simulation

The lack of clinical data for estimated activity concentrations in LVs in the human body during lymphoscintigraphic procedures, and the difficulty in performing these kinds of studies, is due to the nature of lymphatic vessels. They have varying and uncertain diameters and depths; even for a known lymphatic route, the proximal and distal parts can differ in diameter and depth (190). Moreover, the physiological condition of the examined part specifically, and the whole body generally, plays a primary role in determining the ratio of the radioactivity which is trapped in the LVs (192, 193). Many external factors can affect the uptake ratio in the LVs, such as the amount of administered activity and the time delay between the administration of the activity and the scanning procedure. The scattering effect produced by hot spots (e.g. the IS) close to the LV may also influence the ability to detect the vessels. Therefore, the different amounts of activity used to simulate the activity in the LV in both phantoms were selected to determine the detection limit of the HGC.

4.2.3.2 Sentinel lymph node (SLN) activity simulation

In clinical practice, it is a laborious task to determine the specific ratio of SLN to IS activity since there are many radiocolloids (radiopharmaceuticals) with widely varying molecular diameters, which affect the activity flow and spread. The ratio is also strongly affected by time delays between the initial administration of the radioactivity and the surgical procedure. Furthermore, SLNs vary extensively in size, shape and the number of lymphatic suppliers, which may also affect the radioactive dose uptake (194). In addition, many authors endorse stress lymphoscintigraphy for the extremities after the administration of the radioactivity; although this medical practice is not globally employed, it enhances the sensitivity and improves lymphatic flow and the activity uptake in the SLNs, which affects the SLN to IS activity ratio (195-197).

A formalised standardisation of the radioactive material dose to be administered in SLN procedures has not yet been adopted. The suggested and investigated activities vary between 3.7 MBq and 370 MBq depending on the procedure and institution; however, 5 to 30 MBq as the total injected dose for SLN detection scanning is generally accepted and can be considered a sufficient dose for same-day surgical procedures (38). The Administration of Radioactive Substances Advisory Committee (ARSAC), Public Health England – UK, has released notes for guidance on the clinical administration of radiopharmaceuticals and use of sealed radioactive sources (198). These notes recommended diagnostic reference levels for the injected radioactivity in various nuclear medicine procedures. For SLN (melanoma cases) imaging and non-imaging probe studies, it has been suggested that melanoma patients can be administered with 20 MBq of ^{99m}Tc-colloid for the same day procedures and 40 MBq for next day procedures aiming for 10 MBq residual activity at surgery.

For this study, activity simulations for melanoma were conducted for SLN to IS activity ratios of 1:20, 1:50 and 1:100. This range was selected to cover the majority of values in studies (199-201), and to investigate the capability of the HGC in a range of medical scenarios. To improve the simulation, an active background has been added to imitate the uptake in the soft tissues around the SLN.

The typical background to SLN activity ratio ranges between 1:10 and 1:20 (202). This variation depends upon the type and the amount of the injected activity. Delay time between the dose administration and surgery may also affect this ratio. In this study, a 1:10 background activity to SLN activity ratio was used to investigate the worst case scenario.

4.2.4 Imaging procedure

The HGC was used to image both phantoms. The lymphatic vessel phantom was also imaged using a standard/conventional multipurpose single-head rectangular large field of view (LFOV) gamma camera (Nucline™ X-Ring) equipped with Low Energy High Resolution (LEHR) and Low Energy All-Purpose (LEAP) collimators (203). For the HGC, the 0.5 mm and 1 mm pinhole collimators were both used in this study. The SLN and LV

in both phantoms were placed beneath different thicknesses of scattering medium, ranging between 5 mm and 30 mm. In the melanoma phantom, nuclear scans were obtained over varied distances between the IS and the SLN. The IS to SLN centre-to-centre distance was varied between 10 mm and 50 mm in 10 mm intervals. A metallic frame with a clamp held the HGC perpendicular to the phantom's surface. The distance between the collimator and the scattering medium surface was 100 mm. This distance has been selected as it provides a suitable imaging field of view, and allows unrestricted movements for required tools within the surgical field. The acquisition time for both phantoms was between 100 s and 500s.

After the acquisition procedure was performed, specific steps are initiated to enhance the image quality produced by the HGC, and improve the accuracy of the analysis. The main step is the "Blob" Centre-Point detection technique, whereby a Gaussian distribution is fitted to each light 'splash' produced from the scintillator and the peak is displayed (as described previously, page no. 70-72). In this study, all the data from the HGC used to produce graphs are taken from Centre-Point mode images. The gamma images presented were also processed using Image-J software Gaussian Blur filter (Gaussian sigma = 2 pixel) (204).

4.2.5 Measured parameters

For the lymphatic vessel phantom, count profiles were obtained with a fixed collimator to surface distance (100 mm). The target object (i.e. the simulated lymphatic vessel) was positioned underneath different scattering material thicknesses (Figure 4.1 A). The HGC was held perpendicular to the surface of the phantom. The full width at half maximum (FWHM) of the count profiles was recorded.

For the melanoma phantom, the SLN was placed beneath a variety of scattering medium thicknesses (Figure 4.1 B). The HGC was fixed 100 mm away from the surface of the scattering medium. The contrast to noise ratio (CNR) is calculated for the sentinel lymph node at different depths (ranging from 5 mm to 30 mm), at 20 mm from the injection site with various SLN to IS ratios (i.e. 1:20, 1:50 and 1:100). CNR measurements should be conducted for a small field of view gamma camera to advise the operator if a hot

spot (e.g. lesion or SLN) can definitely be assessed as detectable or not. A. Rose (205) gives an approximation that in order to be detectable an object's CNR must exceed 3-5 (205). Nodes with a CNR of 3 visually appeared barely detectable and required colour scaling to be clearly seen, while nodes with a CNR of 5 could generally easily to be seen in images without colour scaling making these reasonable thresholds. The CNR calculation formula utilised in this study is as follows (90, 206)

$$\text{CNR} = \left[\frac{(N_l - N_{bg})}{\sigma_{bg}}\right] \qquad (4.1)$$

Where N_l corresponds to the mean counts of a lesion area (i.e. SLN) and N_{bg} is the average background count level. σ_{bg} is the background counts' standard deviation. ImageJ and Origin 9.1 (207) programs have been utilised for analysing and plotting purposes. A circular region of interest corresponding to the lesion area was defined based on the simulated SLN's size; also, a background region of interest of identical size was chosen.

4.3 Results and Discussion

4.3.1 Characterisation of HGC performance with a lymphatic vessel phantom

4.3.1.1 Performance comparison between LFOV and SFOV gamma cameras

Figure 4.2 shows the relationship between the measured FWHM of the simulated LV at different distances from the IS for both the standard LFOV gamma camera and the HGC. The measured spatial resolution was significantly better (i.e. smaller FWHM) for the HGC than the standard LFOV gamma camera, independent of separation or depth of scattering material. The FWHM of the modelled lymphatic vessel remains at a steady level (variation < 5 %) when the distance from the centre of the IS was more than 15 mm, reflecting the fundamental spatial resolution of each camera (measured at 100 mm from the phantom).
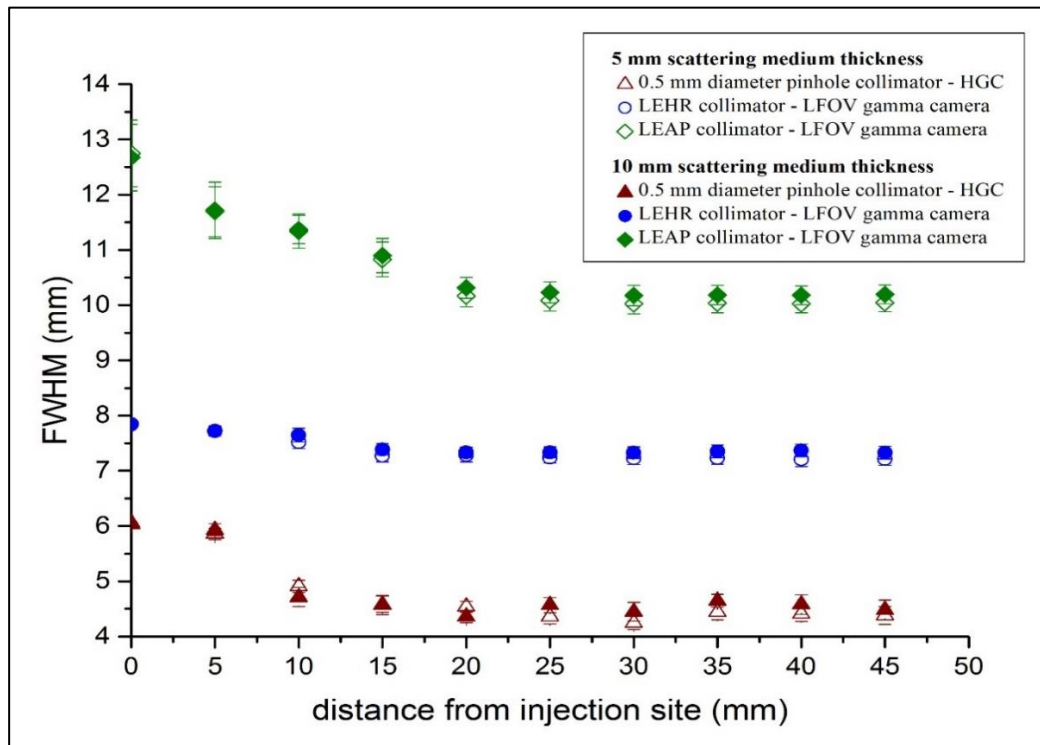
Figure 4.2. Comparison of the full width at half maximum (FWHM) for the lymphatic vessel phantom as a function of distance from the centre of the IS for the HGC and the standard LFOV gamma camera at an acquisition time of 500 s. Circles: FWHM of count profiles produced by the standard LFOV gamma camera with 5 and 10 mm of the scattering medium. Triangles: FWHM of count profiles acquired by the HGC with 5 and 10 mm of the scattering medium. The collimator to phantom distance for both cameras was 100 mm. The distance 0 mm represents the centre of the IS.

In Figure 4.3, at a fixed acquisition time of 500 s, the steady increase in the full width at half maximum (FWHM) shows the degradation in spatial resolution with an increase of scattering medium thickness. The poorest spatial resolution recorded by the HGC in this experiment is 6.3 mm at a 130 mm collimator to source distance and with 30 mm PMMA thickness. Nevertheless, these results are better than those produced by the standard LFOV gamma camera ranging between 7.1 mm and 8.1 mm underneath 5 mm to 30 mm of scattering material utilising LEHR collimator. Moreover, in the normal SLN detection procedure, LEAP collimators are used to improve sensitivity by collecting more counts from the SLN (208). Using the LEAP collimator in this experiment provided a recorded line width for the simulated LV ranging between 9.7 mm and 11. 6 mm for the same experimental setup.

It may be noticed that the spatial resolution of the HGC system degrades slightly faster with increasing the distance between the collimator and the imaged active target due to the nature of pinhole collimation (see chapter 3). However, for clinically relevant scenarios the influence of the degradation in spatial resolution between the two gamma cameras remained relatively small given the limited depths of the LVs inside the human body in most cases. The recorded degradation is comparable to the degradation observed using the LEAP collimator (LFOV gamma camera), the preferable collimator for SLN detection procedures.
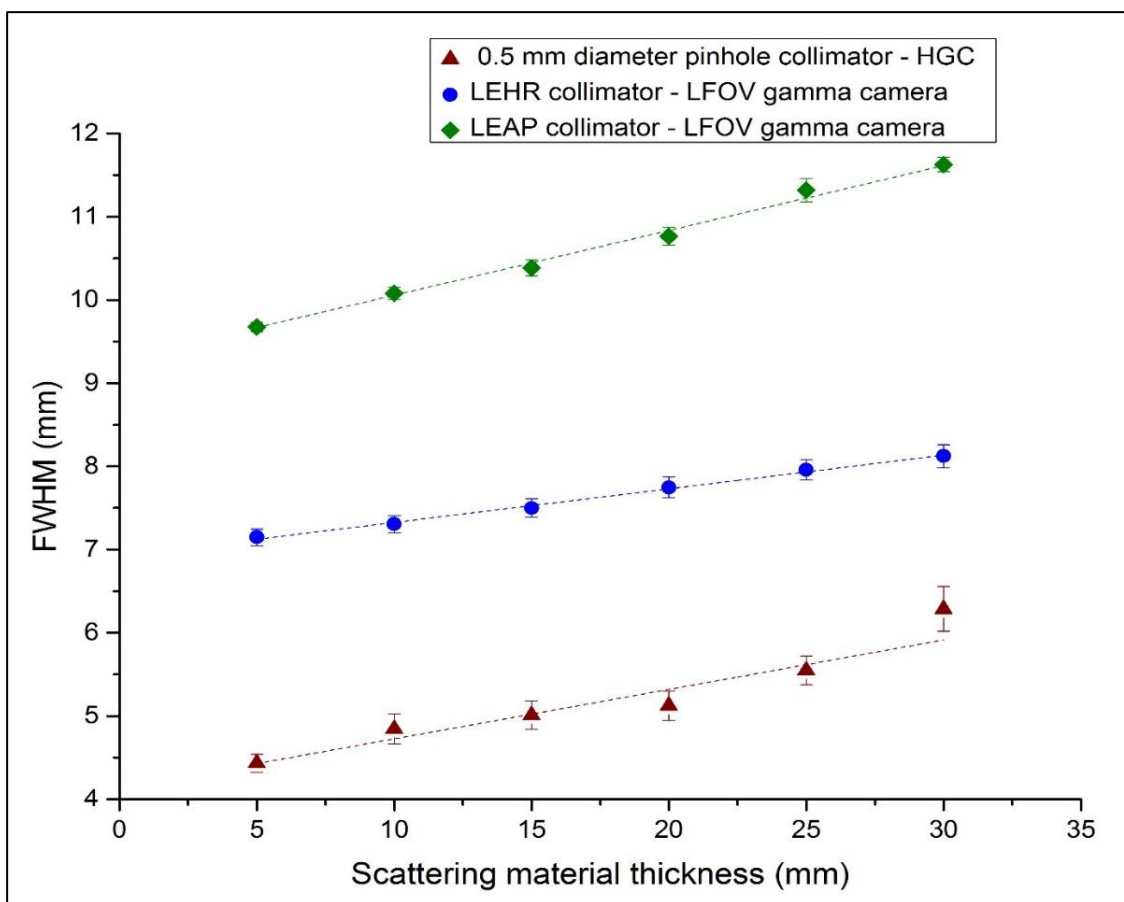
Figure 4.3. Full width at half maximum (FWHM) of the lymphatic vessel phantom as measured by a conventional LFOV gamma camera and the HGC. The simulated IS was not used during the acquisition of the gamma images analysed to produce this graph.

4.3.1.2 Gamma and hybrid imaging with a lymphatic vessel phantom

Intraoperative testing has been carried out with SFOV gamma cameras modified to allow hybrid gamma-optical imaging. Hybrid imaging is proposed as a way of improving the HGC capability for activity localisation during nuclear imaging procedures. The clinical advantage of presenting gamma and optical images simultaneously would be appreciated, mainly in the intraoperative situation, because of the valuable anatomical and functional information provided. Hybrid optical and gamma images of the simulated lymphatic vessel are produced by the HGC, as seen in Figure 4.4, which shows good co-alignment of the optical set with the gamma images. This co-aligned configuration of the HGC allows an accurate localisation of hot spots within the field of view. In clinical practice, the ability to recognise the texture and the shape of abnormal tissues (e.g. lesions) by viewing the fused image, providing functional and anatomical information simultaneously, may improve the HGC detection and localisation accuracy over non-hybrid SFOV gamma systems.

Another prototype hybrid gamma-optical imaging system employed a Sentinella SFOV portable gamma camera, obtainable commercially, with an optical module consisting of a pair of optical cameras has been investigated (209). Calibration was executed by imaging 15 point sources at 15 cm distances, and modalities' homography transformations calculated. The surface contours in the imaging were estimated using dual-optical cameras. Combining this approach with the calibrated transformation meant that the gamma image could be overlaid with an optical image, resulting in a combined image displaying both modalities. Co-registration errors, i.e., the distance between the location offered by the gamma camera and the optical cameras, was 1 cm when imaged from 15 cm. It was impossible to produce fused images for imaging distances less than 5 cm. It was revealed that combined images offered more ease of interpretation than standalone gamma images. While, as previously mentioned, co-registration errors did not allow for fused images to be employed for direct localisation of sources, they were exceptionally helpful in allowing decisions to be made as to how the gamma imaging field of view should be oriented and located. The same dual-camera principles, and combining them with a portable gamma camera, have been employed

to overlay gamma images on optical images (i.e., the opposite of the method employed by the Sentinella system), with co-registration errors being less significant in phantom testing (210).

A reduction, or even elimination, of co-registration errors caused by camera alignment and imaging distance can be affected by mechanically aligning gamma and optical modalities. With the HGC, the portable gamma camera has a mirror located in front of its pinhole collimator at an angle of 45° to the surface of the collimator, which reflects optical photons into the optical camera. Using this setup, the FOV for both gamma and optical elements match each other at any imaging distance. Various hybrid optical-gamma images produced by the HGC, in experimental and clinical settings, at different imaging distances have been provided in chapters 7 and 8.
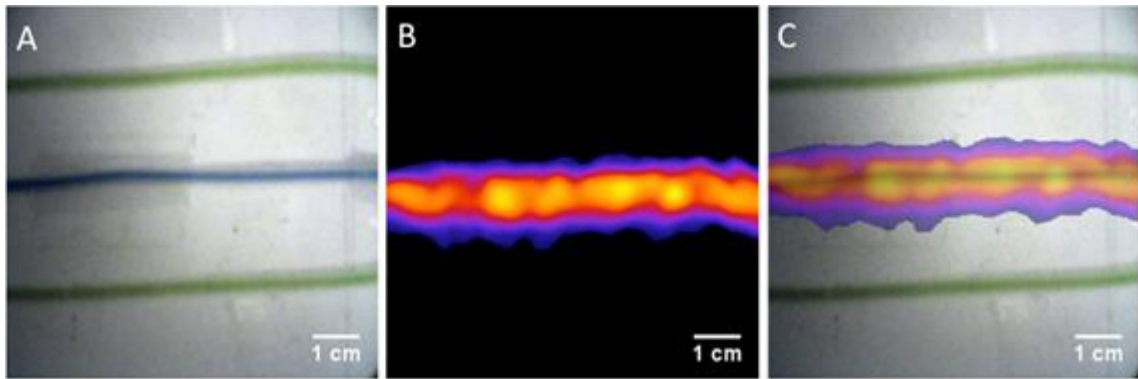
Figure 4.4. Optical (A), gamma (B) and hybrid (C) images for the simulated lymphatic vessel. The middle capillary tube was filled with ^{99m}Tc mixed with blue dye; the upper and lower tubes were filled with green dye only. The gamma image was taken over 500 s with the LVs at a 5 mm Perspex depth.

In Figure 4.5, a dual injection site has been simulated with two Eppendorf tubes. The simulated dual injection site is located within the field of view (FOV). Even in the presence of the high-activity dual injection site (80 MBq) the targeted lymphatic vessel can be imaged within an acquisition time of 100 s. Increasing the acquisition time to approximately 500 s further enhances the gamma image contrast (Figure 4.5 B).
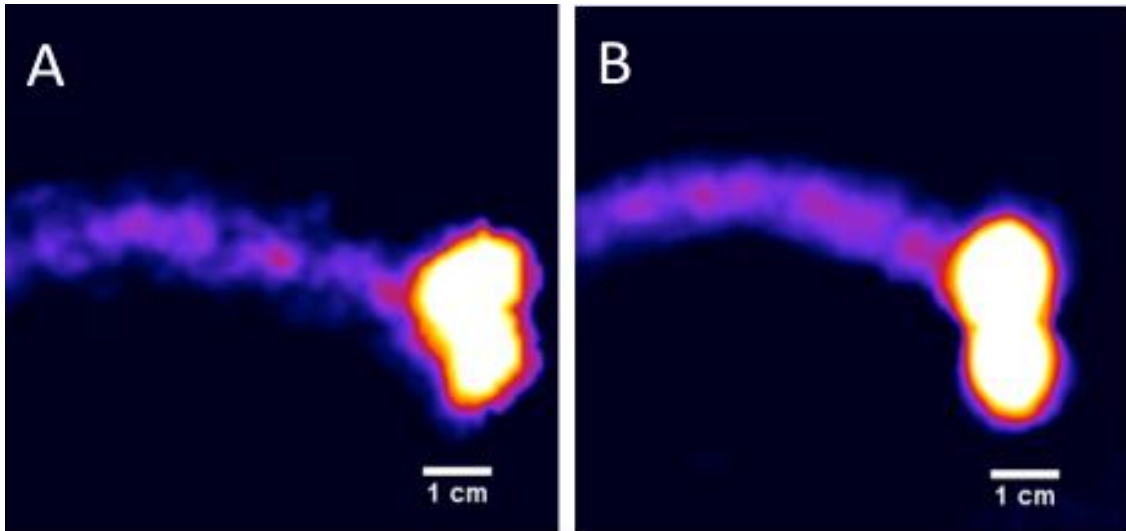
Figure 4.5. Gamma images showing the lymphatic vessel phantom, including the dual IS, for two different acquisition periods; image (A) has an acquisition time of ~ 100 s and image (B) of ~ 500 s. The LV was placed underneath 5 mm of Perspex, with the dual IS placed on the surface of the scattering material.

4.3.2 Characterisation of HGC performance with a melanoma phantom

SLN biopsy procedures use LFOV gamma cameras pre-operatively and gamma probes intraoperatively (211). This study introduces the HGC to the field of SLN detection in melanoma cases and evaluates its capability in SLN detection in different clinical scenarios. The melanoma phantom described in section 4.2.2.2, Figure 4.1 B, is used to simulate the SLN at different positions and varied concentrations of radioactivity.
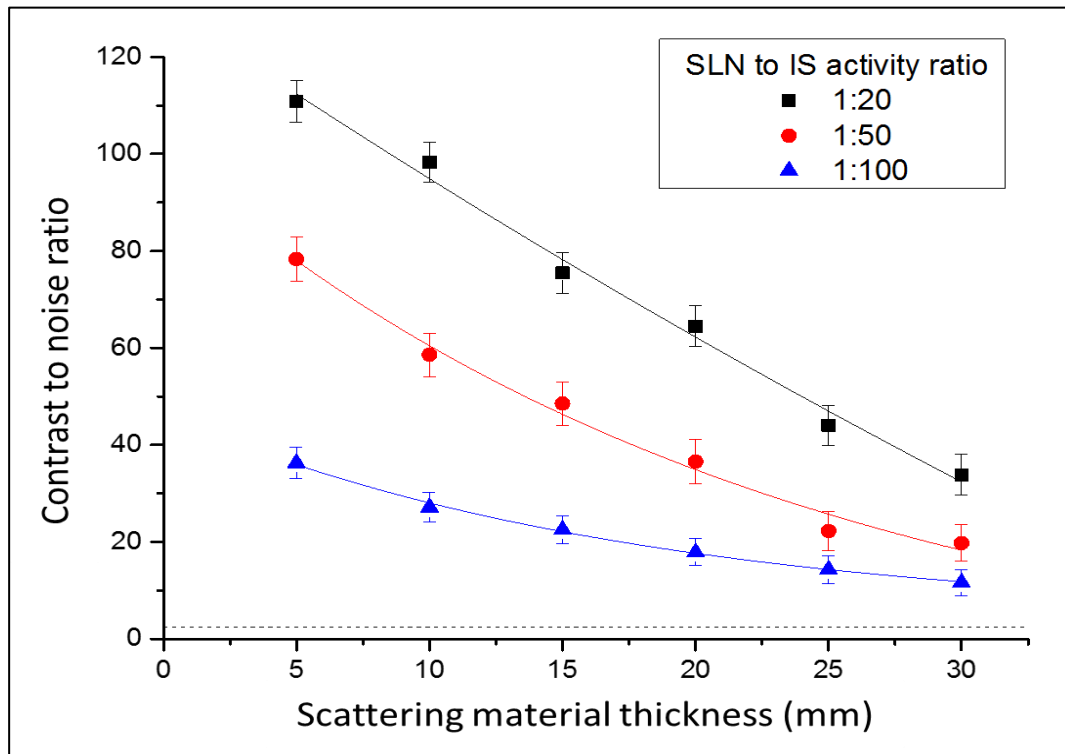
Figure 4.6. Relationship between CNR and varying thicknesses of scattering material (i.e. Perspex plates) for the SLN at 20 mm away from the IS, and 100 mm from the HGC collimator to the surface of the melanoma phantom. The IS activity was 15 MBq. The dotted line at CNR = 3 represents a threshold value of the Rose criterion of detectability (205).

4.3.2.1 Detectability of the sentinel lymph node (SLN)

The detectability of a SLN by a SFOV gamma camera is characterised by measuring the CNR. In Figure 4.6, the SLN to IS activity ratios were 1:20, 1:50 and 1:100, and analysis was performed on gamma images produced by the HGC (fitted with 0.5 mm diameter pinhole collimator) with 100 s acquisition time. Within this short acquisition time, the HGC is able to detect SLNs containing different concentrations of radioactivity with high CNR values. For instance, the worst CNR value recorded is 11.62 at 30 mm depth with 1:100 SLN to IS activity ratio; however, the SLN is clearly detected as seen in Figure 4.7. This value is higher than the threshold value (i.e. 3 - 5) that stated in the Rose criterion (205). Consequently, the HGC's capability to detect SLNs at various scattering thicknesses and with different concentrations of activity reflects the usefulness of the HGC in critical clinical situations (e.g. surgical or interventional procedures).
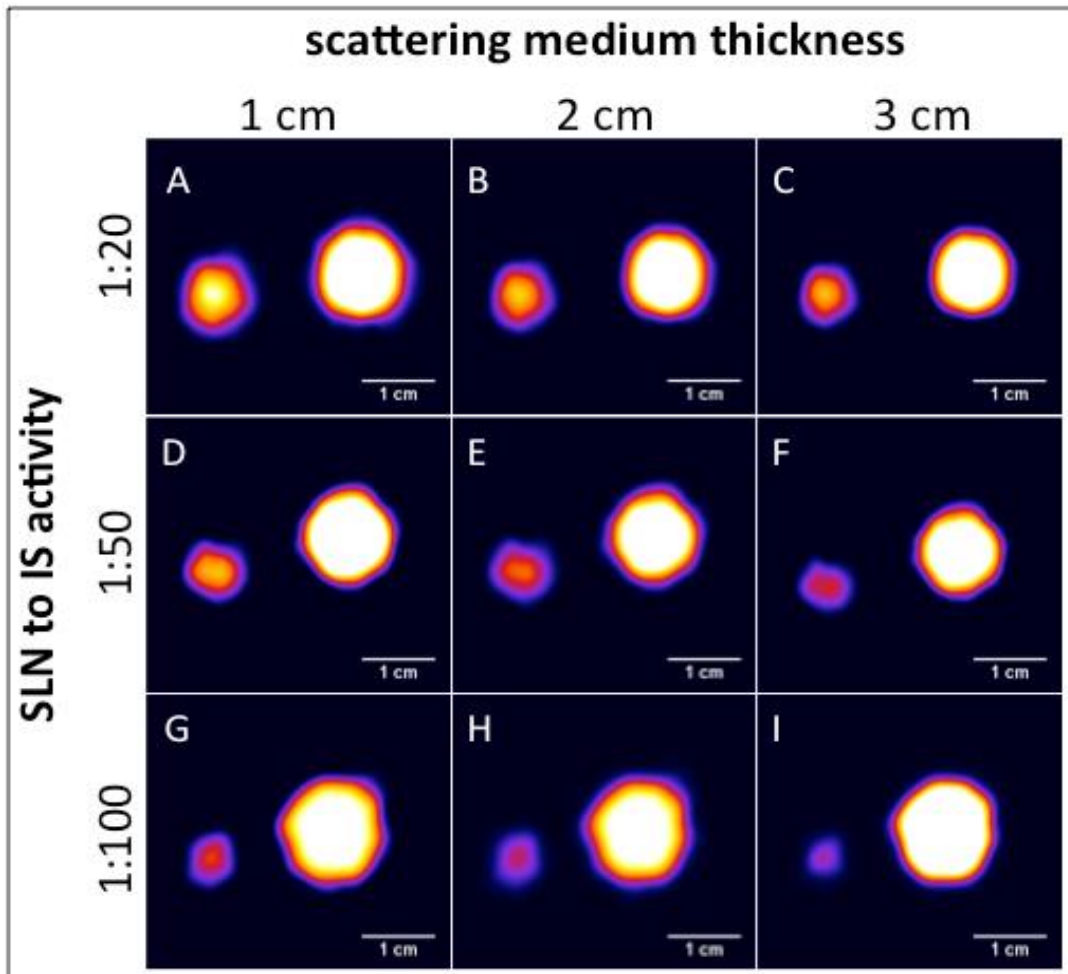
Figure 4.7. Gamma image for the SLN at 20 mm IS to SLN distance (centre to centre); the SLN were placed beneath 10 mm, 20 mm and 30 mm of scattering material thickness, and the SLN to IS activity ratio varied between 1:20 and 1:100 (100 s acquisition time).

It can be seen in Figures 4.6 and 4.7 that changes in radioactivity uptake would influence the HGC's ability to detect the SLN; this effect becomes more pronounced with increasing thicknesses of scattering material. Therefore, for deep SLNs in some clinical cases, applying compression during the functional imaging procedure (e.g. by using a compressing pad) may improve detectability while maintaining a large field of view. The effect of scattering material on HGC SLN detection can be also be minimised by shortening the collimator to surface distance, which will however reduce the field of view, but enhance the system spatial resolution, improve sensitivity, reduce scattering radiation and improve detectability.

Figure 4.7 shows different gamma images with varied simulated SLN to IS radioactivity (i.e., 1:20, 1:50 and 1:100). It also shows the simulated SLN under various scattering medium thicknesses ranging between 1 cm and 3 cm. The acquisition time for these images was 100s. In this short imaging time, the simulated SLN was detected with high CNR values. The HGC successfully detected the simulated SLN while the simulated activity in the SLN was 1:20 SLN to IS ratio and beneath 1 cm to 3 cm of scattering material. The recorded CNR values were comparatively high using the 1:20 activity ratio as they ranged between 98.28 and 33.82. The HGC was also able to detect the simulated SLN with 1:50 SLN to IS activity ratio; the CNR values varied from 19.73 for the simulated SLN beneath 3 cm of scattering medium and 78.38   under 1 cm. The most critical simulated scenario was when the SLN was placed underneath 3 cm of scattering material and the SLN to IS activity ratio was 1:100. The recorded CNR value for the simulated SLN in that situation was 11.62. The CNR values for the simulated SLN with same activity simulation under 1 cm and 2 cm of scattering thicknesses were 27.16 and 17.85, respectively. As seen in Figure 4.7, the SLN was clearly visible under all conditions within the used activity range ($\geq$ 0.15 MBq) and at similar experimental setup ($\leq$ 30 mm depth).

The choice of larger pinhole (i.e. 1.0 mm diameter) will improve the detectability when the separation between the IS and the SLN is larger compared to the change in the spatial resolution; however, the system spatial resolution of the HGC will be affected. A comparison of the detectability between 0.5 mm and 1.0 mm diameter pinhole collimators has been conducted (see Figure 4.8). The poorest CNR value recorded for the 1.0 mm diameter pinhole collimator is 42.51 at 30 mm depth with 1:100 SLN to IS radioactivity ratio. This value is significantly higher than the value recorded using a 0.5 mm diameter pinhole collimator under the same conditions (i.e. same depth and activity concentration). However, the extrinsic spatial resolution of the HGC is degraded using 1.0 mm diameter pinhole collimator.
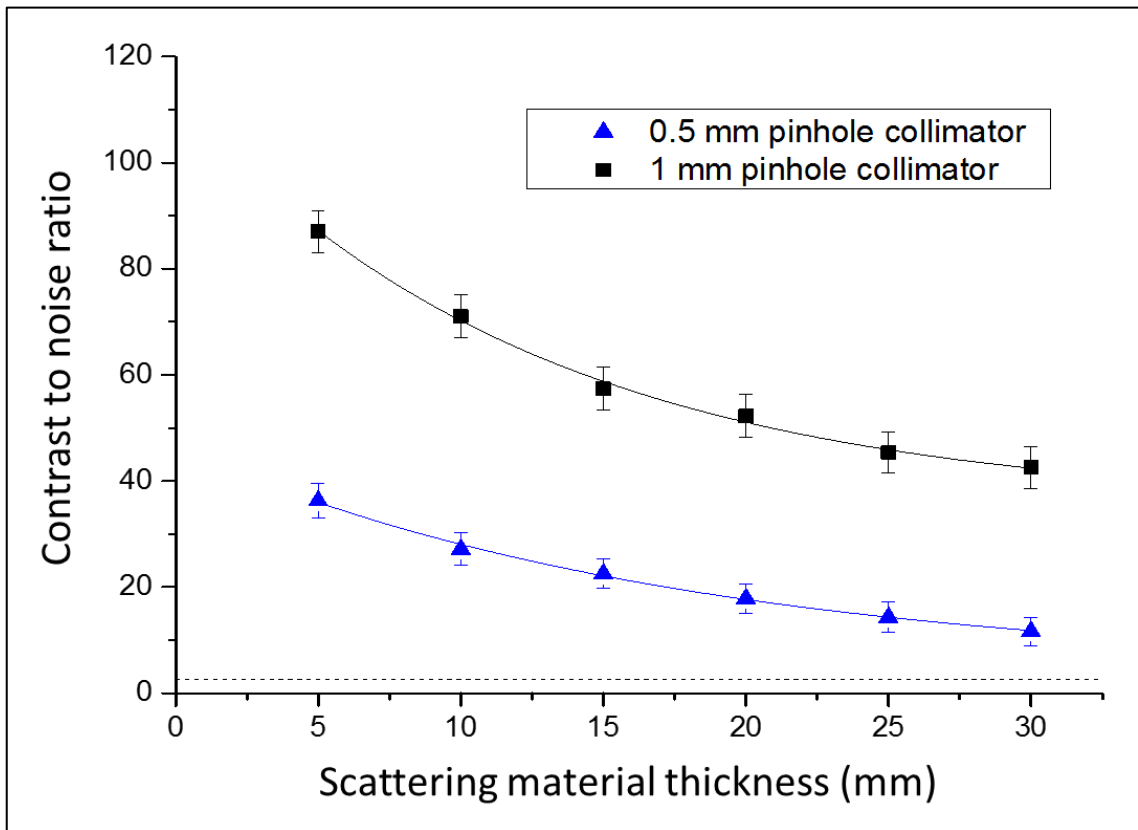
Figure 4.8. Relationship between CNR and varying thicknesses of Perspex for the SLN at 20 mm away from the IS, and 100 mm from the HGC collimator to the surface of the melanoma phantom. 0.5 mm and 1 mm pinhole collimators were used. The IS activity was 15 MBq. The dotted line at CNR = 3 represents a threshold value of the Rose criterion of detectability.

Acquisition time greatly affects detectability. To detect SLNs with small size, low activity uptake or at depth, longer acquisition times would be recommended. Additionally, fitting the HGC with thicker CsI(Tl) scintillator is proposed to improve the capability of detecting low activity accumulations in deep, small SLNs. These adaptations would make the HGC a suitable tool for functional imaging under different clinical conditions (will be discussed in-depth in chapters 5 - 7).
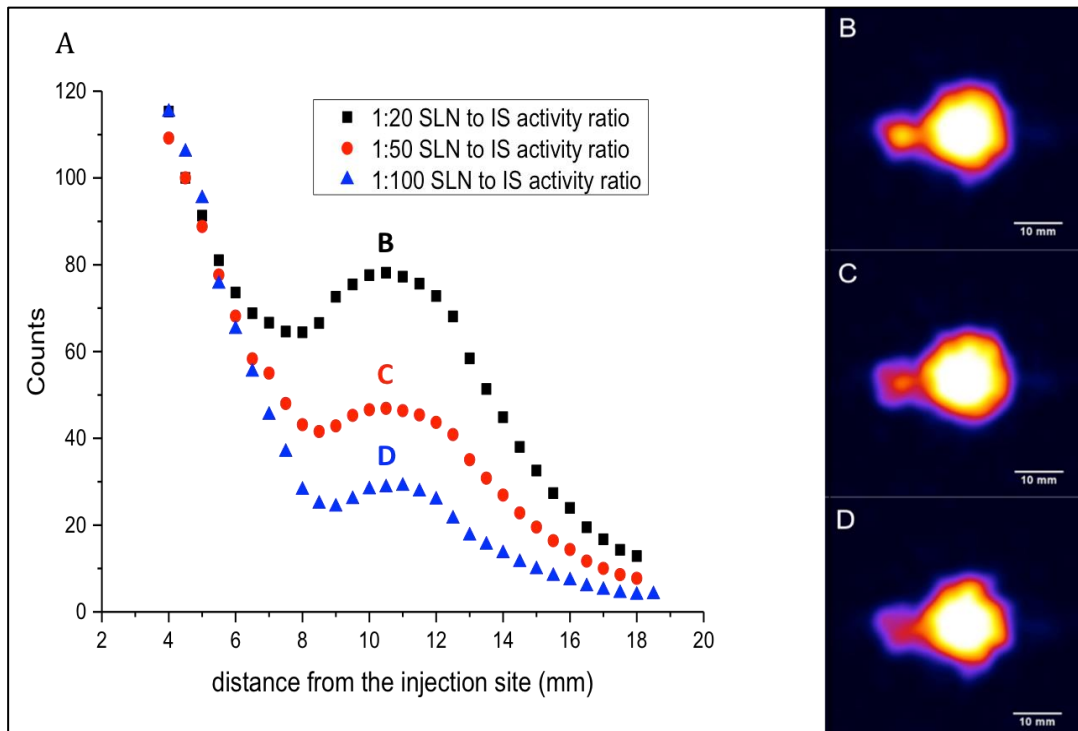
Figure 4.9. (A) Plot of count profiles for the closest simulated SLN to the IS underneath 10 mm of the scattering medium. (B, C and D) Gamma images of the SLN at 1:20, 1:50 and 1:100 SLN to IS activity ratios respectively (10 mm IS to SLN distance). The acquisition time for the images analysed in this graph was 200 s. The IS activity was 15 MBq.

4.3.2.2 Influence of injection site position on SLN detectability

In Figure 4.9, the IS and the SLN were separated by a centre-to-centre distance of 10 mm, i.e. a 1.5 mm edge-to-edge separation when the size of the IS and the SLN are taken into account. Using the 0.5 mm diameter pinhole collimator, the HGC is able to clearly resolve the SLN at the closest point to the IS. As previously discussed, the difference in the concentration of radioactivity noticeably affects the HGC ability to detect lymph nodes. Nevertheless, even with the 1:100 SLN to IS activity ratio the HGC is still capable of resolving the peak of the SLN count profile curve within a 200 s acquisition period. Based on the SLN concept discussed earlier, lymph nodes that are located close to the primary affected region are potential nodes to be metastasised; therefore, the ability of a gamma imaging system to resolve the closest SLN from the IS or the primary site of a tumour would improve the diagnostic process during SLN detection procedures.
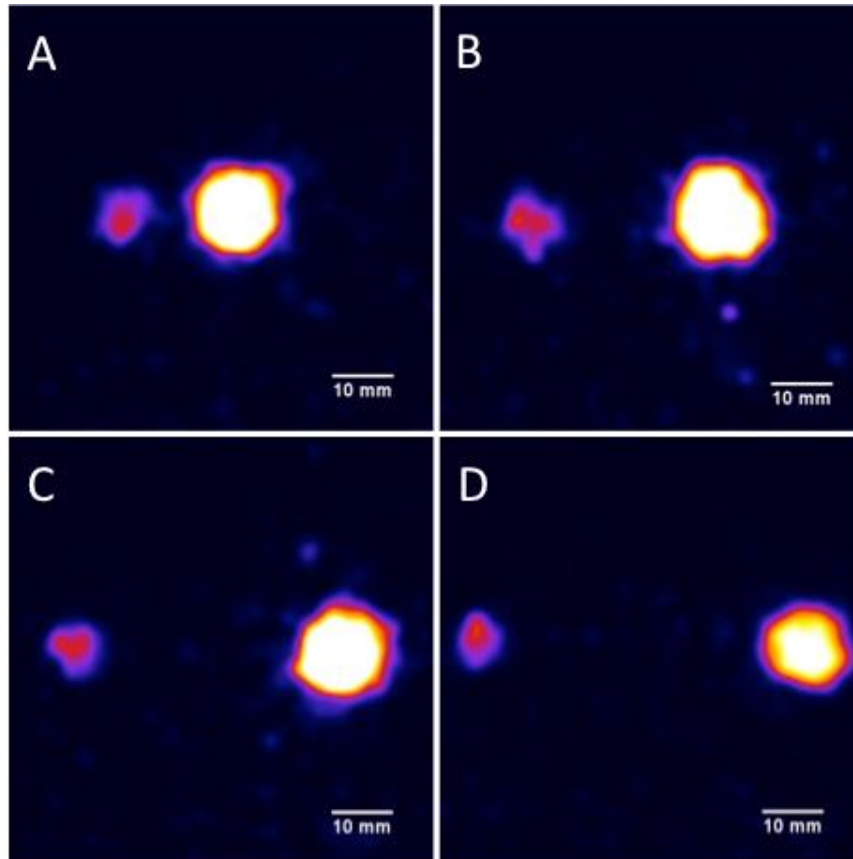
Figure 4.10. Gamma images for the SLN at different IS to SLN distance (centre to centre); (A) 20 mm away from the IS, (B) 30 mm, (C) 40 mm and (D) 50 mm. The SLN and LV were placed beneath 10 mm of Perspex, and the SLN to IS activity ratio was 1:100.

Figure 4.10 represents the gamma images obtained by the HGC equipped with 0.5 mm diameter pinhole collimator for the SLN at 10 mm Perspex depth and various IS to SLN distances ranging from 20 mm to 50 mm. These gamma images were analysed to produce the count profile curves for simulated SLN with an acquisition time of 200 s as shown in Figure 4.11. The apparent SLN count level decreases as the SLN is located stepwise further away from the IS. This behaviour reflects the effect of IS activity on neighbouring anatomical structures. As the amount of radioactivity is increased in the IS, the scattering caused by this activity is increased. However, the HGC is able to resolve counts peaks (i.e. SLNs) at different IS to SLN distances effectively.
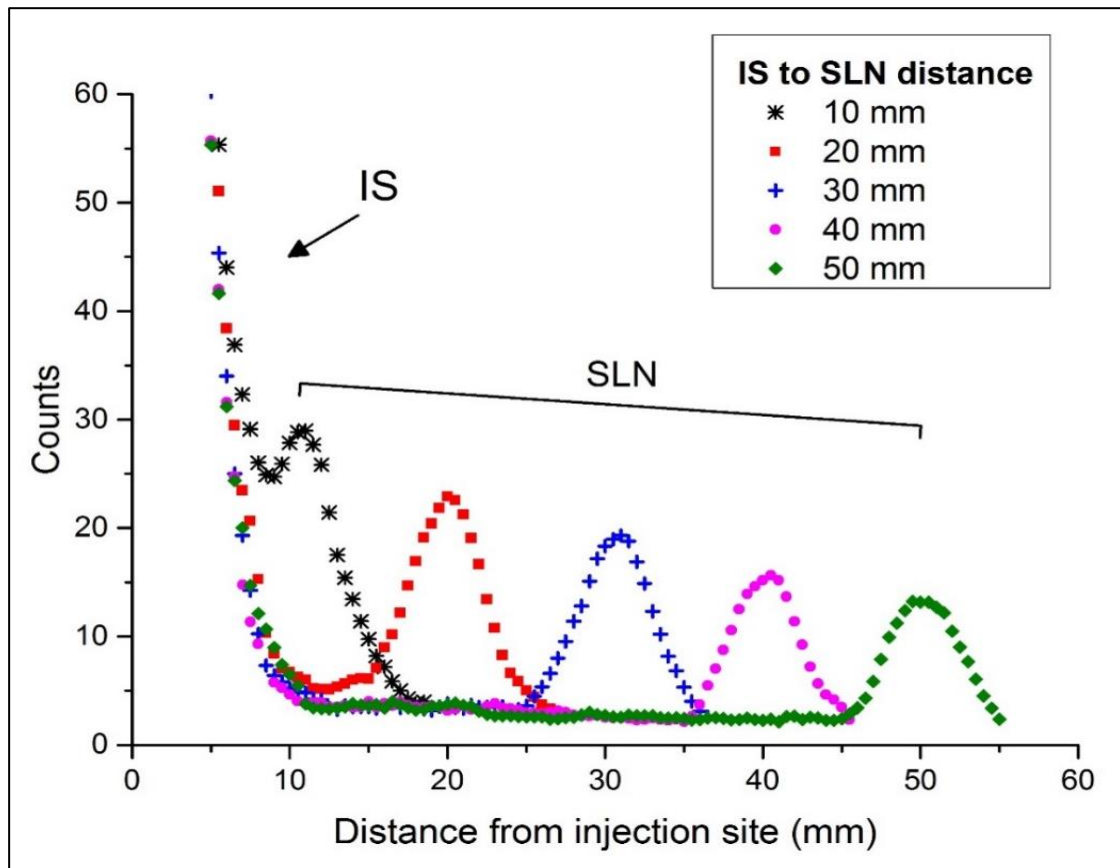
Figure 4.11. Count profile curves of the melanoma phantom obtained at different IS to SLN distances. The SLN to IS ratio was 1:100 and the SLN was located underneath 10 mm of Perspex. Peaks due to IS and SLNs are labelled. The simulated IS activity was 15 MBq.

Administration of high amounts of radioactivity in the IS would increase the uptake (i.e. the detectability) in targeted SLNs far from the IS such as inguinal SLNs, which may be useful for functional imaging during metastasis biopsy procedures. However, neighbouring SLNs (i.e. close to the IS) may be flooded by scattering of the IS radioactivity. Therefore, it has been recommended that for nuclear radioguided SLN biopsy in patients with suspected malignant cutaneous melanoma, the activity of the administered dose should range between 7 and 20 MBq in small volumes (i.e. 0.05 to 0.2 ml based on the skin thickness of the examined anatomical area). Such practice will improve gamma detecting and imaging systems' capability to detect neighbouring SLNs and avoid any chance of collapsing for thin-walled LVs (202, 212).
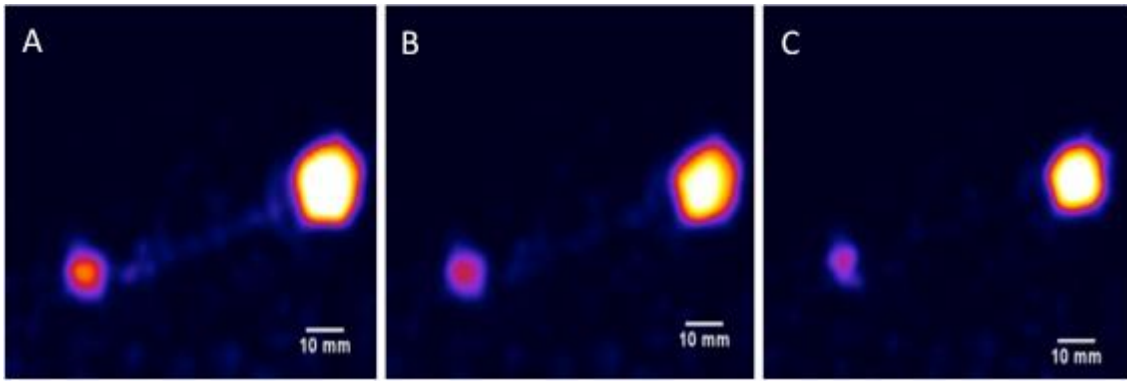
Figure 4.12. Gamma images of SLN and LV placed underneath 30 mm of Perspex and the superficial IS; the SLN to IS activity ratio is 1:20 in (A), 1:50 in (B) and 1:100 in (C). The SLN to IS distance is 50 mm. The IS activity was 15 MBq.

4.3.2.3 Influence of radioactivity concentration on LV and SLN appearance

In Figure 4.12, the same gamma imaging procedure is performed on a specific configuration of the melanoma phantom. The simulated SLN and LV were placed underneath 30 mm of scattering material, and the SLN to IS distance was set at 50 mm. The SLN and LV to IS activity ratio was varied between 1:20 and 1:100. The acquisition time during this imaging process was 200 s.

The SLN is clearly detected for all investigated phantom configurations (i.e. at IS to SLN distances ranging between 10 mm and 50 mm; and thicknesses of Perspex ranging between 5 mm and 30 mm) and for all simulated SLN to IS activity ratios for melanoma detection. The simulated LV is detectable with 1:20 LV to IS activity ratio (i.e. a 0.75 MBq dose). However, the LV was not clearly seen with activity ratios of 1:50 and 1:100 (0.3 MBq and 0.15 MBq) at large depths (Figure 4.12 B and C). It is important to clarify that the activity ratios used with the simulated LV in this study are not estimated based on clinical data, and that the selection of the simulated LV to IS activity ratios for the LV in the melanoma phantom was made to determine the limit of detection with the HGC. The observed changes in the SLN size (Figure 4.12) in the gamma images follow changes in the SLN activity concentration; i.e. the SLN appears smaller when it contains lower radioactivity concentration.

4.4   Conclusion

The lymphatic system is of interest because of its significant role in tumour metastasis. A simulation technique and two lymphoscintigraphic phantoms have been designed and utilised to validate the capability of the Hybrid Gamma Camera (HGC) in lymphatic system imaging. The implementation of this quantitative assessment enables the practical performance of the HGC to be evaluated for lymphatic vessel (LV) and sentinel lymph node (SLN) localisation.

The HGC performance as characterised by this experiment clarifies that it is appropriate for lymphatic vessel drainage imaging and SLN imaging in patients with melanoma. The anatomical view provided by the optical camera improves physical localisation for the radioactivity trapped in LVs and SLNs. Superior FWHM values and good contrast to noise ratios have been recorded in this study. The HGC detected the simulated LV with a spatial resolution ranging between 4.4 and 6.3 mm at 100 mm collimator to surface distance, and it was able to detect the simulated SLN that contained various radioactivity concentrations with good contrast-to-noise ratios (CNRs) values ranging between 11.6 and 110.8, underneath different scattering thicknesses ranging between 5 mm to 30 mm. This HGC capability to detect the simulated LV and SLN (containing ≥ 0.15 MBq of ^{99m}Tc) reflects its suitability for use in critical clinical situations such as interventional and surgical procedures.

The limitations of this experiment include using one size of the simulated SLN; using different SLN sizes will facilitate more detailed evaluation which will allow testing the HGC against a spectrum of nodes sizes at various depths and containing different radioactivity accumulations. The following chapter illustrates further assessments with various simulated setups including different SLNs sizes and a wide range of activity accumulations. These investigations involve using the HGC with different configurations (i.e. different pinhole diameters and different CsI(Tl) scintillator thicknesses) towards detecting lower activities and preserving the spatial resolution with the purpose of making the HGC suitable to more challenging medical scenarios.

Chapter 5: Quantitative investigation of the hybrid gamma camera capability for sentinel lymph node detection

5.1 Introduction

The clinical management of patients with different types of cancer has progressively become less invasive and less surgically radical. For instance, a breast-conserving lumpectomy has replaced the simple mastectomy, which replaced the radical mastectomy in the management of many patients. At present, a transition in the staging approach of this disease from axillary dissection to sentinel lymph node (SLN) biopsy is under consideration and investigation (38). The sentinel lymph node is, briefly, that the first lymph node in a lymphatic vessel route that receives drainage from a tumour; the sentinel lymph node will show metastasis if there has been lymphatic tumour spread. This concept was introduced in more detail in Chapter 2 (page no. 11-13).

Radioguided surgery for sentinel lymph node biopsy (SLNB) is now a well-established technique in the staging of various cancers, with most surgeons using non-imaging gamma probes to locate the uptake of radioactivity in nodes (55). With existing detection approaches (gamma probes, preoperative gamma imaging, and the use of 'blue dye'), a sensitivity rate of 95 % and a false-negative rate of 5 % have been reported for SLNB (213, 214). Although this gives a relative high confidence for detection, enhancements in sensitivity and decreases in false-negative rates can only be of benefit to patients.

Intraoperative imaging has been suggested as a method to aid surgical localisation of regions of radioactive uptake. The proposed demand for small field of view gamma imaging systems, which can be brought into operating theatres, has led to the current development of a number of new intraoperative gamma cameras with widely varying designs and performance capabilities (58, 89, 215, 216). These new imaging systems are challenged by the physiological and anatomical nature of the human lymphatic system, such as lymph nodes' sizes and depths, which require a well-established imaging system that can be used for the majority of the SLN detection procedures (212). A set of testing protocols has been suggested to provide a quantifiable comparison between these systems (64). However, the methods chosen for testing vary and do not always directly relate to the performance of a system in a true clinical situation. This chapter describes a new method for testing camera performance providing information that is designed to be more intuitively understood by end-users.

To quantitatively evaluate the usefulness of using the HGC for scintigraphic imaging of patients with cancer during the SLN biopsy procedure, a lymph-node contrast (LNC) phantom has been designed and fabricated. This phantom is made of Perspex plates (i.e. Poly-methyl methacrylate PMMA), and it is used to study the effect of radioactivity concentration and sentinel lymph node size on the produced gamma image quality and to evaluate HGC resolution and CNR for detection in simulated clinical scenarios. The LNC phantom construction, acquisition procedure and activity simulation are suited to the majority of available intraoperative gamma imaging systems or, with some adjustment, to non-imaging gamma probes, and this test may be utilised to compare different systems' performances.

5.2   Materials and methods

5.2.1 Changes in the configuration of the hybrid gamma camera (HGC)

The handheld small field of view HGC uses a scintillator-based detector. The detector consists of an e2v CCD97 back-illuminated electron multiplying charge-coupled device (EMCCD) coupled to a columnar CsI(Tl) scintillator. The performance of the HGC was investigated with 600 μm and 1500 μm thick scintillators installed, and both 0.5 mm and 1.0 mm diameter pinhole collimators. More details about the HGC design and structure have been provided in Chapter 3.

5.2.2 Lymph-node contrast (LNC) phantom construction

The lymph-node contrast (LNC) phantom consists of two Perspex plates (80 mm × 80 mm per plate); the first plate contains four rectangular wells with the same depth (6 mm), but they could be filled with different radioactive concentrations. This Perspex plate, the "well plate" is used to mimic a warm background (i.e. simulating the uptake of radiopharmaceutical in the surrounding tissues). The second plate has four groups of cylindrical wells with 2.5, 5, 7.5 and 10 mm diameters (6 mm depth); each group contains 4 wells (16 holes in total), see Figure 5.1 A and B. The simulated SLNs sizes are comparable to the majority of the SLNs inside the human body (202).

The LNC phantom covers a range of SLN sizes and contrasts, but the phantom is made more sophisticated by the fact that for a fixed acquisition time, hotspots of the same size in different groups can not only have different activities, but also have a different active background per group (Figure 5.1 C). It can also provide one active background for simulated SLNs of the same size with different contrasts by rotating the background plate by 90 degrees (Figure 5.1 D). This phantom may be used to evaluate the ability of the HGC to detect various sizes of the simulated SLNs containing different activities and having various backgrounds under different scattering material thicknesses. Scattering media could be added to the phantom to simulate deep-seated nodes. The low cost and the simplicity of constructing this phantom compared to the various medical scenarios that can be simulated make it a useful tool for testing and comparing the performance of various medical devices for SLN detection.
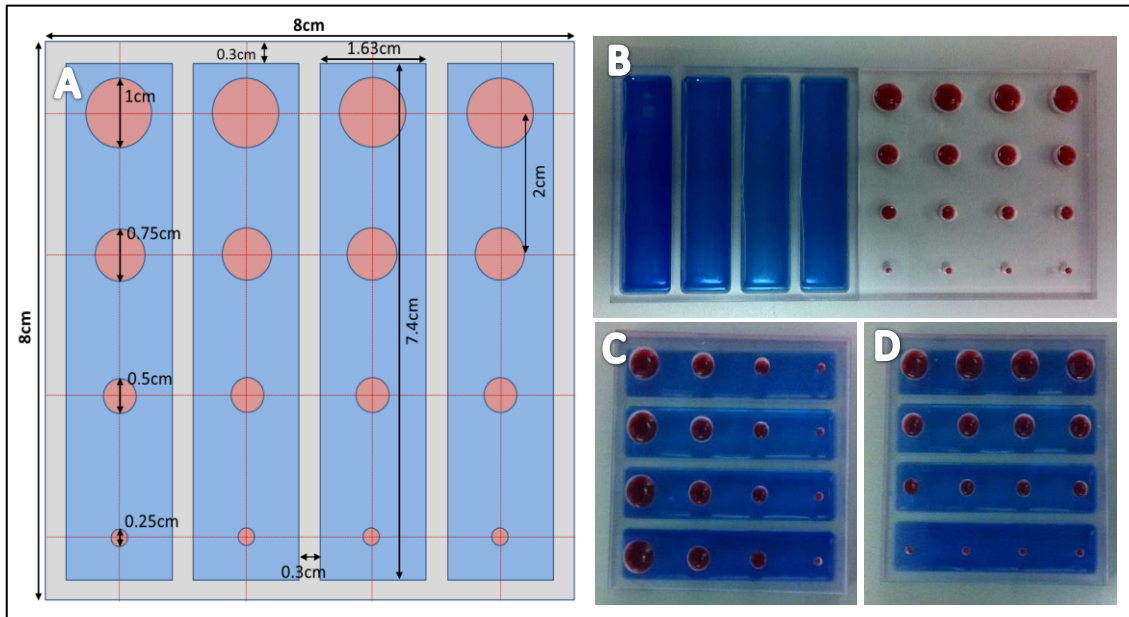
Figure 5.1. Schematic and photographs of the LNC phantom: (A) a diagram of the LNC phantom's dimensions, (B) a representation of the two Perspex plates used to construct the phantom showing the drilled simulated nodes and background square wells, (C) a simulation of different nodes' sizes and activity concentrations with the same level of the activity in the background and (D) a simulation of the same nodes' sizes and different activity concentrations with the same level of the activity in the background.

5.2.3 Radioactivity simulation

From a review of the literature the largest reported ratio of SLN to background activity (NBR) when using ^{99m}Tc was 1:10 (38, 202, 212). This ratio was selected, as a maximum value, to investigate the capability of the HGC in a range of critical medical scenarios, and different activity concentrations were chosen to match this value. The radioactivity concentrations in the simulated SLNs were taken from the available medical data and are presented in Table 5.1. Further details about the activity simulation assumptions and data used for the scientific justification in this experiment have been explained in Chapter 3.

Table 5.1. Summary of ^{99m}Tc activities used in the LNC phantom

Node diameter	Node volume	First row activity (MBq)		Second row activity (MBq)		Third row activity (MBq)		Fourth row activity (MBq)	
		Node	Background	Node	Background	Node	Background	Node	Background
10mm	0.4 ml	4.0		2.0		1.0		0.5	
7.5mm	0.2 ml	2.0		1.0		0.5		0.25	0.375 in 3ml
5mm	0.1 ml	1.0	3 in 3ml	0.5	1.5 in 3ml	0.25	0.75 in 3ml	0.125	
2.5mm	0.02 ml	0.2		0.1		0.05		0.025	

5.2.4 Imaging procedure

The simulated SLNs in the LNC phantom were placed beneath different thicknesses of a scattering medium (i.e. Poly-methyl methacrylate PMMA), ranging between 5 mm and 40 mm [i.e. soft tissues and PMMA densities are 1.04 g/cm^3 and 1.18 g/cm^3; the mass attenuation coefficient values for soft tissues and PMMA are 0.153 cm^2/g and 0.149 cm^2/g, respectively]. A metallic frame with a clamp held the HGC perpendicular to the phantom's surface. Two different pinhole collimators were used during this study (0.5 mm and 1.0 mm diameter pinhole collimators). The distance between the HGC collimator and the simulated SLNs was 100 mm, chosen to provide a clinically useful field of view of 90 mm x 90 mm. Acquisition time for each image varied between 60 s and 240 s, with 240 s taken as an upper limit on the length of time which would be appropriate to use intraoperatively.

In this study, all the gamma images produced by the HGC are taken from Centre-Point mode images with different acquisition periods. These images were also processed using the Image-J software Gaussian Blur filter (Gaussian sigma = 2 pixels). Imaging sets were produced using 0.5 mm and 1.0 mm diameter pinhole collimators and 600 μm and 1500 μm thick scintillators.

5.2.5 Data analysis

The main imaging parameters used to compare the two imaging sets produced using 0.5 and 1.0 mm diameter pinhole collimators were the size and the contrast-to-noise ratio (CNR) of each node. To calculate the imaged size of each node, 1 pixel wide profiles were taken through the centre of the node in the vertical and horizontal directions (see Figure 5.2). A Gaussian curve was fitted to each profile and the reported node sizes defined as the mean of the full-width-at-half-maximum (FWHMs). The measured node spatial FWHM is of interest because it reveals how much the spatial resolution of the gamma camera spreads out the node dimensions in the planar image. The same analysis procedure was used to compare the results produced by utilising two different scintillator thicknesses (i.e. 600 μm and 1500 μm).

CNR is a parameter used to quantify the quality of images and so the ability of a specific medical imaging modality to distinguish between features and background (217). The detectability of high activity features, such as a node, in the presence of an active background depends not only on the contrast of the node but also on its size and the level of background noise. CNR analysis allows all these factors to be considered in a single measurement.

All region-of-interest (ROI) analyses were performed using Image-J and Origin 9.1 programmes. Two ROIs were required to calculate the CNR of each node. The node ROI was defined as a circular ROI centred on the node by eye, with the diameter set to the measured FWHM for that node for consistency (218). When nodes were not easily visible, sizes and positions were used from nodes of the same size with identical setups but higher node activities. The circular background ROI was positioned on a background region of the image (away from all nodes), with a diameter double that of the node ROI. For larger nodes, this required an extra background well to be filled and imaged simultaneously to ensure that there was a large enough background region for measurement. The contrast is calculated as the difference between node and background ROI mean counts values, and the noise is defined as the standard deviation of the background ROI mean counts as explained in chapter 4 (Equation 4.1).

To simplify and summarise the key results of the CNR analysis, two threshold CNR values have been set (3 and 5) based on Albert Rose's (1973) approximation for detectability (205). In order to present the large amount of data collected, data sets were defined by the percentage of visible nodes (i.e. the percentage of nodes with CNR greater than the threshold).
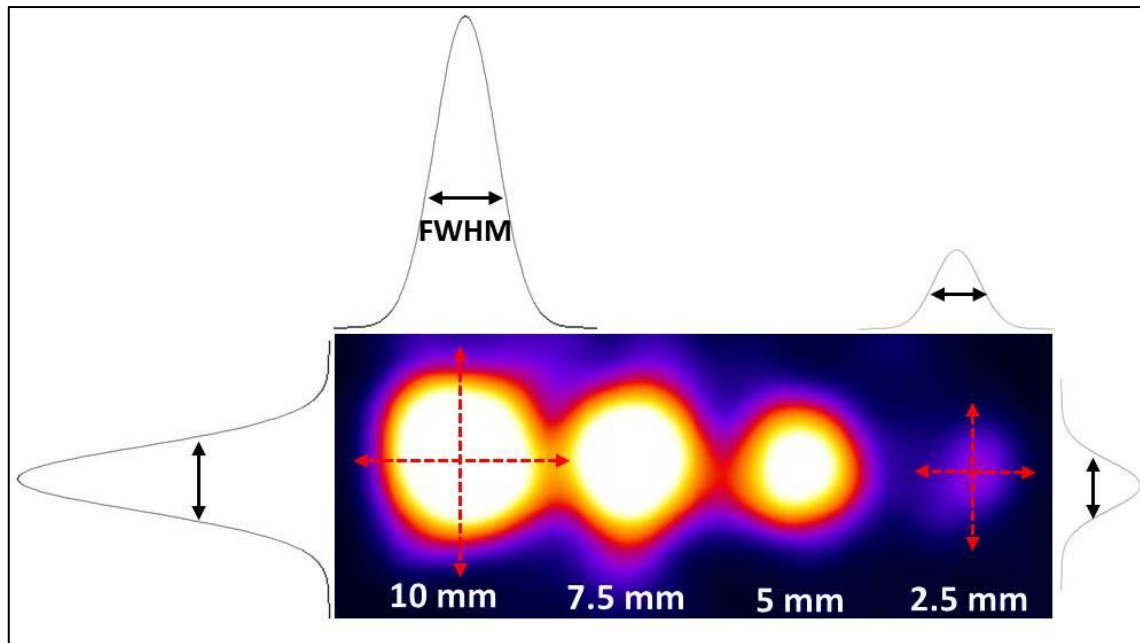
Figure 5.2. Illustration of node image size analysis

5.3 Results

5.3.1 Full width at half maximum (FWHM) measurements for simulated SLNs

Throughout this study, spatial resolution measurements (i.e. FWHM) were recorded to show the effect of using different thicknesses of CsI(Tl) scintillator and different pinhole collimators. These measurements have been utilised to precisely evaluate the ability of the HGC to distinguish the margins of each simulated SLN, as the SLN spatial FWHM reveals the amount of spread in each detected SLN dimension in the gamma images.

The size of the imaged nodes was investigated with different thicknesses of scattering material (i.e. 5 mm to 40 mm), using different scintillator thicknesses (i.e. 600 μm and 1500 μm) and two pinhole sizes (0.5 mm and 1.0 mm in diameter). The acquisition time was selected to be 240 s. In all cases, a steady increase in the FWHM value was recorded when the scattering media thickness was increased. This reflects the expected degradation of spatial resolution due to scattered photons. In all cases, the detected size of the nodes was significantly smaller when imaged with the 0.5 mm pinhole rather than the 1.0 mm pinhole. This is an expected result due to the poorer spatial resolution of larger pinhole collimators.

While using the 600 μm thick CsI(Tl) scintillator and the 0.5 mm diameter pinhole collimator, the HGC had superior spatial resolution for all detected simulated SLNs at different depths of scattering material. For instance, at a fixed acquisition time (i.e. 240s) and 100 mm away from the collimator, the smallest simulated SLN (i.e. 2.5 mm diameter SLN) has been detected with recorded spatial resolution ranging between 6.65 mm and 8.27 mm for 5 mm to 40 mm node depths, respectively. The spatial resolution measurements for the same SLN under the same imaging conditions using the 1.0 mm diameter pinhole collimator and at different depths between 5 mm and 40 mm varied between 12.64 mm and 14.20 mm, respectively (Figure 5.3).
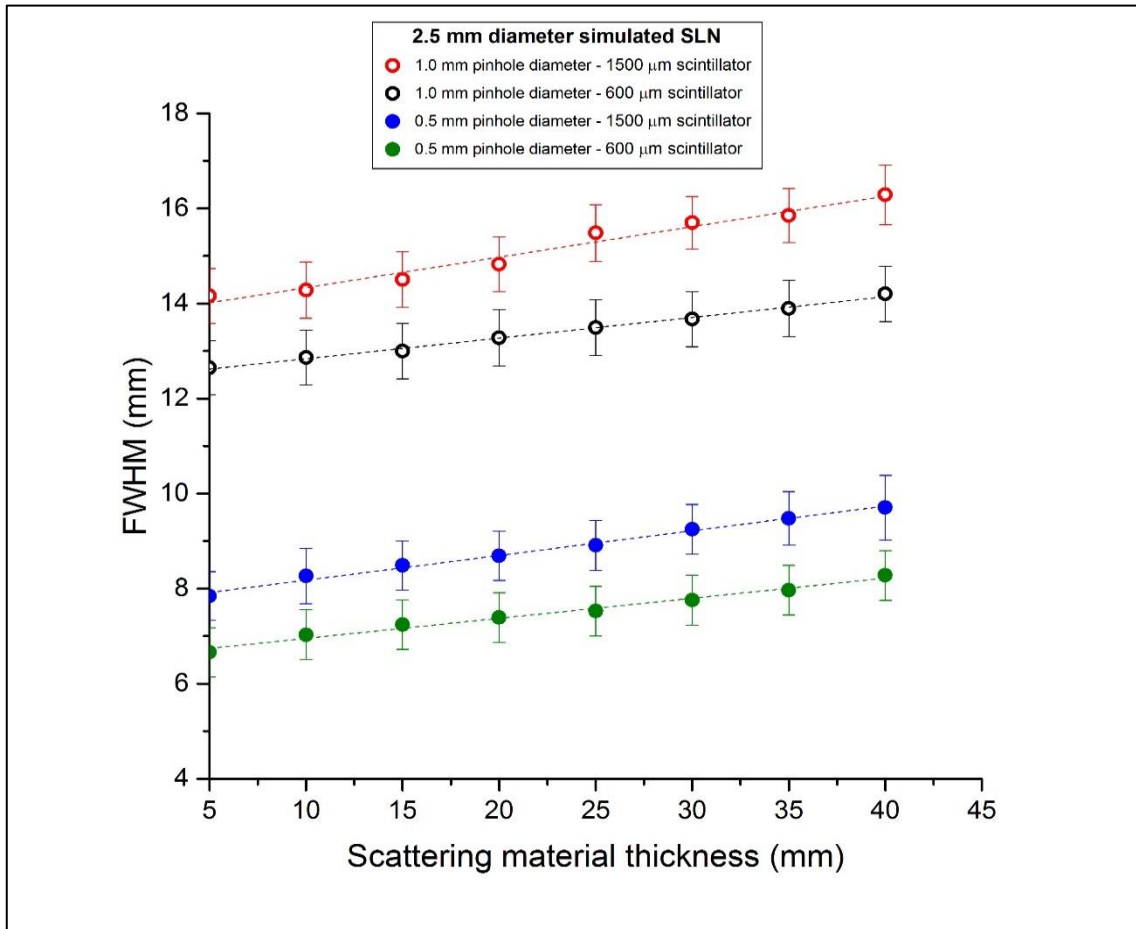
Figure 5.3. Full-width-at-half-maximum (FWHM) recorded values for the smallest simulated SLNs (2.5 mm in diameter). The nodes were imaged using the HGC fitted with two thicknesses of CsI(Tl) scintillator (i.e. 600 μm and 1500 μm) and two pinholes (0.5 mm and 1.0 mm in diameter). The total imaging distance was 100 mm and the acquisition time was 240 s.

The increase in measured node size, averaged over all 4 node sizes, from 5 mm to 40 mm depth was 23.88 % and 17.23 % using the 0.5 mm and 1.0 mm diameter pinhole collimator, respectively, while the HGC was fitted with 600 μm thick CsI(Tl) crystal. In addition, the average variation in size measurements recorded for the full range of depths was 21.96 % for the 0.5 mm diameter pinhole and 16.39 % for the 1.0 mm pinhole, while the HGC was fitted with the 1500 μm thick CsI(Tl) scintillator.

When the HGC was fitted with the thicker CsI(Tl) scintillator (1500 μm thick), the degradation of the overall recorded spatial resolution compared to the results recorded by the HGC while fitted with the 600 μm thick scintillator is relatively small. For instance,

for the same acquisition time (240 s) and at the same simulated depth (ranging from 5 mm to 40 mm), the smallest simulated SLN had spatial resolution values ranging from 7.84 mm to 9.70 mm, and from 14.16 mm to 16.29 mm while using the 0.5 mm and 1.0 mm diameter pinhole collimators respectively (Figure 5.3).

Therefore, the use of the thicker scintillator resulted in some resolution degradation; however, this was small (~10 %) compared to the measured node sizes. This was a minimal change in resolution considering the increase in CNR expected when more than doubling the thickness of the scintillator, as illustrated in following subsections. This preservation of spatial resolution was due to the light-guiding that is provided by the needle structure of the scintillation layer.

5.3.2 Contrast to noise ratio (CNR) analysis for lymph-node contrast (LNC) phantom

CNR analysis is one approach that is used to express the quality of images and the ability of a specific medical imaging modality to distinguish between different targeted tissues. The detectability of radioactivity accumulation in the presence of an active background depends not only on the contrast of the targeted hotspot but also on the size of the observed hotspot and on the accumulated activity surrounding the hotspot. Therefore, performing CNR analysis is an appropriate choice to show the ability of the HGC to detect a specific hotspot.

To aid in analysis of large numbers of results, each data set in this section will be defined as the percentage of imaged nodes which were detectable in the final image, based on a threshold CNR value defined by Rose's approximation. Figure 5.4 gives two examples of detected nodes at two different thresholds (i.e. 3 and 5). In this gamma image, 100 % of the simulated SLN nodes are detectable at a threshold value of 3, and 93.75 % of them are detectable at a threshold value of 5. For instance, nodes marked (A) and (B) are detectable with 6.02 and 3.13 CNR values, respectively (Figure 5.4). Both of these nodes could be visually recognised, suggesting that Rose's thresholds are a reasonable proxy for detectability in this case.
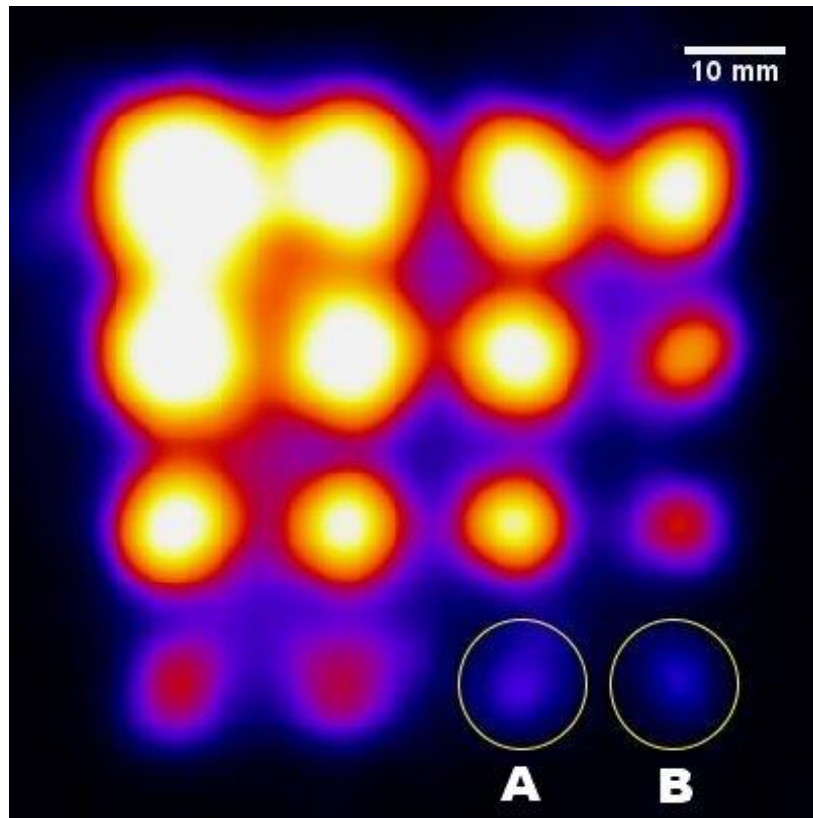
Figure 5.4. Gamma image for the LNC phantom while the simulated SLNs were located beneath 25 mm of scattering material; the HGC, while acquiring this image, was fitted with the 1500 μm thick CsI(Tl) scintillator and the 1.0 mm pinhole collimator, and the acquisition time was 240 s. Circle (A): a node containing 0.05 MBq; circle (B): a node containing 0.025 MBq. The CNR values for node (A) and node (B) are 6.02 and 3.13, respectively.

5.3.2.1 CNR analysis for LNC phantom using the HGC fitted with the 600 μm thick CsI(Tl) scintillator

Using the HGC while it is fitted with the 600 μm thick CsI(Tl) scintillator provides a superior spatial resolution; however, the recorded CNR values were low, mainly for the simulated SLNs with smaller diameters and lower activity accumulation. To clarify this fact, according to the recorded CNR values, the HGC fitted with the 600 μm thick scintillator and both pinhole collimators (i.e. 0.5 mm and 1.0 mm diameters) was unable to detect the smallest simulated SLN (with a 2.5 mm diameter filled with 25 kBq of ^{99m}Tc solution) even under the most favourable conditions. At a 5 mm depth, the simulated SLN detection rate was 93.75 % (i.e. 15 out 16 simulated SLNs) when the HGC was fitted

with the 1.0 mm diameter pinhole collimator, a threshold CNR value of 3, and at an acquisition time ranging from 120 s to 240 s. However, the HGC, fitted with the 600 µm thick CsI(Tl) scintillator, was able to detect all simulated SLNs that were filled with different radioactivity concentrations varying between 4 MBq and 0.05 MBq in the same experimental setup and with the same acquisition time (Figure 5.5 D).

A very low detection rate was recorded while the HGC was fitted with the 0.5 mm diameter pinhole collimator at a 60 s acquisition time applying both threshold values (i.e. 3 and 5). For example, the detection rate ranged from 50 % to 20 % while applying the threshold value of 5 for the simulated SLNs placed underneath 5 mm to 40 mm scattering thicknesses (Figure 5.5 A). The detection value was slightly improved when the threshold value 3 was applied; the recorded detection rate for the simulated SLNs gradually decreased from 68.75 % at 5 mm depth down to 31.25 % at a 40 mm depth (Figure 5.5 B). Using the 1.0 mm diameter pinhole collimator improved the HGC's sensitivity; therefore, during the same acquisition time (i.e. 60 s) and while the simulated SLNs were positioned beneath 5 mm to 40 mm thick scattering material, the recorded detection value varied between 68.75 % and 31.25 % and between 87.5 % and 43.75 % at the threshold values of 5 and 3, respectively (Figure 5.5 C,D).

The HGC has recorded good detection rates for the simulated SLNs, varying between 87.5 % and 75 % while the camera was fitted with the 0.5 mm diameter pinhole collimator at a 5 mm depth and using a threshold value of 5 during an acquisition time ranging between 120 s and 240 s (the detection rate was between 87.5 % and 81.25 % in the same experimental setup and the same acquisition time while the threshold value was 3). With the same imaging conditions, utilising the 1.0 mm diameter pinhole collimator, the HGC was able to detect 87.5 % of the simulated SLNs at the threshold value of 5. Furthermore, when the threshold value of 3 was applied, the recorded detection rate is 93.75 % with the same imaging conditions.

At a 20 mm depth, a low detection rate was recorded while the HGC was fitted with the 0.5 mm diameter pinhole collimator; it varied between 62.5 % and 50 % for a scanning time extended from 120 s to 240 s at a threshold value of 5 (Figure 5.5 A). This rate improved at a threshold value of 3, as the detection rate was between 75 % and 68.75 % (Figure 5.5 B). The HGC, at the same depth and same imaging conditions, was able to detect more simulated SLNs while it was fitted with the 1.0 mm diameter pinhole collimator; the detection rate varied between 81.25 % and 68.75 % at a threshold value of 5 and between 87.50 % and 81.25 % at a threshold value of 3 (Figure 5.5 C,D).

In the most challenging simulated scenario in this experiment, when the simulated SLNs were located at a 40 mm depth, while the HGC was fitted with the 0.5 mm diameter pinhole collimator, the detection rate ranged between 50 % and 31.25 % and between 62.50 % and 50 % at the threshold values of 5 and 3, respectively (Figure 5.5 A,B). Using the 1.0 mm diameter pinhole collimator for this scenario is preferable, as the recorded detection rate indicates a good visibility at the 40 mm depth. The HGC fitted with the 1.0 mm diameter pinhole collimator recorded a detection rate ranging from 68.75 % to 50 % at a threshold value of 5 and from 75 % to 56.25 % at a threshold value of 3 (Figure 5.5 C,D). It is worth mentioning that the noticeable change in the detection rate after applying the two stated threshold values (i.e. 3 and 5) indicates that the HGC fitted with the 600 μm thick CsI(Tl) scintillator records relatively low CNR values for the simulated SLNs, particularly for small simulated SLNs filled with a low radioactivity solutions.
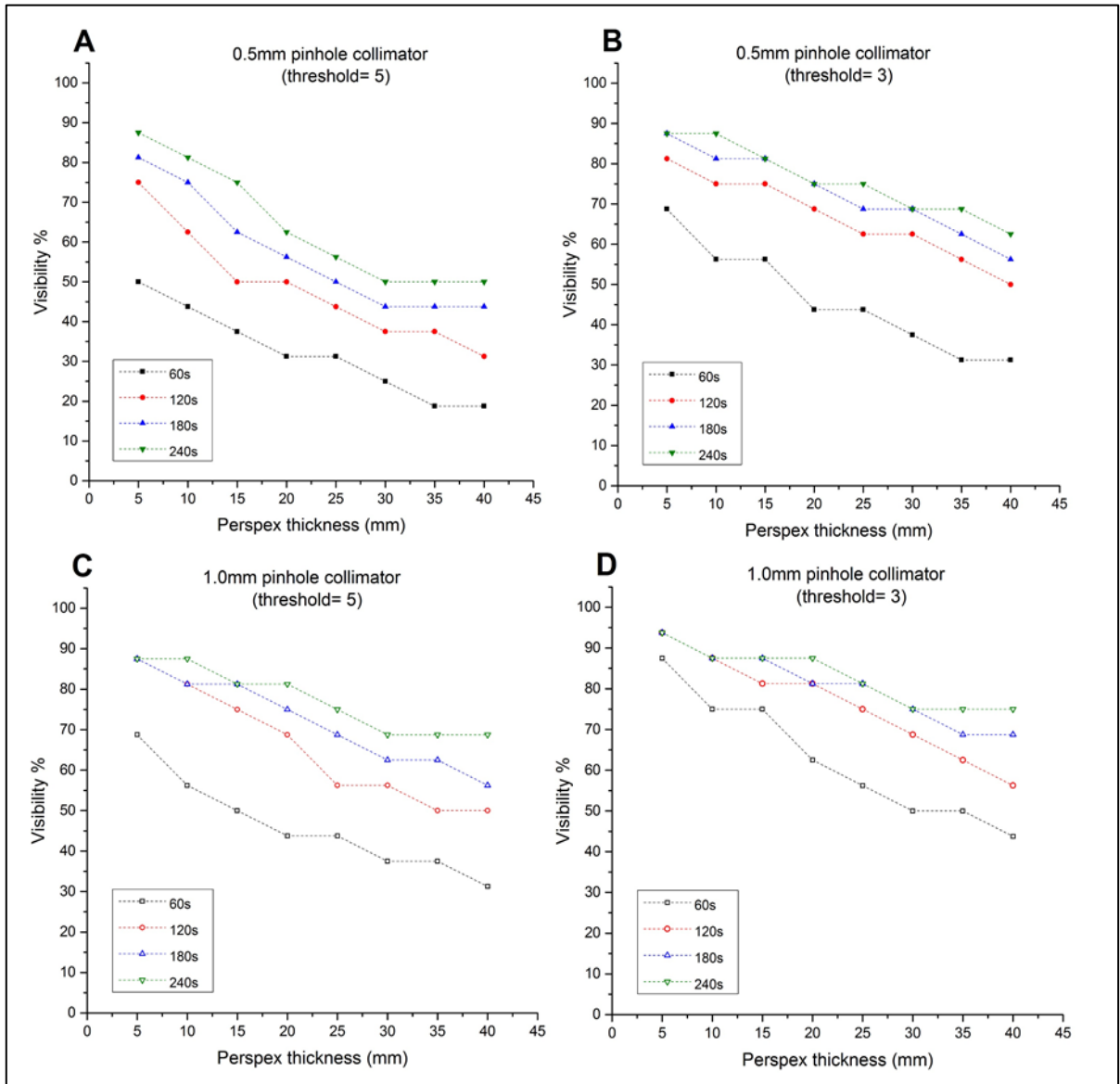
Figure 5.5. Graphs show the relationship between the simulated SLNs depths and the visibility (i.e. detection rate); these graphs represent the ability of the HGC fitted with the 600 µm thick CsI(Tl) scintillator and two different pinhole collimators (i.e. 0.5 mm and 1.0 mm in diameter) to detect the simulated SLNs at different threshold values.

5.3.2.2 CNR analysis for LNC phantom using the HGC fitted with the 1500 µm thick CsI(Tl) scintillator

The HGC, when fitted with the 1500 µm thick CsI(Tl) scintillator, is able to provide a comparably good spatial resolution compared to the camera fitted with the 600 µm thick CsI(Tl) scintillator due to the light-guiding characteristic that is provided by the needle structure of the scintillator's internal layer. Moreover, the system sensitivity is increased compared to the HGC fitted with the 600 µm thick CsI(Tl) scintillator. The recorded CNR values for the simulated SLNs were noticeably improved, and the HGC could detect simulated SLNs with small diameters and low activity accumulation.

Based on the recorded CNR values, the HGC fitted with the 1500 µm thick scintillator and using the 1.0 mm diameter pinhole collimator is able to detect the smallest simulated SLN with a 2.5 mm diameter filled with 25 kBq of ^{99m}Tc solution. For instance, the HGC recorded superior CNR values at an acquisition time of 240 s, as the recorded detection rate for the simulated SLNs was 100 % at a 25 mm depth and 93.75 % (i.e. 15 out of 16) at a 40 mm depth applying the threshold value of 3 (Figure 5.6 D). Furthermore, at the same threshold value, the HGC can detect 100 % of the simulated SLNs at a 10 mm depth and an acquisition time of 120 s; the same detection value can be recorded in the same experimental setup, while the simulated SLNs are positioned underneath 20 mm of scattering material and with an acquisition time of 180 s (Figure 5.6 D).

While the HGC was fitted with the 1.0 mm diameter pinhole collimator, the recorded detection rate ranged from 100 % to 87.5 % for the simulated SLNs located at 5 mm depth and for an acquisition time ranging between 60 s and 240 s at the threshold value of 5 (Figure 5.6 C). With the same experimental setup and the same acquisition time, the detection rate varied between 100 % and 93.75 % at the threshold value of 3 (Figure 5.6 D). Additionally, at the same acquisition time and under a 20 mm depth, the detection rate ranged from 93.75 % to 75 % at the threshold value of 5, and from 100 % to 87.5 % at the threshold value of 3 (Figure 5.6 C,D).

At the most extreme simulated depth (i.e. 40 mm), with the HGC was fitted with the 1.0 mm diameter pinhole collimator and for an acquisition time ranging between 60 s and 240 s, the HGC was able to record a detection rate varying between 81.25 % and 50 % at the threshold value of 5 and between 93.75 % and 75 % at the threshold value of 3 (Figure 5.6 C,D).

Using the HGC fitted with the 0.5 mm diameter pinhole collimator provides good spatial resolution compared to the 1.0 mm diameter pinhole collimator; however, the recorded CNR values for the simulated SLNs were low while using the 0.5 mm diameter pinhole collimator. As an example, the HGC fitted with the 1500 µm thick scintillator and the 0.5 mm diameter pinhole collimator was unable to detect the smallest simulated SLN with a 2.5 mm diameter filled with 25 kBq of ^{99m}Tc solution with the selected acquisition period (i.e. 60 s to 240 s). For instance, at 5 mm depth and 240 s acquisition time, the simulated SLN detection rate was 93.75 % (i.e. 15 out 16 simulated SLNs) at the threshold value of 3 (Figure 5.6 B).

At a 5 mm depth and an acquisition time ranging from 60 s to 240 s, while the HGC was fitted with the 0.5 mm diameter pinhole collimator, the recorded detection value ranged from 75 % to 87.5 % at the threshold value of 5 and from 87.5 % to 93.75 % at the threshold value of 3. Furthermore, at the same acquisition time, the HGC was able to detect 56.25 % to 81.25 % of the simulated SLNs located underneath 20 mm of the scattering material at the threshold value of 5 and between 75 % and 93.75 % at the threshold value of 3. At a 40 mm depth, the recorded CNR values were low due to the large depth of the simulated SLNs and the low sensitivity of the HGC while it fitted with the 0.5 mm diameter pinhole collimator. For example, the recorded detection rate, during an acquisition period ranging from 60 s and 240 s, was between 37.50 % and 68.75 % at the threshold value of 5 and between 62.50 % and 81.25 % at the threshold value of 3.
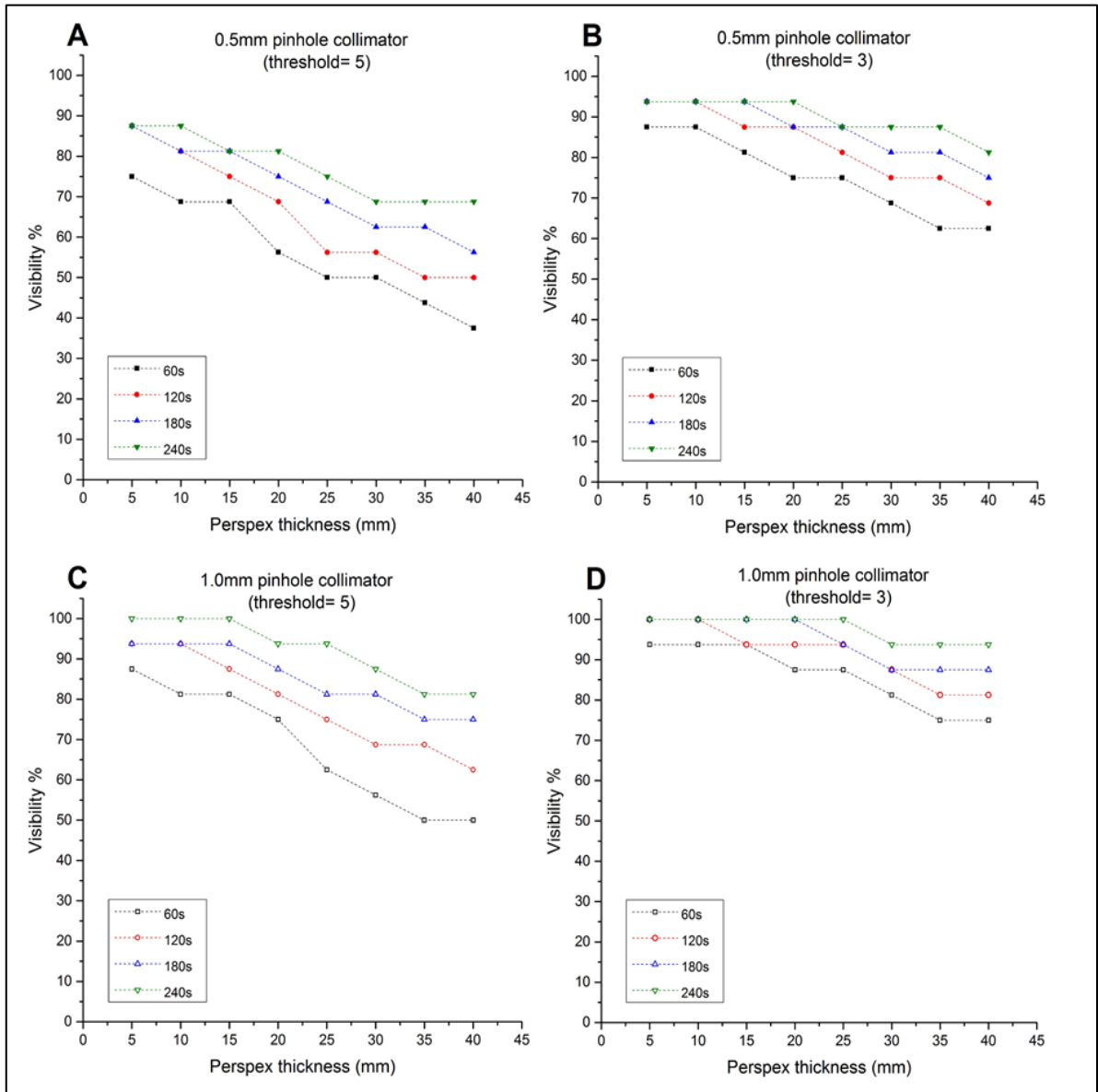
Figure 5.6. Graphs showing the relationship between the simulated SLN depths and the visibility (i.e. detection rate). These graphs represent the ability of the HGC fitted with the 1500 μm thick CsI(Tl) scintillator and two different pinhole collimators (i.e. 0.5 mm and 1.0 mm in diameter) to detect the simulated SLNs at different threshold values (3 and 5).

In general, the detectability of the HGC depends on the thickness of the scintillator and the diameter of the pinhole. The recorded detection values, as previously reported, for the HGC while fitted with the 1500 μm thick scintillator are better while preserving good spatial resolution, which makes the use of this thicker scintillator more justifiable. Detection levels were lowest for short acquisition times, for small and deep-seated nodes, and when the smaller pinhole diameter was used, as would be expected. A summary of the results for the visibility of the simulated SLNs when they were located at depths between 10 mm and 40 mm and 60 s acquisition time with the CNR threshold set at 3, are presented in Table 5.2.

Table 5.2. Summary of the visibility for the simulated SLNs for a 60 s acquisition time (CNR threshold = 3)

SLNs depth	Simulated SLNs visibility (%)			
	600 μm thick CsI(Tl) scintillator		1500 μm thick CsI(Tl) scintillator	
	0.5 mm diameter pinhole collimator	1.0 mm diameter pinhole collimator	0.5 mm diameter pinhole collimator	1.0 mm diameter pinhole collimator
10 mm	56.25	75	87.5	93.75
20 mm	43.75	62.5	75	87.5
30 mm	37.5	50	68.75	81.25
40 mm	31.25	43.75	62.5	75

5.3.3 Influence of adjacent active tissues on the detected sentinel lymph nodes

The ability of any gamma camera to resolve the targeted tissue from surrounding active tissues is one of the key factors in evaluating the usability and the capability of the system to be used in critical cases. The LNC phantom was designed and constructed to evaluate the simulated SLN detectability in the presence of active adjacent structures. As shown in Figure 5.1, the LNC phantom simulated different sizes of the SLNs with a small, fixed centre-to-centre distance between the simulated SLNs (i.e. 20 mm). The first row of the LNC phantom was selected to show the effect of the adjacent active tissues because of the higher activity concentrations, as the activity injected in the four simulated SLNs ranged from 4 MBq to 0.2 MBq.
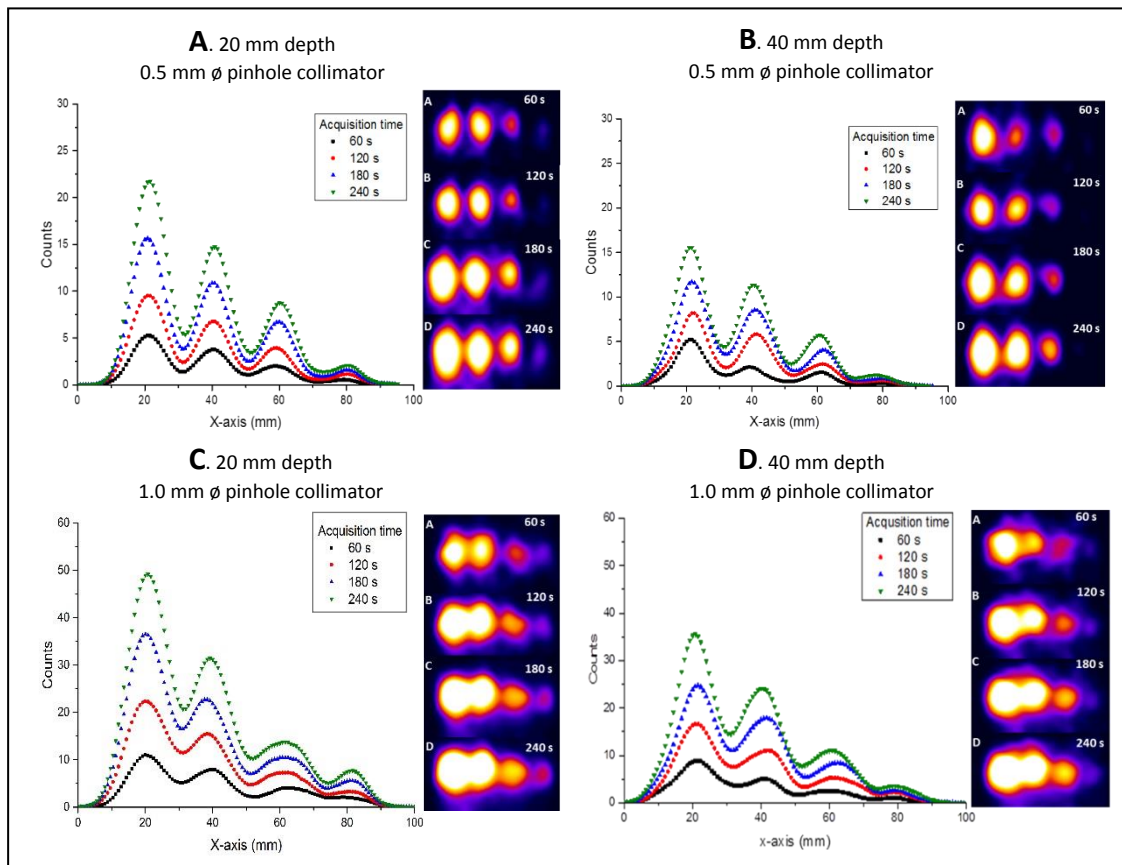
Figure 5.7. Count profile curves and corresponding gamma images of the simulated SLNs at two different depths (i.e. 20 mm and 40 mm), while the HGC was fitted with the 600 μm thick CsI(Tl) scintillator and two different pinhole collimators (i.e. 0.5 mm and 1.0 mm diameter) and at different acquisition periods (i.e. 60 s to 240 s).

It can be seen in Figure 5.7 that the simulated SLNs are generally distinguishable, which reflects the ability of the HGC to detect specific targeted structures in the presence of active surrounding tissues. As previously discussed, the HGC, while fitted with the 0.5 mm diameter pinhole collimator, can provide a superior spatial resolution; however, the recorded CNR values are low, mainly for the small simulated SLNs (i.e. 2.5 mm diameter). The effect of the accumulated activity surrounding the targeted tissues can be minimised by utilising the 0.5 mm diameter pinhole collimator (Figures 5.7 and 5.8 A,B); nevertheless, using the 1.0 mm diameter pinhole collimator improves the ability of the camera to detect more counts with good spatial resolution particularly with limited imaging times (Figures 5.7 and 5.8 C,D).
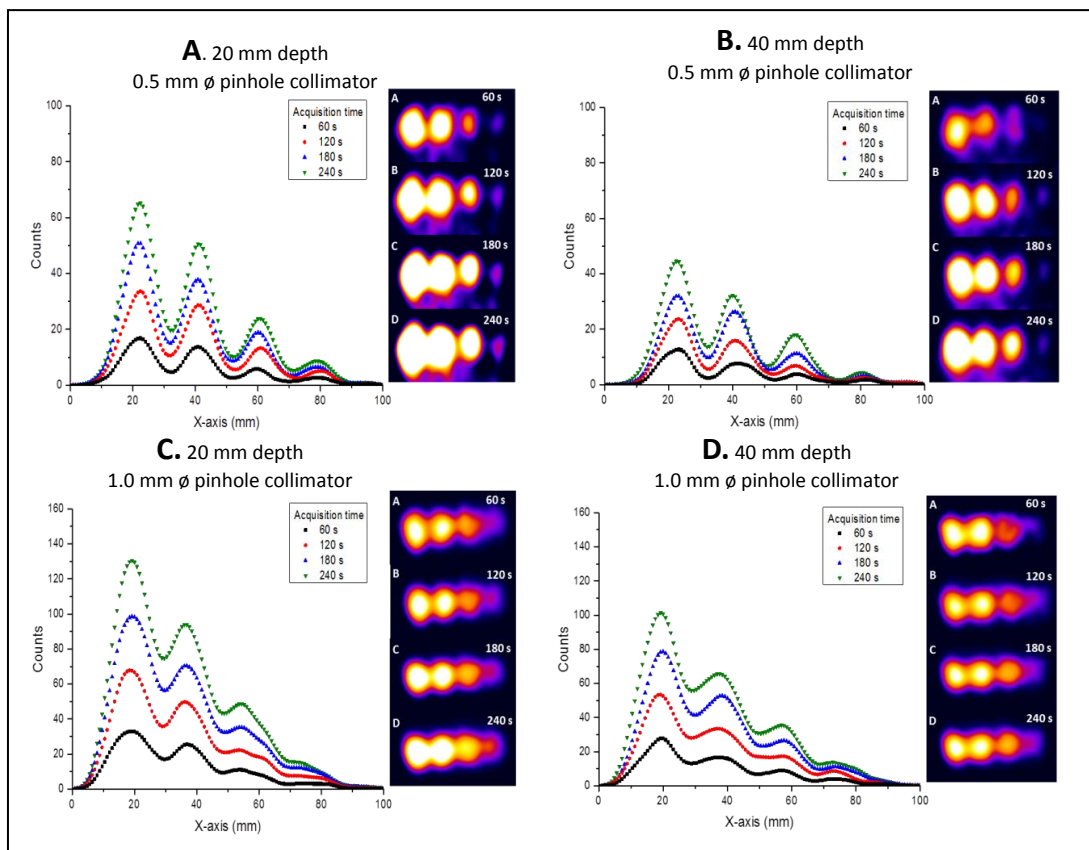
Figure 5.8. Count profile curves and corresponding gamma images of the simulated SLNs at two different depths (i.e. 20 mm and 40 mm) while the HGC is fitted with the 1500 μm thick CsI(Tl) scintillator and two different pinhole collimators (i.e. 0.5 mm and 1.0 mm diameter) and at different acquisition periods (i.e. 60 s to 240 s).

Using a thicker scintillator (i.e. 1500 µm thick CsI[Tl] scintillator) can be a practical and reliable choice that provides high CNR values and preserves a high level of spatial resolution (Figure 5.8). To make more clearer, the HGC is able to resolve the spot for the smallest simulated SLN (i.e. 2.5 mm diameter) at a 40 mm depth while the HGC is fitted with the 0.5 mm diameter pinhole collimator and the 1500 µm thick CsI(Tl) scintillator at an acquisition period ranging between 120 s and 240 s.

5.4   Discussion

The demands for technologies that improve patients' management in the surgical theatre speed up the process of developing many medical imaging systems (219, 220). Currently, the standard device that is used to detect radiopharmaceutical uptake in the targeted tissues intraoperatively is the non-imaging gamma probe (see Chapter 2). These non-imaging gamma probes are able to locate the site of activity, and they have a good ability to detect a very low accumulation of radioactivity (<10 kBq) in a short acquisition time (i.e. within seconds) (221, 222). However, these devices are unable to easily provide further details about targeted tissues' configuration; they suffer from degradation of radial sensitivity when the targeted tissues are placed deeper than 20 mm, as the background signal may mask the targeted tissues' signal (221, 222). To determine the exact location using the non-imaging probe, the sensitive window of the gamma probe should be closely positioned to the targeted tissues. Therefore, the visual estimation of the depth is difficult to obtain using gamma probes, and these non-imaging systems are not helpful for preoperative evaluation.

Using the standard gamma camera as a preoperative imaging tool to evaluate the targeted tissues and precisely estimate their depths is a laborious task. There are various factors that may affect the preoperative evaluation using standard gamma cameras, including poor spatial resolution gamma images compared to the gamma images produced by the HGC, which indicates the difficulties of detecting a small SLN within active background areas (223). The size of the standard gamma camera may affect its ability to provide multiple views for a specific targeted area in cases such as breast imaging.

Moreover, the information that is provided preoperatively cannot be confirmed intraoperatively using the standard gamma camera, because of its size and the difficulties of providing these huge devices in busy, limited spaces such as operating theatres (224).

The HGC is able to distinguish various hot spots within its field of view with a good spatial resolution, although currently it requires longer imaging times than non-imaging probes especially to detect smaller and weaker nodes. The HGC can also provide visual guidance with a relatively large field of view, and is able to monitor and distinguish between different active anatomical structures such as SLNs within a limited area, which may override the benefit of a more sensitive gamma probe in some situations (141). Furthermore, hybrid images (i.e. fused optical-gamma imaging) would enhance the accuracy of localisation process during surgical procedures. This camera can also be utilised to confirm the completion of the surgical procedure and reduce the chance of undetected SLNs.

This study shows the capability of the HGC to fulfil the majority of the requirements that should be provided in a small field of view imaging device to be used for pre-, intra- and post-operative investigations. The ability of the HGC to detect a small simulated SLN with a 2.5 mm diameter that contains small amounts of radioactive material ranging from 0.2 MBq to 25 kBq in a maximum acquisition time of 240 s and at 120 mm collimator-to-source distance indicates its usefulness for critical surgical procedures. The limits on HGC use will be due to sensitivity and the comparatively long acquisition times required, although for the activities investigated in this study the majority of nodes were visible even with a 60 s acquisition time and a 40 mm node depth when the most ideal camera configuration was used.

This study indicates that of the two thicknesses used the 1500 μm scintillator is the best choice for clinical use. With the thicker scintillator, the recorded CNR values were noticeably improved, and the HGC was able to detect the simulated SLNs with smaller diameters and lower activity accumulation. The 1500 μm thick scintillator did have a poorer spatial resolution than the 600 μm thick scintillator; however, the change in resolution (~10 %) was relatively small compared to the change in detectability (> 52 %

difference at 40 mm depth in 60 s acquisition time). The findings from this study suggest that an even thicker scintillator may be beneficial for SLN mapping and this will need to be investigated further.

The HGC can be configured with two different pinhole collimators (i.e. 0.5 mm and 1 mm diameter), and these two collimators are easily changeable, which gives the ability to the camera's operator to fit the collimator that meets the requirement of any gamma imaging procedures. For the majority of uses, particularly intraoperatively, the 1.0 mm diameter pinhole is the appropriate choice as its higher sensitivity greatly improves CNR at the cost of degraded spatial resolution. Unlike for scintillator thickness, however, this change is significant with resolution worsening by about 50 % compared to the 0.5 mm pinhole. For this reason, for rapid sensitive imaging as would be required intraoperatively, the 1.0 mm diameter pinhole collimator is preferred. Nevertheless, there are situations where there is no strict acquisition time limit or spatial resolution is of particularly importance, such as postoperative imaging, and in those cases the operator may instead choose the 0.5 mm diameter pinhole collimator as more appropriate. The positioning of the camera and the location of the targeted features were also shown to affect detectability. Placing the head of the HGC as close as possible to the target area will improve both the spatial resolution and the sensitivity, with the sensitivity varying with the square of distance from the radioactive source; however, the size of the field of view will be affected.

It has been reported that two of the developed small field-of-view gamma camera systems have the ability to detect < 7 kBq beneath up to 40 mm of scattering material in a short acquisition time (≤ 60 s) (83, 84). However, the low system spatial resolution provided by these small field of view gamma cameras will affect the ability to distinguish the margins of the targeted tissues from the adjacent normal active tissues, which may affect the progress of any intraoperative SLN detection procedure.

To clarify this point more, if these systems are able to detect the SLNs within a short acquisition time, they may require more time to take other views from various sides of the targeted area to distinguish the normal tissues from the abnormal tissues, particularly in situations where a sentinel lymph node has been removed and the

118

lymphatic vessels have been cut, with the possibility of more widespread distribution of the radioactivity within the surgical field.

5.5 Conclusion

Sentinel lymph node detection procedures have grown together with an existing demand for developing medical procedures that enhance patient management and improve diagnosis processes. The hybrid gamma camera (HGC) has been developed to provide additional localisation information during procedures such as sentinel lymph node (SLN) biopsies.

In this study, a lymph-node contrast phantom and an evaluative technique that involved idealised physiological scenarios were used to study the ability of the HGC to detect varying radioactivity concentrations and sentinel lymph node sizes. Spatial resolution measurements and contrast-to-noise ratio (CNR) analyses of the simulated SLNs were used as the main criteria to compare imaging sets produced by the HGC with acquisition times ranging between 60 s and 240 s. The HGC could successfully detect 87.5 % to 100 % (acquisition times between 60s and 240 s) and 75 % to 93.75 % of the SLNs positioned beneath 20 mm and 40 mm thicknesses of scattering material, respectively. The results suggest that the most appropriate camera configuration for intraoperative SLN imaging was a 1500 μm thick scintillator and a 1.0 mm diameter pinhole.

the HGC showed poor performance while it fitted with the 0.5 mm diameter pinhole collimator in localising deep-seated low activity simulated SLNs (i.e. 40 mm depth); this is due to the large depth of the SLNs and the low sensitivity of the HGC while it fitted with the 0.5 mm diameter pinhole collimator, even with the thicker CsI(Tl) scintillator (i.e. 1500 μm thick) and long acquisition time (i.e. 240 s), which suggested that an even thicker columnar CsI(Tl) scintillator may be beneficial to provide superior resolution gamma images during SLN mapping procedures while the HGC fitted with the 0.5 mm diameter pinhole collimator.

The evaluation of the HGC in this study shows that it can be used for SLN imaging. The capability of the HCG to detect low activity uptake in a small SLN indicates its usefulness as an intraoperative imaging system during critical surgical SLN procedures.

Chapter 6: Design and implementation of a prototype head and neck phantom for the performance evaluation of gamma imaging systems

6.1   Introduction

In clinical practice, there has been much attention on preoperative lymphoscintigraphic imaging for melanoma, oral cancer, and parotid gland carcinomas; it is a well-recognised procedure that has contributed to the improvement of surgical outcomes (225, 226). Imaging is used to identify lymphatic drainage paths and locate sentinel lymph nodes (SLNs) that may contain disseminated disease. SLN mapping and biopsy in the head and neck usually follow preoperative lymphoscintigraphic imaging (227). This procedure is used to determine the status of SLNs, and has been shown to provide crucial prognostic details of metastatic growth (228).

Performing preoperative lymphoscintigraphic imaging and SLN mapping procedures in the head and neck region is challenging in terms of anatomy (229). The head and neck region contains several hundred lymph nodes that are distributed over different depths and have numerous different lymphatic suppliers, which complicates tracing of lymphatic drainage mechanisms (230). Furthermore, the natural anatomical and physiological intricacies of the lymphatic network in the head and neck region pose technical difficulties in the case of preoperative lymphoscintigraphy and SLN mapping procedures. As structures in the head and neck are so closely packed, it is common for the large amount of radioactivity in the injection site to mask the signal from nearby SLNs (231). Head and neck anatomy is complex and variable, with lymphatic drainage

patterns differing between patients; 4 % of SLNs detected related to oral cavity tumours are on the contralateral side of the neck (232). The identification of sentinel lymph nodes can also be hampered by the rapid displacement of the intradermally injected radioisotope, which may accumulate in several lymph nodes within a short period.

This study aims to develop and standardise a test object and protocols particularly suited for SFOV compact gamma cameras but which can be equally useful for large field of view (LFOV) systems. A flexible insert was designed for a commercially available head and neck phantom. This insert effectively imitates human tissues including simulating SLNs and a life-size thyroid gland. The phantom insert was designed to be reproducible at relatively low cost; allowing this test object to be incorporated into different quality assurance protocols. It is proposed that this phantom can be employed in assessing the clinical usefulness of SFOV gamma imaging systems in SLN mapping and small organ imaging.

6.2 Materials and methods

6.2.1 Head and neck phantom

The outer shell of the phantom was obtained from The Phantom Laboratory (233). This comprised a shell manufactured from ~ 3.2 mm thick cellulous acetate butyrate (CAB) mounted on a polycarbonate end plate, a transparent plastic selected because of its low water absorption and its strength. The anthropomorphic head and neck phantom is constructed to allow filling with water or other tissue equivalent liquids. The shape of the outer shell imitates the head and neck contours of an average size adult male; the maximum axial height being 255 mm and the maximum transverse width 175 mm (Figure 6.1 A).

An anatomical insert (further details discussed below, see Figures 6.1 and 6.2) was used in conjunction with the outer shell of the phantom. This insert was modular and could include a simulated thyroid gland, trachea, cervical spine, lymph nodes and injection sites in any combination, together with various locations for lymph nodes and injection sites.

6.2.1.1 Anatomical simulation

Comprehensive data were collected to obtain the anatomical characteristics of the human neck, and tissue equivalent materials were selected for mimicking soft, cartilaginous and bone tissues. The size of a thyroid of a healthy adult was chosen for simulation. Various studies have been published summarising the geometric information of the healthy thyroid from medical imaging investigations (73, 74, 234-239). The average geometric measurements of healthy male thyroid glands given in these papers was used in the design of the thyroid phantom (Table 6.1).
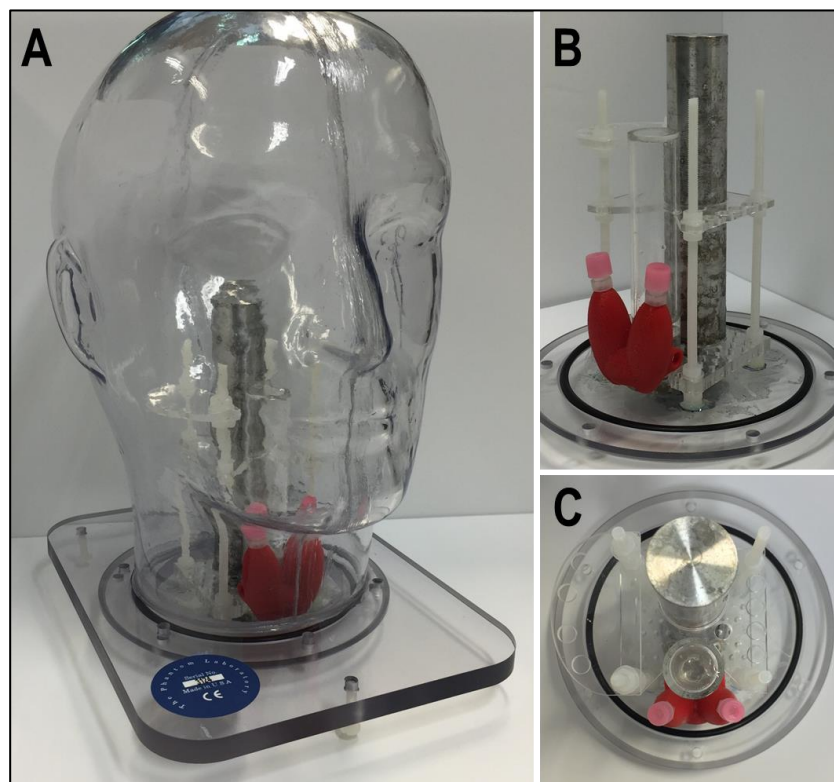
Figure 6.1. Photographs of the head and neck phantom (A); the internal jig with the attached thyroid phantom from antero-lateral view (B) and apex view (C).

Table 6.1. Summary of the anthropomorphic thyroid phantom parameters

Outer shell thickness (mm)	Internal Lobe dimensions (mm)			Internal Isthmus dimensions (mm)		
	vertical length	maximum width	maximum depth	vertical length	maximum width	maximum depth
3	42	17.5	10	12	15	5

Once the size had been determined the structure was manufactured using 3D printing (the Dimension Elite™ 3D Printer (240)). A red coloured Acrylonitrile Butadiene Styrene (ABS) thermoplastic polymer material (chemical formula: $(C_8H_8 \cdot C_4H_6 \cdot C_3H_3N)_n$) was used to manufacture the outer shell of the thyroid insert (Figures 6.2 and 6.3); the inner sealed space was filled with water mixed with the desired radioactivity concentration (~10 ml volume). Two syringe filling valves allowed filling the inner space with the radioactive solution (Figure 6.3).
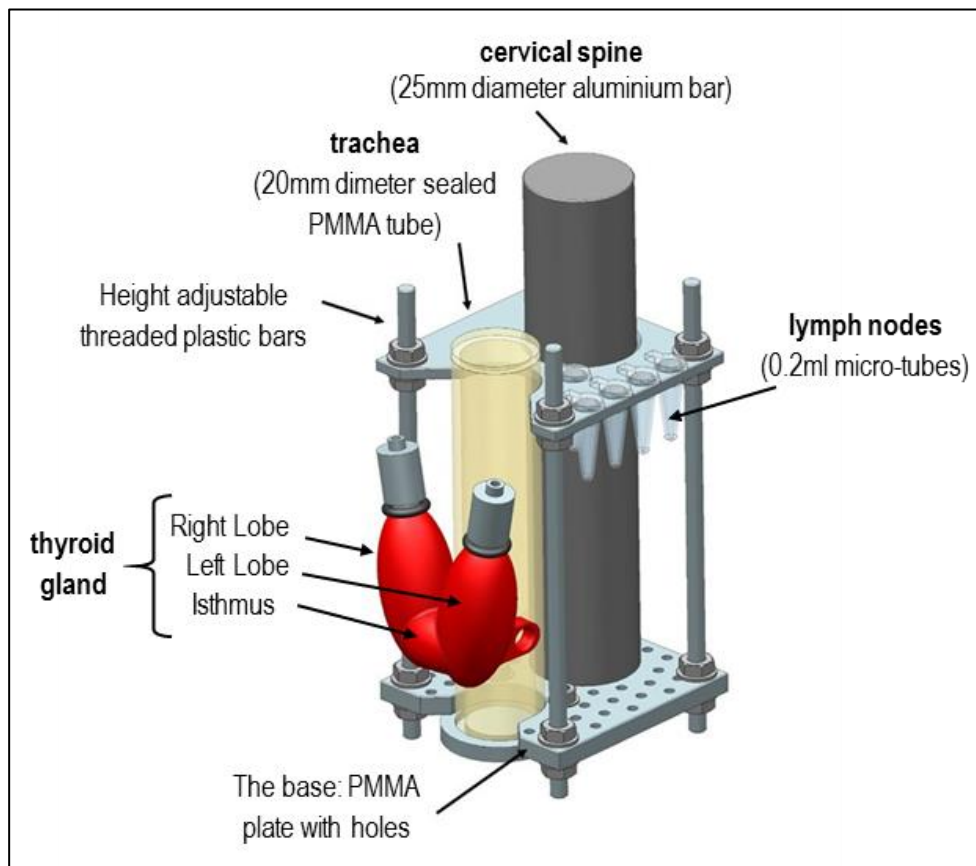
Figure 6.2. Schematic of the internal jig with the mounted simulated thyroid gland and sentinel lymph nodes (SLNs).

A simulated trachea was constructed to hold the life-size thyroid phantom. The trachea was designed and manufactured as a sealed cylinder filled with air and was made of polymethyl methacrylate (PMMA), chemical formula: $(C_5O_2H_8)_n$, (height = 150 mm, diameter = 20 mm, thickness = 3 mm). The anthropomorphic thyroid phantom was manually attached to the trachea simulator in its appropriate anatomical position. The internal jig also included a cylindrical rod of aluminium that was used to imitate the

cervical spine in the neck region (height = 200 mm, diameter = 25 mm). The materials chosen to simulate the head and neck parts of the phantom show an acceptable degree of similarity to normal human tissues as characterised in a number of published studies (see Table 6.2).

Table 6.2. Comparison of the densities for the materials utilised for the phantom designing with real human tissues (189, 241-246).

Materials	Density g/cm³	Mass attenuation coefficient (cm²/g)	Calculated Hounsfield Unit (HU)
Water	1	0.154	0
Thyroid gland	0.98	-	-
ABS thermoplastic polymer	1.06 - 1.08	0.152	46 – 66
Bone tissues	1.7 – 2.0	0.156	722-1026
Aluminium	2.69	0.137	1393
Soft tissues	1.04	0.153	33
PMMA	1.18	0.149	142
Trachea	0.98 – 1.1	-	-
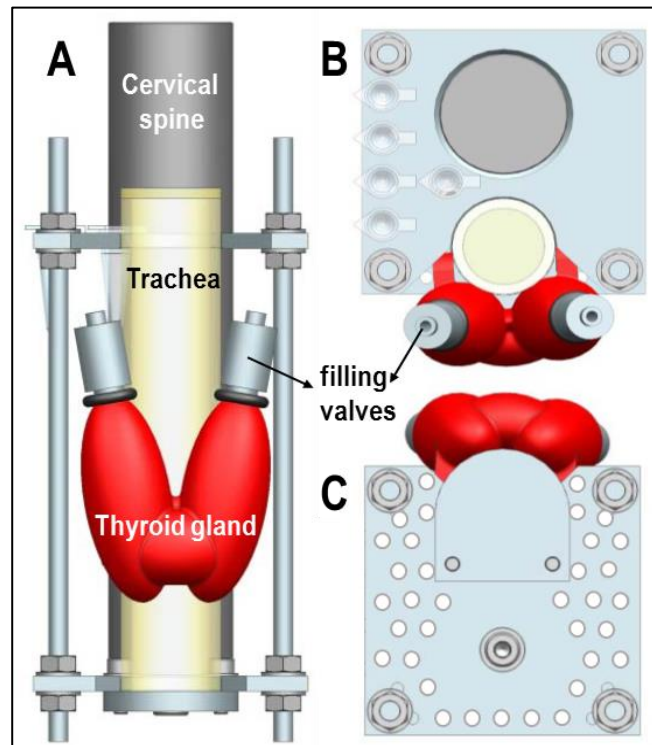
Figure 6.3. Schematic diagram of the anthropomorphic thyroid phantom (red) showing the shape and position relative to the simulated trachea: anterior (A), superior (B), and inferior (C) views.

6.2.1.2 Sentinel lymph nodes (SLN) and injection site simulation

Low profile plastic micro-tubes (0.2 ml) with attached caps have been used to simulate SLNs or injection sites. These are easily removed from the phantom (along with the thyroid) for easy storage while any activity decays. These tubes can be filled with various activity concentrations to simulate a range of clinical scenarios e.g. high activity for an injection site, low activity for a SLN.

A selection of PMMA plates, 3 mm thick, were designed, containing drilled holes to hold the micro-tubes, which attach directly to the insert (Figure 6.2). Node placement can be varied by adjusting the height of the plates on the insert, varying the shape of plate used (see Figure 6.4 for example shapes) and by changing the hole a node is set in. For instance, deep, posterior and superficial cervical lymph nodes can be simulated and located in their accurate anatomical place and can be individually filled with different radioactivity concentrations. The phantom design enables reproducible node placements for different applications.

6.2.2 Radioactivity distribution and imaging procedure

When simulating a scintigraphic procedure, the amounts of radioactivity should be a true reflection of the activity concentrations reached in clinical situations. In practice, identifying the particular radioactive material concentration for SLNs in the head and neck region can be a difficult task due to the different nature of radiopharmaceuticals and patient anatomy and physiology.

For this study, four simulated SLNs were placed at superficial (15 mm depth) and deep (30 mm depth) locations in the head and neck region with various concentrations of ^{99m}Tc solution ranging between 0.1 MBq and 1 MBq, as shown in Figure 6.4. These concentrations have been selected with the guidance of available clinical data (38, 154, 247-249). The uptake of ^{99m}Tc pertechnetate in the thyroid gland is considered to be between 1 to 5 % of administrated activities ranging between 185 and 370 MBq (250). In the UK, the recommended administered radioactivity for thyroid gland imaging is 80 MBq (198); from these figures 15 MBq of ^{99m}Tc was taken as an appropriate amount of activity to represent the radioactivity uptake in the thyroid gland.

The average amount of activity usually administered for head and neck lymphoscintigraphy is 20 MBq (251), and it was assumed that half of the injected activity will be distributed in the tissues surrounding the targeted SLNs. This background activity was simulated through mixing 10 MBq of ^{99m}Tc solution with the water filling the outer shell of the head and neck phantom.
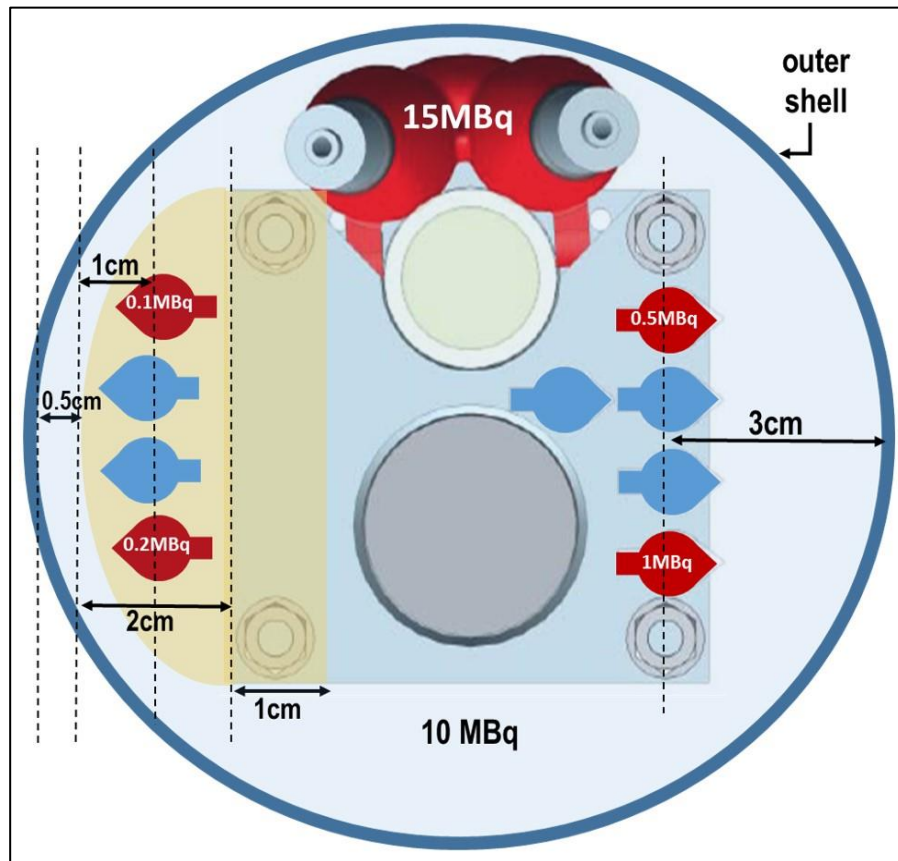
Figure 6.4. A schematic diagram showing a cross section through the neck region of the phantom, showing the position and amount of radioactivity in the simulated lymph nodes.

6.2.3 SPECT-CT Imaging

The phantom was also investigated using a Philips BrightView XCT dual head SPECT-CT system in the nuclear medicine clinic at Queen's Medical Centre, Nottingham (252, 253). The phantom was fastened to the patient table with the patient head support in place. The camera was fitted with a low energy, high resolution parallel-hole collimator and image data was acquired in a 128 x 128 matrix through 120 angular increments each of 20 s per angle over a 360 degree rotation. The data were processed on a dedicated nuclear medicine computer (Hermes Medical Solutions, London, UK). Reconstruction was performed using the Ordered-Subsets Expectation Maximisation (OSEM) with 15 subsets and with 4 iterations and displayed in sagittal, transverse and coronal planes. The reconstructed images were filtered with a 3D Gaussian function having a full width at half maximum of 8 mm. CT imaging was performed with 120 kVp and 20 mAs.

127

6.2.4 SFOV Imaging

The Hybrid Gamma Camera (HGC) a 1500 µm thick caesium iodide doped with thallium (CsI(Tl)) scintillator coupled to an Electron Multiplying Charge Coupled Device (EMCCD) (i.e. e2v CCD97 BI) and a tungsten pinhole collimator. Detailed information of the HGC is available in chapter 3. Two pinhole collimators (0.5 mm and 1.0 mm diameter) were fitted to the camera interchangeably during the study. Various collimator-to-surface distances (ranging between 80 mm and 200 mm) were selected to produce gamma images with a range of field of views. An additional hybrid optical-gamma anterior view of the neck region was acquired to illustrate the localisation information provided by fused images.

For the gamma images produced by the HGC, count profiles were acquired for the simulated thyroid gland gamma images at a collimator-to-surface distance of 120 mm using both pinhole collimators. Furthermore, two circular regions of interest (ROIs) were identified corresponding to the simulated SLN size to obtain contrast and noise values. The contrast was then calculated as the difference between node and background ROI mean count values, with noise being defined as the standard deviation in the background ROI for calculating the contrast to noise ratio (CNR) of the simulated SLN, as explained earlier (Chapter 4, page no. 80-81).

6.3   Results

6.3.1 SPECT and SPECT-CT imaging

SPECT-CT images were used to validate the anatomical structure of the phantom. The appearances of the simulated thyroid gland in the coronal plane images were similar to those of a healthy thyroid (Figure 6.5). Furthermore, the accurate positioning of the simulated thyroid gland and the uniform distribution of radioactivity throughout both lobes and the Isthmus reflect the design accuracy of the phantom and its suitability for various gamma imaging performance tests.
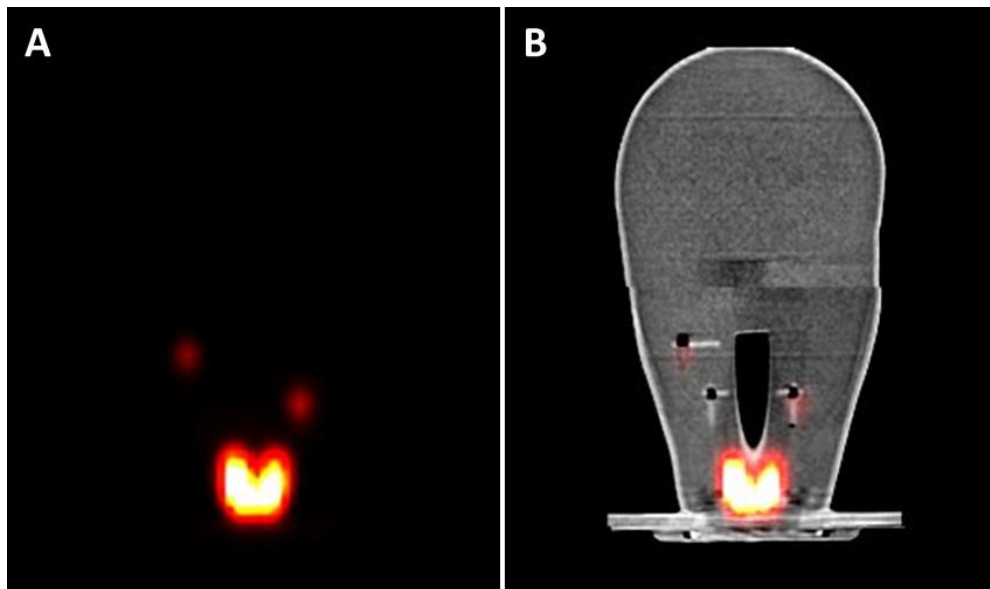
Figure 6.5. Coronal SPECT (A) and SPECT-CT (B) images showing the position of the simulated SLNs and the simulated thyroid gland within the phantom.

Figure 6.6 shows the SPECT-CT images through the midsagittal plane of the phantom. These images show the structure of the internal jig components including the simulated cervical spine, trachea and thyroid gland. A variation in X-ray contrast is demonstrated in the images for different simulated anatomical structures in line with the proposed appearance of these structures in real life, which proves the suitability of the materials used to simulate the outer shell and the internal parts of the phantom.
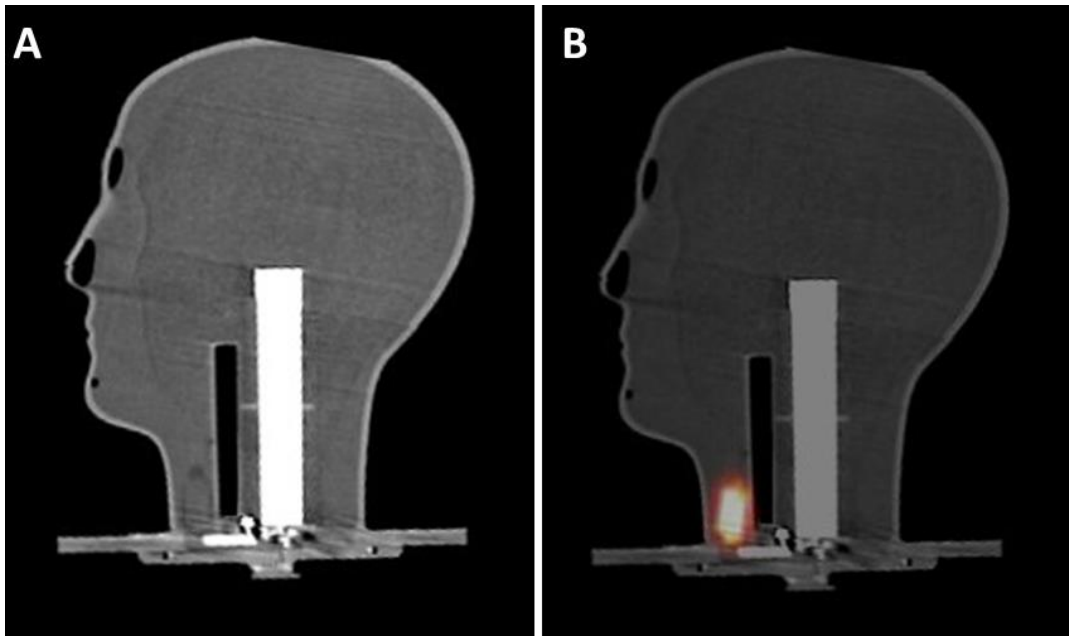
Figure 6.6. CT (A) and SPECT-CT (B) images of the midsagittal plane of the head and neck phantom showing the simulated thyroid gland, trachea and cervical spine.

In Figure 6.7, two simulated superficial SLNs were placed in the area of the parotid gland, having two different low activity concentrations, to simulate targeted parotid SLNs (Figure 6.7 A and B). In Figure 6.7 (C and D), deep simulated cervical SLNs (i.e. 30 mm depth) were located in their accurate anatomical position taking into account the position of the simulated trachea and cervical spine. Both lobes of the simulated thyroid gland can be identified in the proper position attached to the simulated trachea in a way that can provide valuable information about the capability of different gamma scanning systems in imaging the thyroid gland, Figure 6.7 (E and F).

The simulated SLNs were also imaged through the sagittal plane. SPECT and SPECT-CT images, in the sagittal plane, were acquired to image the deep SLNs (30 mm depth) in the cervical region (figure 6.8, A and B) and the superficial SLNs (15 mm depth) in the parotid region (Figure 6.8, C and D).
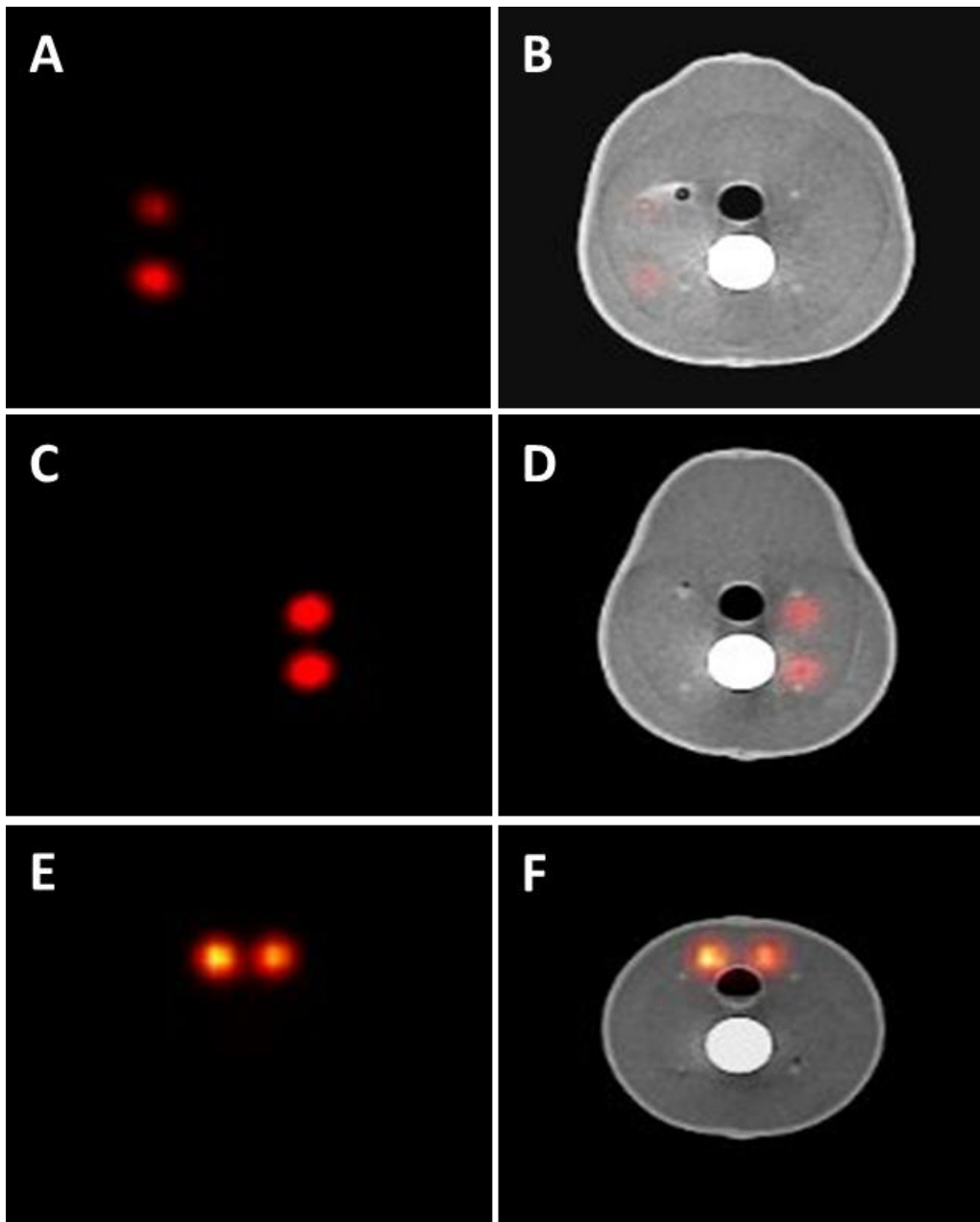
Figure 6.7. SPECT and SPECT-CT images in the transverse plane, representing the anatomical structure of the head and neck phantom; images (A) and (B) show two superficially low activity uptake simulated SLNs in gamma and hybrid modes (0.1 and 0.2 MBq, respectively). Images (C) and (D) show two deeper seated, higher activity uptake simulated SLNs in gamma and hybrid modes (0.5 and 1.0 MBq, respectively). Images (E) and (F) show the thyroid level SPECT and SPECT-CT images in the neck region (15 MBq).
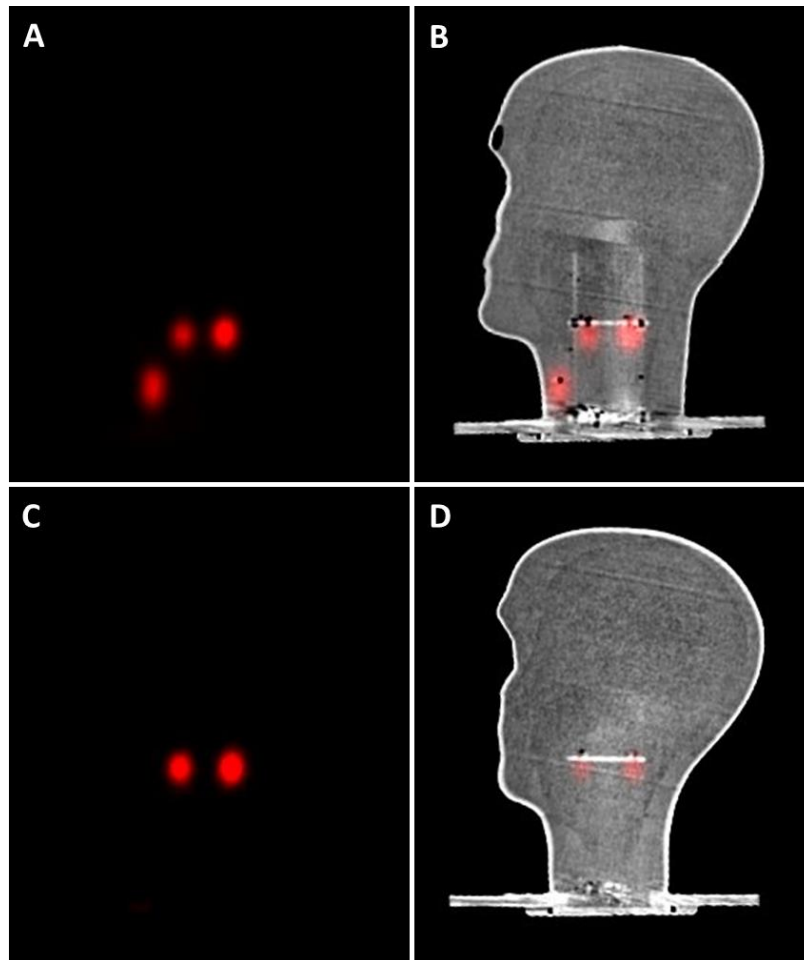
Figure 6.8. SPECT and SPECT-CT images in the sagittal plane showing the deeper simulated SLNs (0.5 – 1.0 MBq) and the simulated thyroid gland in (A) and (B); Images (C) and (D) show the simulated superficial SLNs at the parotid gland level (0.1 – 0.2 MBq).

6.3.2 SFOV hybrid gamma camera (HGC) imaging

The anthropomorphic head and neck phantom was employed to show the capabilities of the HGC for imaging small organs and mapping SLNs in the head and neck region. The imaging protocol and anthropomorphic phantom, are suitable for different SFOV gamma imaging systems and the experimental setup can be replicated for comparison purposes.

6.3.2.1 Thyroid phantom images

Hybrid gamma and optical images were acquired using the HGC with both pinhole collimators (0.5 mm and 1.0 mm in diameter) for thyroid imaging. The thyroid images produced through both pinhole collimators vary in terms of spatial resolution and number of acquired counts. Figure 6.9 shows the different gamma images acquired for the simulated thyroid gland utilising both pinhole collimators in a time series with acquisition time varying between 100 s and 400 s. The differences between each collimator can be clearly observed and the clarity of the acquired images improves with increasing acquisition period. At a 120 mm collimator-to-surface distance, the degradation of spatial resolution while utilising the 1.0 mm diameter pinhole collimator is clear from the images in Figure 6.9 (left-hand side).
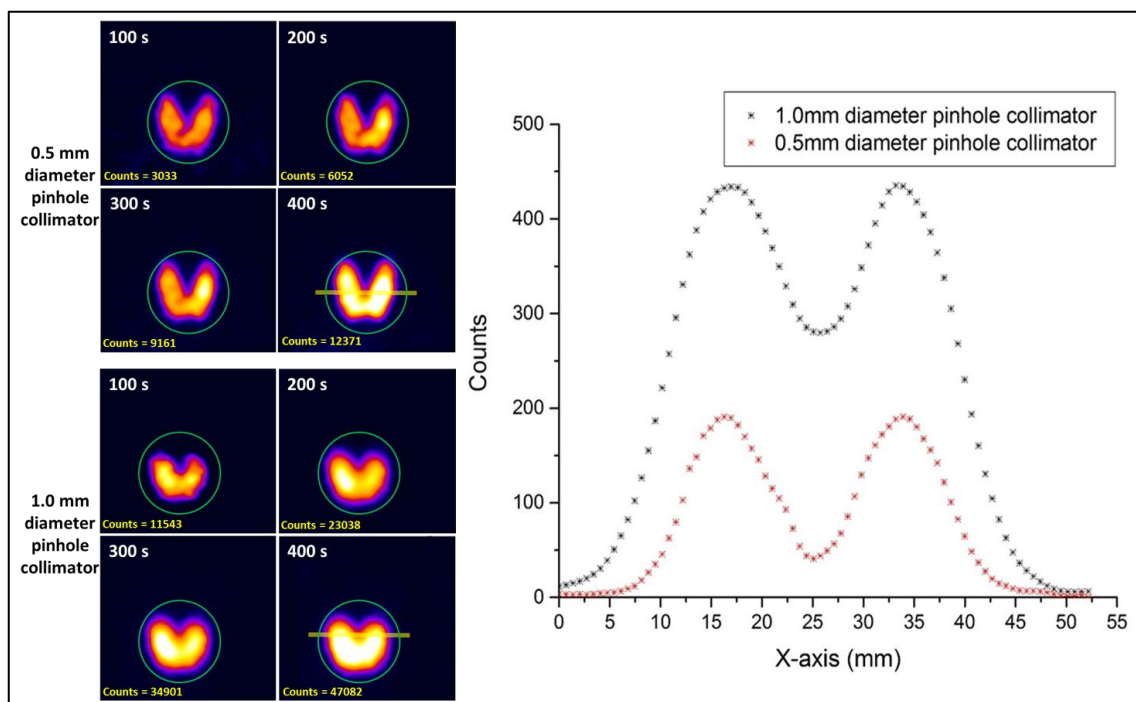
Figure 6.9. Left-hand side: planar HGC gamma images of the simulated thyroid gland at a 120 mm collimator-to-surface distance acquired with different acquisition times ranging from 100 to 400 s using both pinhole collimators (0.5 mm and 1.0 mm diameter). Right-hand side: count profiles plot for the data acquired from anterior gamma images for the simulated thyroid gland (400 s) using 0.5 mm and 1.0 mm diameter pinhole collimators. The yellow line in both thyroid gamma images (400 s) represents the cross-section area of the acquired data for both count profiles.

The count profiles through the middle of the simulated thyroid gland images provided by both pinhole collimators were obtained. Figure 6.9 (right-hand side) shows the difference in the spatial profiles when using the two collimators. Employing the thyroid phantom in quantitative assessment protocols would optimise the ability of the device's operator to choose the suitable configuration of a gamma imaging system to satisfy existing medical needs; furthermore, the phantom will be a helpful tool to determine appropriate settings for the patient and the imaging system for clinical imaging studies.

The HGC can produce optical-gamma fused images at different distances from the targeted tissues. Figure 6.10 (A and B) represent anterior hybrid images for the thyroid phantom for two different imaging distances (100 mm and 200 mm) from the camera. The acquisition time for the acquired thyroid gamma images was 400 s using the 0.5 mm diameter pinhole collimator.
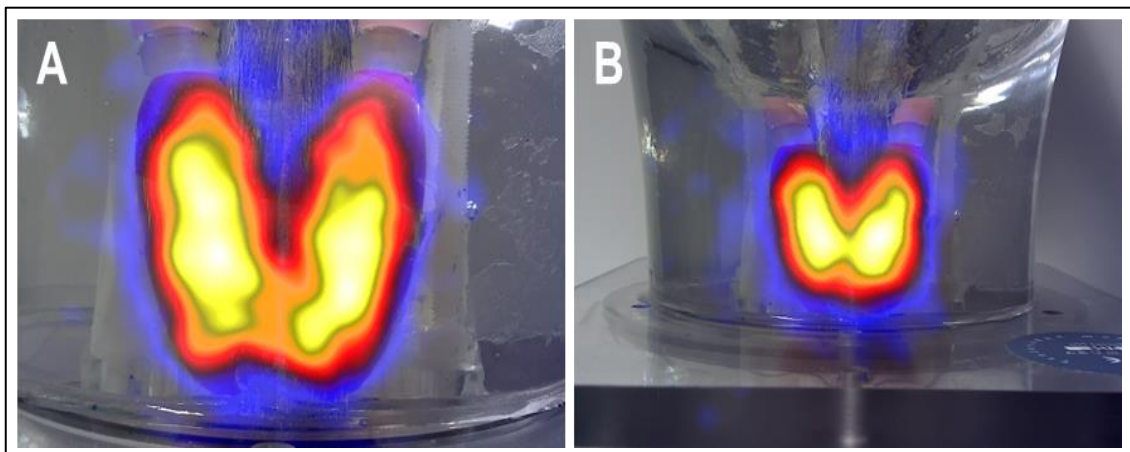
Figure 6.10. Hybrid HGC images of the simulated thyroid gland at a distance of 100 mm (A) and 200 mm (B) from the phantom surface.

6.3.2.2 Simulated sentinel lymph node (SLNs) images

Imaging targeted areas intraoperatively during SLN mapping procedures requires a swift imaging process that is able to detect any potential lymph nodes within the field of view. To achieve this target, SFOV gamma imaging systems for intraoperative imaging should be able to provide gamma images for the targeted SLN at a short acquisition time. The anthropomorphic head and neck phantom was employed to simulate a situation where there are four SLNs distributed at two different vertical levels and depths. Using both

pinhole collimators and with the HGC position at a distance of 80 mm from the surface of the phantom, several gamma images were acquired from the lateral view at different acquisition times ranging from 10 s to 300 s.
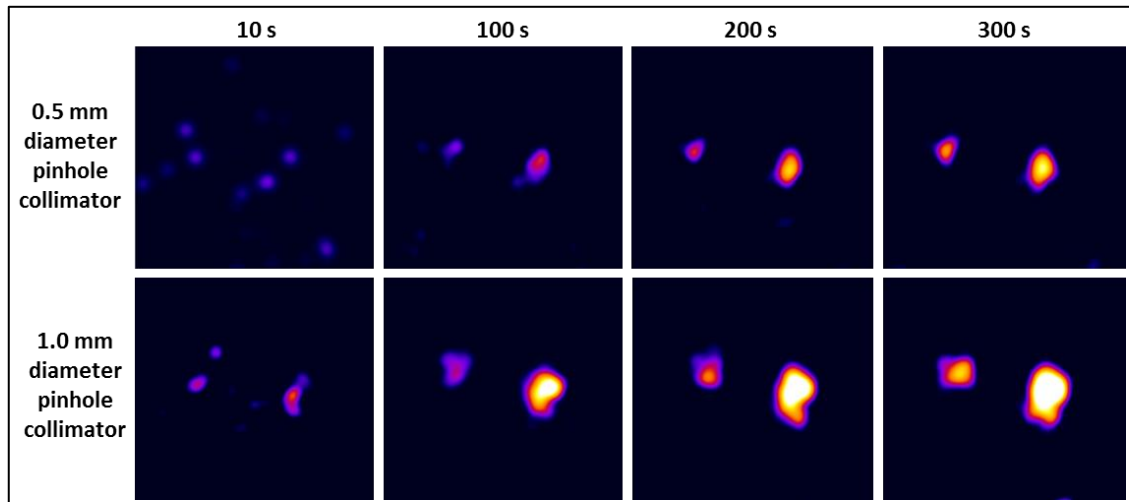
Figure 6.11. Planar HGC gamma images for the two simulated, superficial SLNs (0.1 and 0.2 MBq) at an 80 mm collimator-to-surface distance utilising both pinhole collimators (i.e. 0.5 mm and 1.0 mm diameter); the acquisition time varied between 10 s and 300 s.

Figure 6.11 shows gamma images of the two simulated superficial SLNs at the parotid gland level containing two different radioactivity concentrations (i.e. 0.1 MBq and 0.2 MBq). The HGC is able to clearly detect both simulated SLNs using the 1.0 mm diameter pinhole collimator at a short acquisition time (i.e. 100 s). In contrast, the ability to detect these simulated SLNs degrades when the HGC is fitted with the 0.5 mm diameter pinhole collimator. However, using longer acquisition times helps to provide a detailed image with an acceptable level of visualisation (Figure 6.11 – upper row). These images show the advantage of using the 1.0 mm diameter pinhole collimator for the imaging of low activity accumulation targeted areas at short acquisition times, as the main purpose of utilising SFOV gamma imaging systems intraoperatively is to localise the site of SLNs. This demonstrates that the HGC is capable of detecting a small amount of accumulated activity (0.1 MBq) in a reasonable acquisition time (i.e. <100 s). For higher activity accumulation targeted areas, using pinhole collimators with smaller diameters will provide superior spatial resolution with a good level of detectability (Figure 6.12).
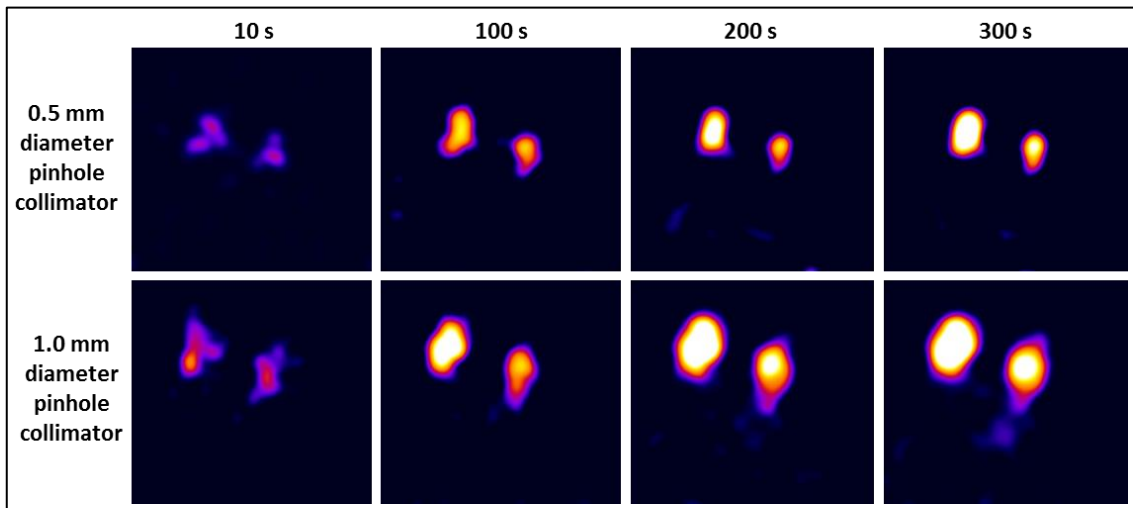
Figure 6.12. Planar HGC gamma images for the two simulated, deep SLNs (0.5 and 1.0 MBq) at an 80 mm collimator-to-surface distance; both pinhole collimators (0.5 mm and 1.0 mm diameter) were used and the acquisition time varied between 10 and 300 s.

As a further measure, CNR calculations were performed for the detected SLNs at an 80 mm distance between both pinhole collimators and the surface of the head and neck phantom for a 100 s acquisition time (Figure 6.13). The recorded CNR values for the simulated SLNs having low activity accumulations are higher when the HGC was fitted with the 1.0 mm diameter pinhole collimator. For instance, the recorded CNR values for the superficially simulated SLN (15 mm depth) containing 0.1 MBq of ^{99m}Tc using 0.5 mm and 1.0 mm diameter pinhole collimators are 6.48 and 16.42, respectively (~ 87 % difference).
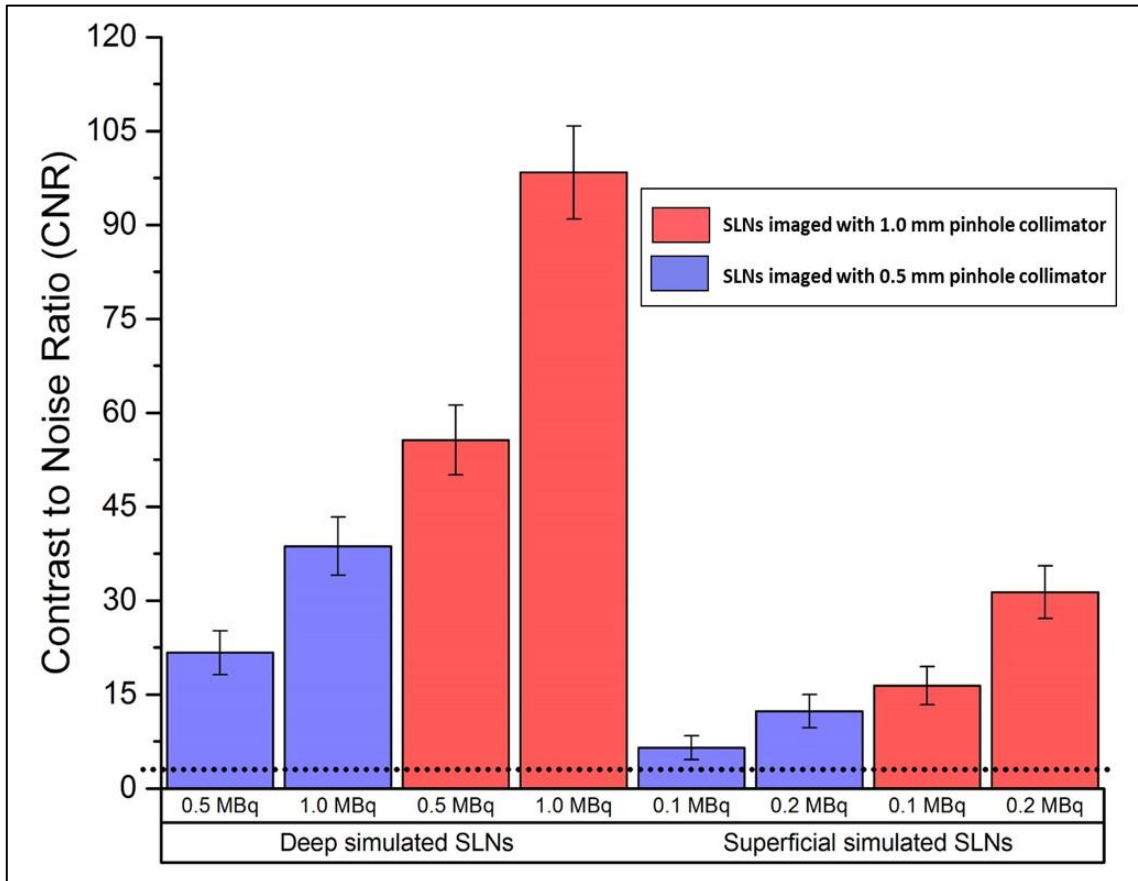
Figure 6.13. Bar chart showing the recorded contrast to noise ratio (CNR) values of different radioactivity concentrations for the simulated superficial and deep SLNs (i.e. 15 mm and 30 mm depth) for a 100 s acquisition time. The dotted line at CNR = 3 represents a threshold value of the Rose criterion of detectability.

6.4   Discussion

Phantoms are commonly used to assess nuclear imaging devices. These range from relatively crude arrangements consisting of tanks with chambers and spheres through to 3D printed phantoms for the evaluation of image processing. The use of an anthropomorphic phantom has the advantage of providing accurate anatomical and functional detail which may be used for both the assessment of equipment and user training.

The current development in computer-aided design (CAD) and 3D printing machines has facilitated the process of constructing inexpensive complex 3D medical phantoms which can be patient specific. The combination of computer aided modelling, advanced medical imaging technologies (i.e. computed tomography scanner, ultrasound devices etc.) and rapid prototyping provided by 3D printers has improved the ability to fabricate objects comparable to human parts in micro and macro architecture scales (254). Future developments could include the insertion of 3D printed lesions or tumours using information obtained from CT or magnetic resonance (MR) medical images.

The images presented show the flexibility of the head and neck phantom to simulate many clinical scenarios; i.e. lymph nodes can be simulated at any selected position following lymphatic drainage pathways in the head and neck regions. This work was mainly aimed at assessing the capabilities of SFOV cameras; however, the phantom could equally be used with LFOV SPECT-CT cameras. Currently, there are many SFOV gamma imaging systems employed in intraoperative imaging (Table 3.2). However, anthropomorphic phantoms have still not been standardised or utilised to quantify the capability of these different systems to detect targeted tissues during intraoperative procedures such as SLN mapping. Furthermore, the imaging of small organs is an area in which portable SFOV gamma cameras can provide further flexible techniques comparable to the conventional nuclear scanning techniques in cases like thyroid scans and lacrimal drainage procedures.

This study has shown the suitability of the HGC for small organ imaging such as thyroid imaging and lymph node detection in head and neck. The ability to interchange collimators helps the user prepare the HGC according to the purpose of the study; for example, in cases where good spatial resolution is a requirement, such as thyroid imaging, using a 0.5 mm diameter pinhole collimator would be suitable for a reasonable acquisition time. Nevertheless, in critical or time dependent cases where sensitivity is of particular importance, like SLN mapping, the 1.0 mm diameter pinhole collimator would be the proper choice. Therefore, the ability of the HGC to utilise both pinhole collimators enhances its practicality and improve its ability to meet the needs of SFOV gamma imaging systems.

The standardisation of a test protocol for SFOV portable gamma systems will provide an opportunity to collect data across various medical centres and research groups. Moreover, it will contribute towards a technical baseline for researchers and clinical practitioners to consider when assessing their SFOV gamma imaging systems.

6.5   Conclusion

In this study, a novel anthropomorphic head and neck phantom was designed and fabricated. The internal parts and outer shell of the phantom provided life-size adult head and neck, thyroid gland, trachea and cervical spine. In addition, different SLNs at various depths and locations, having any desired activity concentration, could be simulated. The anatomical structure of the anthropomorphic head and neck phantom was demonstrated using SPECT-CT imaging.

This phantom was employed to evaluate the capability of a novel SFOV camera - the HGC - in simulated scenarios such as SLN mapping of the head and neck region and to show the possibility of using these gamma systems in small organ imaging such as thyroid imaging procedures.

The performance of a novel HGC was investigated using the head and neck phantom. Both pinhole collimators (0.5 mm and 1.0 mm diameter) were utilised and a quantitative comparison between their performances during various gamma imaging scenarios was carried out. The results showed the ability of the HGC to image small organs, such as the thyroid gland, and to detect lymph nodes in SLN mapping procedures. The phantom provides a valuable tool for assessing camera imaging abilities prior to use in the surgical settings. This anthropomorphic phantom can be employed to validate imaging techniques for recently developed SFOV imaging system. The anatomical accuracy of its design would help in validating qualitative assessment protocol for imaging head and neck lymph nodes, and helping to qualitatively compare the capabilities of different gamma imaging systems. Further investigation for this concept is illustrated in the following chapter.

Chapter 7: Qualitative evaluation of the hybrid gamma camera capability for sentinel lymph node detection in the head and neck region

7.1 Introduction

The head and neck region is one of the main targeted regions in the human body for primary cutaneous melanoma (15-35 % of melanoma patients) (255). Head and neck melanomas frequently affect adults and are rarely diagnosed in children; i.e. limited to children with a large congenital nevus are predictably diagnosed with head and neck melanomas (256, 257). Various studies show that the staging levels of head and neck melanomas are higher than melanomas in other parts of the human body; moreover, the survival rate of head and neck melanoma patients is lower compared to other types of cancer and associated with poor prognosis (251, 256, 258, 259). Such evidence has encouraged clinicians and researchers to improve early head and neck melanoma detection procedures. The impact of early detection of lymphatic involvement in such cases is significant, as about 15-20 % of head and neck melanoma patients are diagnosed with regional metastasis (260, 261).

As discussed earlier, sentinel lymph node biopsy (SLNB) procedures have been performed in head and neck melanoma patients since the early 90s and have become the gold standard for staging and evaluating melanoma patients (24, 262). Currently, sentinel lymph nodes (SLNs) found to be positive are one of the prime prognostic indicators of survival rate (263). However, head and neck melanoma patients' management utilising the SLNB procedure is challenging. Lymphatic trees in the head and neck region are complicated, and the drainage is often unpredictable given multi-

lymphatic channels carrying the lymph from the melanoma primary site to various SLNs; thus, there is a substantive discordance between the expected drainage behaviour and the behaviour detected during lymphoscintigraphic studies (264, 265).

For instance, it has been reported that in 97 head and neck melanoma cases, there is a recognised discordance between the predicted drainage and the lymphoscintigraphic imaging outcomes in 34 % of detected SLNs (266). Such behaviour will increase the probability of false negative results during the SLNB procedures performed for the head and neck melanoma cases, which suggest poorer prognosis and reduced accuracy of the SLNB procedures in such cases compared to other parts of the human body (248).

There are some technical challenges facing clinicians while performing SLNB procedures including the location of the injection site and the proximal potential SLNs, which could be overlooked during the SLNB procedures, making the isolation of SLNs more challenging (267). Moreover, in some cases, the primary site of a tumour is difficult to access preoperatively, such as in the larynx region or the region around the base of the tongue. In such cases, radioactivity is administrated intraoperatively and the chance of masking potential SLNs close to the site of injection is increased (268).

Furthermore, in some clinical situations, a potential SLN is located close to sensitive tissues; for example, 25-30 % of detected SLNs in the head and neck region are situated in the parenchyma of the parotid gland. Performing SLNB procedures on these nodes places the facial nerves at risk of injury. As a result, some surgeons may choose to do a superficial parotidectomy prior to SLNB procedures (269).

Therefore, there is the need for a new technology that can fill this technical gap and improve the detection and isolation procedures of potential SLNs in head and neck melanoma cases. The goal of this study is to qualitatively evaluate the capability of the hybrid gamma camera (HGC) to detect simulated SLNs and compare the performance of its pinhole collimators (0.5 mm and 1.0 mm in diameter), in the head and neck region using the anthropomorphic head and neck phantom (previously discussed in the chapter 6). An initial quantitative comparison was conducted using the anthropomorphic head and neck phantom to evaluate the capability of the HGC (see

Chapter 6). This study expands the scope of our phantom usage to involve observer evaluation of the gamma images acquired using the HGC.

7.2 Materials and methods

In this study, the HGC has been fitted with a 1.5 mm thick columnar CsI(Tl) scintillator. Two pinhole collimators (0.5 mm and 1.0 mm in diameter) have been utilised interchangeably. The anthropomorphic head and neck phantom (see Chapter 6 for more details) allows the positioning of simulated SLNs at various depths and levels within the phantom, which improves the accuracy of simulating SLNs in their accurate anatomical position. During data acquisition, the phantom was positioned on its side and the HGC was mounted perpendicularly over the phantom surface using a retort stand (i.e. lateral viewing). The phantom was positioned over a small, aluminium foldable lifting table (Jack Scissor Lift Platform), which has been used to adjust the imaging distance without moving the HGC or changing the phantom positioning.

7.2.1 Radioactivity distribution and imaging procedure

Low profile, capped plastic Eppendorf tubes (0.2 ml) have been utilised to simulate the SLNs. These tubes allow for easy, accurate filling of the desired radioactivity concentrations, as well as isolating the radioactivity from the surrounding background. Six tubes have been filled with various radioactivity concentrations and distributed over three different anatomical levels (i.e. parotid gland, neck and submandibular levels). These three levels have been selected as common sites for affected lymph nodes in the head and neck region; however, using the anthropomorphic head and neck phantom also allows for deep cervical, occipital and submental lymph nodes to be simulated.

Three SLNs groups have been distributed to simulate the expected radioactivity accumulation in potential SLNs at different anatomical regions in the head and neck. Each group of the simulated SLNs has two different radioactivity concentrations (i.e. 0.1 MBq and 0.2 MBq) in a fixed volume (i.e. 0.2 ml). These simulated SLNs groups distributed over three anatomical levels; for instance, two simulated SLNs, 0.1 MBq and

0.2 MBq, have been placed in the parotid gland, submandibular, and neck levels (i.e. six SLNs in total).

A constant, uniform background radioactivity dose has been selected to be 10 MBq; this radioactivity concentration has been chosen based on the assumption that half of the injected activity in the injection site (IS) will be distributed in the surrounding tissue (see Chapter 4 for more details).

Four imaging distances ranging between 40 mm and 100 mm collimator to the phantom's surface distance are used. For each anatomical level, each imaging distance, and each utilised pinhole collimator, cumulative gamma images were acquired in increments of 5 s until reaching 120 s. A summary of the planned experimental setup and imaging procedure has been provided in Figure 7.1.
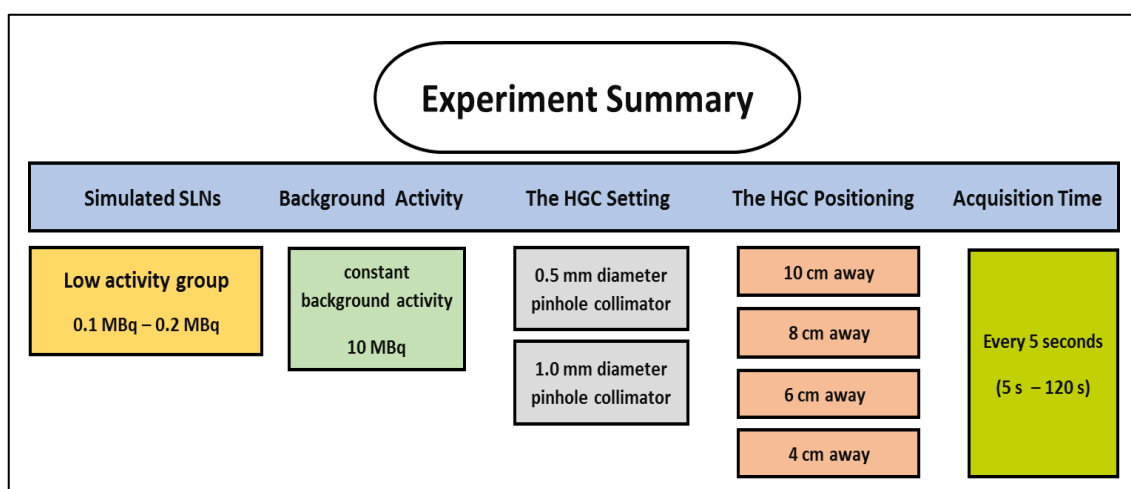
Figure 7.1. A schematic diagram showing a summary of the activity distribution, collimators used, and experimental imaging conditions.

7.2.2 Data analysis and HGC gamma images display

Six independent observers, including two nuclear medicine specialists and four medical physicists who have experience of different nuclear medicine procedures and gamma images, participated in this qualitative node-detection observer (NDO) study.

A total of 576 gamma images for the low radioactivity concentration group have been produced and analysed. All the raw gamma images produced by the HGC are processed using Centre-Point processing mode images (see Chapter 3 for more details). These images were also processed using the Image-J software Gaussian Blur filter (Gaussian sigma = 2 pixels).

Statistical significance comparisons for the observer results were calculated utilising a paired t-test to compare the performance of the HGC's pinhole collimators (0.5 mm and 1.0 mm in diameter). Pairing is utilised to minimise bias and improve precision. This statistical test is commonly used for various detectability or metric tests during medical imaging assessments (270). Such a test is performed to compare two samples of paired populations. In this study, two paired samples were produced using two different HGC pinhole collimators (i.e. 0.5 mm and 1.0 mm in diameter). These two samples were acquired under the same experimental conditions except for using two different pinhole sizes. Produced gamma images have been distributed over three controlled viewing sessions, giving the observer more flexibility while reading through the images. The question of interest in this study concerns the number of detected hot spots in each displayed gamma image. The statistical software package, SPSS Statistics, was used to conduct the paired sample t-test evaluation (271).

To deal with outliers (rare data points with far higher or lower values compared to the majority of data) that can be a source of bias for the produced data and may potentially lead to inappropriate research conclusions, there were three separate gamma images acquired for each simulated clinical setting. For instance, a gamma image for the two simulated SLNs (0.1 and 0.2 MBq) placed in the submandibular region was shown to an observer who inserted number 9 in the image, which represented the number of SLNs they recognised in the gamma image. The observer was provided with another 3 gamma

images; the first gamma image showing the simulated SLN containing 0.1 MBq, the second one showing the SLN with 0.2 MBq, and the third gamma image showing the background only without simulated SLNs. Based on the observer readings for these three images, the detected outlier will be corrected.

A customised JavaScript code has been written to display the HGC gamma images. The HGC gamma images were numbered and organised in three specific resource folders, then the JavaScript code retrieved the selected resource file and presented its gamma images randomly to minimise the possibility of predicting the location of simulated SLNs based on previous gamma images. The observers have been provided with a friendly interface screen that represented the HGC gamma image one by one. An instruction sheet explaining the study purpose, how to run the JavaScript code, and how to store the inserted readings has been provided to the observers (Appendix A). The observer was asked about the number of recognised hot spots in each presented gamma image and they were able to insert any number ranging between zero and nine.

The interface provides the observer with a tracking number for the images that are already observed and the residual gamma images. All data inserted during the viewing session is auto organised and attached to its corresponding images, then the code reconstructs the whole data in a single spreadsheet for every viewing session of each observer. A single MacBook Pro laptop was used to run the JavaScript code and record observers' readings. Figure 7.2 shows the user friendly interface screen for the JavaScript code; further details about coding script are provided in Appendix B.
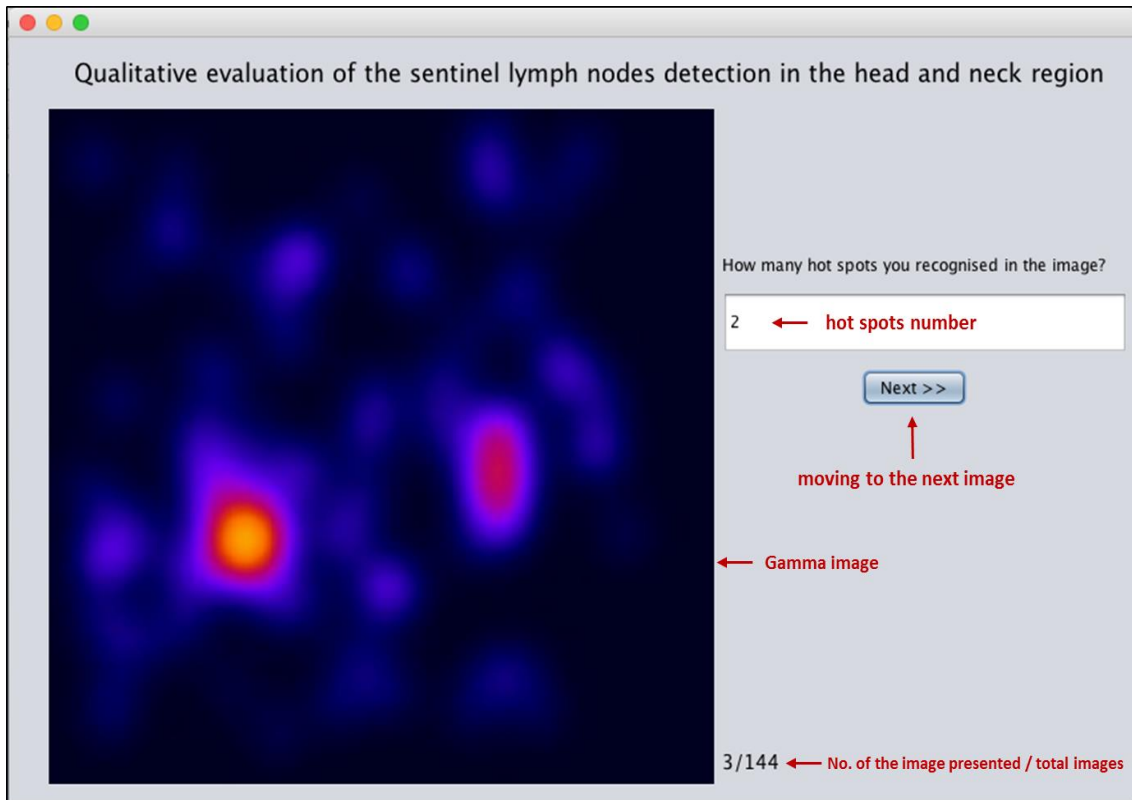
Figure 7.2. Screenshot of the JavaScript code interface screen

7.3   Results

During the experiment, it has been assumed that a surgeon (or a nuclear medicine specialist) has screened the head and neck region in a patient using the HGC and has also scanned three potential areas of the existing SLNs. The three gamma images produced after this scanning procedure and the number of detected SLNs in the three images are considered as one data point (i.e. maximum detection rate = 6 visible nodes and minimum detection rate = 0 visible nodes). This assumption has been made to build constructive, comprehensive datasets representing the supposed imaging technique while using the HGC during head and neck region SLNB procedures.

7.3.1 The influence of acquisition time on the node detection rate

The two produced sets of data (96 values in each data set) used to perform the paired t-test are reasonably normally distributed. No outliers appeared within both sets of data. Figure 7.3 shows a box plot and raw data fitted with a Gaussian distribution curve, which is used to illustrate the distribution of both datasets. Generally, the HGC has recorded a good detection rate using the 1.0 mm diameter pinhole collimator. As seen in Figure 7.3, all simulated SLNs have been detected in 25 % of the 1.0 mm diameter pinhole collimator's dataset; moreover, a minimum detection rate of 3 out of 6 simulated nodes has been recorded in 75 % of the same dataset.

In this qualitative study, the performed paired t-test on the whole datasets produced shows that the observers have recorded a significantly greater number of detected SLNs (i.e. p-value < 0.005) while the HGC fitted with the 1.0 mm diameter pinhole collimator at different imaging distances (mean= 4.32 ± 0.18) in comparison to the data produced using the 0.5 mm diameter pinhole collimator (mean= 3.03 ± 0.21), as seen in Figure 7.3. The observers recorded an ~ 79 % detection rate of the simulated SLNs in 25 % of the gamma images acquired using the 0.5 mm pinhole. Tables 7.1 and 7.2 summarise the descriptive statistical values of both datasets and the performed paired t-test evaluation.

Table 7.1. Descriptive statistics of the compared two datasets

	Data points	Mean	Standard deviation	Standard error of the mean
0.5 mm diameter pinhole collimator	96	3.03	2.05	0.21
1.0 mm diameter pinhole collimator	96	4.32	1.75	0.18

Table 7.2. Summary of the main paired samples test results

	Mean	Standard deviation	Standard error of the mean	t-value	Degree of freedom
Paired samples test statistics	1.29	0.77	0.08	16.49	95
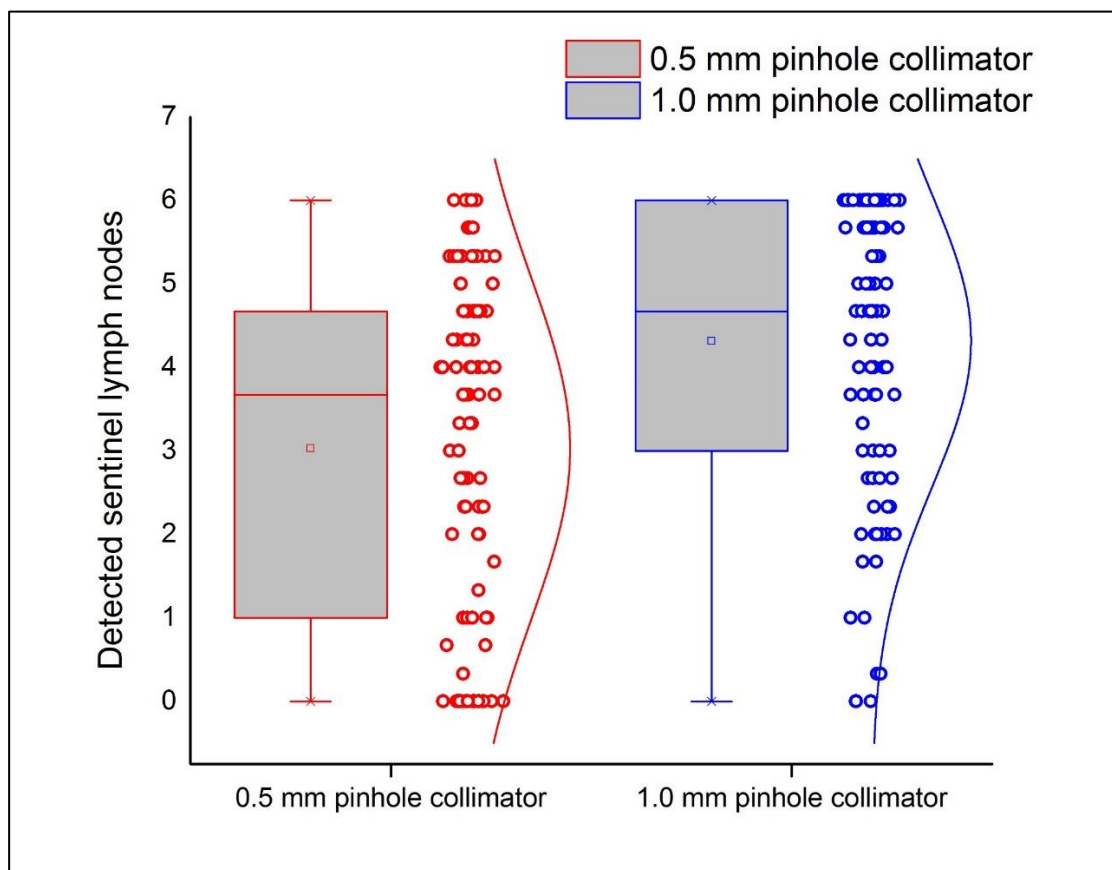
Figure 7.3. Box plot showing the distribution of both datasets (96 data points) produced using 0.5 mm and 1.0 mm diameter pinhole collimators with raw jittered datasets fitted with a Gaussian distribution. These data were acquired over an acquisition time ranging between 5 s and 120 s (5 s intervals).

The histogram fitted to the raw data, produced using the 0.5 mm diameter pinhole collimator, is recognisably skewed (Figure 7.4 A). This feature represents the poor detection rate of the simulated SLNs at short acquisition periods (i.e. between 5 s and 60 s) while the HGC is fitted with a small pinhole. For instance, 50 % of the dataset has detection rate values situated between 0 and 1 detected SLNs (Figure 7.4 A). In contrast, more than 4 out of 6 simulated SLNs are detected using the HGC while it is fitted with a 1.0 mm diameter pinhole collimator in 25 % of the same dataset. On the other hand, data acquired in acquisition times ranging between 60 s and 120 s (Figure 7.4 B) shows a higher detection rate. Additionally, using the 1.0 mm diameter pinhole collimator, ~ 95 % of the simulated SLNs are detected in 75 % of that dataset (Figure 7.4 B).
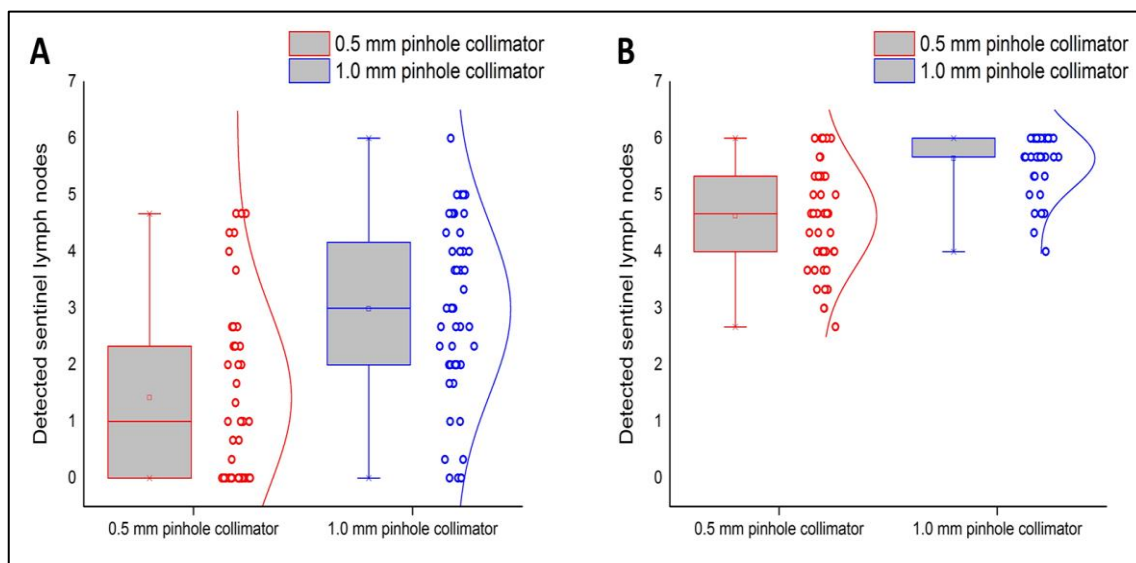
Figure 7.4. Two box plots showing the distribution of both datasets, with the raw jittered data fitted with a Gaussian distribution, produced using both pinhole collimators (0.5 mm and 1.0 mm in diameter) in two different acquisition periods; (A) box plot represents datasets acquired over an acquisition time ranging between 5 s and 60 s (48 data points), and (B) shows datasets with acquisition times ranging between 60 s and 120 s (5 s intervals).

A paired t-test evaluation has been run in the presented datasets in Figure 7.4. The datasets were compared based on the acquisition periods differences. Results indicated a well-recognised statistically significant mean difference between these datasets (i.e. p-value < 0.005).

7.3.2 The influence of imaging distance on the node detection rate

Generally, the result of increasing the distance between a gamma camera and the targeted region is a sensitivity degradation, which affects the ability of the camera to detect radioactive spots within its field of view. Nevertheless, while using a pinhole collimator, increasing the imaging distance expands the field of view, providing an opportunity to screen a larger area, and reduces the total scanning time. Therefore, reasonable compromises between these influential factors should be considered.
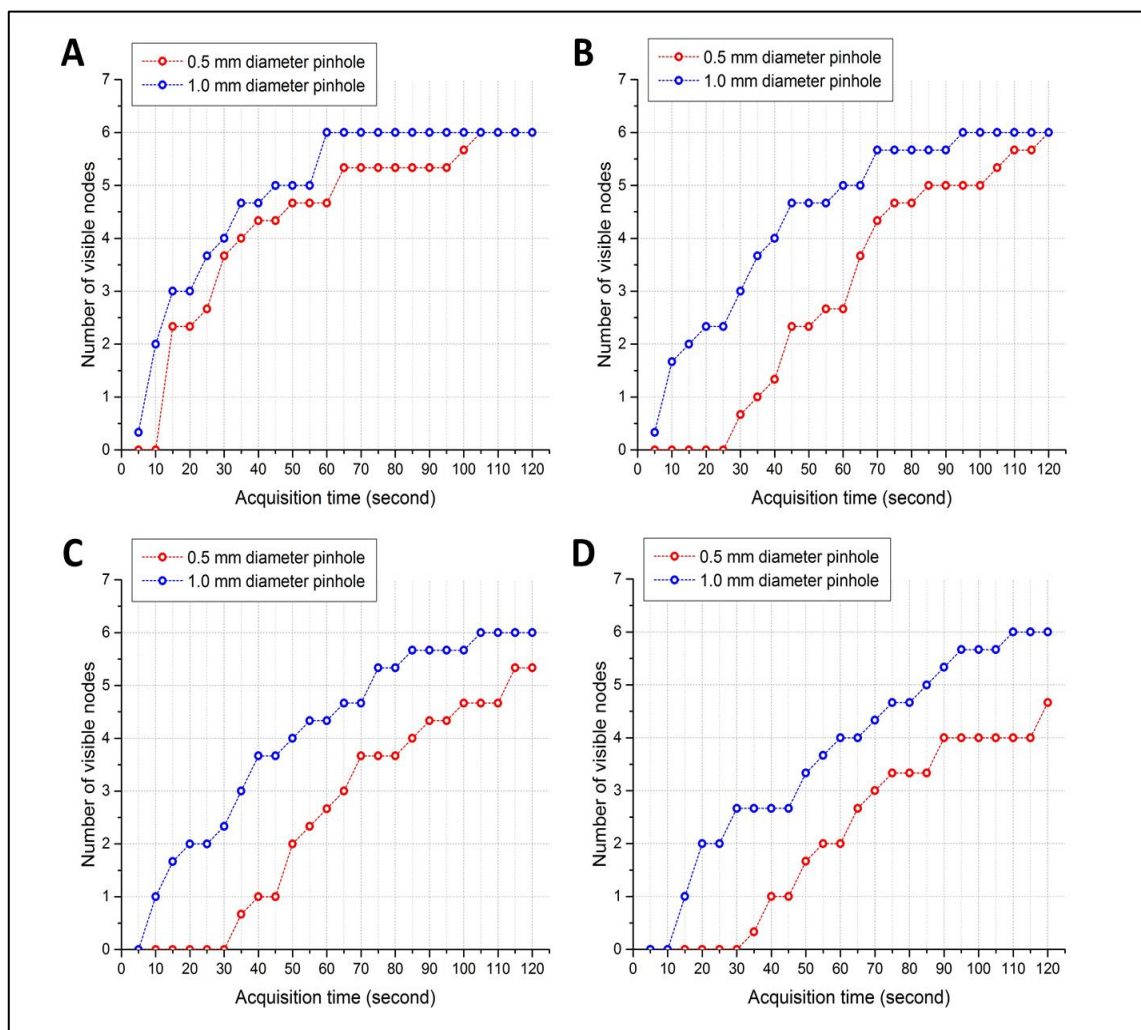
Figure 7.5. Graphs showing the relationship between the number of detected simulated SLNs and the acquisition time at different distances; (A) 4 cm away, (B) 6 cm away, (C) 8 cm away and (D) 10 cm away.

Overall, all the simulated SLNs have been detected at different anatomical positioning and imaging distance within two minutes using both pinholes at 4 cm and 6 cm imaging distances (Figure 7.5 A and B). In contrast, the percentage differences between the values of detected simulated SLNs using 0.5 mm and 1.0 mm diameter pinhole collimators are 11.75 % and 25 % at 8 cm and 10 cm imaging distances, respectively (Figure 7.5 C and D).

While using the 1.0 mm diameter pinhole collimator, the observers were able to visualise all simulated SLNs in 60 s acquisition time at 4 cm imaging distance. However, the use of a smaller pinhole (i.e. 0.5 mm in diameter) resulted in lower detection, as all simulated SLNs were detected in 105 s scanning time at the same distance, hence an extra 45 s was required compared to the 1.0 mm pinhole (Figure 7.5 A). A low detection rate was observed while using the 0.5 mm pinhole collimator at short acquisition times; for instance, at 25 s acquisition time, less than 44.50 % of simulated SLNs can be visualised at the shortest imaging distance (4 cm) compared to 61.20 % while utilising the 1.0 mm pinhole under identical imaging conditions (Figure 7.5 A).

Figure 7.6 illustrates the total of the detected simulated SLNs at several imaging distances using both pinhole collimators in the three screened areas in the head and neck region. While qualitatively comparing the performance of the HGC with both pinholes, it can be seen that the HGC fitted with the 0.5 mm pinhole resulted in a higher detection rate at 4 cm compared to the 10 cm imaging distance, when results were compared to the values produced utilising the 1.0 mm pinhole. The differences between total detected simulated SLNs using both collimators is 26.24 % difference at 4 cm, and 83.46 % difference at 10 cm imaging distance. The justification for this behaviour is that the HGC fitted with the 0.5 mm diameter pinhole collimator is strongly affected while acquiring gamma images for low radioactive accumulation regions at short acquisition times, and by increasing the scanning distance due to low collimator sensitivity, compared to the 1.0 mm pinhole. This behaviour can also be seen when the total detected SLNs are compared at different imaging distances. When using the 0.5 mm diameter pinhole collimator, there is an 88.72 % difference in the total detected SLNs at 4 cm and 10 cm imaging distances; in contrast, a 32.56 % difference is recorded using the 1.0 mm pinhole at the same imaging distances.
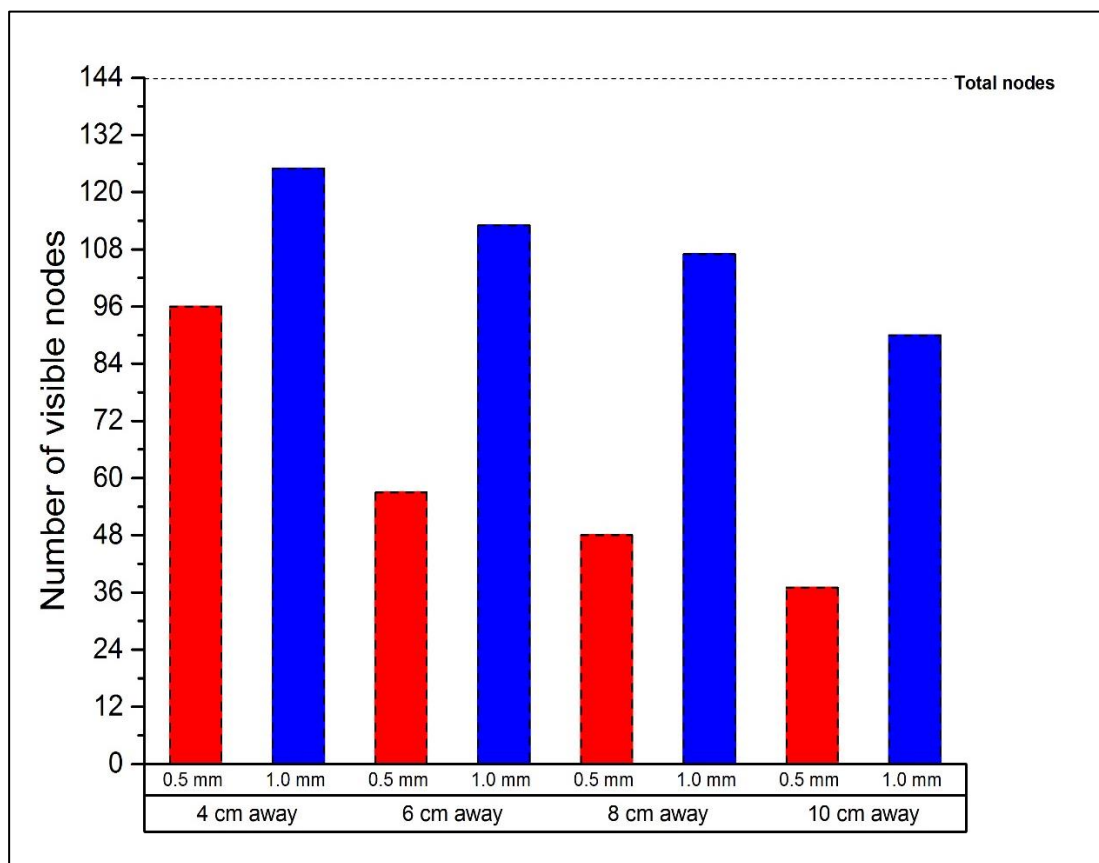
Figure 7.6. Bar chart representing the total number of detected simulated SLNs using both pinholes (i.e. 0.5 mm and 1.0 mm in diameter) at various scanning distances ranging between 4 cm and 10 cm.

7.4   Discussion

Sentinel lymph node detection procedures and techniques in the head and neck region are contested research areas; the anatomical complexity of this region is the main challenge for researchers and medical research centres, and there is a need to find a suitable and effective solution to detect, target, and isolate potential SLNs intraoperatively. Employing intraoperative SFOV gamma imaging systems could be a reasonable and practical solution that can provide real-time 2D imaging for the radioactivity distribution in the surgical field. The HGC is one system that can provide gamma imaging and has an advantage of providing hybrid optical-gamma imaging as previously discussed (see Chapter 3).

Observer studies play an important role in the evaluation and optimisation of many medical imaging modalities and are considered as a gold standard to judge the modality's capability. The qualitative NDO study was designed and performed to evaluate the usage of the HGC fitted with two pinhole collimators interchangeably (i.e. 0.5 mm and 1.0 mm in diameter). Based on the analysis of the readers' observations for the data produced using both pinholes, the HGC shows a superior detection rate for the simulated SLNs (0.1 MBq and 0.2 MBq) using the 1.0 mm diameter pinhole collimator at different places in the head and neck region and various imaging distances within a 120 s acquisition time. This makes the HGC a suitable imaging device that can facilitate SLNB procedures and prompt the detection of the targeted potential SLN.

Using the HGC will help surgeons to explore the area of interest in the head and neck region to prove the existence of a SLN within the surgical field and precisely localise its position, or screen the surgical field after removing the node to confirm no residual SLNs. The imaging distance range used (4 cm to 10 cm) and the ability of the HGC to detect all the simulated low radioactivity accumulation nodes at these distances within short acquisitions (< 120 s) will enable the operator to visualise larger areas (FOV diameter at 10 cm imaging distance ≈ 10 cm) then explore any suspicious affected areas closely to visualise more details. This technique will enhance the cognisance of any metastasised tissues or discordant unpredicted drainage (a common case in the head and neck region). Such information could not be provided by the routinely used non-imaging gamma probe intraoperatively, which can potentially affect the prognosis in such cases.

The simplicity of interchanging both pinhole collimators could help to improve the imaging outcome using the HGC. Increasing the acquisition time and reducing the imaging distance will allow the use of the 0.5 mm diameter pinhole collimator, mainly in the cases where a higher spatial resolution is required, such as during targeting a small area packed with several, small potential SLNs or scanning an adjacent SLN to the radioactivity injection site. It has been previously reported that a competitive SFOV gamma camera has been used during cancer surgeries and the time required to localise and isolate SLNs with the SFOV gamma camera ranges between 4 and 20 minutes (144).

Therefore, using longer acquisition times will help the HGC while it is fitted with the 0.5 mm diameter pinhole, allowing it to record more counts while preserving a higher level of spatial resolution.

7.5   Conclusion

In this chapter, the HGC has been evaluated when fitted with two pinhole collimators interchangeably (0.5 mm and 1.0 mm in diameter) and utilising a novel anthropomorphic head and neck phantom. A qualitative node-detection observer (NDO) study has been designed and conducted. Two main phantom imaging datasets (96 data points each) were produced using both pinhole collimators through imaging simulated SLNs embedded in three different areas within the head and neck phantom at different imaging distances (4, 6, 8 and 10 cm) and varied acquisition times, ranging between 5 s and 120 s.

A customised JavaScript code was developed to randomise and display imaging datasets. Paired t-test evaluation has been performed on the normally produced distributed datasets. In general, the HGC was able to record good detection rates using the 1.0 mm diameter pinhole collimator. A 100 % detection rate of the simulated SLNs has been recorded in 25 % of the dataset produced using the 1.0 mm pinhole and an average of 3 out of 6 simulated SLNs were detected in 75 % of that dataset. While using the 1.0 mm diameter pinhole collimator, all simulated SLNs can be observed in 60 s acquisition time at 4 cm imaging distance whereas employing the 0.5 mm in diameter resulted in lower detection, as all simulated SLNs were visualised in 105 s scanning time at the same distance. The qualitative node-detection observer (NDO) study will be improved through involving more simulated SLNs groups (having higher radioactivity) and increasing the acquisition time to study the limitation of each pinhole collimator in more depth and compare the produced results with other gamma imaging modalities. Furthermore, the analysis method can be improved through acquiring gamma images for the simulated SLNs using the standard LFOV gamma camera to precisely determine the sensitivity and specificity against the routinely used procedure.

Chapter 8: The hybrid gamma camera performance in non-invasive routine scintigraphic imaging procedures: A clinical feasibility study

8.1   Introduction

Small field of view (SFOV) gamma imaging systems have undergone substantial technological development. However, these imaging systems have not yet been standardised for routine clinical and surgical practices. Some SFOV gamma cameras have passed the prototyping stage and are available commercially. Clinical evaluation studies for the majority of these SFOV gamma imaging systems are still in the feasibility study or pilot research stage.

SFOV gamma imaging systems can fill the technological gap arising in difficult scenarios, enabling scintigraphic imaging procedures to be performed in intensive care units, operating rooms, or outpatient care units (272). Furthermore, this technology may contribute towards more accurate surgical procedures by providing dynamic scintigraphic imaging of the affected tissues in intraoperative settings (141, 143, 273). The hybrid gamma camera (HGC), as previously discussed, is a handheld SFOV camera that is capable of providing gamma and optical images simultaneously.

The co-aligned configuration of the optical and gamma cameras may improve the outcome of the scintigraphic imaging procedures by providing the functional information and anatomical view of the radioactivity distribution within the examined area.

In this chapter, the results of our first clinical feasibility study using the HGC will be discussed. In this study, the HGC was used to perform non-invasive hybrid gamma-optical imaging procedures on patients attending their routine scintigraphic imaging appointments in a nuclear medicine clinic. The resultant hybrid and gamma images were subjectively evaluated to determine the appropriate areas to utilise the HGC in future medical work.

8.2 Methods and patient scanning

8.2.1 The hybrid gamma camera configuration

The HGC is a scintillator-based detector. The detector consists of an e2v CCD97 back-illuminated electron multiplying charge-coupled device coupled to a columnar scintillator (CsI[Tl]). This clinical feasibility study involved an evaluation of the HGC's clinical performance with 600 μm and 1500 μm thick scintillators installed. Gamma imaging was performed with two tungsten pinhole collimators with an acceptance angle of 60°, with pinholes 0.5 mm or 1.0 mm in diameter. More details about the HGC design are provided in Chapter 3.

8.2.2 Patient recruitment and imaging

As part of the performance evaluation of the HGC, patients were recruited for a comparative clinical study. This study was carried out with the support, and under the clinical supervision of our research group partners in the Nuclear Medicine Clinic at Queen's Medical Centre (QMC), Nottingham University Hospital's NHS Trust. This medical trial received ethical approval from Research and Innovation, Nottingham University Hospitals NHS Trust and the UK National Research Ethics Committee (Reference no. 12/EM/0201). For more details about the ethical approval, see appendix C, page no. 190.

In this feasibility study, patient participation was based on availability and suitability rather than targeting a specific procedure or condition. This was to ensure a broad range of nuclear medicine procedures could be investigated. The aim was to subjectively evaluate the capability of the HGC against conventional, routinely used gamma-imaging systems in the nuclear medicine department.

Patients who visited the Nuclear Medicine Clinic at QMC for routine scintigraphic imaging procedures were formally requested to participate in this clinical study (i.e. by providing written informed consent). The recruited patients underwent scanning using the HGC after being administered a radioactive material, and after having the scheduled scintigraphic imaging procedure in line with the ethical approval protocol (see appendix D, page no. 191). The HGC was used to acquire both hybrid optical-gamma and gamma images of the targeted area, and a subjective visual evaluation of the images produced by the HGC and the conventional gamma imaging systems was carried out for each medical case. This subjective evaluation was performed by nuclear medicine specialists, who are experts in evaluating gamma images for routine nuclear medicine procedures. The conventional gamma images produced in the Nuclear Medicine Clinic at QMC, which were included in this clinical feasibility study, were acquired by either a General Electric Discovery NM/CT 67 (GE Healthcare, Waukesha, Wisconsin, USA) or a Philips Brightview XCT (Philips Healthcare, Milpitas, California, USA). All clinical images were anonymised.

8.3   Results and discussion

This clinical study involved 31 patients undergoing a range of routine nuclear imaging procedures (age range: 30–83 years, age mean: 58.6 years). For these procedures, one of two radioisotopes were administered (^{99m}Tc and ^{123}I) either as a pure solution or as a labelled pharmaceutical agent for precise targeting, such as ^{99m}Tc-labelled hydroxydiphosphonate (HDP) for bone scintigraphy. A summary of the procedures investigated can be found in Table 8.1.

Table 8.1. Summary of observed medical cases, administered radioisotopes, delivered activities (MBq), and mean HGC acquisition time

Type of procedures	Radionuclide	Administered activity (MBq)	Acquisition time (mean ±SD) (s)	Number of participants
Bone scintigraphy	^{99m}Tc	600–627	266±55	3
DaTscan (Brain scan)	^{123}I	185	893±519	2
Lacrimal drainage scintigraphy	^{99m}Tc	1 per in each eye	263±87	3 (1 excluded)
Leukocyte scintigraphy	^{99m}Tc	100–225	345±200	2 (1 excluded)
Thyroid scintigraphy	^{99m}Tc	75–78	127±63	3
	^{123}I	18.5–20	297±98	5
Lymphoscintigraphy	^{99m}Tc	10–20 per injection site	349±105	12 (4 excluded)
Sentinel lymph node biopsy (SLNB)	^{99m}Tc	20.5	200	1

Various nuclear medicine procedures have been investigated including lacrimal drainage scans, lymphoscintigraphy, bone scintigraphy, thyroid scintigraphy, and DaTscan (a nuclear scanning procedure used to assess Parkinson's disease).

Two versions of the HCG were fitted with CsI(Tl) scintillators of two different thicknesses (600 µm and 1500 µm). Furthermore, both cameras were fitted with either a 0.5 mm or a 1.0 mm diameter pinhole collimator. While thin scintillators and narrow pinholes provided superior spatial resolution, a longer acquisition time was needed to obtain sufficient photon counts in the gamma images.

Table 8.2. List of clinical studies conducted using the Hybrid Gamma Camera (HGC)

Patient number	Type of procedure	Camera configuration		Subjective assessment of image quality
		Pinhole collimator diameter (mm)	scintillator thickness (mm)	
001	Bone scintigraphy	1.0	0.6	Poor
002		1.0	0.6	Poor
003		1.0	1.5	Poor
004	DaTscan (Brain scan)	0.5	0.6	Poor
005		0.5	0.6	Poor
006	Lacrimal drainage scintigraphy	0.5	0.6	NA[*]
007		0.5	0.6	Good
008		1.0	0.6	Good
009	Leukocyte scintigraphy	1.0	1.5	NA[*]
010		1.0	1.5	Poor
011	Thyroid scintigraphy	0.5	0.6	Poor
012		0.5	0.6	Poor
013		1.0	0.6	Good
014		1.0	1.5	Good
015		1.0	1.5	Good
016		1.0	1.5	Good
017		1.0	1.5	Good
018		1.0	1.5	Good
019	Lymphoscintigraphy	0.5	0.6	NA[*]
020		0.5	0.6	Good
021		0.5	0.6	Good
022		0.5	0.6	NA[*]
023		1.0	1.5	Good
024		1.0	1.5	Good
025		1.0	1.5	Good
026		1.0	1.5	Good
027		1.0	1.5	Good
028		1.0	1.5	Good
029		1.0	1.5	NA[*]
030		1.0	1.5	NA[*]
031	SLNB	1.0	1.5	Good

* Study terminated due to camera error

8.3.1 DaTscan studies

A DaTscan (brain scan: ^{123}I-ioflupane) was performed in the case of two patients using the HGC. Focal accumulation of radioactivity was not observed, particularly in the striatal region of the brain, in either case. In such cases, nuclear tomographic imaging is routinely requested; however, the HGC is not designed to provide tomographic imaging, which may limit the clinical usefulness of the HGC in this type of procedure. However, some preclinical studies reported the possibility of using a single head SFOV gamma camera for ^{123}I-ioflupane brain scanning (274, 275). In these studies, the SFOV gamma camera was combined with a mechanical structure to enable tomographic imaging by offering 180° rotation during the gamma image acquisition (274).

Furthermore, positioning a SFOV gamma camera to image the striatum is a laborious task, and this makes it difficult to use SFOV gamma cameras for localisation, or as an exploratory tool, during deep brain stimulation (DBS) surgery in the presence of customised stereotactic localisation tools and preoperative 3D computed tomographic scanning (276-278). The use of SFOV gamma cameras to provide intraoperative imaging guidance during DBS surgery has not been reported in the available literature.

It is worth mentioning that some research has shown that planar vertex view scanning could help to provide gamma images, that can be used for diagnosis purposes, with a short acquisition time (i.e. 5 minutes), using an LFOV gamma camera. Such a technique provided promising results in the diagnosis of Parkinson's disease. It was found that this imaging technique benefited the diagnostic plan as an alternative choice in situations where patients could not tolerate the long acquisition time (i.e. 32 minutes) of SPECT imaging (279).

8.3.2 Thyroid and parathyroid scintigraphy

Scintigraphy is the gold standard for functional imaging evaluation of the thyroid gland. The thyroid gland is assessed in nuclear medicine departments using two methods. First, a thyroid scan is performed to spot lumps, hyperthyroidism, and thyroid inflammation (thyroiditis). The second test is an iodine uptake scan that is performed to evaluate

thyroid function, identify the cause of abnormal levels of thyroid hormone, and assess patients with proven thyroid cancer (280).

8.3.2.1 Diagnostic scanning for the thyroid gland

In this study, four thyroid patients were recruited. Patients were injected with either ^{99m}Tc or ^{123}I based on the medical investigation. Figure 8.1 shows images produced by the HGC and LFOV gamma camera of a thyroid patient administrated with ~20 MBq of ^{123}I. During this acquisition, the HGC was fitted with a 600 μm thick CsI(Tl) scintillator and a 1.0 mm diameter pinhole collimator. A subjective evaluation of the images from the HGC and the LFOV gamma camera indicate good agreement in terms of the pattern of radioactivity accumulation. In both gamma images, a focal tracer uptake was reported in the right lobe of the thyroid with no uptake in the left lobe (Figure 8.1 A and B). Optical guidance for the accumulation site was provided by the hybrid imaging facility using the HGC (Figure 8.1 C).
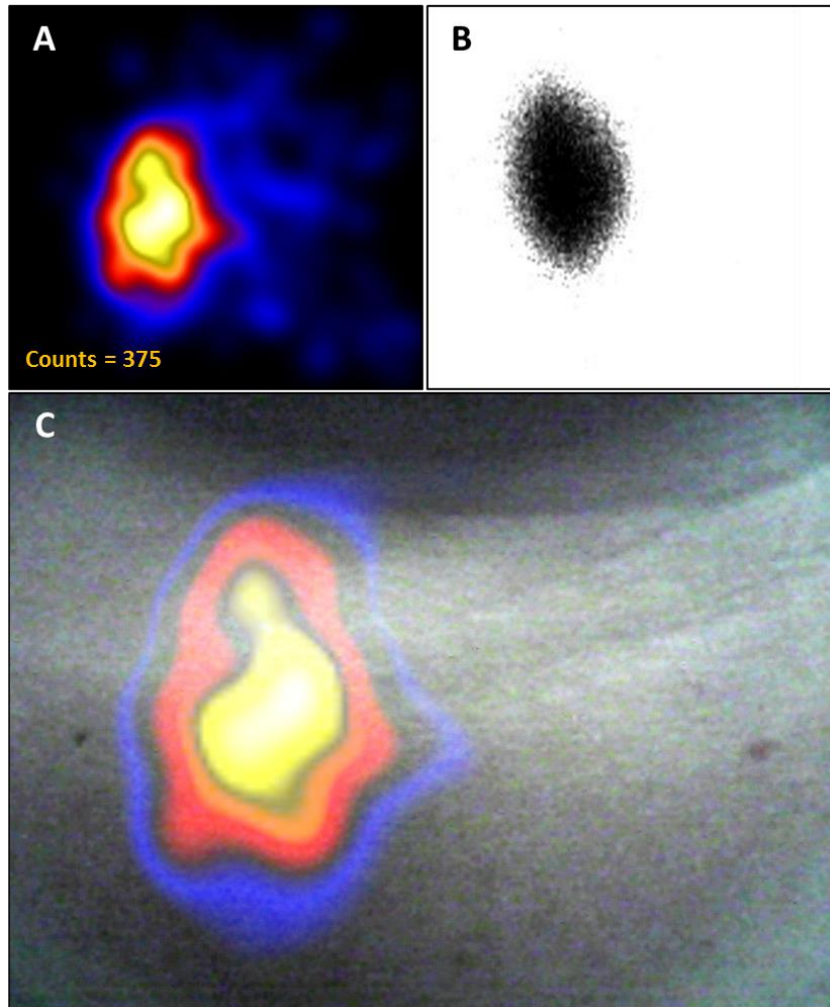
Figure 8.1. Thyroid anterior gamma and hybrid images acquired using the HGC (A and C) and conventional LFOV gamma camera (B). The acquisition time for both gamma images was 300 s; these images were acquired 110 min after administration of the radioisotope. (Case study no. 013)

Figure 8.2 shows thyroid scintigraphic images obtained using the HGC and LFOV gamma camera. The patient was administered with ~18.5 MBq of ^{123}I. Anterior gamma scanning was performed with the HGC fitted with a 1500 µm thick CsI(Tl) scintillator and a collimator with a pinhole of diameter 1.0 mm. Both gamma images show focally increased tracer uptake in the right lobe, and in the left upper pole, medial side, of the thyroid. The thyroid gland's shape, size, and the agreement of the activity distribution between both gamma images show the capability of the HGC as a functional imaging tool in such cases. However, a larger study population is needed to confirm this observation.
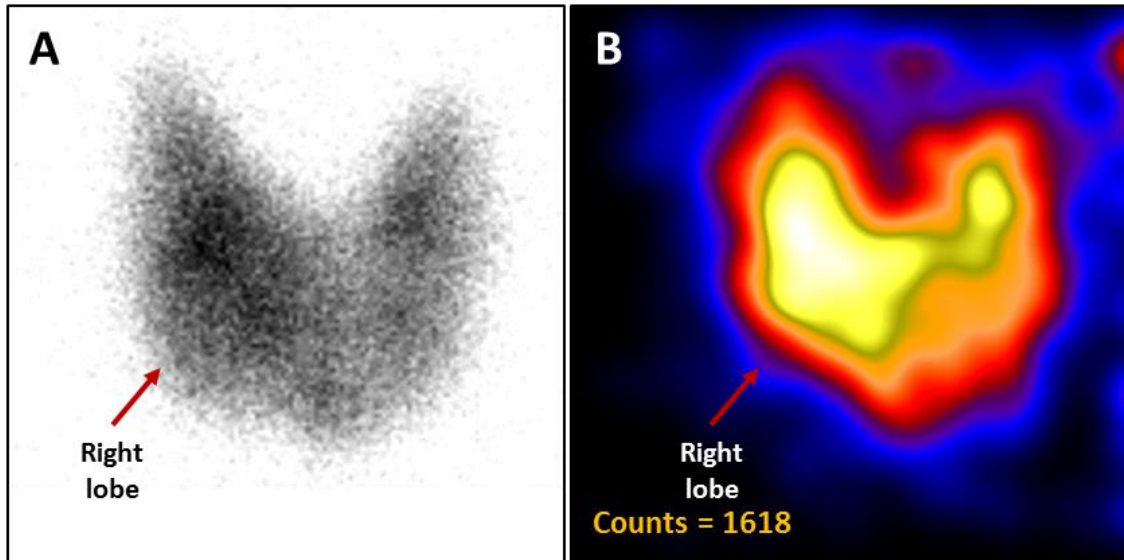
Figure 8.2. Anterior view gamma images for the thyroid gland, after ~18.5 MBq of ^{123}I solution was administrated intravenously; images were acquired using the LFOV gamma camera (A) and HGC (B). The acquisition time for both resultant gamma images was 300 s. (Case study no. 014)

8.3.2.2 Parathyroid and thyroid glands surgery

The treatment of primary hyperparathyroidism is exclusively based on surgical intervention (i.e. parathyroidectomy). Intraoperative gamma probes and ultrasonic scanning are used to localise the abnormal sites during minimally invasive parathyroidectomy procedures. However, in cases of ectopic parathyroid glands, parathyroid hyperplasia, or intrathyroidal glands, the sensitivity of gamma probes and ultrasonic guidance is degraded (281). Several reports of surgical trials claim that the use of intraoperative SFOV gamma imaging systems leads to a recognisable improvement in localising abnormal tissues of the parathyroid glands (143, 281, 282). An evaluation of concordanced information from the intraoperative gamma camera findings, pre-surgical diagnosis, parathyroid hormone (PTH) readings, and surgical findings showed that the intraoperative scintigraphic imaging findings were in agreement with the findings of surgical procedures and pathological tests (282).

Some surgeons have reported that such imaging technology could completely replace the use of intraoperative gamma probes in minimally invasive parathyroidectomy procedures. These findings could improve the management of minimally invasive surgical procedures in "difficult" situations.

During our clinical trial, patients undergoing parathyroid scintigraphy were not available for recruitment. However, a simple simulation of a parathyroid scan was carried out using the head and neck phantom and bespoke thyroid gland phantom (see Chapter 6 for more details). Four micro Eppendorf vials (0.2 ml) were used to simulate the parathyroid glands, and these simulated glands were attached to the back wall of the thyroid phantom. Four different ^{99m}Tc activity concentrations were chosen to simulate the parathyroid glands (1 to 4 MBq), and the simulated thyroid gland was filled with 10 MBq of ^{99m}Tc solution (Figure 8.3). Using the HGC fitted with 1500 µm thick CsI(Tl) scintillator and pinhole collimators (0.5 mm and 1.0 mm diameter pinholes), the resultant gamma images showed potential for detecting parathyroid glands with different activity concentrations over a reasonable acquisition time. Recruiting patients with parathyroid gland symptoms to undergo scanning using the HGC would help confirm these assumptions.
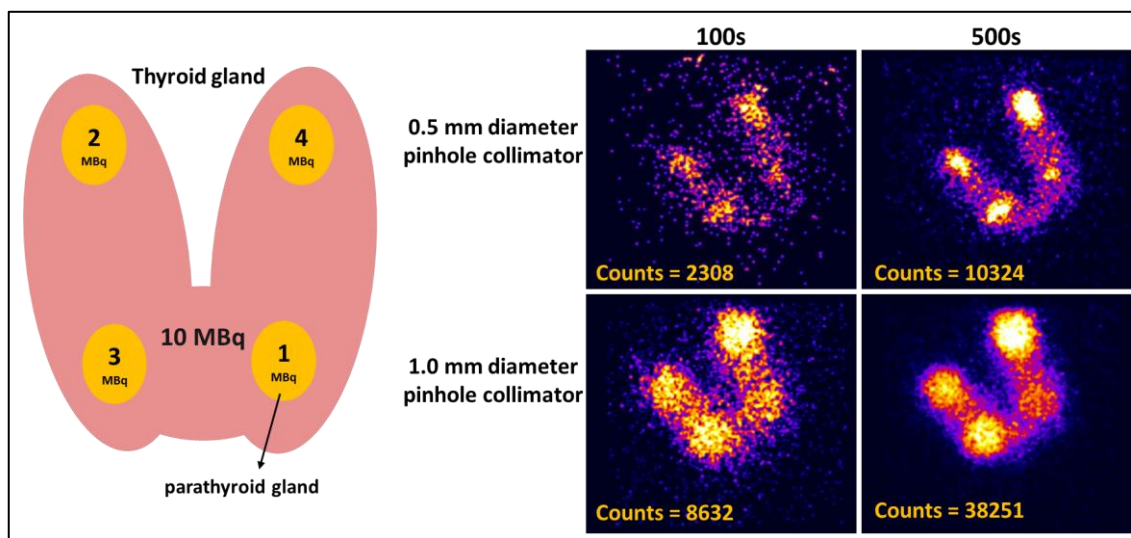
Figure 8.3. Left-hand side: A schematic diagram showing the position and amount of radioactivity in the simulated thyroid and parathyroid glands. Right-hand side: Four gamma images acquired at two different acquisition times (100 s and 500 s) using the HGC with exchangeable 0.5 mm and 1.0 mm diameter pinhole collimators.

The HGC could make a beneficial contribution to thyroid gland surgical procedures. The hybrid optical-gamma imaging facility of the HGC can help to provide definite anatomical information about the activity accumulation site (Figure 8.4). Hybrid imaging of the radioactivity distribution at different distances using the HGC could help screen the adjacent tissues in the neck region and facilitate precise localisation of the site of abnormality. Furthermore, the HGC could be located closer to the targeted site to provide hybrid images of the affected tissues intraoperatively (Figure 8.4 A). This hybrid imaging technique could be beneficial in localising potential SLNs intraoperatively in critical head and neck surgical procedures, such as thyroid cancer surgery.

A surgical study claimed that an SFOV gamma camera helps improve the localisation and characterisation of small nodules in the thyroid gland. Owing to the superior spatial resolution provided by the SFOV gamma camera as compared to the conventional LFOV gamma camera, the SFOV gamma camera is able to detect small thyroid nodules (<10 mm in diameter), which are usually not easily distinguished from the surrounding healthy tissues in conventional thyroid scintigraphic images (283).

Surgical studies on parathyroid and thyroid glands with intraoperative gamma imaging are still in the preliminary stages; however, this technology is attracting increasing attention.
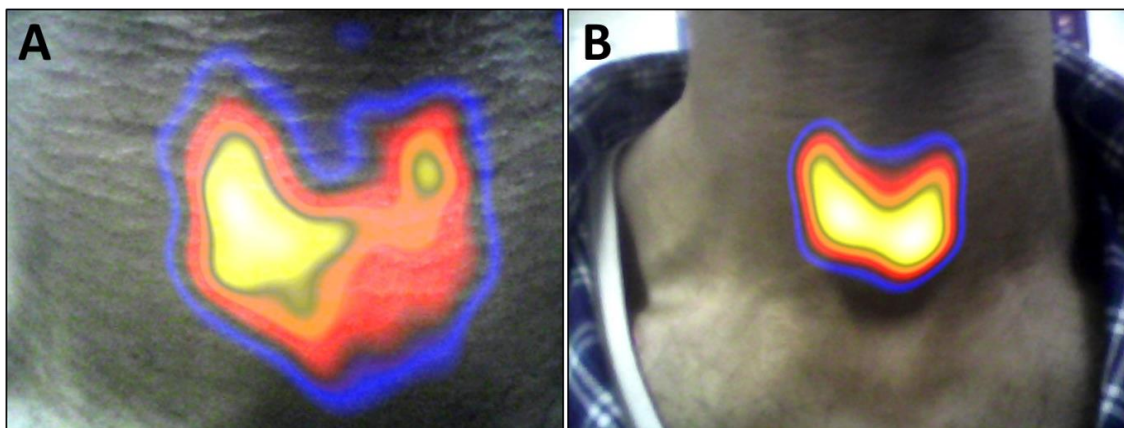
Figure 8.4. Hybrid optical gamma images of the thyroid gland, after administration of ~18.5 MBq of ^{123}I solution intravenously, acquired using the HGC for 300 s acquisition time at ~8 cm (A) and ~17 cm (B) collimator-to-skin surface distance. (Case study no. 014)

8.3.3 Bone scan and leukocyte studies (white blood cell scan)

Three bone scans and two leukocyte scans were carried out (Table 8.2). The bone scanning procedure was restricted to the patients' hands. The gamma images show the accumulation of the injected radioactive agent in the patients' hands. Figure 8.5 (A) shows an example of the gamma image of the bone scan of the patients' fingers. This gamma image was acquired approximately 3 hours after administering the ^{99m}Tc-HDP solution. The HGC was fitted with a 1.0 mm diameter pinhole collimator and placed ~45 mm above the patient's thumb. However, these gamma images were not sufficient to claim the potential usefulness of the HGC in such cases because of the lack of focal accumulation at these sites in the recruited patients.

An important point to consider is that SFOV gamma cameras could be used for osteitis detection in patients with diabetic foot and those requiring osteoid osteoma excision (284). Osteoid osteoma appears as a focal uptake in bone scans, and the osteomas can be surgically removed under the guidance of SFOV gamma cameras. The use of a high resolution handheld gamma imager during osteoid osteoma surgery has been reported (284).

A SFOV gamma camera with a gamma probe shows definite advantages over a non-imaging gamma probe alone, namely faster and more precise detection of osteoid osteomas than with the non-imaging gamma probe when an osteoid osteoma is found close to a potential site of radiation accumulation such as the urinary bladder. Furthermore, an intraoperative gamma imaging system can clearly illustrate the presence of a double-nidus osteoid osteoma and help assess resection completion (284). Therefore, recruiting more patients with osteoid osteoma in the future should be attempted to evaluate the capability of HGC in detecting these kinds of bone abnormalities.
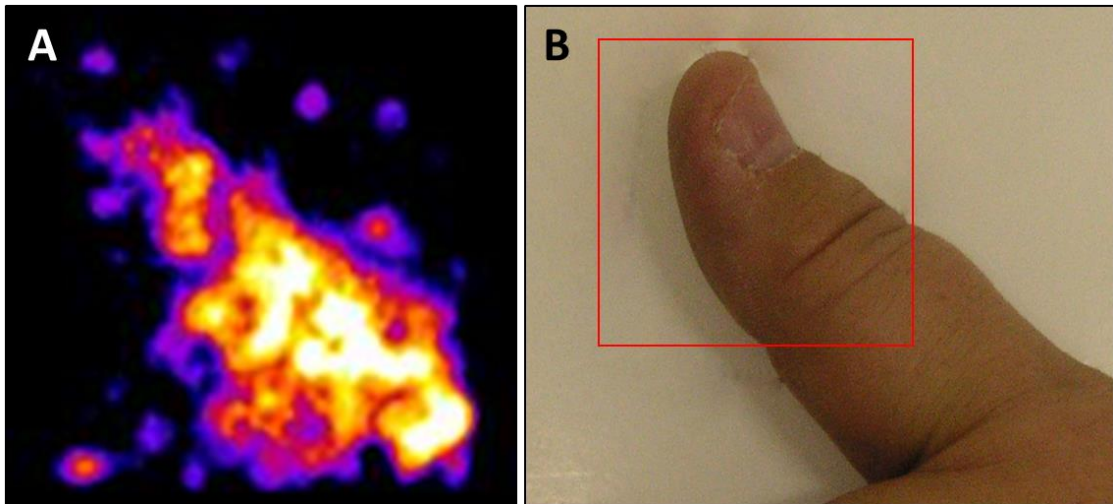
Figure 8.5. (A) HGC gamma image of ^{99m}Tc-HDP distribution in the thumb of a patient previously administered ^{99m}Tc-HDP; acquisition time ~16.6 min. (B) Optical image shows the targeted area. (Case study no. 001)

Two patients underwent leukocyte scintigraphy in this feasibility study (Table 8.2). One patient was not scanned due to a technical problem with the HGC system. The other patient was imaged with the HGC fitted with a 1500 μm thick CsI(Tl) scintillator and a 1.0 mm diameter pinhole collimator; however, no focal accumulation was observed. This could be justified by the lack of knowledge about the position of the focal accumulation reported after the LFOV gamma camera imaging procedure. The use of SFOV gamma cameras for performing leukocyte scintigraphy needs further clinical investigation to evaluate the definite diagnostic contribution of this technique.

8.3.4 Lymphoscintigraphy

Seven lymphoscintigraphy scans were investigated in this trial. These cases included patients suffering from oedema. It was difficult to trace the flow of activity along the lower extremities owing to the low sensitivity of the HGC as compared to the conventional gamma camera and the difficulty in using the HGC to image the patients' legs at different orientations. However, the HGC was able to provide gamma and hybrid images for the injection site (i.e. between toes) for all imaged cases, confirming its ability to show focal accumulation corresponding to anatomical landmarks on the patient's skin surface (Figure 8.6).
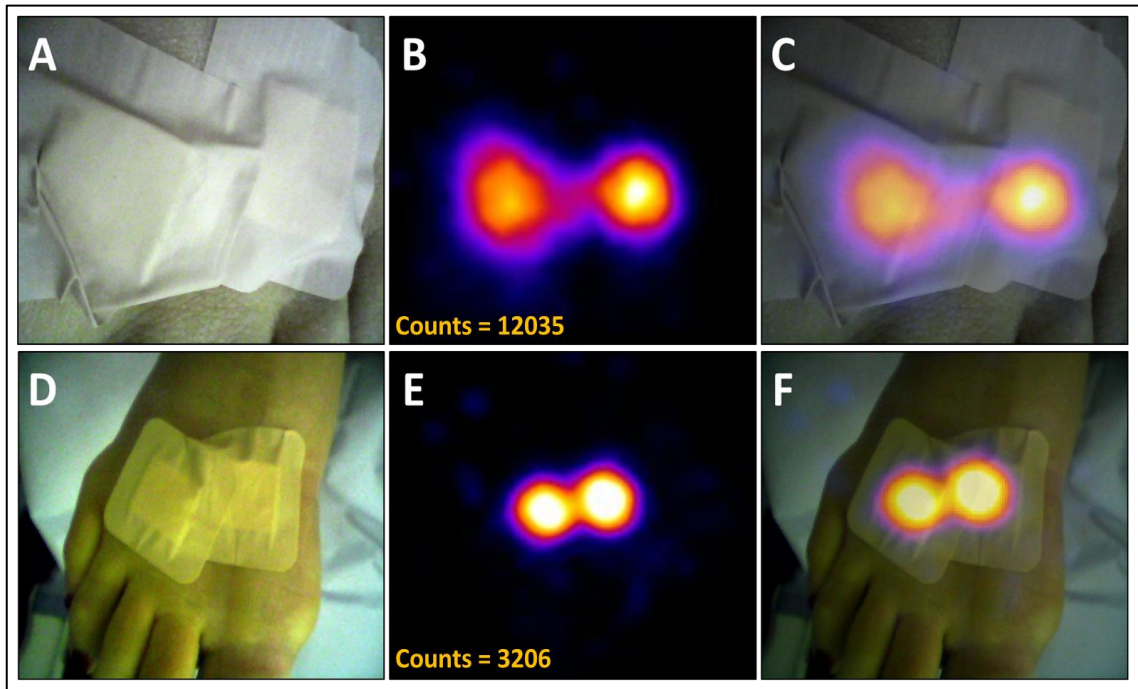
Figure 8.6. Optical (left), gamma (centre), and hybrid (right) images of the injection site during investigation of lymphoscintigraphy scans acquired in 300 s acquisition time at ~8 cm (A, B, C) and ~15 cm (D, E, F) collimator to skin surface distance. (Case study no. 019)

The HGC was able to localise focal uptakes in the left inguinal region. Figure 8.7 shows two gamma images produced using a conventional LFOV gamma camera with a 17 min acquisition time (Figure 8.7 A) and the HGC with a 5 min acquisition time (Figure 8.7 B). These gamma images show good agreement in terms of focal tracer uptake detected by the HGC and LFOV gamma camera. This observation suggests the possibility of using the HGC intraoperatively during surgical management of inguinal SLNs corresponding to different malignancies such as melanoma.
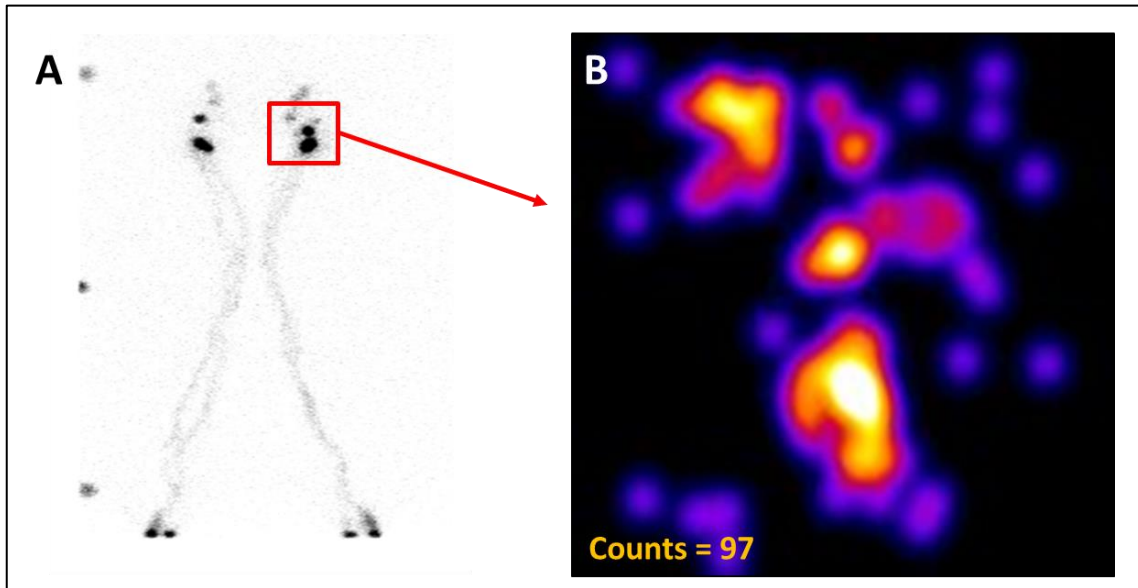
Figure 8.7. (A) Anterior LFOV gamma image of the lymphoscintigraphy scan of the patient's lower extremities (17 min acquisition time). (B) The HGC gamma image of the left inguinal region shows focal uptake with 5 min acquisition time. (Case study no. 022)

8.3.5 Sentinel lymph node biopsy (SLNB)

Promising initial results have been collected recently for a melanoma patient using the HGC. This melanoma patient was assigned to SLNB procedures and the produced images were acquired preoperatively (Figure 8.8). These gamma and hybrid images show the capability of the HGC to follow the drainage of the lymph and localise a potential SLN in the inguinal region. Within a short acquisition time (~ 3 mins), the HGC was able to provide a distinct gamma image at 16 cm imaging distance, which reflects the usefulness of such a system as it can provide a relatively large field of view and a good level of detection.
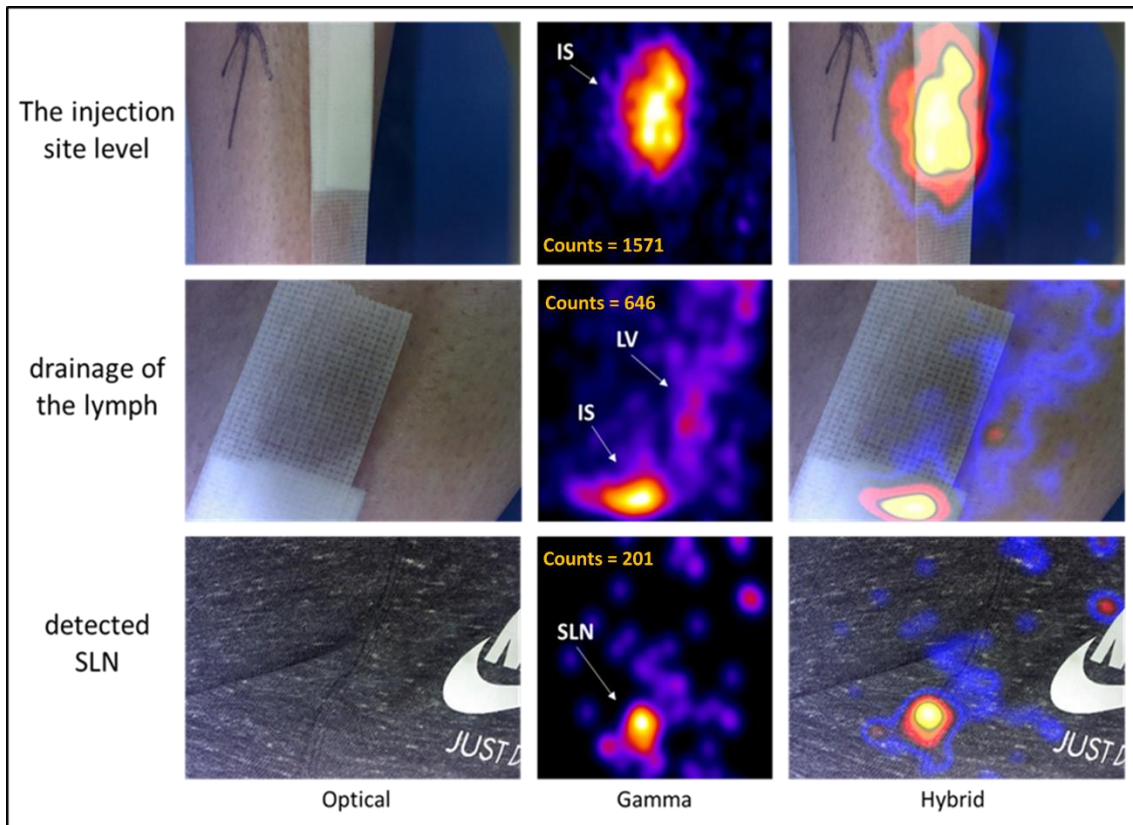
Figure 8.8. Optical, gamma and hybrid images obtained for a melanoma patient acquired in 200 s. Upper raw images showing the administrated radioactivity site in the patient's left leg (20.5 MBq of ^{99m}Tc nanocolloids) acquired at an 11 cm imaging distance, middle raw images representing the drainage of the lymph acquired at a 9 cm imaging distance, and lower raw images showing the detected SLN (left inguinal region) at 16 cm imaging distance. (Case study no. 030)

8.3.6 Lacrimal drainage scintigraphy

Lacrimal drainage scintigraphy is a non-invasive, diagnostic nuclear medicine procedure carried out to investigate the patency of the lacrimal drainage ducts. It can also be used in cases of dry eye syndrome to evaluate tear flow (285). Furthermore, this test can be employed to assess tear ducts during pre- and post-operative clinical evaluation during eyelid surgery (i.e. blepharoplasty cases) (286).

The conventional LFOV gamma camera and the HGC were used to image the gamma emission in the lacrimal scintigraphic scans of three patients. For these scans, 1 MBq of ^{99m}Tc-pertechnetate was administrated in each eye. The radioactive solution was

administered as a single drop released through a micropipette placed on the lateral canthus of both eyes of the patients. A head support metallic frame fitted with a chin rest and a head strap was used to position the patient's head to minimise the effect of body movement. Figures 8.9 and 8.10 show the gamma and hybrid images obtained using both gamma cameras. The images obtained by the HGC (200 s acquisition time) clearly show activity clearance from the nasolacrimal duct to the nasal cavity (Figure 8.9 B and C). It can be seen that the distribution of the radioactivity solution is different in the gamma images obtained by the HGC and LFOV gamma camera as a result of lacrimal clearance by blinking and the time gap between imaging procedures (Figure 8.9 B, D and E).
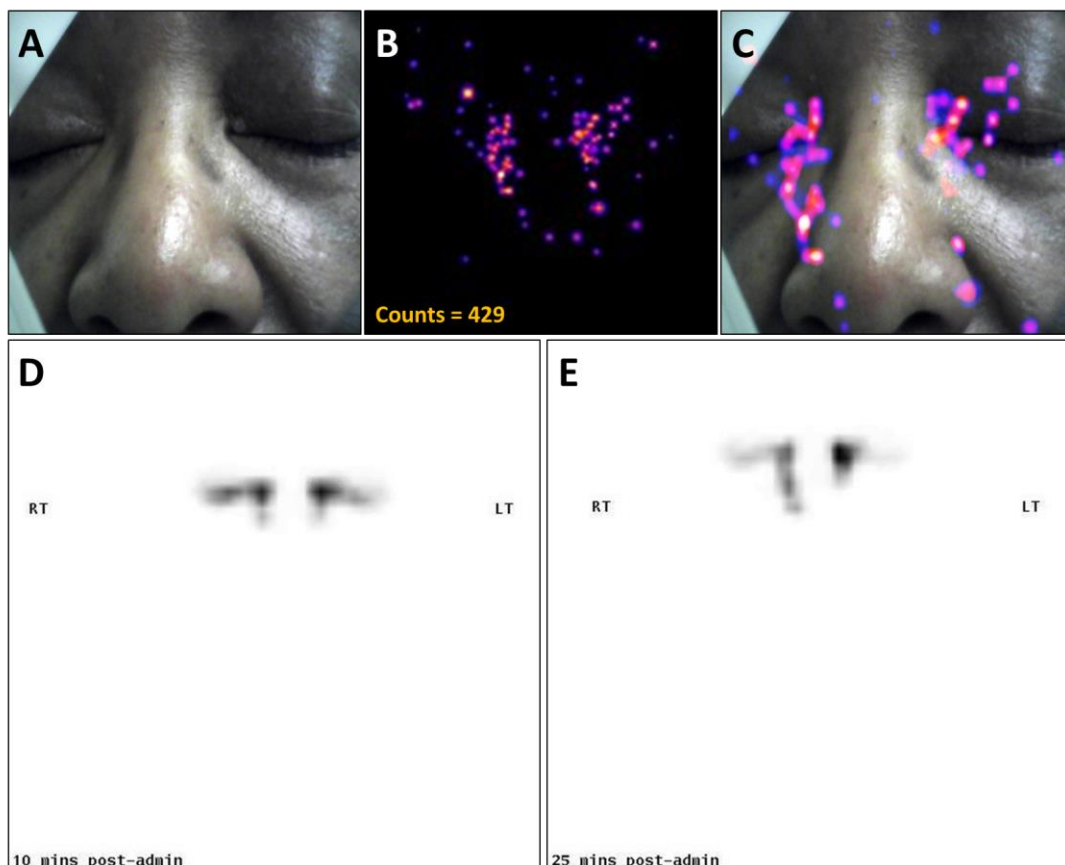
Figure 8.9. (A, B, C) Optical, gamma, and hybrid images for the lacrimal drainage system using the HGC fitted with a 600 µm-thick CsI(Tl) scintillator and a 0.5 mm-diameter pinhole collimator (200 s acquisition time). (D, E) Gamma images of the lacrimal drainage ducts of both eyes obtained by the conventional LFOV gamma camera at 2 time intervals after activity administration (i.e. 10 and 25 min after administration). (Case study no. 007)
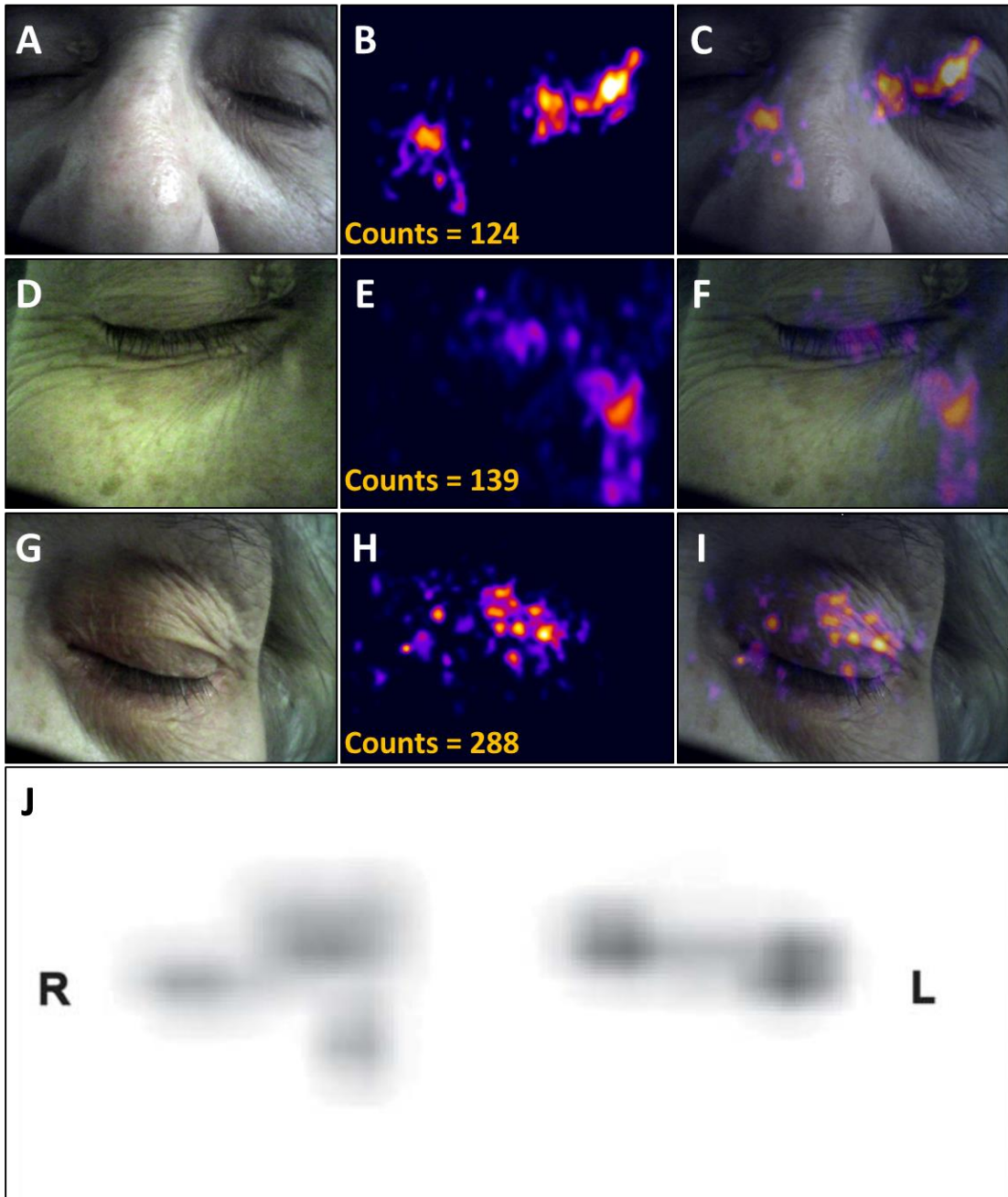
Figure 8.10. Optical, gamma, and hybrid images for both eyes acquired using the HGC at ~10 cm collimator-to-skin surface distance (A, B, C) and for each eye at ~5 cm collimator-to-skin surface distance (D-I); the acquisition time for the HGC was 300 s. (J) A gamma image of the lacrimal drainage ducts of both eyes produced by the LFOV gamma camera. (Case study no. 008)

Figure 8.10 shows good agreement between the images produced by the HGC and the conventional LFOV gamma camera. A functional impedance to the flow situation (i.e. duct stenosis) is clearly seen in the left eye as the radioactive solution accumulated in the medial canthus but failed to drain through the nasolacrimal duct into the nasal cavity (Figure 8.10 H, I, and J). The hybrid optical-gamma imaging facility can help localise the obstruction by the superimposition of the gamma image onto the anatomical optical image (Figure 8.10 C, F, and I). This technique will allow precise evaluation of the lacrimal duct's patency in pre-, intra-, and post-operative situations, leading to more robust diagnostic and therapeutic procedures.

8.4 Conclusion

In this feasibility study, the first clinical results of medical hybrid gamma and optical imaging using the HGC have been reported. The HGC was used to evaluate several assigned clinical cases in the nuclear medicine department, Queen's Medical Centre (QMC), University of Nottingham. This study involved various medical procedures, such as thyroid scintigraphy, lymphoscintigraphy, and lacrimal scintigraphy. The HGC showed good potential in imaging the thyroid gland, lacrimal drainage ducts, and lymphatic tissues in an acquisition time similar to that of conventional gamma imaging procedures. The HGC fitted with a 1500 µm thick CsI(Tl) scintillator is preferable for clinical use owing to its sensitivity enhancement. The exchangeable pinhole collimators (i.e. 0.5 mm and 1.0 mm in diameter) provide good flexibility as the operator can adjust the pinhole collimator to meet the technical and clinical needs for any assigned gamma imaging procedure.

The optical imaging feature of the HGC had a positive impact on the clinical imaging procedures carried out in this study, as it provided the anatomical context of the targeted area. Hybrid imaging using the HGC can provide valuable information about the location, shape, and activity distribution in the affected regions in pre-, intra- or post-operative clinical settings. Furthermore, the size of the HGC and its flexibility could help surgeons enhance their invasive surgical techniques in cases such as cancer surgeries, as the HGC can facilitate precise localisation of the primary site of the cancer

and the surrounding tissues. Such technology could help surgeons reduce the need to sacrifice marginal healthy tissues, which would in turn improve the outcomes of surgical interventions, including minimising the effect of surgery on the patients' quality of life.

Clearly, larger cohorts of patient populations should be recruited in the future for more in-depth clinical evaluation of the efficacy of the HGC. Future studies should consider conducting comparative, objective, and qualitative evaluations of the efficiency of the HGC in routinely performed procedures in nuclear medicine. Additionally, research involving therapeutic cases at nuclear medicine departments has the potential to determine the possibility of using the HGC for treatment evaluation including drug uptake in the targeted tissues. Hence, further investigations on the intraoperative use of the HGC should be considered in future. It is worth mentioning that restricted access to the recruited patients' data, including their medical reports and acquired planar and SPECT gamma images limited the possibility of quantitative comparisons between the HGC and routinely used gamma imaging systems in clinical settings.

Chapter 9: Conclusions

9.1 Research Summary

The Hybrid Gamma Camera (HGC) has been designed and manufactured to facilitate various diagnostic nuclear medicine procedures with superior spatial resolution imaging. The research work presented in this thesis has considered the capability of the HGC to image various tissues and organs with different radioactivity concentrations in targeted regions around the human body in both experimental and clinical settings.

Two generations of the HGC (i.e. 0.6 mm and 1.5 mm thick columnar CsI(Tl) scintillators) have been used and evaluated during this research. Furthermore, the performance of the HGC has been tested with two different pinhole collimators (i.e. 0.5 mm and 1.0 mm in pinhole diameter). The HGC is co-aligned with an optical imaging system, providing real-time hybrid optical-gamma imaging. The functionality assessment of such an imaging system can only be achieved by utilising medical phantoms and employing that system in clinical trials.

In this thesis, various assessment protocols have been performed using different bespoke phantoms simulating clinical scenarios. Several simulation techniques and different lymphoscintigraphic and anthropomorphic phantoms have been designed, manufactured and utilised to validate the capability of the HGC in lymphatic system and small organ imaging. Furthermore, the HGC has been tested on patients during routine gamma imaging procedures in nuclear medicine clinics. Quantitative and qualitative evaluations of the HGC imaging system were conducted; these tests were used to explore potential uses and improve technical and practical aspects of the HGC.

The implementation of the quantitative and qualitative assessments carried out during the work include in this thesis provides the knowledge necessary to make the HGC suitable for challenging medical scenarios, which will aid enhancement of patient management during intraoperative or routine gamma imaging procedures.

The ability of the HGC to detect deep-situated sentinel lymph nodes (SLNs) and those nodes located near the injection site of radioactivity have been intensively investigated. The presented results have illustrated that the HGC is able to resolve SLNs from the injection site, for a different range of radioactivity concentrations and depths, which indicates that using this camera could improve the detection rate of these challenging, potential SLNs that are difficult to localise and isolate using non-imaging gamma probes.

This research work indicates that of the two columnar CsI(Tl) scintillators thicknesses used, the 1500 μm scintillator is the suitable choice for clinical use. While the HGC was fitted with the 1500 μm scintillator, the measured contrast-to-noise ratio (CNR) values were recognisably improved, i.e. the HGC can detect simulated SLNs with low radioactivity accumulations (<0.1 MBq). During the scanning of the lymph-node contrast (LNC) phantom, the HGC fitted with the 1500 μm thick scintillator has a poorer spatial resolution compared to the 600 μm thick scintillator; however, the change in spatial resolution (~ 10 %) was relatively small compared to the change in detectability (> 52 % difference at 40 mm depth in 60 s acquisition time).

The HGC showed poor performance while it fitted with the 0.5 mm diameter pinhole collimator in localising deep-seated low activity simulated SLN (i.e. 40 mm depth); this is due to the large depth of the SLNs and the low sensitivity of the HGC while it fitted with the 0.5 mm diameter pinhole collimator, even with the thicker CsI(Tl) scintillator and long acquisition time (i.e. 240 s). This an essential issue, and it needs to be improved to provide rapid, sensitive, precise gamma imaging as would be required intraoperatively. These findings suggest that using an even thicker columnar CsI(Tl) scintillator may be beneficial for SLN mapping while preserving suitable spatial resolution levels. This should be explored in future work.

The tremendous advances of computer-aided design technologies along with the improvement of three-dimensional (3D) printing machines have expedited the process of designing and manufacturing cost-effective anthropomorphic medical phantoms that can represent a specific abnormality or mimic the complex structure of a targeted region within the human body in micro- and macro-architecture scales. An anthropomorphic simulated normal adult thyroid gland was designed and 3D printed in-house. The 3D printed thyroid gland and simulated SLNs were attached to a bespoke internal jig inserted into a head and neck phantom. This phantom was utilised during the quantitative and qualitative assessment of the HGC's capability to detect SLNs and image small organs. The presented work shows the flexibility of the phantom for imitating different nuclear medicine procedures and abnormal scenarios in the head and neck region. The anatomical accuracy of its parts allows validation of the qualitative assessment protocol for head and neck lymph nodes imaging and helps investigate the capability of using the HGC in thyroid gamma imaging procedures.

The standardisation of such test protocols, presented in this thesis for small field of view (SFOV) gamma cameras, will aid collection of further data across various medical centres and research groups for performance comparison purposes. In addition, it will contribute towards a technical baseline for scientists and SFOV gamma imaging systems' developers to consider when assessing their SFOV gamma imaging systems. The availability of phantoms that can provide an accurate anthropomorphic physical simulation for a specific part or organ within the human body would help to precisely judge the capabilities of a medical imaging device before proceeding to the process of recruiting patients, and, at the same time, these phantoms can be used to evaluate the impact of any technical modification on an existing medical imaging modality. Further investigation into the use of bespoke phantoms and their fabrication using 3D printing technology would be an interesting area of research with the potential to improve the efficiency of SFOV imaging.

This thesis reports the clinical results utilising the HGC. By employing the HGC during various routine nuclear medicine procedures, it shows promising outcomes in cases such as thyroid scintigraphy and lacrimal drainage scintigraphy. Moreover, the

presented gamma images show the ability of the HGC to localise focal uptakes (i.e. potential SLNs) in the inguinal region with good agreement in terms of focal tracer uptake with the conventional gamma imaging system. This observation suggests the possibility of using the HGC intraoperatively during surgical management of inguinal SLNs corresponding to different malignancies such as melanoma. Expanding the clinical trial by recruiting more patients is important to evaluate the capabilities of the HGC in each specific nuclear medicine procedure in more depth; moreover, increasing the examined population will facilitate the validation and standardisation of specific scanning protocols to use with SFOV gamma imaging systems.

9.2   Future work

Currently, technological improvements and research opportunities covering the whole spectrum of medical imaging modalities aim to enhance patient management and improve diagnosis and prognosis for challenging medical cases, e.g. cancer patients. SFOV gamma imaging systems are considered a suitable solution that can provide valuable information about the targeted region within the human body for challenging cases or during critical surgical procedures.

Therefore, there are many potential research areas to explore while studying the HGC, in addition to various aspects that can be expanded in the existing research work. In this section, four proposed areas of further study are illustrated.

9.2.1 Phantoms and test objects

The availability of 3D printing machines and advanced software technology that can extract the anatomical details of any targeted tissues or organs from the available medical images produced using various medical imaging modalities (such as CT and MRI scanners), making it possible to construct accurate anthropomorphic 3D phantoms that can be used for testing different medical imaging devices.

In this thesis, a 3D-printed normal adult thyroid gland is presented and used to evaluate the capabilities of the HGC in handling thyroid imaging procedures. The design of this phantom can be improved to imitate specific thyroid abnormalities including

hyperthyroidism and hypothyroidism. Furthermore, this 3D-printed anthropomorphic thyroid gland phantom can be improved to include a range of thyroid cold and hot nodules; simulating this nodule will help to quantitatively and qualitatively evaluate the HGC imaging behaviour in such cases for comparison with other competitive or routinely used gamma imaging modalities for thyroid scanning procedures.

At the time of writing this thesis, the thyroid phantom is currently being used to assess the possibility of employing the HGC in scanning iodine (^{131}I) sources during the monitoring stage of thyroid therapeutic procedures in hyperthyroidism or thyroid cancer patients. Along with the anatomical accuracy of this phantom, using it for such testing is preferable as it is a well-sealed, easy-fill container that can provide secure isolation of the inserted radioactive material from the surrounding environment, and can be safely stored, while using relatively long half-life isotopes (i.e. ^{131}I half-life = 8.02 days).

During this research, an anthropomorphic breast phantom has been designed and constructed to be utilised in testing and optimising the use of the HGC in breast cancer management procedures. This fillable breast phantom can be used with different sizes and shapes of inserts to mimic primary sites of a tumour and potential SLNs. Several experiments have been conducted utilising the breast phantom through simulating a range of radioactivity concentrations and abnormal conditions. The preoperative radioactive seed localisation (RSL) procedure has been simulated using the breast phantom. This increasingly used technique enhances the localisation process by embedding an iodine-125 seed (^{125}I) into a non-palpable breast lesion preoperatively (287).

Initial observations were encouraging enough to suggest an extended experiment with more in-depth analysis to show the required acquisition time needed to detect a range of ^{125}I seeds having various radioactivity concentrations at different depths with the phantom. Furthermore, a comprehensive characterisation of the HGC using ^{125}I seeds and the anthropomorphic breast phantom will pave the way to employ the HGC to localise these radioactive seeds during the surgical resection of non-palpable breast lesions.

9.2.2 Preclinical and clinical evaluation

Using the HGC for preclinical imaging purposes is a potential area of research. This could provide accurate localisation of the radioactivity distribution within examined mice using two modes of imaging — gamma and hybrid optical gamma imaging. The HGC is proposed to precisely localise radioactivity accumulations in vivo and in vitro.

Validating the possibility of using the HGC in preclinical studies by increasing the number of mice, and growing different types of tumour, will broaden the horizon of using the HGC. Furthermore, it could be a potential tool to study drug delivery in preclinical studies. In-depth research should be carried out to evaluate the appropriate scintillator thickness and pinhole collimator's diameter to fit this purpose.

Using the HGC in clinical settings should be expanded by utilising the HGC intraoperatively. Promising initial results have been collected recently for melanoma patients using the HGC (see chapter 8). These results reflect the usefulness of such a system as it can provide a relatively large field of view and a good level of detection. Confirming the usefulness of the HGC in the detecting, localising and isolating process of SLNs in surgical settings is one of the agreed steps that will be conducted in future. However, more work should be planned and conducted including finding a surgical partner who would like to test the HGC in surgical settings. Performing a surgical study of this kind may need an intensive training course for the surgeons or surgical care practitioners to provide them with the essential aspects about the system's performance, how to handle it and the process of acquiring and analysing gamma and hybrid images. It is worth mentioning that introducing such a system to the surgical theatre may require some modification on the existing system to meet the requirements of CE marking (certification mark). Furthermore, various quality assurance tests and comprehensive documentation for the HGC system need to be conducted and prepared as a mandatory requirement to apply for ethical approval.

9.2.3 Technical improvement

There are many technical aspects that can be investigated and improved. Designing, manufacturing and testing a commercial model of the HGC (including the selection of a hygienic outer shell material, designing a multi-joint supporting arm, and surgical-friendly materials) is a mandatory task that needs to be conducted in future. The HGC collimators' design is a potential area to conduct further research, as the effect of using different pinhole sizes to provide rapid gamma imaging or more precise preclinical imaging needs to be investigated. Furthermore, investigating other types and thicknesses of scintillators is an existing research field to improve the performance of the HGC (173). Coupling the scintillator with the CCD is an important aspect to consider, as an effective coupling could improve the overall system performance including the energy resolution.

Moreover, The HGC needs to be tested in realistic environments to evaluate the capability of the cooling mechanism, assuming that the HGC system can be used in warm places or run for a few hours continuously. Furthermore, the HGC head shielding may require an extensive evaluation in terms of design to keep the camera as light as possible and to minimise any possibility of radiation leakage. This aspect may involve selecting another material for shielding with a high atomic number and/or changing the internal shielding design.

However, one of the most innovative ideas to be considered is the development of a SFOV multimodality hybrid gamma-optical imaging system that can provide optical, NIR-fluorescence and gamma images simultaneously. Recently, an increasing number of scholars have turned their attention to the application of fluorescent light within the near-infrared (NIR) window, wavelengths between 700 and 900 nm, as a novel intraoperative imaging technology that can be employed to delineate tumour margins and assess SLNs. This innovative method achieves a higher spatial resolution than more traditional nuclear medicine technologies; it can be employed to examine real-time lymph flow under the skin prior to making an incision (288). NIR fluorescence offers several further advantages including ease of preparation and application, low hazard and toxicity, common availability, affordability, multi-detection capability, and the

provision of distinct molecular information. It is due to these benefits that interest in NIR fluorescence technologies has increased in more recent years. Although the NIR fluorescence approach could enhance imaging at greater depths, the optimum resolution at which images should be taken remains at 5–15 mm under the skin surface (288, 289). As a means of overcoming this limitation, NIR fluorescence and gamma emitting agents have been combined to facilitate SLN navigation in head and neck melanoma, oral cavity lesions, and prostate cancer. This complementary multimodal surgical approach combines the favourable penetration capability of the radio-labelled colloid with the greater spatial resolution of NIR fluorescence techniques as a means of enhancing the accuracy of target identification and reducing the length of surgical procedures (289).

A recent prototype design of such a system includes a modification of the original HGC imaging system by replacing the optical camera with a near-infrared (NIR) camera. A bespoke LED ring placed in the frontal face of the detector to provide an excitation light for the imaged fluorescence source (excitation wavelength = 785 nm) (290). This SFOV multimodality imaging system has potential for mapping fluorescent and gamma probes during guided surgical procedures. Furthermore, it could facilitate preclinical imaging studies with the capability of providing a hybrid imaging mode. Merging different imaging technologies in a single SFOV imaging modality could improve the overall sensitivity and specificity during the process of localising affected tissues during critical surgical settings. However, to reach that stage of full functionality, this prototype multimodality imaging system should be characterised in experimental setting. There is a need to design and manufacture suitable phantoms with the desired optical properties to simulate human soft tissues. Then, these phantoms can be utilised to study the detection limitations of the fluorescence camera. The hardware of this prototype system is an existing area for further development, including the system's configuration, system sensitivity and alignment. Furthermore, preclinical research is a potential area to examine the system and evaluate its performance.

Improving the hardware of the HGC imaging system needs a parallel improvement for the imaging software. The imaging system should provide a real-time hybrid imaging option to facilitate the process of positioning the HGC for scanning procedures. In addition, adding a new modality to the HGC imaging system, i.e. the fluorescence camera, requires a sophisticated imaging software that provides options for the produced images' fusion, so the end user will be able to fuse fluorescence-gamma images, optical-gamma images, and fluorescence-optical images. The imaging software needs a friendly interface that allows easier handling of the device during critical situations, such as intraoperative imaging procedures. To meet the expected functionality, this aspect needs to be carefully approached through interviewing surgeons and surgical-care practitioners. The imaging software should support specified data file formats, such as DICOM, to allow proper filing for the produced data and facilitate any quantitative or qualitative evaluation of the images. Additional ergonomic features would be good to add, including acquisition time on the acquired images, patient's name and file number, and changing colour palette choices.

9.2.4 The environmental use of the HGC

Radioactive contamination mapping poses a significant risk of exposing personnel to dangerous radiation doses. In addition, it is time consuming to map radioactive contamination in nuclear plants during maintenance or decommission operations. Zones of interest are commonly examined using a dose-rate meter that is either remotely operated or even operated by hand in some situations. However, the accuracy of this method is limited because it does not allow the assessment of a large number of measures and it is not always effective, especially when several sources are being investigated and/or the background level is high. Compact portable gamma-imaging systems represent a promising technology that allows radiation safety workers to identify and assess sources remotely and relatively quickly without the need for personnel to enter the irradiating zone.

A portable imaging system that can provide optical and gamma imaging simultaneously can be used for environmental radiation monitoring. The HGC is fitted with a pinhole collimator, which facilitates a larger field of view when increasing the distance from the primary source of radiation contamination, and allows the screening of large areas. Moreover, the availability of a hybrid optical-gamma imaging facility will simplify the process of localising the source of radiation within the field of view. For using the HGC in this setting, it needs to be characterised using various radioactivity sources with different gamma energies, and then it can be evaluated for specific radiation contamination scenarios. Using the HGC imaging system may require employing a remote control system to allow fitting the HGC imaging head on a robot to explore contaminated areas. Such a concept could expand the scope of using the HGC, another possible area for further research.

Appendices

Appendix A. Qualitative study instruction sheet (Chapter 7)

UNIVERSITY OF LEICESTER

Qualitative evaluation of the sentinel lymph nodes detection in the head and neck region

Introduction

Thank you for participating in this qualitative study. This study aims to provide more understanding of the capability of the hybrid gamma camera (HGC) through employing it in scanning an anthropomorphic head and neck phantom. You will find below the procedure of running the java code that is developed to present various gamma images for you to evaluate.

How to run the code?

You will be provided with a MacBook Pro laptop to run the java code. The laptop password is **1408**. Once you logged in, you will find the data folders on the Desktop, and they are named as follow: **test1, test2 … test4**. Please, be aware of that running this java code for the same data folder twice will overwrite your previous readings. To avoid this problem, there is an empty folder on the Desktop having your name; you need to copy and paste the whole data folder (i.e. test1 or test2) to your folder as a backup to avoid reading through the data set again.

There are 7 steps you should follow to run the code:

1. Press **Ctrl + space button** to open the searching bar
2. Type the word "**terminal**", and press **Enter**
3. The terminal window will appear. You need to type the directory of the data files "**cd Desktop/**", then press **Enter**
4. Type the name of the data folder "**cd test1/**", and make sure you use the right number of the data set file to avoid overwriting your previous readings, then press **Enter**.
5. Open the sources file by typing "**cd src/**", then press **Enter**
6. Compile the study's java code through entering "**javac qualitativestudy/Main.java**", then press **Enter**
7. Run the java code via typing "**java –cp . qualitativestudy/Main**", then press **Enter**

Figure 1 shows a screenshot of the terminal window after entering all the running commands for the java code. You need to be careful while you typing the commands to be able to run the code.
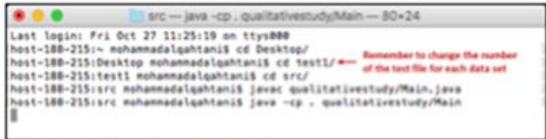
Figure 1. Screenshot of the terminal window

After you run the java code, you will be asked to insert a number representing how many hot spots you recognised in the image, and you will be able to insert any number ranging between 0 and 9. Each data folder will contain a maximum of 144 images. Figure 2 shows a screenshot of the java code interface, and its details.
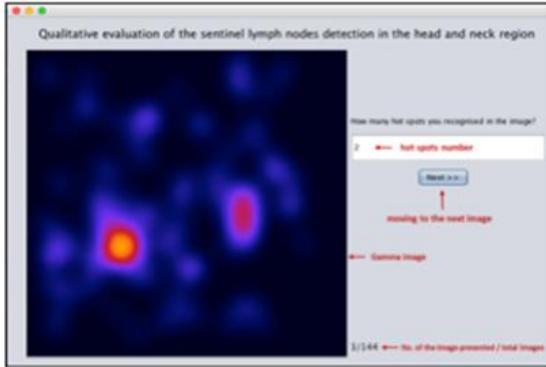
Figure 2. Screenshot of the java code interface

Appendix B. Qualitative study – bespoke JavaScript code for displaying and randomising gamma images (Chapter 7)

```java
1   package qualitativestudy;
2
3 ▼ import java.awt.event.KeyEvent;
4   import java.io.File;
5   import java.io.FileNotFoundException;
6   import java.io.FileOutputStream;
7   import java.io.PrintWriter;
8   import java.net.URL;
9   import java.util.ArrayList;
10  import java.util.Arrays;
11  import java.util.Collections;
12  import java.util.Map;
13  import java.util.Map.Entry;
14  import java.util.TreeMap;
15  import javax.swing.ImageIcon;
16  import javax.swing.JOptionPane;
17
18 ▼ public class Main extends javax.swing.JFrame {
19
20      // Location of input images
21      URL PATH = getClass().getResource("../images");
22      PrintWriter pw;
23
24      ArrayList<File> images;
25      int totalImages;
26      Map<Integer, String> data;
27
28 ▼    public Main() {
29          data = new TreeMap<>();
30          loadImages();
31          initComponents();
32          displayNextImage();
33      }
34
35 ▼    /**
36       * Triggered by the Next button event.
37       * Renders the image & image count
38       */
39 ▼    private void displayNextImage() {
40          lblCount.setText((totalImages - images.size() + 1) + "/" + totalImages);
41          lblImage.setIcon(new ImageIcon(images.get(0).getPath()));
42      }
43
44 ▼    /**
45       * Read images from the directory path & load the names in an ArrayList
46       * Create an empty output file (Results.csv)
47       */
48 ▼    private void loadImages() {
49 ▼        try {
50              new File(PATH.getPath() + "/results.csv").delete(); // Delete output file if exists
51              File folder = new File(PATH.toURI());
52              // Read all the images with extension .jpg
53 ▼            images = new ArrayList<>(Arrays.asList(folder.listFiles((File pathname) -> {
54                  return pathname.getName().toLowerCase().endsWith("jpg");
55              })));
56              // Randomize the list of images
57              Collections.shuffle(images);
58              totalImages = images.size();
59 ▼        } catch (Exception e) {
60              JOptionPane.showMessageDialog(null, "Unable to collect images");
61              System.exit(0);
62          }
63      }
64
65 ▼    /**
66       * Initialise components (auto created by Drag & Drop interface)
67       */
68      @SuppressWarnings("unchecked")
69      // <editor-fold defaultstate="collapsed" desc="Generated Code">
70 ▼    private void initComponents() {
71
72          jLabel1 = new javax.swing.JLabel();
73          jLabel2 = new javax.swing.JLabel();
74          btnNext = new javax.swing.JButton();
75          lblCount = new javax.swing.JLabel();
76          lblImage = new javax.swing.JLabel();
77          txtSpots = new javax.swing.JTextField();
78
79          setDefaultCloseOperation(javax.swing.WindowConstants.EXIT_ON_CLOSE);
80
81          jLabel1.setFont(new java.awt.Font("Lucida Grande", 0, 18)); // NOI18N
82          jLabel1.setText("<html>Qualitative evaluation of the sentinel lymph nodes detection in the head and neck
            region</html>");
83
84          jLabel2.setText("How many hot spots you recognised in the image?");
85
86          btnNext.setText("Next >>");
```

```
 87            btnNext.setEnabled(false);
 88 ▼         btnNext.addActionListener(new java.awt.event.ActionListener() {
 89 ▼             public void actionPerformed(java.awt.event.ActionEvent evt) {
 90                 btnNextActionPerformed(evt);
 91             }
 92         });
 93
 94            lblCount.setFont(new java.awt.Font("Lucida Grande", 0, 14)); // NOI18N
 95            lblCount.setText("jLabel3");
 96
 97 ▼         txtSpots.addKeyListener(new java.awt.event.KeyAdapter() {
 98 ▼             public void keyTyped(java.awt.event.KeyEvent evt) {
 99                 txtSpotsKeyTyped(evt);
100             }
101 ▼             public void keyPressed(java.awt.event.KeyEvent evt) {
102                 txtSpotsKeyPressed(evt);
103             }
104 ▼             public void keyReleased(java.awt.event.KeyEvent evt) {
105                 txtSpotsKeyReleased(evt);
106             }
107         });
108
109           javax.swing.GroupLayout layout = new javax.swing.GroupLayout(getContentPane());
110           getContentPane().setLayout(layout);
111           layout.setHorizontalGroup(
112               layout.createParallelGroup(javax.swing.GroupLayout.Alignment.LEADING)
113               .addGroup(layout.createSequentialGroup()
114                   .addGroup(layout.createParallelGroup(javax.swing.GroupLayout.Alignment.LEADING)
115                       .addGroup(layout.createSequentialGroup()
116                           .addGap(49, 49, 49)
117                           .addComponent(jLabel1, javax.swing.GroupLayout.PREFERRED_SIZE, javax.swing.GroupLayout.DEFAULT_SIZE,
                               javax.swing.GroupLayout.PREFERRED_SIZE))
118                       .addGroup(layout.createSequentialGroup()
119                           .addGap(30, 30, 30)
120                           .addComponent(lblImage, javax.swing.GroupLayout.PREFERRED_SIZE, 500,
                               javax.swing.GroupLayout.PREFERRED_SIZE)
121                           .addPreferredGap(javax.swing.LayoutStyle.ComponentPlacement.RELATED)
122                           .addGroup(layout.createParallelGroup(javax.swing.GroupLayout.Alignment.LEADING)
123                               .addComponent(lblCount)
124                               .addComponent(jLabel2)
125                               .addGroup(layout.createSequentialGroup()
126                                   .addGap(105, 105, 105)
127                                   .addComponent(btnNext))
128                               .addComponent(txtSpots, javax.swing.GroupLayout.PREFERRED_SIZE, 305,
                                   javax.swing.GroupLayout.PREFERRED_SIZE))))
129                   .addContainerGap(javax.swing.GroupLayout.DEFAULT_SIZE, Short.MAX_VALUE))
130           );
131           layout.setVerticalGroup(
132               layout.createParallelGroup(javax.swing.GroupLayout.Alignment.LEADING)
133               .addGroup(layout.createSequentialGroup()
134                   .addContainerGap(javax.swing.GroupLayout.DEFAULT_SIZE, Short.MAX_VALUE)
135                   .addComponent(jLabel1, javax.swing.GroupLayout.PREFERRED_SIZE, 41, javax.swing.GroupLayout.PREFERRED_SIZE)
136                   .addGroup(layout.createParallelGroup(javax.swing.GroupLayout.Alignment.TRAILING)
137                       .addGroup(layout.createSequentialGroup()
138                           .addGap(114, 114, 114)
139                           .addComponent(jLabel2)
140                           .addPreferredGap(javax.swing.LayoutStyle.ComponentPlacement.UNRELATED)
141                           .addComponent(txtSpots, javax.swing.GroupLayout.PREFERRED_SIZE, 46,
                               javax.swing.GroupLayout.PREFERRED_SIZE)
142                           .addPreferredGap(javax.swing.LayoutStyle.ComponentPlacement.UNRELATED)
143                           .addGroup(layout.createParallelGroup(javax.swing.GroupLayout.Alignment.LEADING)
144                               .addComponent(btnNext)
145                               .addGroup(javax.swing.GroupLayout.Alignment.TRAILING, layout.createSequentialGroup()
146                                   .addGap(0, 0, Short.MAX_VALUE)
147                                   .addComponent(lblCount, javax.swing.GroupLayout.PREFERRED_SIZE, 33,
                                       javax.swing.GroupLayout.PREFERRED_SIZE))))
148                       .addGroup(layout.createSequentialGroup()
149                           .addPreferredGap(javax.swing.LayoutStyle.ComponentPlacement.RELATED,
                               javax.swing.GroupLayout.DEFAULT_SIZE, Short.MAX_VALUE)
150                           .addComponent(lblImage, javax.swing.GroupLayout.PREFERRED_SIZE, 400,
                               javax.swing.GroupLayout.PREFERRED_SIZE)))
151                   .addContainerGap(17, Short.MAX_VALUE))
152           );
153
154           pack();
155       }// </editor-fold>
156
157 ▼     /**
158        * Next button event, iterates the images in the ArrayList
159        * and then write the reader response to the output file (results.csv)
160        */
161 ▼     private void btnNextActionPerformed(java.awt.event.ActionEvent evt) {
162           System.out.println(images.get(0).getName());
163           System.out.println(images.get(0).getName().split("\\.")[0]);
164           // Write the image name & number of hotspots entered by the user into a Hash object.
165           data.put(Integer.valueOf(images.get(0).getName().split("\\.")[0]), txtSpots.getText());
166           images.remove(0);
167           // Check if there is enough image in the ArrayList to process
168 ▼         if (images.size() > 0) {
169               displayNextImage();
170               txtSpots.setText("");
171               btnNext.setEnabled(false);
172 ▼         } else { // If not write the Hash (user response) into the output file (results.csv)
```

```
172 ▼            } else { // If not write the Hash (user response) into the output file (results.csv)
173 ▼                try {
174                      pw = new PrintWriter(new FileOutputStream(PATH.getPath() + "/results.csv"));
175 ▼                } catch (FileNotFoundException ex) {
176                      JOptionPane.showMessageDialog(null, "Error: Unable to write to output file.");
177                      System.exit(0);
178                  }
179                  StringBuilder sb = new StringBuilder();
180
181                  // Output format: Filename | # of hot spots
182                  sb.append("Filename");
183                  sb.append(",");
184                  sb.append("# of hot spots");
185                  sb.append("\n");
186 ▼                for (Entry<Integer, String> e : data.entrySet()) {
187                      sb.append("image " + e.getKey() + ".jpg");
188                      sb.append(",");
189                      sb.append(e.getValue());
190                      sb.append("\n");
191                  }
192                  pw.write(sb.toString());
193                  pw.close();
194
195                  JOptionPane.showMessageDialog(null, "Complete!!!");
196                  System.exit(0);
197              }
198          }
199
200 ▼    private void txtSpotsKeyPressed(java.awt.event.KeyEvent evt) {
201
202          }
203
204 ▼    /**
205      * Restricts user input to only numeric
206      */
207 ▼    private void txtSpotsKeyTyped(java.awt.event.KeyEvent evt) {
208          char c = evt.getKeyChar();
209          int len = txtSpots.getText().length();
210 ▼        if (len > 0 || !((c >= '0') && (c <= '9') || (c == KeyEvent.VK_BACK_SPACE) || (c == KeyEvent.VK_DELETE))) {
211              getToolkit().beep();
212              evt.consume();
213          }
214      }
215
216 ▼    /**
217      * Keeps the focus on Next button throughout the execution
218      */
219 ▼    private void txtSpotsKeyReleased(java.awt.event.KeyEvent evt) {
220          int len = txtSpots.getText().length();
221 ▼        if(len == 0) {
222              btnNext.setEnabled(false);
223 ▼        } else {
224              btnNext.setEnabled(true);
225              getRootPane().setDefaultButton(btnNext);
226              btnNext.requestFocus();
227          }
228      }
229
230 ▼    /**
231      * @param args the command line arguments
232      */
233 ▼    public static void main(String args[]) {
234          /* Set the Nimbus look and feel */
235          //<editor-fold defaultstate="collapsed" desc=" Look and feel setting code (optional) ">
236 ▼        /* If Nimbus (introduced in Java SE 6) is not available, stay with the default look and feel.
237          * For details see http://download.oracle.com/javase/tutorial/uiswing/lookandfeel/plaf.html
238          */
239 ▼        try {
240 ▼            for (javax.swing.UIManager.LookAndFeelInfo info : javax.swing.UIManager.getInstalledLookAndFeels()) {
241 ▼                if ("Nimbus".equals(info.getName())) {
242                      javax.swing.UIManager.setLookAndFeel(info.getClassName());
243                      break;
244                  }
245              }
246 ▼        } catch (ClassNotFoundException ex) {
247              java.util.logging.Logger.getLogger(Main.class.getName()).log(java.util.logging.Level.SEVERE, null, ex);
248 ▼        } catch (InstantiationException ex) {
249              java.util.logging.Logger.getLogger(Main.class.getName()).log(java.util.logging.Level.SEVERE, null, ex);
250 ▼        } catch (IllegalAccessException ex) {
251              java.util.logging.Logger.getLogger(Main.class.getName()).log(java.util.logging.Level.SEVERE, null, ex);
252 ▼        } catch (javax.swing.UnsupportedLookAndFeelException ex) {
253              java.util.logging.Logger.getLogger(Main.class.getName()).log(java.util.logging.Level.SEVERE, null, ex);
254          }
255          //</editor-fold>
256
```

```
257         /* Create and display the form */
258 ▼      java.awt.EventQueue.invokeLater(new Runnable() {
259 ▼          public void run() {
260              new Main().setVisible(true);
261          }
262      });
263      }
264
265      // Variables declaration - do not modify
266      private javax.swing.JButton btnNext;
267      private javax.swing.JLabel jLabel1;
268      private javax.swing.JLabel jLabel2;
269      private javax.swing.JLabel lblCount;
270      private javax.swing.JLabel lblImage;
271      private javax.swing.JTextField txtSpots;
272      // End of variables declaration
273
274  }
275
```

Appendix C. Ethical approval of the feasibility clinical study using the HGC (Chapter 8)

1

NHS
Health Research Authority

NRES Committee East Midlands - Leicester
The Old Chapel
Royal Standard Place
Nottingham
NG1 6FS

Telephone: 0115 8839425
Facsimile: 0115 8839294

12 June 2012

Professor AC Perkins
Professor of Medical Physics
Nottingham University
Department of Medical Physics
A floor Medical School
QMC, Nottingham
NG7 2UH

Dear Professor Perkins,

Study title:	A pilot study to develop and evaluate a prototype hand held hybrid gamma camera
REC reference:	12/EM/0201
Protocol number:	12023

The Research Ethics Committee reviewed the above application at the meeting held on 01 June 2012. Thank you for attending to discuss the study.

Ethical opinion

- The committee asked you whether the clinical manager will be part of the care team. You confirmed that Ms Elaine Blackshaw who is the clinical manager is part of the team.

- The committee asked you how many images are usually taken. You confirmed that this is not usually anymore than half a dozen.

- The committee stated to you that the withdrawal process is not clear and there are inconsistencies between documents. You confirmed that participants can stop anytime during taking the images.

- The committee asked you whether participants will be identified by their initials and code or just by code. You stated that participants can just be identified by code.

- The committee asked you how participants can be related back to their images. You explained that the gamma camera can take images which will be given an anonymous code, you stated that there are two cameras being used which one is a standard gamma camera. The committee went on to say that it should be explicit in the Participant Information Sheet that two cameras will be used.

- The committee asked you what their definition of vulnerable is as this is not included in the exclusion or inclusion criteria. You confirmed that they deem vulnerable people to be those who cannot consent for themselves.

- The committee stated that if they are not including participants who are non English speakers then this should be part of the exclusion criteria.

A Research Ethics Committee established by the Health Research Authority

2

- The committee asked you whether the amount of money to be given from the funders is correct as this seems too much. You confirmed that this is an error and they will be given 9,000 pounds for funding.

- The committee asked you whether refreshments and travel expenses will be reimbursed. You confirmed that tea and coffee will be provided as well payment of £10 for food and that travel expenses.

- The committee stated that the Participant Information Sheet wording implies that readers will join the study and this should be reworded. You confirmed that this could be done.

- The committee asked you whether the email address provided in the Participant Information Sheet is case sensitive. You confirmed that the email address is not case sensitive.

- The committee asked what the gamma camera actually looks like as there is no diagram provided. You brought a gamma camera to pass around the committee members.

- The committee stated that the complaints section in the Participant Information Sheet should be on one page. You explained that the University of Nottingham advised on the layout of the Participant Information Sheet, but that this can be changed.

The members of the Committee present gave a favourable ethical opinion of the above research on the basis described in the application form, protocol and supporting documentation, subject to the conditions specified below.

Ethical review of research sites

NHS Sites

The favourable opinion applies to all NHS sites taking part in the study, subject to management permission being obtained from the NHS/HSC R&D office prior to the start of the study (see "Conditions of the favourable opinion" below).

Conditions of the favourable opinion

The favourable opinion is subject to the following conditions being met prior to the start of the study.

Management permission or approval must be obtained from each host organisation prior to the start of the study at the site concerned.

Management permission ("R&D approval") should be sought from all NHS organisations involved in the study in accordance with NHS research governance arrangements.

Guidance on applying for NHS permission for research is available in the Integrated Research Application System or at http://www.rdforum.nhs.uk.

Where a NHS organisation's role in the study is limited to identifying and referring potential participants to research sites ("participant identification centre"), guidance should be sought from the R&D office on the information it requires to give permission for this activity.

3

For non-NHS sites, site management permission should be obtained in accordance with the procedures of the relevant host organisation.

Sponsors are not required to notify the Committee of approvals from host organisations

1. The following amendments are required to the Participant Information Sheet;
a) It should be made explicit that two gamma cameras will be used
b) The first sentence in section 'What are the possible disadvantages and risks of taking part?' should be re-worded
c) In section 'What if there is a problem?' the researchers contact details should also be listed
d) The wording that implies that readers will definitely be joining the study should be reworded
e) It should be clear that withdrawal can take place at any time before and during imaging

2. The Consent Form should be given to the participants separately and not apart of the Participant Information Sheet.

It is responsibility of the sponsor to ensure that all the conditions are complied with before the start of the study or its initiation at a particular site (as applicable).

You should notify the REC in writing once all conditions have been met (except for site approvals from host organisations) and provide copies of any revised documentation with updated version numbers. Confirmation should also be provided to host organisations together with relevant documentation

Approved documents

The documents reviewed and approved at the meeting were:

Document	Version	Date
Evidence of insurance or indemnity		24 April 2012
Investigator CV		30 April 2012
Letter from Sponsor		01 May 2012
Other: The prototype hand held hybrid gamma camera		31 January 2012
Participant Consent Form	1.0	30 April 2012
Participant Information Sheet	1.0	30 April 2012
Protocol	1.0	30 April 2012
REC application	90180/319202/1/503	30 April 2012

Membership of the Committee

The members of the Ethics Committee who were present at the meeting are listed on the attached sheet.

Statement of compliance

The Committee is constituted in accordance with the Governance Arrangements for Research Ethics Committees and complies fully with the Standard Operating Procedures for Research Ethics Committees in the UK.

4

After ethical review

Reporting requirements

The attached document "After ethical review – guidance for researchers" gives detailed guidance on reporting requirements for studies with a favourable opinion, including:

- Notifying substantial amendments
- Adding new sites and investigators
- Notification of serious breaches of the protocol
- Progress and safety reports
- Notifying the end of the study

The NRES website also provides guidance on these topics, which is updated in the light of changes in reporting requirements or procedures.

Feedback

You are invited to give your view of the service that you have received from the National Research Ethics Service and the application procedure. If you wish to make your views known please use the feedback form available on the website.

Further information is available at National Research Ethics Service website > After Review

12/EM/0201	Please quote this number on all correspondence

With the Committee's best wishes for the success of this project

Yours sincerely

pp J. Parkement
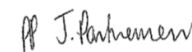
Dr Carl Edwards
Chair

Email: jessica.parfrement@nottspct.nhs.uk

Enclosures: List of names and professions of members who were present at the meeting and those who submitted written comments
"After ethical review – guidance for researchers"

Copy to: Sponsor - Mr Paul Cartledge

R&D Contact - Dr Maria Koufali

Appendix D. Participant Information Sheet and the consent form - the feasibility clinical study using the HGC (Chapter 8)

The University of Nottingham

Queen's Medical Centre Campus
Department of Medical Physics
Derby Road
Nottingham
NG7 2UH

Participant Information Sheet
Final version 3.0: 27/01/2014

Title of Study:
A pilot study to develop and evaluate a prototype hand held hybrid gamma camera

Name of Researcher(s):   Prof AC Perkins and Ms E Blackshaw
Dr JE Lees, D Bassford and S Botterill

Invitation:
Thank you for thinking about taking part in this medical research study. Before you decide to take part it is important for you to understand why the research is being done and what it will involve. Please take time to read the following information carefully and think about whether or not you want to take part in this study. You might wish to discuss it with your friends, relatives and the research team (contact details at the end of this document). Ask us if there is anything that is not clear or if you would like more information.

Thank you for reading this.

What is the purpose of the study?
Scientists from the University of Leicester Space Research Centre and Nottingham University have been working together to develop a hand held hybrid medical gamma camera. The hybrid camera can take both a photograph and a gamma ray image of sites in the body. Gamma images are routinely taken in nuclear medicine clinics and use gamma rays that are very similar to X-rays. Gamma images are formed from medicines containing a small amount of radioactivity that are administered as part of a test to diagnose health problems. These radioactive medicines are known as radiopharmaceuticals and are similar to X-rays At the moment gamma cameras are very big machines that cannot be moved. This restricts the type of patients who can benefit from this technology as only patients who are relatively mobile and can attend the clinic have access to

Page 1 of 6

A pilot study to develop and evaluate a prototype hand held hybrid gamma camera
Participant Information Sheet Final Version 3.0 date 27/01/2014

gamma camera tests. Patients in places such as operating theatres and intensive care units do not have access to a gamma camera as they can not be easily moved. This is why we are developing a smaller portable model to help these patients.

We are inviting males and females aged greater than 18 years who will receive a radiopharmaceutical injection as part of a routine diagnostic test to take part in this study which will be running until end May 2015.

Why have I been invited?
You have been chosen because you are to receive a radiopharmaceutical injection as part of the test that you that have been referred for in the Nuclear Medicine Clinic.

Do I have to take part?
No - it is up to you whether or not you want to take part. If you do decide to take part, Professor Perkins or one of his representatives will discuss the study with you. You will be given this information sheet to keep. You will also be asked to sign a consent form (a copy will be given to you).

What will happen to me if I take part?
The research will take place at the Nuclear Medicine Clinics in the Department of Medical Physics, at Queen's Medical Centre and Nottingham City Hospital. You will be attending one of these clinics for your diagnostic test.

You will arrive at the Nuclear Medicine Clinic as requested on your patient letter. You will receive your radiopharmaceutical from the clinic staff, this may be swallowed or injected and is detailed in the patient letter explaining your test. You may also receive some initial diagnostic images on the Nuclear Medicine clinic gamma camera following the administration of the radiopharmaceutical. Again your patient letter will explain the diagnostic test requirements.

After the initial diagnostic images (if required) have been taken and you are willing to take part in the research study, we will ask you to sign the consent form agreeing to participate in this study. Once this is done we will make arrangements with yourself and the clinic staff responsible for you, to take some images using the small research camera being developed. If you are happy we might also ask that we take some

Page 2 of 6

A pilot study to develop and evaluate a prototype hand held hybrid gamma camera Participant Information Sheet Final Version 3.0 date 27/01/2014

images with the large gamma camera which is used for research purposes only. This will take place in a separate room in the same department. Gamma cameras do not emit radiation or X-rays, do not involve you lying in a tunnel and you do not have to take your clothes off. Each image will take no longer than 5 minutes. You can choose to stay for only one image or many more if you have the time and you are free to withdraw at any time. These images will remain anonymous and it will not be possible to identify you from them.

Once we have obtained our images you will be offered refreshment (tea / coffee) and will return back to the clinic for the continuation of your test or go on to any other tests that may be booked for you, or be able to go home. The research is at an early stage and we will ensure that by participating in this study that you do not miss or compromise any current or further tests.

Expenses and payments
We will compensate you for taking part by giving you an allowance of £10 for your participation. This is to help cover taxi fares, car parking and any other expenses you incur by taking part in this study.

What are the possible disadvantages and risks of taking part?
We do not expect side effects from participating in this study. We are simply asking that you might consider giving some of your time to help us in this research project while you are attending your clinic appointment

We do not regard that there are any risks involved in taking part in this study.

What are the possible benefits of taking part?
You will not directly benefit from taking part in this study. However in the future the study may benefit patients (operating theatre/intensive care) who cannot get to a camera for a diagnostic test.

What if there is a problem?
If you have a concern about any aspect of this study, you should ask to speak to the researchers who will do their best to answer your questions. The researchers contact details are given at the end of this information sheet. If you remain unhappy and wish to complain formally, the normal National Health Service complaints mechanisms should be available to you. PALS (Patient Advice and Liaison Service) telephone 0800 183 0204

Will my taking part in the study be kept confidential?
We will follow ethical and legal practice and all information about you will be handled in confidence.

If you join the study, some parts of your medical records and the data collected for the study will be looked at by authorised persons from the University of Nottingham who are organising the research. They may also be looked at by authorised people to check that the study is being carried out correctly. All will have a duty of confidentiality to you as a research participant and we will do our best to meet this duty.

All information which is collected about you during the course of the research will be kept **strictly confidential**, stored in a secure and locked office, and on a password protected database. Any information about you that leaves the hospital will have your name and address removed (anonymised) and a unique code will be used so that you cannot be recognised from it. It is possible that images in this study will be used in scientific publications / presentations.

Your contact details (address, telephone number) will not be kept be kept for longer than one year following completion of the study. All other data (research data) will be kept securely for 7 years. After this time your data will be disposed of securely. During this time all precautions will be taken by all those involved to maintain your confidentiality, only members of the research team will have access to your personal data.

You should be aware that there is a possibility that your data may be transferred to a country outside the EAA (all European Union Member States plus Iceland, Liechtenstein and Norway). However, you will not be identified by name.

What will happen if I don't want to carry on with the study?
Your participation is voluntary and you are free to withdraw at any time, without giving any reason, and without your legal rights being affected. If you withdraw then the information collected so far cannot be erased and this information may still be used in the project analysis.

What will happen to the results of the research study
There is a possibility that the results of the study will be published in scientific journals, or presented at scientific conferences, you will not be identified by name and any images used will not allow identification of you.

Who is organising and funding the research?
The study is being organised by the University of Nottingham and is being funded by the Science Technology Facilities Council (CLASP Award).

Who has reviewed the study?
All research in the NHS is looked at by an independent group of people, called a Research Ethics Committee to protect your safety, rights, well being and dignity. This study has been reviewed and given a favourable opinion by the Leicester Research Ethics committee. This study has also been reviewed and approved by NHS Trust Research and Development Committee (R&D).

Further information and contact details
If you would like further information from experts not involved in this study we recommend that you talk to Dr D Pye (Consultant Clinical Scientist, Head of Nuclear Medicine Clinic – 0115 9249924 X 64893) for the Nottingham University Hospitals NHS Trust if you have concerns.

Contact for further information:

For any further information about this study please contact:

ELAINE BLACKSHAW DEPARTMENT OF MEDICAL PHYSICS, QMC.

TELEPHONE: 0115 9709283, ext. 62934

EMAIL: ELAINE.BLACKSHAW@NOTTINGHAM.AC.UK.

Thank you for reading this and considering taking part in the study

The University of Nottingham

NHS

Queen's Medical Centre Campus
Department of Medical Physics
Derby Road
Nottingham
NG7 2UH

CONSENT FORM
Final version 3.0: 27th January-2014

A PILOT STUDY TO DEVELOP AND EVALUATE A PROTOTYPE HAND HELD HYBRID GAMMA CAMERA

REC ref: 12/EM/0201

Name of Researchers: Prof AC Perkins and Ms E Blackshaw
Dr JE Lees, D Bassford and S Botterill

Subject number _____   **Please initial box**

1. I confirm that I have read and understand the information sheet version number 3.0 dated: 27-01-14 for the above study and have had the opportunity to ask questions.

2. I understand that my participation is voluntary and that I am free to withdraw at any time, without giving any reason, and without my medical care or legal rights being affected. I understand that should I withdraw then the information collected so far cannot be erased and that this information may still be used in the project analysis.

3. I understand that relevant sections of my data collected in the study may be looked at by authorised individuals from the University of Nottingham, the research group and regulatory authorities where it is relevant to my taking part in this study. I give permission for these individuals to have access to these records and to collect, store, analyse and publish information obtained from my participation in this study. I understand that my personal details will be kept confidential and that my contact details will be destroyed within one year of the study completion.

4. I agree to the transfer of my anonymised data outside of the EEA (European Economic Area).

5. I agree to take part in the above study.

Name of Participant	Date	Signature

Name of Person taking consent (if different from Principal Investigator)	Date	Signature

Name of Principal Investigator	Date	Signature

2 copies: 1 for participant, 1 for the study masterfile

Bibliography

1.   Wernick MN, Aarsvold JN. Emission Tomography: The Fundamentals of PET and SPECT. 1st ed. California, USA: Elsevier Academic Press; 2004.

2.   Le Roux PY, Robin P, Salaun PY. New developments and future challenges of nuclear medicine and molecular imaging for pulmonary embolism. Thrombosis research. 2017.

3.   Gutfilen B, Valentini G. Radiopharmaceuticals in nuclear medicine: recent developments for SPECT and PET studies. BioMed research international. 2014;2014:426892.

4.   Landau SM, Thomas BA, Thurfjell L, Schmidt M, Margolin R, Mintun M, et al. Amyloid PET imaging in Alzheimer's disease: a comparison of three radiotracers. European journal of nuclear medicine and molecular imaging. 2014;41(7):1398-407.

5.   Baum RP. Therapeutic Nuclear Medicine 1st ed. Berlin, Heidelberg: Springer; 2014.

6.   Heller S, Zanzonico P. Nuclear probes and intraoperative gamma cameras. Seminars in nuclear medicine. 2011;41(3):166-81.

7.   Kopelman D, Blevis I, Iosilevsky G, Hatoum OA, Zaretzki A, Shofti R, et al. Sentinel node detection in an animal study: evaluation of a new portable gamma camera. International surgery. 2007;92(3):161-6.

8.   Perkins AC, Lees JE. Gamma Cameras for Interventional and Intraoperative Imaging. 1st ed: CRC Press; 2016.

9.   Newman LA. Current issues in the surgical management of breast cancer: a review of abstracts from the 2002 San Antonio Breast Cancer Symposium, the 2003 Society of Surgical Oncology annual meeting, and the 2003 American Society of Clinical Oncology meeting. The breast journal. 2004;10 Suppl 1:S22-5.

10.   Goyal A, Newcombe RG, Mansel RE, Chetty U, Ell P, Fallowfield L, et al. Role of routine preoperative lymphoscintigraphy in sentinel node biopsy for breast cancer. European journal of cancer. 2005;41(2):238-43.

11.   Tafra L, McMasters KM, Whitworth P, Edwards MJ. Credentialing issues with sentinel lymph node staging for breast cancer. American journal of surgery. 2000;180(4):268-73.

12.   Mathelin C, Salvador S, Bekaert V, Croce S, Andriamisandratsoa N, Liegeois P, et al. A new intraoperative gamma camera for the sentinel lymph node procedure in breast cancer. Anticancer Res. 2008;28(5B):2859-64.

13.   Mathelin C, Salvador S, Croce S, Andriamisandratsoa N, Huss D, Guyonnet JL. Optimization of sentinel lymph node biopsy in breast cancer using an operative gamma camera. World journal of surgical oncology. 2007;5(1):132.

14.   Mathelin C, Salvador S, Huss D, Guyonnet JL. Precise Localization of Sentinel Lymph Nodes and Estimation of Their Depth Using a Prototype Intraoperative Mini - Camera in Patients with Breast Cancer. Journal of Nuclear Medicine. 2007;48(4):623-9.

15.   Britten AJ. A method to evaluate intra-operative gammaprobes for sentinel lymph node localisation. European Journal of Nuclear Medicine. 1999;26(2):8.

16.   Aarsvold JN, Alazraki NP. Update on detection of sentinel lymph nodes in patients with breast cancer. Seminars in nuclear medicine. 2005;35(2):116-28.

17.   Schmid-Schonbein GW. Microlymphatics and lymph flow. Physiological reviews. 1990;70(4):987-1028.

18.   Tran Cao HS, McElroy M, Kaushal S, Hoffman RM, Bouvet M. Imaging of the interaction of cancer cells and the lymphatic system. Advanced drug delivery reviews. 2011;63(10-11):886-9.

19.   Cronenwett JL, Johnston KW. Rutherford's Vascular Surgery. 8th ed: Saunders; 2014.

20.   Standring S. Gray's Anatomy: The Anatomical Basis of Clinical Practice. 41st ed: Elsevier; 2016.

21.   Tanis PJ, Nieweg OE, Valdes Olmos RA, Kroon BB. Anatomy and physiology of lymphatic drainage of the breast from the perspective of sentinel node biopsy. Journal of the American College of Surgeons. 2001;192(3):399-409.

22.   Aukland K, Reed RK. Interstitial-Lymphatic Mechanisms in the Control of Extracellular Fluid Volume. Physiol Rev. 1993;73(1):1-78.

23.   Mariani G, Moresco L, Viale G, Villa G, Bagnasco M, Canavese G, et al. Radioguided Sentinel Lymph Node Biopsy in Breast Cancer Surgery. J Nucl Med. 2001;42(8):1198-215.

24.   Morton DL, Wen DR, Wong JH, Economou JS, Cagle LA, Storm FK, et al. Technical details of intraoperative lymphatic mapping for early stage melanoma. Archives of surgery. 1992;127(4):392-9.

25.   Kapteijn BA, Nieweg OE, Petersen JL, Rutgers EJ, Hart AA, van Dongen JA, et al. Identification and biopsy of the sentinel lymph node in breast cancer. European journal of surgical oncology. 1998;24(5):427-30.

26.   Coit DG. The "true" sentinel lymph node: in search of an operational definition of a biological phenomenon. Annals of surgical oncology. 2001;8(3):187-9.

27.   Balch CM, Ross MI. Sentinel Lymphadenectomy for Melanoma?Is It a Substitute for Elective Lymphadenectomy? Annals of Surgical Oncology. 1999;6(5):416-7.

28.   Morton DL, Bostick PJ. Will the True Sentinel Node Please Stand? Annals of Surgical Oncology. 1999;6(1):12-4.

29.   Boxen I, McCready D, Ballinger JR. Sentinel node detection and definition may depend on the imaging agent and timing. Clin Nucl Med. 1999;24(6):390-4.

30.   DeCicco C, Sideri M, Bartolomei M, Maggioni A, Colombo N, Bocciolone L, et al. Sentinel node detection by lymphoscintigraphy and gamma detecting probe in patients with vulvar cancer. Journal of Nuclear Medicine. 1997;38(5):115-.

31.   Gershenwald JE, Tseng C-h, Thompson W, Mansfield PF, Lee JE, Bouvet M, et al. Improved sentinel lymph node localization in patients with primary melanoma with the use of radiolabeled colloid. Surgery. 1998;124(2):203-10.

32.   Taylor A, Jr., Murray D, Herda S, Vansant J, Alazraki N. Dynamic lymphoscintigraphy to identify the sentinel and satellite nodes. Clinical nuclear medicine. 1996;21(10):755-8.

33.   Noguchi M. Sentinel lymph node biopsy and breast cancer. The British journal of surgery. 2002;89(1):21-34.

34.   Wilhelm AJ, Mijnhout GS, Franssen EJ. Radiopharmaceuticals in sentinel lymph-node detection - an overview. Eur J Nucl Med. 1999;26(4 Suppl):S36-42.

35.   Leidenius MH, Leppanen EA, Krogerus LA, Smitten KA. The impact of radiopharmaceutical particle size on the visualization and identification of sentinel nodes in breast cancer. Nuclear medicine communications. 2004;25(3):233-8.

36.   Nieweg OE, Jansen L, Valdes Olmos RA, Rutgers EJ, Peterse JL, Hoefnagel KA, et al. Lymphatic mapping and sentinel lymph node biopsy in breast cancer. Eur J Nucl Med. 1999;26(4 Suppl):S11-6.

37.   Chinol M, Paganelli G. Current status of commercial colloidal preparations for sentinel lymph node detection. Eur J Nucl Med. 1999;26(5):560.

38.   Giammarile F, Alazraki N, Aarsvold JN, Audisio RA, Glass E, Grant SF, et al. The EANM and SNMMI practice guideline for lymphoscintigraphy and sentinel node localization in breast cancer. European journal of nuclear medicine and molecular imaging. 2013;40(12):1932-47.

39.   Clarke D, Khonji NI, Mansel RE. Sentinel node biopsy in breast cancer: ALMANAC trial. World journal of surgical oncology. 2001;25(6):819–22.

40.   Bourgeois P. Scintigraphic investigations of the lymphatic system: the influence of injected volume and quantity of labeled colloidal tracer. J Nucl Med. 2007;48(5):693-5.

41.   Valdes-Olmos RA, Jansen L, Hoefnagel CA, Nieweg OE, Muller SH, Rutgers EJ, et al. Evaluation of mammary lymphoscintigraphy by a single intratumoral injection for sentinel node identification. J Nucl Med. 2000;41(9):1500-6.

42.   Werner JA, Dunne AA, Ramaswamy A, Folz BJ, Brandt D, Kulkens C, et al. Number and location of radiolabeled, intraoperatively identified sentinel nodes in 48 head and neck cancer patients with clinically staged N0 and N1 neck. European archives of oto-rhino-laryngology. 2002;259(2):91-6.

43.   Ikomi F, Kawai Y, Ohhashi T. Recent advance in lymph dynamic analysis in lymphatics and lymph nodes. Annals of vascular diseases. 2012;5(3):258-68.

44.   Ikomi F, Hanna GK, Schmidschonbein GW. Mechanism of Colloidal Particle Uptake into the Lymphatic-System - Basic Study with Percutaneous Lymphography. Radiology. 1995;196(1):107-13.

45.   O'Morchoe CC, Jones WR, 3rd, Jarosz HM, O'Morchoe PJ, Fox LM. Temperature dependence of protein transport across lymphatic endothelium in vitro. The Journal of cell biology. 1984;98(2):629-40.

46.   Lund T, Wiig H, Reed RK, Aukland K. A New Mechanism for Edema Generation - Strongly Negative Interstitial Fluid Pressure Causes Rapid Fluid-Flow into Thermally Injured Skin. Acta Physiol Scand. 1987;129(3):433-5.

47.   Engeset A, Sokolowski J, Olszewski WL. Variation in output of leukocytes and erythrocytes in human peripheral lymph during rest and activity. Lymphology. 1977;10(4):198-203.

48.   Olszewski W, Engeset A, Jaeger PM, Sokolowski J, Theodorsen L. Flow and composition of leg lymph in normal men during venous stasis, muscular activity and local hyperthermia. Acta physiologica Scandinavica. 1977;99(2):149-55.

49.   Woolfenden JM, Barber HB. Radiation Detector Probes for Tumor-Localization Using Tumor-Seeking Radioactive-Tracers. Am J Roentgenol. 1989;153(1):35-9.

50.   Moffat FL. Targeting gold at the end of the rainbow: Surgical gamma probes in the 21st century. J Surg Oncol. 2007;96(4):286-9.

51.   Ricard M. Intraoperative detection of radiolabeled compounds using a hand held gamma probe. Nuclear Instruments and Methods in Physics Research Section A: Accelerators, Spectrometers, Detectors and Associated Equipment. 2001;458(1-2):26-33.

52.   Zanzonico P, Heller S. The intraoperative gamma probe: Basic principles and choices available. Seminars in nuclear medicine. 2000;30(1):33-48.

53.   Schneebaum S, Even-Sapir E, Cohen M, Shacham-Lehrman H, Gat A, Brazovsky E, et al. Clinical applications of gamma-detection probes – radioguided surgery. European Journal of Nuclear Medicine. 1999;26(S1):S26-S35.

54.   Sarikaya I, Sarikaya A, Reba RC. Gamma probes and their use in tumor detection in colorectal cancer. International seminars in surgical oncology : ISSO. 2008;5:25.

55.   Povoski SP, Neff RL, Mojzisik CM, O'Malley DM, Hinkle GH, Hall NC, et al. A comprehensive overview of radioguided surgery using gamma detection probe technology. World journal of surgical oncology. 2009;7.

56.   Tsuchimochi M, Hayama K, Oda T, Togashi M, Sakahara H. Evaluation of the efficacy of a small CdTe gamma-camera for sentinel lymph node biopsy. J Nucl Med. 2008;49(6):956-62.

57.   Tsuchimochi M, Sakahara H, Hayama K, Funaki M, Ohno R, Shirahata T, et al. A prototype small CdTe gamma camera for radioguided surgery and other imaging applications. European journal of nuclear medicine and molecular imaging. 2003;30(12):1605-14.

58.   Pitre S, Menard L, Ricard M, Solal M, Garbay JR, Charon Y. A hand-held imaging probe for radio-guided surgery: physical performance and preliminary clinical experience. European journal of nuclear medicine and molecular imaging. 2003;30(3):339-43.

59.   Alan C. Perkins, Lees JE. Gamma Cameras for Interventional and Intraoperative Imaging: CRC Press; 2016.

60.   Chapman. J, Hugg. J, Vesel. J, Bai. C, Blevis. I, Barrett H, et al. Performance measurement of scintillation cameras. Rosslyn: National Electrical Manufacturers Association: NEMA NU 1; 2007.

61.   Muehllehner G. Standards for Performance Measurements in Scintillation Cameras. Japanese Journal of Radiological Technology. 1981;37(3):373-4.

62.   Murphy PH. Acceptance testing and quality control of gamma cameras, including SPECT. J Nucl Med. 1987;28(7):1221-7.

63.   Busemann Sokole E, Plachcinska A, Britten A, Lyra Georgosopoulou M, Tindale W, Klett R. Routine quality control recommendations for nuclear medicine instrumentation. European journal of nuclear medicine and molecular imaging. 2010;37(3):662-71.

64.   Bhatia BS, Bugby SL, Lees JE, Perkins AC. A scheme for assessing the performance characteristics of small field-of-view gamma cameras. Phys Med. 2015;31(1):98-103.

65.   Trevert E. Something about X Rays for everybody: Lynn: Bubier Publishing; 1896.

66.   Hill R, Holloway L, Baldock C. A dosimetric evaluation of water equivalent phantoms for kilovoltage x-ray beams. Physics in medicine and biology. 2005;50(21):N331-44.

67.   Pantelis E, Karlis AK, Kozicki M, Papagiannis P, Sakelliou L, Rosiak JM. Polymer gel water equivalence and relative energy response with emphasis on low photon energy dosimetry in brachytherapy. Physics in medicine and biology. 2004;49(15):3495-514.

68.   Sokole EB, Graham LS, Todd-Pokropek A, Wegst A, Robilotta C, Krisanachinda A. IAEA quality control atlas for scintillation camera systems. Vienna: International Atomic Energy Agency; 2003.

69.   Becker D, Charkes ND, Dworkin H, Hurley J, McDougall IR, Price D, et al. Procedure guideline for thyroid uptake measurement: 1.0. Society of Nuclear Medicine. J Nucl Med. 1996;37(7):1266-8.

70.   Jaszczak RJ, Li J, Wang H, Zalutsky MR, Coleman RE. Pinhole collimation for ultra-high-resolution, small-field-of-view SPECT. Physics in medicine and biology. 1994;39(3):425-37.

71.   Li J, Jaszczak RJ, Greer KL, Coleman RE. A filtered backprojection algorithm for pinhole SPECT with a displaced centre of rotation. Physics in medicine and biology. 1994;39:165-76.

72.   Seret A. Hot and cold contrasts in high-resolution Tc-99m planar scintigraphy: a survey of fifty-two camera heads using the PICKER thyroid phantom. Phys Med. 2010;26(3):166-72.

73.   Cerqueira RAD, Maia AF. Development of thyroid anthropomorphic phantoms for use in nuclear medicine. Radiation Physics and Chemistry. 2014;95:174-6.

74.   Hermosilla A, Diaz Londono G, Garcia M, Ruiz F, Andrade P, Perez A. Design and manufacturing of anthropomorphic thyroid-neck phantom for use in nuclear medicine centres in Chile. Radiation protection dosimetry. 2014;162(4):508-14.

75.   Hoffman EJ, Cutler PD, Guerrero TM, Digby WM, Mazziotta JC. Assessment of accuracy of PET utilizing a 3-D phantom to simulate the activity distribution of [18F]fluorodeoxyglucose uptake in the human brain. Journal of cerebral blood flow and metabolism. 1991;11(2):A17-25.

76.   Hoffman EJ, Cutler PD, Digby WM, Mazziotta JC. 3-D Phantom to Simulate Cerebral Blood-Flow and Metabolic Images for PET. Ieee Transactions on Nuclear Science. 1990;37(2):616-20.

77.   Vines DC, Ichise M, Liow J, Toyama H, Innis RB. Evaluation of 2 Scatter Correction Methods Using a Striatal Phantom for Quantitative Brain SPECT. J Nucl Med Technol 2003;31(3):157-60.

78.   Iida H, Hori Y, Ishida K, Imabayashi E, Matsuda H, Takahashi M, et al. Three-dimensional brain phantom containing bone and grey matter structures with a realistic head contour. Annals of nuclear medicine. 2013;27(1):25-36.

79.   Jonasson LS, Axelsson J, Riklund K, Boraxbekk CJ. Simulating effects of brain atrophy in longitudinal PET imaging with an anthropomorphic brain phantom. Physics in medicine and biology. 2017;62(13):5213-27.

80.   Tran-Gia J, Schlogl S, Lassmann M. Design and Fabrication of Kidney Phantoms for Internal Radiation Dosimetry Using 3D Printing Technology. J Nucl Med. 2016;57(12):1998-2005.

81.   Woliner-van der Weg W, Deden LN, Meeuwis AP, Koenrades M, Peeters LH, Kuipers H, et al. A 3D-printed anatomical pancreas and kidney phantom for optimizing SPECT/CT reconstruction settings in beta cell imaging using (111)In-exendin. EJNMMI physics. 2016;3(1):29.

82.   Robinson AP, Tipping J, Cullen DM, Hamilton D, Brown R, Flynn A, et al. Organ-specific SPECT activity calibration using 3D printed phantoms for molecular radiotherapy dosimetry. EJNMMI physics. 2016;3(1):12.

83.   Kopelman D, Blevis I, Iosilevsky G, Reznik A, Chaikov A, Weiner N, et al. A newly developed intra-operative gamma camera: performance characteristics in a laboratory phantom study. European journal of nuclear medicine and molecular imaging. 2005;32(10):1217-24.

84.   Riccardi L, Gabusi M, Bignotto M, Gregianin M, Vecchiato A, Paiusco M. Assessing good operating conditions for intraoperative imaging of melanoma sentinel nodes by a portable gamma camera. Phys Med. 2015;31(1):92-7.

85.   Lees JE, Bassford DJ, Blackshaw PE, Perkins AC. Design and use of mini-phantoms for high resolution planar gamma cameras. Appl Radiat Isot. 2010;68(12):2448-51.

86.   Fathala A. Myocardial perfusion scintigraphy: techniques, interpretation, indications and reporting. Annals of Saudi medicine. 2011;31(6):625-34.

87.   Sfakianaki E, Sfakianakis GN, Georgiou M, Hsiao B. Renal scintigraphy in the acute care setting. Seminars in nuclear medicine. 2013;43(2):114-28.

88.   Peterson TE, Furenlid LR. SPECT detectors: the Anger Camera and beyond. Physics in medicine and biology. 2011;56(17):R145-82.

89.   Tsuchimochi M, Hayama K. Intraoperative gamma cameras for radioguided surgery: technical characteristics, performance parameters, and clinical applications. Phys Med. 2013;29(2):126-38.

90.   Cherry SR, Sorenson JA, Phelps ME. Physics in Nuclear Medicine. 4th ed. Philadelphia: ELSEVIER; 2012.

91.   Saha GB. Physics and Radiobiology of Nuclear Medicine. 4th ed. New York: Springer; 2013.

92.   Powsner RA, Powsner ER. Essential Nuclear Medicine Physics. 2nd ed. Massachusetts, USA: Blackwell Publishing Ltd; 2006.

93.   Cantone MC, Hoeschen C. Radiation Physics for Nuclear Medicine. 1st ed. Heidelberg: Springer; 2011.

94.   Anger H. Scintillation Camera with Multichannel Collimators. Journal of Nuclear Medicine. 1964;5:515-31.

95.   Moses WW. Current trends in scintillator detectors and materials. Nuclear Instruments and Methods in Physics Research Section A: Accelerators, Spectrometers, Detectors and Associated Equipment. 2002;487(1-2):123-8.

96.   Weisenberger AG, Kross B, Majewski S, Wojlck R, Bradley EL, Saha MS. Design features and performance of a CsI(Na) array based gamma camera for small animal gene research. IEEE Transactions on Nuclear Science. 1998;45(6):3053-8.

97.   van Eijk CW. Inorganic scintillators in medical imaging. Physics in medicine and biology. 2002;47(8):R85-106.

98.   Short MD. Gamma-camera systems. Nuclear Instruments and Methods in Physics Research. 1984;221(1):142-9.

99.   Yang P, Harmon CD, Doty FP, Ohlhausen JA. Effect of Humidity on Scintillation Performance in Na and Tl Activated CsI Crystals. Ieee Transactions on Nuclear Science. 2014;61(2):1024-31.

100.   Keszthelyi-Landori S. NaI(Tl) camera crystals: imaging capabilities of hydrated regions on the crystal surface. Radiology. 1986;158(3):823-6.

101.   Zanzonico P. Principles of nuclear medicine imaging: planar, SPECT, PET, multi-modality, and autoradiography systems. Radiation research. 2012;177(4):349-64.

102.   Wong TZ, Turkington TG, Polascik TJ, Coleman RE. ProstaScint (capromab pendetide) imaging using hybrid gamma camera-CT technology. AJR American journal of roentgenology. 2005;184(2):676-80.

103.   Patt BE, Iwanczyk JS, Tull CR, Wang NW, Tornai MP, Hoffman EJ. High resolution CsI(Tl)/Si-PIN detector development for breast imaging. Ieee Transactions on Nuclear Science. 1998;45(4):2126-31.

104.   Meikle SR, Kench P, Kassiou M, Banati RB. Small animal SPECT and its place in the matrix of molecular imaging technologies. Physics in medicine and biology. 2005;50(22):R45-61.

105.   Jones EA, Phan TD, Blanchard DA, Miley A. Breast-specific gamma-imaging: molecular imaging of the breast using 99mTc-sestamibi and a small-field-of-view gamma-camera. Journal of nuclear medicine technology. 2009;37(4):201-5.

106.   Giokaris N, Loudos G, Maintas D, Karabarbounis A, Lembesi M, Spanoudaki V, et al. Partially slotted crystals for a high-resolution gamma-camera based on a position sensitive photomultiplier. Nucl Instrum Meth A. 2005;550(1-2):305-12.

107.   Giokaris N, Loudos G, Maintas D, Karabarbounis A, Lembesi M, Spanoudaki V, et al. Comparison of CsI(Tl) and CsI(Na) partially slotted crystals for high-resolution SPECT imaging. Nuclear Instruments and Methods in Physics Research Section A. 2006;569(2):185-7.

108.   Harbert JC, Eckelman WC, Neumann RD. Nuclear Medicine: Diagnosis and Therapy. 1st ed. New York: Thieme Medical; 1996.

109.   Cree MJ, Bones PJ. Towards direct reconstruction from a gamma camera based on Compton scattering. IEEE transactions on medical imaging. 1994;13(2):398-407.

110.   Basko R, Zeng GL, Gullberg GT. Application of spherical harmonics to image reconstruction for the Compton camera. Physics in medicine and biology. 1998;43(4):887-94.

111.   Jaszczak RJ, Floyd CE, Jr., Manglos SH, Greer KL, Coleman RE. Cone beam collimation for single photon emission computed tomography: analysis, simulation, and image reconstruction using filtered backprojection. Medical physics. 1986;13(4):484-9.

112.   Bruyant PP. Analytic and iterative reconstruction algorithms in SPECT. J Nucl Med. 2002;43(10):1343-58.

113.   Seo Y, Wong KH, Sun M, Franc BL, Hawkins RA, Hasegawa BH. Correction of photon attenuation and collimator response for a body-contouring SPECT/CT imaging system. J Nucl Med. 2005;46(5):868-77.

114.   Gerber MS, Miller DW. Letter: Parallel-hole collimator design. J Nucl Med. 1974;15(8):724-5.

115.   Muehllehner G, Dudek J, Moyer R. Influence of hole shape on collimator performance. Physics in medicine and biology. 1976;21(2):242-50.

116.   Moore SC, Kouris K, Cullum I. Collimator design for single photon emission tomography. Eur J Nucl Med. 1992;19(2):138-50.

117.   Keller EL. Optimum dimensions of parallel-hole, multi-aperture collimators for gamma-ray cameras. J Nucl Med. 1968;9(6):233-5.

118.   Bugby SL. Development of a hybrid portable medical gamma camera. Leicester, UK: University of Leicester; 2015.

119.   Van Audenhaege K, Van Holen R, Vandenberghe S, Vanhove C, Metzler SD, Moore SC. Review of SPECT collimator selection, optimization, and fabrication for clinical and preclinical imaging. Medical physics. 2015;42(8):4796-813.

120.   Tsui BM, Gullberg GT. The geometric transfer function for cone and fan beam collimators. Physics in medicine and biology. 1990;35(1):81-93.

121.   Habraken JBA, de Bruin K, Shehata M, Booij J, Bennink R, Smit BLFV, et al. Evaluation of high-resolution pinhole SPECT using a small rotating animal. Journal of Nuclear Medicine. 2001;42(12):1863-9.

122.   Weber DA, Ivanovic M. Pinhole SPECT: ultra-high resolution imaging for small animal studies. J Nucl Med. 1995;36(12):2287-9.

123.   Siman W, Kappadath SC. Performance characteristics of a new pixelated portable gamma camera. Medical physics. 2012;39(6):3435-44.

124.   Hruska CB, Weinmann AL, Tello Skjerseth CM, Wagenaar EM, Conners AL, Tortorelli CL, et al. Proof of concept for low-dose molecular breast imaging with a dual-head CZT gamma camera. Part II. Evaluation in patients. Medical physics. 2012;39(6):3476-83.

125.   Castro IF, Soares AJ, Moutinho LM, Ferreira MA, Ferreira R, Combo A, et al. Characterization of a small CsI(Na)-WSF-SiPM gamma camera prototype using ^{99m}Tc. Journal of Instrumentation. 2013;8(03):C03008-C.

126.   Sanchez F, Fernandez MM, Gimenez M, Benlloch JM, Rodriguez-Alvarez MJ, Garcia de Quiros F, et al. Performance tests of two portable mini gamma cameras for medical applications. Medical physics. 2006;33(11):4210-20.

127.   Sun X, Liu JJ, Wang YS, Wang L, Yang GR, Zhou ZB, et al. Roles of preoperative lymphoscintigraphy for sentinel lymph node biopsy in breast cancer patients. Japanese journal of clinical oncology. 2010;40(8):722-5.

128.   Peek MC, Kovacs T, Baker R, Hamed H, Kothari A, Douek M. Is blue dye still required during sentinel lymph node biopsy for breast cancer? Ecancermedicalscience. 2016;10:674.

129.   Bricou A, Duval MA, Charon Y, Barranger E. Mobile gamma cameras in breast cancer care - a review. European journal of surgical oncology. 2013;39(5):409-16.

130.   Mariani G, Guiliano AE, Strauss HW. Radioguided Surgery: A Comprehensive Team Approach. 1st ed. New York: Springer; 2007.

131.   Abe A, Takahashi N, Lee J, Oka T, Shizukuishi K, Kikuchi T, et al. Performance evaluation of a hand-held, semiconductor (CdZnTe)-based gamma camera. European journal of nuclear medicine and molecular imaging. 2003;30(6):805-11.

132.   Parnham KB, Davies RK, Vydrin S, Ferraro F, Jimbo M, Ryou H. Development, design and performance of a CdZnTe-based nuclear medical imager. Journal of Nuclear Medicine. 2002;43(5):229p-p.

133.   Menard L, Charon Y, Solal M, Ricard M, Laniece P, Mastrippolito R, et al. Performance characterization and first clinical evaluation of a intra-operative compact gamma imager. IEEE Transactions on Nuclear Science. 1999;46(6):2068-74.

134.   Kerrou K, Pitre S, Coutant C, Rouzier R, Ancel PY, Lebeaux C, et al. The usefulness of a preoperative compact imager, a hand-held gamma-camera for breast cancer sentinel node biopsy: final results of a prospective double-blind, clinical study. J Nucl Med. 2011;52(9):1346-53.

135.   Oda T, Hayama K, Tsuchimochi M. Evaluation of small semiconductor gamma camera--simulation of sentinel lymph node biopsy by using a trial product of clinical type gamma camera. Kaku igaku The Japanese journal of nuclear medicine. 2009;46(1):1-12.

136.   Scopinaro F, Tofani A, di Santo G, Di Pietro B, Lombardi A, Lo Russo M, et al. High-resolution, hand-held camera for sentinel-node detection. Cancer biotherapy & radiopharmaceuticals. 2008;23(1):43-52.

137.   Ferretti A, Chondrogiannis S, Marcolongo A, Rubello D. Phantom study of a new hand-held gamma-imaging probe for radio-guided surgery. Nuclear medicine communications. 2013;34(1):86-90.

138.   Chondrogiannis S, Ferretti A, Facci E, Marzola MC, Rampin L, Tadayyon S, et al. Intraoperative hand-held imaging gamma-camera for sentinel node detection in patients with breast cancer: feasibility evaluation and preliminary experience on 16 patients. Clinical nuclear medicine. 2013;38(3):e132-6.

139.   Garbay J, Ricard M, Lumbroso J, Rimareix F, Uzan C, Gouy S, et al. A new hand-held gamma camera for sentinel node detection in breast cancer. The Minicam experience in 50 cases. Cancer Research. 2014;69(2 Supplement):1021.

140.   Olcott PD, Habte F, Foudray AM, Levin CS. Performance characterization of a miniature, high sensitivity gamma ray camera. IEEE Transactions on Nuclear Science. 2007;54(5):1492-7.

141.   Olcott P, Pratx G, Johnson D, Mittra E, Niederkohr R, Levin CS. Clinical evaluation of a novel intraoperative handheld gamma camera for sentinel lymph node biopsy. Phys Med. 2014;30(3):340-5.

142.   Sanchez F, Benlloch JM, Escat B, Pavon N, Porras E, Kadi-Hanifi D, et al. Design and tests of a portable mini gamma camera. Medical physics. 2004;31(6):1384-97.

143.   Ortega J, Ferrer-Rebolleda J, Cassinello N, Lledo S. Potential role of a new hand-held miniature gamma camera in performing minimally invasive parathyroidectomy. European journal of nuclear medicine and molecular imaging. 2007;34(2):165-9.

144.   Vidal-Sicart S, Paredes P, Zanon G, Pahisa J, Martinez-Roman S, Caparros X, et al. Added value of intraoperative real-time imaging in searches for difficult-to-locate sentinel nodes. J Nucl Med. 2010;51(8):1219-25.

145.   Paredes P, Vidal-Sicart S, Zanon G, Roe N, Rubi S, Lafuente S, et al. Radioguided occult lesion localisation in breast cancer using an intraoperative portable gamma camera: first results. European journal of nuclear medicine and molecular imaging. 2008;35(2):230-5.

146.   Ghosh D, Michalopoulos NV, Davidson T, Wickham F, Williams NR, Keshtgar MR. Sentinel node detection in early breast cancer with intraoperative portable gamma camera: UK experience. Breast. 2017;32:53-9.

147.   Stoffels I, Poeppel T, Boy C, Mueller S, Wichmann F, Dissemond J, et al. Radio-guided surgery: advantages of a new portable gamma-camera (Sentinella) for intraoperative real time imaging and detection of sentinel lymph nodes in cutaneous malignancies. Journal of the European Academy of Dermatology and Venereology : JEADV. 2012;26(3):308-13.

148.   Cardona-Arbonies J, Mucientes-Rasilla J, Moreno Elola-Olaso A, Salazar-Andia G, Prieto-Soriano A, Chicharo de Freitas J, et al. Contribution of the portable gamma camera to detect the sentinel node in breast cancer during surgery. Revista espanola de medicina nuclear e imagen molecular. 2012;31(3):130-4.

149.   Motomura K, Noguchi A, Hashizume T, Hasegawa Y, Komoike Y, Inaji H, et al. Usefulness of a solid-state gamma camera for sentinel node identification in patients with breast cancer. J Surg Oncol. 2005;89(1):12-7.

150.   Rhodes DJ, Hruska CB, Phillips SW, Whaley DH, O'Connor MK. Dedicated dual-head gamma imaging for breast cancer screening in women with mammographically dense breasts. Radiology. 2011;258(1):106-18.

151.   Hruska CB, O'Connor MK, Collins DA. Comparison of small field of view gamma camera systems for scintimammography. Nuclear medicine communications. 2005;26(5):441-5.

152.   Hruska CB, Weinmann AL, O'Connor MK. Proof of concept for low-dose molecular breast imaging with a dual-head CZT gamma camera. Part I. Evaluation in phantoms. Medical physics. 2012;39(6):3466-75.

153.   Aarsvod JN, Greene CM, Mintzer RA, Grant SF, Styblo TM, Alazraki NP, et al. Intraoperative gamma imaging of axillary sentinel lymph nodes in breast cancer patients. Physica Medica. 2006;21:76-9.

154.   Vermeeren L, Valdes Olmos RA, Klop WM, Balm AJ, van den Brekel MW. A portable gamma-camera for intraoperative detection of sentinel nodes in the head and neck region. J Nucl Med. 2010;51(5):700-3.

155.   Vidal-Sicart S, Vermeeren L, Sola O, Paredes P, Valdes-Olmos RA. The use of a portable gamma camera for preoperative lymphatic mapping: a comparison with a conventional gamma camera. European journal of nuclear medicine and molecular imaging. 2011;38(4):636-41.

156.   Fernández MM, Benlloch JM, Cerdá J, Escat B, Giménez EN, Giménez M, et al. A flat-panel-based mini gamma camera for lymph nodes studies. Nuclear Instruments and Methods in Physics Research Section A: Accelerators, Spectrometers, Detectors and Associated Equipment. 2004;527(1-2):92-6.

157.   Brouwer OR, van den Berg NS, Matheron HM, van der Poel HG, van Rhijn BW, Bex A, et al. A hybrid radioactive and fluorescent tracer for sentinel node biopsy in penile carcinoma as a potential replacement for blue dye. European urology. 2014;65(3):600-9.

158.   Bugby SL, Lees JE, Ng AH, Alqahtani MS, Perkins AC. Investigation of an SFOV hybrid gamma camera for thyroid imaging. Phys Med. 2016;32(1):290-6.

159.   Lees JE, Bassford DJ, Blake OE, Blackshaw PE, Perkins AC. A high resolution Small Field Of View (SFOV) gamma camera: a columnar scintillator coated CCD imager for medical applications. Journal of Instrumentation. 2011;6(12):C12033-C.

160.   Lees JE, Bassford DJ, Blake OE, Blackshaw PE, Perkins AC. A Hybrid Camera for simultaneous imaging of gamma and optical photons. Journal of Instrumentation. 2012;7(06):P06009-P.

161.   Russo P, Curion AS, Mettivier G, Esposito M, Aurilio M, Caraco C, et al. Evaluation of a CdTe semiconductor based compact gamma camera for sentinel lymph node imaging. Medical physics. 2011;38(3):1547-60.

162.   Aarsvold JN, Mintzer RA, Greene C, Grant SF, Styblo TM, Murray DR, et al. Gamma cameras for intraoperative localization of sentinel nodes: Technical requirements identified through operating room experience. Ieee Nucl Sci Conf R. 2003:1172-6.

163.   Aarsvod JN, Greene CM, Mintzer RA, Grant SF, Styblo TM, Alazraki NP, et al. Intraoperative gamma imaging of axillary sentinel lymph nodes in breast cancer patients. Phys Med. 2006;21 Suppl 1:76-9.

164.   Goertzen AL, Thiessen JD, McIntosh B, Simpson MJ, Schellenberg J. Characterization of a Handheld Gamma Camera for Intraoperative Use for Sentinel

Lymph Node Biopsy. 2013 Ieee Nuclear Science Symposium and Medical Imaging Conference (Nss/Mic). 2013.

165.   Netter E, Pinot L, Menard L, Duval MA, Janvier B, Lefebvre F, et al. The Tumor Resection Camera (TReCam), a multipixel imaging probe for radio-guided surgery. IEEE Nuclear Science Symposium Conference Record (NSS/MIC) 2009:2573-6.

166.   Bricou A, Duval MA, Bardet L, Benbara A, Moreaux G, Lefebvre F, et al. Is there a role for a handheld gamma camera (TReCam) in the SNOLL breast cancer procedure? Quarterly Journal on Nuclear Medicine and Molecular Imaging. 2015.

167.   Engelen T, Winkel BM, Rietbergen DD, KleinJan GH, Vidal-Sicart S, Olmos RA, et al. The next evolution in radioguided surgery: breast cancer related sentinel node localization using a freehandSPECT-mobile gamma camera combination. American Journal of Nuclear Medicine and Molecular Imaging. 2015;5(3):233-45.

168.   Ozkan E, Eroglu A. The Utility of Intraoperative Handheld Gamma Camera for Detection of Sentinel Lymph Nodes in Melanoma. Nucl Med Mol Imaging. 2015;49(4):318-20.

169.   Fujii T, Yamaguchi S, Yajima R, Tsutsumi S, Uchida N, Asao T, et al. Use of a handheld, semiconductor (cadmium zinc telluride)-based gamma camera in navigation surgery for primary hyperparathyroidism. The American Surgeon. 2011;77(6):690-3.

170.   Lees JE, Hales JM. Imaging and quantitative analysis of tritium-labelled cells in lymphocyte proliferation assays using microchannel plate detectors originally developed for X-ray astronomy. J Immunol Methods. 2001;247(1-2):95-102.

171.   Lees JE, Fraser GW, Keay A, Bassford D, Ott R, Ryder W. The high resolution gamma imager (HRGI): a CCD based camera for medical imaging. Nuclear Instruments and Methods in Physics Research Section A: Accelerators, Spectrometers, Detectors and Associated Equipment. 2003;513(1-2):23-6.

172.   Lees JE, Bassford D, Fraser GW, Monk D, Early M, Ott RJ, et al. Investigation of scintillator coated CCDs for medical imaging. IEEE Transactions on Nuclear Science. 2006;53(1):9-13.

173.   Bugby SL, Jambi LK, Lees JE. A comparison of CsI:Tl and GOS in a scintillator-CCD detector for nuclear medicine imaging. Journal of Instrumentation. 2016;11(09):P09009-P.

174.   Bugby SL, Lees JE, Bhatia BS, Perkins AC. Characterisation of a high resolution small field of view portable gamma camera. Phys Med. 2014;30(3):331-9.

175.   Hamamatsu Photonics U.K. Limited, 2 Howard Court, 10 Tewin Road, AL7 1BW Welwyn Garden City, Hertfordshire, U.K.

176.   e2v Technologies Ltd., 106 Waterhouse Lane, CM1 2QU Chelmsford, U.K.

177.   Melcor CP 0.8 127 06L thermoelectric device. RS Components Ltd, Birchington Road, NN17 9RS Corby, Northants, UK.

178.   Mettivier G, Montesi MC, Russo P. Design of a compact gamma camera with semiconductor hybrid pixel detectors: imaging tests with a pinhole collimator. Nuclear Instruments and Methods in Physics Research Section A: Accelerators, Spectrometers, Detectors and Associated Equipment. 2003;509(1-3):321-7.

179.   Williams MB, Stolin AV, Kundu BK. Investigation of efficiency and spatial resolution using pinholes with small pinhole angle. IEEE Transactions on Nuclear Science. 2003;50(5):1562-8.

180.   Jeon H, Kim H, Cha BK, Kim JY, Cho G, Chung YH, et al. Performance evaluation for pinhole collimators of small gamma camera by MTF and NNPS analysis: Monte Carlo simulation study. Nuclear Instruments and Methods in Physics Research Section A: Accelerators, Spectrometers, Detectors and Associated Equipment. 2009;604(1-2):93-6.

181.   Bugby SL, Lees JE, Perkins AC. Modelling image profiles produced with a small field of view gamma camera with a single pinhole collimator. Journal of Instrumentation. 2012;7(11):P11025-P.

182.   Karpanen T, Alitalo K. Molecular biology and pathology of lymphangiogenesis. Annual review of pathology. 2008;3:367-97.

183.   Harvey AJ, Kaestner SA, Sutter DE, Harvey NG, Mikszta JA, Pettis RJ. Microneedle-based intradermal delivery enables rapid lymphatic uptake and distribution of protein drugs. Pharmaceutical research. 2011;28(1):107-16.

184.   Jurisic G, Detmar M. Lymphatic endothelium in health and disease. Cell and tissue research. 2009;335(1):97-108.

185.   Dixon JB. Lymphatic lipid transport: sewer or subway? Trends in endocrinology and metabolism: TEM. 2010;21(8):480-7.

186.   Berger DH, Feig BW, Podoloff D, Norman J, Cruse CW, Reintgen DS, et al. Lymphoscintigraphy as a predictor of lymphatic drainage from cutaneous melanoma. Annals of Surgical Oncology. 1997;4(3):247-51.

187.   Vidal M, Vidal-Sicart S, Torrents A, Perissinotti A, Navales I, Paredes P, et al. Accuracy and reproducibility of lymphoscintigraphy for sentinel node detection in patients with cutaneous melanoma. J Nucl Med. 2012;53(8):1193-9.

188.   Morton DL, Wen DR, Wong JH, Economou JS, Cagle LA, Storm FK, et al. Technical Details of Intraoperative Lymphatic Mapping for Early Stage Melanoma. Archives of surgery. 1992;127(4):392-9.

189.   Ferreira CC, Ximenes RE, Garcia CAB, Vieira JW, Maia AF. Total mass attenuation coefficient evaluation of ten materials commonly used to simulate human tissue. Journal of Physics: Conference Series. 2010;249:012029.

190.   Pan W-R, le Roux CM, Levy SM. Alternative lymphatic drainage routes from the lateral heel to the inguinal lymph nodes: anatomic study and clinical implications. ANZ Journal of Surgery. 2011;81(6):431-5.

191.   Kiyono K, Sone S, Sakai F, Imai Y, Watanabe T, Izuno I, et al. The number and size of normal mediastinal lymph nodes: a postmortem study. AJR American journal of roentgenology. 1988;150(4):771-6.

192.   Suami H, Pan WR, Taylor GI. Historical Review of Breast Lymphatic Studies. Clinical anatomy. 2009;22(5):531-6.

193.   Pan WR, Suami H, Taylor GI. Senile changes in human lymph nodes. Lymphatic research and biology. 2008;6(2):77-83.

194.   Keshtgar MRS, Ell PJ. Sentinel lymph node detection and imaging. European journal of nuclear medicine and molecular imaging. 1999;26(1):57-67.

195.   Jensen MR, Simonsen L, Karlsmark T, Bulow J. Lymphoedema of the lower extremities--background, pathophysiology and diagnostic considerations. Clinical physiology and functional imaging. 2010;30(6):389-98.

196.   Ogawa Y, Hayashi K. [99mTc-DTPA-HSA lymphoscintigraphy in lymphedema of the lower extremities: diagnostic significance of dynamic study and muscular exercise]. Kaku igaku The Japanese journal of nuclear medicine. 1999;36(1):31-6.

197.   Cambria RA, Gloviczki P, Naessens JM, Wahner HW. Noninvasive evaluation of the lymphatic system with lymphoscintigraphy: a prospective, semiquantitative analysis in 386 extremities. Journal of vascular surgery. 1993;18(5):773-82.

198.   ARSAC. Notes for Guidance on the Clinical Administration of Radiopharmaceuticals and Use of Sealed Radioactive Sources. UK: Public Health England; 2018.

199.   van der Ent FWC, Kengen RAM, van der Pol HAG, Hoofwijk AGM. Sentinel node biopsy in 70 unselected patients with breast cancer: increased feasibility by using 10 mCi radiocolloid in combination with a blue dye tracer. European Journal of Surgical Oncology. 1999;25(1):24-9.

200.   Gray RJ, Pockaj BA, Roarke MC. Injection of (99m)Tc-labeled sulfur colloid the day before operation for breast cancer sentinel lymph node mapping is as successful as injection the day of operation. American journal of surgery. 2004;188(6):685-9.

201.   McCarter MD, Yeung H, Yeh S, Fey J, Borgen PI, Cody HS, 3rd. Localization of the sentinel node in breast cancer: identical results with same-day and day-before isotope injection. Annals of surgical oncology. 2001;8(8):682-6.

202.   Mariani G, Gipponi M, Moresco L, Villa G, Bartolomei M, Mazzarol G, et al. Radioguided sentinel lymph node biopsy in malignant cutaneous melanoma. Journal of Nuclear Medicine. 2002;43(6):811-27.

203.   Mediso Medical Imaging Systems (2011), NUCLINE™ X-RING-R (HR), -C. Hungary.

204.   Tiago Ferreira WR. ImageJ User Guide2012.

205.   Albert R. Vision: human and electronic. New York Plenum Press; 1973.

206.   Dickerscheid D, Lavalaye J, Romijn L, Habraken J. Contrast-noise-ratio (CNR) analysis and optimisation of breast-specific gamma imaging (BSGI) acquisition protocols. EJNMMI research. 2013;3(1):21.

207.   OriginLab. User Guide [http://www.originlab.com/doc/]. http://www.originlab.com/doc/: OriginLab Corporation; [cited 2017 December].

208.   Hiroyuki Tsushima TT, Takashi Yamanaga, Hiroto Kizu, Yoshihiro Shimonishi, Kazuhisa Kosakai,Atsushi Noguchi and Masahisa Onoguchi. Usefulness of Medium-Energy Collimator for Sentinel Node Lymphoscintigraphy Imaging in Breast Cancer Patients. Journal of nuclear medicine technology. 2006;34:153-8.

209.   Hellingman D, Vidal-Sicart S, de Wit-van der Veen LJ, Paredes P, Valdes Olmos RA. A New Portable Hybrid Camera for Fused Optical and Scintigraphic Imaging: First Clinical Experiences. Clinical nuclear medicine. 2016;41(1):e39-43.

210.   Haneishi H, Shimura H, Hayashi H. Image Synthesis Using a Mini Gamma Camera and Stereo Optical Cameras. IEEE Transactions on Nuclear Science. 2010;57(3):1132-8.

211.   Ross MI, Reintgen DS. Role of lymphatic mapping and sentinel node biopsy in the detection of melanoma nodal metastases. European journal of cancer. 1998;34 Suppl 3:S7-11.

212.   Mariani G, Erba P, Manca G, Villa G, Gipponi M, Boni G, et al. Radioguided sentinel lymph node biopsy in patients with malignant cutaneous melanoma: the nuclear medicine contribution. J Surg Oncol. 2004;85(3):141-51.

213.   Tafra L, McMasters KM, Edwards MJ. Credentialing issues with sentinel lymph node staging for breast cancer. The American Journal of Surgery. 2000;180(4):268-73.

214.   Posther KE, McCall LM, Blumencranz PW, Burak WE, Beitsch PD, Hansen NM, et al. Sentinel Node Skills Verification and Surgeon Performance. Transactions of the Meeting of the American Surgical Association. 2005;123(&NA;):287-96.

215.   Lees JE, Bugby SL, Bhatia BS, Jambi LK, Alqahtani MS, McKnight WR, et al. A small field of view camera for hybrid gamma and optical imaging. Journal of Instrumentation. 2014;9(12):C12020-C.

216.   Fiorini C, Gola A, Peloso R, Longoni A, Lechner P, Soltau H, et al. Imaging performances of the DRAGO gamma camera. Nuclear Instruments and Methods in Physics Research Section A: Accelerators, Spectrometers, Detectors and Associated Equipment. 2009;604(1-2):101-3.

217.   Tapiovaara MJ, Wagner RF. SNR and noise measurements for medical imaging: I. A practical approach based on statistical decision theory. Physics in medicine and biology. 1993;38(1):71-92.

218.   Alzimami KS, Sassi SA, Alfuraih AA, Spyrou NM. Investigation of the potential use of LaBr3:Ce scintillators for scintimammography imaging. Nuclear Instruments and Methods in Physics Research Section A: Accelerators, Spectrometers, Detectors and Associated Equipment. 2011;633:S282-S5.

219.   Fass L. Imaging and cancer: a review. Molecular oncology. 2008;2(2):115-52.

220.   Evans JW, Peters AM. Gamma camera imaging in malignancy. European journal of cancer. 2002;38(16):2157-72.

221.   Tiourina T, Arends B, Huysmans D, Rutten H, Lemaire B, Muller S. Evaluation of surgical gamma probes for radioguided sentinel node localisation. European journal of nuclear medicine and molecular imaging. 1998;25(9):1224-31.

222.   Britten AJ. A method to evaluate intra-operative gamma probes for sentinel lymph node localisation. European journal of nuclear medicine and molecular imaging. 1999;26(2):76-83.

223.   Alqahtani MS, Lees JE, Bugby SL, Jambi LK, Perkins AC. Lymphoscintigraphic imaging study for quantitative evaluation of a small field of view (SFOV) gamma camera. Journal of Instrumentation. 2015;10(07):P07011-P.

224.   Gitsch E, Philipp K, Pateisky N. Intraoperative lymph scintigraphy during radical surgery for cervical cancer. J Nucl Med. 1984;25(4):486-9.

225.   Chen SL, Iddings DM, Scheri RP, Bilchik AJ. Lymphatic mapping and sentinel node analysis: current concepts and applications. CA: a cancer journal for clinicians. 2006;56(5):292-309.

226.   Stoeckli SJ, Steinert H, Pfaltz M, Schmid S. Sentinel lymph node evaluation in squamous cell carcinoma of the head and neck. Otolaryngology--head and neck surgery : official journal of American Academy of Otolaryngology-Head and Neck Surgery. 2001;125(3):221-6.

227.   Hellingman D, de Wit-van der Veen LJ, Klop WM, Olmos RA. Detecting near-the-injection-site sentinel nodes in head and neck melanomas with a high-resolution portable gamma camera. Clinical nuclear medicine. 2015;40(1):e11-6.

228.   Gershenwald JE, Thompson W, Mansfield PF, Lee JE, Colome MI, Tseng CH, et al. Multi-institutional melanoma lymphatic mapping experience: the prognostic value

of sentinel lymph node status in 612 stage I or II melanoma patients. Journal of clinical oncology. 1999;17(3):976-83.

229.   Lin D, Franc BL, Kashani-Sabet M, Singer MI. Lymphatic drainage patterns of head and neck cutaneous melanoma observed on lymphoscintigraphy and sentinel lymph node biopsy. Head & neck. 2006;28(3):249-55.

230.   Even-Sapir E, Lerman H, Lievshitz G, Khafif A, Fliss DM, Schwartz A, et al. Lymphoscintigraphy for sentinel node mapping using a hybrid SPECT/CT system. Journal of Nuclear Medicine. 2003;44(9):1413-20.

231.   Jansen L, Koops HS, Nieweg OE, Doting MH, Kapteijn BA, Balm AJ, et al. Sentinel node biopsy for melanoma in the head and neck region. Head & neck. 2000;22(1):27-33.

232.   Stoeckli SJ. Sentinel node biopsy for oral and oropharyngeal squamous cell carcinoma of the head and neck. The Laryngoscope. 2007;117(9):1539-51.

233.   The-Phantom-Laboratory. RSVP Phantom™ Head II with Bite Feature Manual - Radiosurgery Verification Phantom. Salem, NY 12865-0511: The Phantom Laboratory; 2015.

234.   Richard P. Spencer RW. Size and Positional Relationships Between Thyroid Lobes in the Adult As Determined by Scintillation Scanning. J Nucl Med. 1965;6:53-8.

235.   Tong ECK, Rubenfeld S. Scan Measurements of Normal and Enlarged Thyroid-Glands. Am J Roentgenol. 1972;115(4):706.

236.   Won HS, Han SH, Oh CS, Chung IH, Won HJ, Kim JH. Location and morphometry of the thyroid isthmus in adult Korean cadavers. Anatomical science international. 2013;88(4):212-6.

237.   Oppenheimer JH, Volpé R. Measurement of Thyroid Function. 1990:124-39.

238.   Ozgur Z, Celik S, Govsa F, Ozgur T. Anatomical and surgical aspects of the lobes of the thyroid glands. European archives of oto-rhino-laryngology : official journal of the European Federation of Oto-Rhino-Laryngological Societies. 2011;268(9):1357-63.

239.   Harjeet A, Sahni D, Jit I, Aggarwal AK. Shape, measurements and weight of the thyroid gland in northwest Indians. Surgical and radiologic anatomy : SRA. 2004;26(2):91-5.

240.   Stratasys-Inc. Dimension® Elite 3D Printer User Guide2011.

241.   ICRP. Basic Anatomical and Physiological Data for Use in Radiological Protection Reference Values. Ann ICRP 2002;32:3-4.

242.   ICRU. Tissue substitutes in radiation dosimetry and measurement. Journal of the International Commission on Radiation Units and Measurment 1989;Report 44.

243.   Jones AK, Hintenlang DE, Bolch WE. Tissue-equivalent materials for construction of tomographic dosimetry phantoms in pediatric radiology. Medical physics. 2003;30(8):2072-81.

244.   Staton RJ, Pazik FD, Nipper JC, Williams JL, Bolch WE. A comparison of newborn stylized and tomographic models for dose assessment in pediatric radiology. Health Phys. 2003;84(6):S258-S9.

245.   Larry A. DeWerd MK. The Phantoms of medical and health physics: Devices for research and development New York Springer; 2014.

246.   Berger MJ, Hubbell JH, Seltzer SM, Chang J, Coursey JS, Sukumar R, et al. XCOM: photon cross sections database. NIST Standard reference database. 1998;8(1):3587-97.

247.   Mar MV, Miller SA, Kim EE, Macapinlac HA. Evaluation and localization of lymphatic drainage and sentinel lymph nodes in patients with head and neck melanomas by hybrid SPECT/CT lymphoscintigraphic imaging. Journal of nuclear medicine technology. 2007;35(1):10-6.

248.   G. Giudice SL, F. Robusto, V. Ronghi, E. Nacchiero, G. Giardinelli, G. Di Gioia, L. Ragusa, M. Pascone. Sentinel lymph node biopsy in head and neck melanoma. Giornale di Chirurgia 2014;35(5-6):149-55.

249.   Balch CM, Soong SJ, Atkins MB, Buzaid AC, Cascinelli N, Coit DG, et al. An Evidence-based Staging System for Cutaneous Melanoma. CA: A Cancer Journal for Clinicians. 2004;54(3):131-49.

250.   Mettler FA, Guiberteau MJ. Essentials of Nuclear Medicine Imaging. 6th ed. Philadelphia, PA: Elsevier Inc.; 2012.

251.   Leong SP. Role of selective sentinel lymph node dissection in head and neck melanoma. J Surg Oncol. 2011;104(4):361-8.

252.   Philips. BrightView XCT SPECT/CT system. United States: Philips, Available in: http://www.usa.philips.com/healthcare/product/HC882482/brightview-xct-spect-scanner; 2017.

253.   E. Hansis, A. Da Silva, H. Hines, J. Garrard, D. Sowards-Emmerd, L. Shao. BrightView XCT – flat-panel cone-beam CT with iterative reconstruction for localization and attenuation correction. Philips Healthcare – Nuclear Medicine, San Jose, CA. 2011.

254.   Chia HN-H. Improvement of 3D Printing Resolution by the Development of Shrinkable Materials. Los Angeles: University of California; 2014.

255.   Gomez-Rivera F, Santillan A, McMurphey AB, Paraskevopoulos G, Roberts DB, Prieto VG, et al. Sentinel node biopsy in patients with cutaneous melanoma of the head and neck: recurrence and survival study. Head & neck. 2008;30(10):1284-94.

256.	Shanon E, Samuel Y, Adler A, Rapoport Y, Redianu C. Malignant melanoma of the head and neck in children. Review of the literature and report of a case. Archives of otolaryngology. 1976;102(4):244-7.

257.	Tariq S, Shallwani H, Waqas M, Bari ME. Congenital and infantile malignant melanoma of the scalp: A systematic review. Annals of medicine and surgery. 2017;21:93-5.

258.	Garbe C, Büttner P, Bertz J, Burg G, D'Hoedt B, Drepper H, et al. Primary cutaneous melanoma. Prognostic classification of anatomic location. Cancer. 1995;75(10):2492-8.

259.	Agnese DM, Maupin R, Tillman B, Pozderac RD, Magro C, Walker MJ. Head and neck melanoma in the sentinel lymph node era. Archives of otolaryngology--head & neck surgery. 2007;133(11):1121-4.

260.	Gibbs P, Robinson WA, Pearlman N, Raben D, Walsh P, Gonzalez R. Management of primary cutaneous melanoma of the head and neck: The University of Colorado experience and a review of the literature. J Surg Oncol. 2001;77(3):179-85; discussion 86-7.

261.	Kane WJ, Yugueros P, Clay RP, Woods JE. Treatment outcome for 424 primary cases of clinical stage I cutaneous malignant melanoma of the head and neck. Head & neck. 1997;19(6):457-65.

262.	Alex JC, Krag DN. The gamma-probe-guided resection of radiolabeled primary lymph nodes. Surgical oncology clinics of North America. 1996;5(1):33-41.

263.	Leong SP, Accortt NA, Essner R, Ross M, Gershenwald JE, Pockaj B, et al. Impact of sentinel node status and other risk factors on the clinical outcome of head and neck melanoma patients. Archives of otolaryngology--head & neck surgery. 2006;132(4):370-3.

264.	Leong SPL, Achtem TA, Habib FA, Steinmetz I, Morita E, Allen RE, et al. Discordancy between clinical predictions vs lymphoscintigraphic and intraoperative mapping of sentinel lymph node drainage of primary melanoma. Arch Dermatol. 1999;135(12):1472-6.

265.	Patuzzo R, Maurichi A, Camerini T, Gallino G, Ruggeri R, Baffa G, et al. Accuracy and prognostic value of sentinel lymph node biopsy in head and neck melanomas. J Surg Res. 2014;187(2):518-24.

266.	Obrien CJ, Uren RF, Thompson JF, Howmangiles RB, Petersenschaefer K, Shaw HM, et al. Prediction of Potential Metastatic Sites in Cutaneous Head and Neck Melanoma Using Lymphoscintigraphy. American journal of surgery. 1995;170(5):461-6.

267.	Ikram M, Akhtar S, Maseeh-uz-Zaman, Junaid M, Dhari T, Ahmad Z, et al. Sentinel node localisation using pre-operative lymphoscintigraphy and intraoperative gamma probe in early oral cavity cancer. J Pak Med Assoc. 2013;63(8):976-9.

268.	Hoft S, Maune S, Muhle C, Brenner W, Czech N, Kampen WU, et al. Sentinel lymph-node biopsy in head and neck cancer. British journal of cancer. 2004;91(1):124-8.

269.	Willis AI, Ridge JA. Discordant lymphatic drainage patterns revealed by serial lymphoscintigraphy in cutaneous head and neck malignancies. Head & neck. 2007;29(11):979-85.

270.	Keeble C, Baxter PD, Gislason-Lee AJ, Treadgold LA, Davies AG. Methods for the analysis of ordinal response data in medical image quality assessment. The British journal of radiology. 2016;89(1063):20160094.

271.	Norusis M. IBM SPSS Statistics 19 Statistical Procedures Companion. United States: Pearson Education 2011.

272.	Orero A, Vidal-Sicart S, Roe N, Muxi A, Rubi S, Duch J, et al. Monitoring system for isolated limb perfusion based on a portable gamma camera. Nuklearmedizin Nuclear medicine. 2009;48(4):166-72.

273.	Vermeeren L, Klop WM, van den Brekel MW, Balm AJ, Nieweg OE, Valdes Olmos RA. Sentinel node detection in head and neck malignancies: innovations in radioguided surgery. Journal of oncology. 2009;2009:681746.

274.	Scopinaro F, Massari R, Varvarigou AD, D'Alessandria C, Trotta C, Di Santo GP, et al. High resolution small animal single photon emission computed tomography: uptake of [99mTc]bombesin and [123I]ioflupane by rat brain. The quarterly journal of nuclear medicine and molecular imaging : official publication of the Italian Association of Nuclear Medicine. 2007;51(2):204-10.

275.	Scopinaro F, Paschali E, Di Santo G, Antonellis T, Massari R, Trotta C, et al. Bombesin receptors and transplanted stem cells in rat brain: High-resolution scan with 99mTc BN1.1. Nuclear Instruments and Methods in Physics Research Section A: Accelerators, Spectrometers, Detectors and Associated Equipment. 2006;569(2):525-8.

276.	D'Haese PF, Cetinkaya E, Konrad PE, Kao C, Dawant BM. Computer-aided placement of deep brain stimulators: from planning to intraoperative guidance. IEEE transactions on medical imaging. 2005;24(11):1469-78.

277.	Schrader B, Hamel W, Weinert D, Mehdorn HM. Documentation of electrode localization. Movement disorders : official journal of the Movement Disorder Society. 2002;17 Suppl 3:S167-74.

278.	D'Haese PF, Pallavaram S, Konrad PE, Neimat J, Fitzpatrick JM, Dawant BM. Clinical accuracy of a customized stereotactic platform for deep brain stimulation after accounting for brain shift. Stereotactic and functional neurosurgery. 2010;88(2):81-7.

279.	Langford J, Kemp P, Bolt L, Hoffmann S, Fleming J. DaTSCANTM: can a planar vertex view be of any use? Nuclear medicine communications. 2003;24(4):462.

280.   David Becker, N. David Charkes, Howard Dworkin, James Hurley, I. Ross McDougall, David Price, et al. Procedure Guideline for Thyroid Scintigraphy : 1.0. J Nucl Med. 1996;37:1264-6.

281.   Scerrino G, Castorina S, Melfa GI, Lo Piccolo C, Raspanti C, Richiusa P, et al. The intraoperative use of the mini-gamma camera (MGC) in the surgical treatment of primary hyperparathyroidism Technical reports and immediate results from the initial experience. Ann Ital Chir. 2015;86(3):212-8.

282.   Kitagawa W, Shimizu K, Kumita S, Akasu H, Kumazaki T, Tanaka S. Radio-guided parathyroidectomy for primary hyperparathyroidism combined with video-assisted surgery using the solid-state, multi-crystal gamma camera. J Surg Oncol. 2002;80(3):173-5.

283.   Spanu A, Soluri A, Scopinaro F, Falchi A, Mangano AM, Marongiu P, et al. A new radioisotopic procedure in small-size thyroid nodule detection: a preliminary study. European journal of nuclear medicine and molecular imaging. 2003;30(1):358.

284.   D'Errico G, Rosa MA, Soluri A, Scafe R, Galli M, Chiarini S, et al. Radioguided biopsy of osteoid osteoma: usefulness of imaging probe. Tumori. 2002;88(3):S30-2.

285.   Esra Arzu Gencoglu, Dilek Dursun, Yonca A. Akova, Fethi Cengiz, Hulya Yalcin, Koyuncu A. Tear clearance measurements in patients with dry eye syndrome using qualitative lacrimal scintigraphy. Ann Nucl Med. 2005;19(7):581–7.

286.   Detorakis ET, Zissimopoulos A, Katernellis G, Drakonaki EE, Ganasouli DL, Kozobolis VP. Lower Eyelid Laxity in Functional Acquired Epiphora: Evaluation With Quantitative Scintigraphy. Ophthalmic Plastic & Reconstructive Surgery. 2006;22(1):25-9.

287.   Jakub JW, Gray RJ, Degnim AC, Boughey JC, Gardner M, Cox CE. Current status of radioactive seed for localization of non palpable breast lesions. American journal of surgery. 2010;199(4):522-8.

288.   Dip FD, Ishizawa T, Kokudo N, Rosenthal RJ. Fluorescence Imaging for Surgeons: Concepts and Applications. ed s, editor: Springer International Publishing; 2015.

289.   Vahrmeijer AL, Hutteman M, van der Vorst JR, van de Velde CJH, Frangioni JV. Image-guided cancer surgery using near-infrared fluorescence. Nat Rev Clin Oncol. 2013;10(9):507-18.

290.   Lees JE, Bugby SL, Alqahtani MS, Jambi LK, Dawood NS, McKnight WR, et al. A Multimodality Hybrid Gamma-Optical Camera for Intraoperative Imaging. Sensors. 2017;17(3).